Ultrafast Dynamic Probing of Matter Under Extreme Conditions Using High-Repetition-Rate Laser Wakefield Accelerators

by

Mario Diego Balcazar Munoz-Reyes

A dissertation submitted in partial fulfillment
of the requirements for the degree of
Doctor of Philosophy
(Nuclear Engineering and Radiological Sciences)
in the University of Michigan
2023

Doctoral Committee:

Professor Alexander G. R. Thomas, Co-Chair
Professor Carolyn Kuranz, Co-Chair
Professor Karl M. Krushelnick
Research Scientist John A. Nees
Professor Louise Willingale

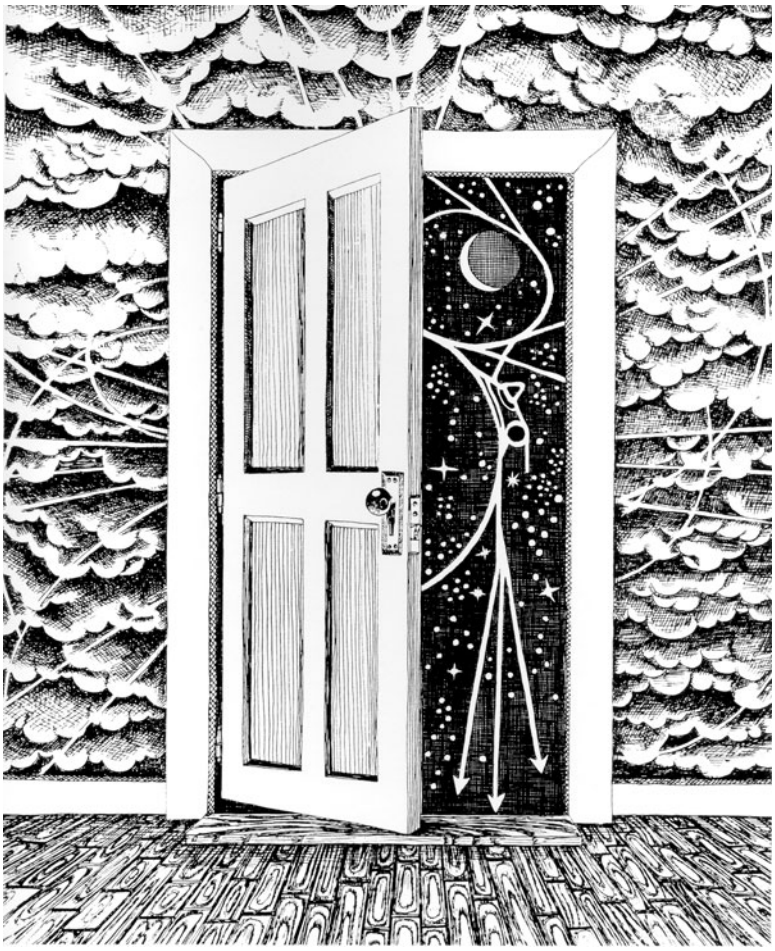

Mario Diego Balcazar Munoz-Reyes
balcazar@umich.edu
ORCID iD: 0000-0003-1151-0316

DEDICATION

This dissertation is the culmination of years of hard work and perseverance, made possible by the steady support and belief of my family and friends. Thank you for your endless encouragement, laughter, and companionship. Your love has provided me with strength during my most challenging moments and made my successes all the more meaningful.

With gratitude,
Mario

ACKNOWLEDGMENTS

My deepest gratitude goes to my advisor and mentor, Prof. Alexander Thomas, for his unwavering patience, wisdom, and brilliant ideas. His profound understanding of physics has been instrumental in my growth as a researcher, and his guidance has consistently inspired me to aim higher. I am profoundly thankful to Prof. Carolyn Kuranz, for her expertise in high-energy-density physics and academic research, her passion and care for students, and for her incredible support, which made this dissertation possible.

Sincerest thanks to my committee members, who have each played a significant role in shaping my academic journey: Prof. Karl Krushelnick, for his total support academically, professionally, and personally, and consistent encouragement; Research Scientist John Nees, for his mentorship and uncountable lessons, which have transformed me into the scientist that I am today; Prof. Louise Willingale, for her brilliant and creative ideas, as well as her sincere kindness.

The series of experiments conducted for this dissertation were supported by LaserNetUS and performed at the BELLA Center in Lawrence Berkeley National Lab. They were conceived collaboratively by A. G. R. Thomas, C. C. Kuranz, F. Albert, S. P. D. Mangles, N. Lemos, and C. G. R. Geddes with experimental support from H-E Tsai, T. Ostermayr, R. Jacob, Q. Chen, B. Greenwood, S. Hakimi, E. Los, R. Simpson, E. Grace, B. Kettle, P. Campbell, Y. Ma, and P. King. The experiments at BELLA HTT received technical and engineering support from Z. Eisentraut, T. Sipla, and M. Kirkpatrick. Target development was performed by M. D. Balcazar with support from J. Nees. Simulations were performed by M. D. Balcazar with support from M. Trantham, R. Young, and C. C. Kuranz. Electric field reconstructions were performed by M. D. Balcazar with support and algorithms developed by P. Campbell, A. G. R. Thomas, and L. Willingale. Data and simulation analysis was performed by M. D. Balcazar with support from A. G. R. Thomas, C. C. Kuranz, P. Campbell, L. Willingale, and K. Krushelnick. Especial acknowledgments are owed to C. G. R. Geddes, J. Van Tilborg, C. Schroeder, E. Esarey, and all members of the BELLA Center for their support throughout the experimental campaigns.

TABLE OF CONTENTS

DEDICATION ii

ACKNOWLEDGMENTS iii

LIST OF FIGURES vi

LIST OF APPENDICES xii

LIST OF ACRONYMS xiii

ABSTRACT xv

CHAPTER

1 Introduction 1

1.1 Motivation 1
1.2 High-intensity lasers and plasma wakefield acceleration 3
1.3 Dissertation outline 6

2 Background 8

2.1 Laser wakefield acceleration 8
2.1.1 Introduction 8
2.1.2 The relativistic ponderomotive force 9
2.1.3 Electron acceleration in a wakefield 11
2.1.4 Generation of betatron radiation in a plasma channel 17
2.2 High-energy-density physics 20
2.2.1 Introduction 20
2.2.2 Hydrodynamic fluid equations 21
2.2.3 Multi-fluid model 24
2.2.4 Shock waves and jump conditions 26
2.2.5 Overview of hydrodynamic instabilities 28

3 Methods 30

3.1 Introduction 30
3.2 BELLA HTT laser system 30
3.2.1 Experimental chamber setup 32
3.3 Diagnostics 34

3.3.1 Optical characterization . . . 34
3.3.2 Description of gas target . . . 35
3.3.3 Electron beam characterization . . . 36
3.3.4 X-ray beam characterization . . . 38
3.4 Analysis . . . 46
3.4.1 Phase-contrast X-ray imaging . . . 46
3.4.2 Density retrieval . . . 51
3.4.3 Electron beam probing and field recovery . . . 56
3.4.4 Computational modeling: FLASH 4.0 . . . 61

4 Liquid Targets for High-Repetition-Rate Experiments . . . 68

4.1 Motivation . . . 68
4.2 Experiment . . . 69
4.3 Discussion . . . 74

5 Dynamic Ultrafast X-Ray Imaging of Shocks in Water . . . 75

5.1 Introduction . . . 75
5.2 Experiment . . . 76
5.3 Results & Simulations . . . 79
5.4 Discussion . . . 85

6 Hydrodynamic Instabilities in Shocked Liquid Jets . . . 88

6.1 Introduction . . . 88
6.2 Results & Simulations . . . 89
6.3 Discussion . . . 95

7 Relativistic Electron Beam Probing Using Laser Wakefield Accelerators . . . 99

7.1 Introduction . . . 99
7.2 Experiment . . . 100
7.3 Results & Simulations . . . 102
7.4 Discussion . . . 113

8 Conclusion and Outlook . . . 122

APPENDICES . . . 125

BIBLIOGRAPHY . . . 130

LIST OF FIGURES

FIGURE

1.1 (a) Multiple laser beams are focused inside an ICF hohlraum [140] and their energy is converted into X-rays, which then compress a fuel capsule until it implodes to create fusion plasma. Figure reproduced from [100]. (b) An X-ray radiograph of the plastic capsule and inner Deuterium-Tritium ice layer showing plastic ablator, DT ice layer, and re-entrant Au cone for the layered HGR platform. Figure reproduced from [158]. (c) Simulation of Rayleigh-Taylor hydrodynamic instability created on LLNL's BlueGene/L supercomputer using Miranda code. Figure reproduced from [99]. 2

3.1 Block diagram showing the BELLA HTT dual-beam laser system architecture. The BELLA HTT system is designed for the generation of ultrafast laser pulses capable of producing LWFA electron beams for Thomson scattering and pump-probe experiments. 31

3.2 Diagram of the BELLA HTT experimental chamber configuration for the pump-probe experiments performed in this dissertation. 33

3.3 Images of focal spots, profiles of focal spots in the transverse direction at focus position, and plots of the laser spots mode maxima and second moments as a function of the longitudinal direction: z-scan. (a) LWFA driver laser and (b) shock heater laser. . . 34

3.4 (left) Measurement of t_0 from both HTT beams for a given delay stage position taken with a photodiode and oscilloscope. (right) Tracking measurement of heater laser spot x and y centroids as a function of delay stage position. 35

3.5 Image of scintillating lanex screen from magnetic spectrometer showing a typical shot with the resulting electron energy (MeV) vs angle (mrad). 36

3.6 (a) Plot of electron beam spectrometer screens for 400 consecutive shots. Displaying the energy range for the beams as well as the calculated charge density. (b) Energy spectrum for the electron beam averaging over 400 shots. The standard deviation on the charge density is also displayed. (c) Scatter plot for 400 shots measuring mean momentum, charge, and divergence of the beam. 37

3.7 (a) Picture of the Ross filter wheel retrieved from Ref. [78] displaying all different channels, materials, and thicknesses in micrometers. (b) Quantum efficiency curve of the Princeton Instruments PI-MTE X-ray CCD camera displaying transmission percentage as a function of photon energy. (c) Material response curves for all channels in the filter wheel as a function of X-ray photon energy. (d) Energy bins from the subtracting of Ross filter pair response curves. The bins are created by the difference in K-edges from two materials that have the same response curve but a different energy range. 39

3.8 (a) Image of Ross filter wheel taken with the HTT betatron X-rays. (b) Comparison of photon counting for all channels in the filter wheel between synthetic best fit and measured data. (c) Estimated synchrotron spectrum given a best-fit critical energy for seven shots. 41
3.9 (a) Expected Fresnel diffraction pattern of a monoenergetic radiation source interfering with a half-plane straight edge as a function of source size. (b) Expected Fresnel diffraction pattern of a monoenergetic radiation source interfering with a half-plane straight edge as a function of source energy. (c) Expected Fresnel diffraction pattern of a polychromatic radiation source interfering with a half-plane straight edge as a function of source size. 44
3.10 (a) Betatron X-ray image of a sharp edge. (b) Lineouts for multiple images and fit of the Fresnel diffraction pattern for a synchrotron spectrum with multiple source sizes. . 46
3.11 Synthetic density map projected along the imaging direction. Synthetic phase-contrast X-ray image (ideal) for a monochromatic radiation source. Synthetic phase-contrast X-ray image (ideal) for a polychromatic radiation source. Synthetic phase-contrast X-ray image (real) for a polychromatic radiation source and finite source size. (a) Images for Gaussian function and (b) corresponding lineouts. (c) Images for top-hat function and (d) corresponding lineouts. 48
3.12 Synthetic density map projected along the imaging direction. Synthetic phase-contrast X-ray image (ideal) for a monochromatic radiation source. Synthetic phase-contrast X-ray image (ideal) for a polychromatic radiation source. Synthetic phase-contrast X-ray image (real) for a polychromatic radiation source and finite source size. (a) Images for cosine function and (b) corresponding lineouts. (c) Images for sinc function and (d) corresponding lineouts. 49
3.13 Synthetic density map projected along the imaging direction. Recovered density map from the synthetic phase-contrast X-ray image with a monochromatic radiation source. Recovered density map from the synthetic phase-contrast X-ray image with polychromatic radiation source. Recovered density map from the synthetic phase-contrast X-ray image with polychromatic radiation source and finite source size. (a) Images for Gaussian function and (b) corresponding lineouts. (c) Images for top-hat function and (d) corresponding lineouts. 53
3.14 Synthetic density map projected along the imaging direction. Recovered density map from the synthetic phase-contrast X-ray image with a monochromatic radiation source. Recovered density map from the synthetic phase-contrast X-ray image with polychromatic radiation source. Recovered density map from the synthetic phase-contrast X-ray image with polychromatic radiation source and finite source size. (a) Images for cosine function and (b) corresponding lineouts. (c) Images for sinc function and (d) corresponding lineouts. 54
3.15 Diagram depicting the geometry for electron beam deflectometry. 56
3.16 Map of user-defined deviation angles α_x and α_y as well as the resulting image I obtained from the calculated potential field $\mathbf{\Phi}$. 58

3.17 (a) Map of deflection potential field Φ as well as a map of the iteratively recovered potential field. (b) Image obtained from the user-defined potential field Φ as well as a calculated image from recovered potential field. (c) Image of magnetic field defined by the user as well as magnetic field recovered by the algorithm. Plots of their corresponding lineouts are displayed for comparison. 60
3.18 (a) Plot of time-power pairs which define the evolution of the laser pulse in FLASH. (b) Spatial intensity profile for $x > 0$. Colors displayed represent time evolution. (c) 3D representation of the FLASH laser pulse constructed from the spatial intensity profile and time-power pairs evolution. (d) Intensity profile of laser pulse in the transverse x and y directions. 66

4.1 Cylindrical jet target CAD assembly. (left) Side view and (right) isometric view. The design includes $3\times$ picomotors controlling the nozzle in the x, y, z directions and $2\times$ translation stages for aligning the target to the experimental probe. 70
4.2 Close-up pictures of a cylindrical water target. (left) A water jet diameter of ~ 100 μm and (right) photo taken inside the vacuum chamber with alignment cameras and a jet diameter of ~ 50 μm. 71
4.3 Photograph showing the configuration of the liquid microjet catcher. 72
4.4 Example photo showing a ~ 30 μm cylindrical water jet target configured in a laser wakefield accelerator pump-probe experiment setup. 73

5.1 (a) Experimental configuration for pump-probe ultrafast X-ray imaging of shocks in water. (b) Characterization of the electron beam, 460 shots were taken continuously measuring the mean momentum, charge, and FWHM divergence angle. (c) Energy spectrum of the betatron X-ray source, measured by imaging a filter wheel with samples of different materials and thicknesses and fitting a synthetic spectrum to the data. (d) Betatron X-ray source size is measured by imaging a sharp knife-edge and fitting the expected Fresnel diffraction pattern for different source sizes. 77
5.2 Time evolution plots for 3D FLASH simulations of laser-water interaction. (a) x-y plane shows a laser-driven shock propagating through the target. (b) y-z plane displays the high-density wrapping around the cylindrical target. (c) x-z plane showing the 3D effects of shock generation from the top, compressing the target symmetrically from around the surface. 79
5.3 (a) Projected density from 3D FLASH radiation hydrodynamic simulation of the interaction of a 200 ps long laser pulse with a 30 μm cylindrical water jet target for $0 < t < 1$ ns. (b) Synthethic phase-contrast X-ray images of laser-driven shock waves using FLASH simulations and solving the Fresnel-Kirchoff integrals for a complex wave distribution. Experimental (c) single-shot and (d) ten-shot average betatron phase-contrast X-ray images of the laser-water interaction. (e) Density map recovered from experimental phase-contrast X-ray images. The water stream flows from left to right, while the long laser pulse propagates from the top. 80

5.4 (a) Center lineouts for phase-contrast X-ray images of the shocked target, both for simulation and experiment. (b) Center lineouts for projected density of the shocked target, both from FLASH 3D simulation and recovered from experimental phase-contrast X-ray images. (c) Plot of shock velocity across the target. Measured by tracking the point of highest density in FLASH, and point of darkest signal in phase-contrast X-ray images. (d) Plot of shock magnitude (density jump) as a function of time. Measured by tracking the magnitude of the projected density as a function of time, both in FLASH simulations as well as from the density recovery analysis of the experimental images. 82
5.5 (a) 2D slice from 3D FLASH simulation of laser water interaction with no surrounding vapor density. (b) 2D slice from 3D FLASH simulation of laser water interaction with a surrounding vapor profile. (c) Experimentally measured data of laser water interaction displayed with Meijering filter, showing compression of the cylindrical target from multiple directions. 84

6.1 Experimental setup used for LWFA betatron X-ray imaging of laser-shocked water at later times $+2 < t < +8$ ns. Particular emphasis is placed on the active correction of the pointing of the shock driver laser to ensure proper alignment with the target as the delay line is varied. 89
6.2 (a) Sketch of the Richtmyer-Meshkov process describing 1: deflection of post-shock fluid from shock normal, 2: introduction of vorticity at the interface, and 3: amplification of structure by the introduced vorticity (b) Sketch used for analyzing the behavior when an oblique shock encounters an interface using different components of the interaction. For convenience, η and β as shown are taken to be positive angles. 90
6.3 (a) Projected density from 3D FLASH simulation. A sinusoidal perturbation was introduced to the radius of the cylindrical water target to observe the evolution of the Richtmyer-Meshkov process. (b) The amplification of the perturbation structure can be observed in the simulations at lower densities. (c) Time delay scan of laser-water interaction captured experimentally using single-shot betatron X-ray imaging. The shock proceeds from left to right, resulting in the displacement of the back interface and subsequent instability formation, displaying the evolution of the Richtmyer-Meshkov process. 91
6.4 (a) Phase-contrast X-ray images of hydrodynamic instability (average of 5 shots per time-step) at $3 < t < 6$ ns. (b) The wavelength of the perturbations is relatively constant and recovered through Fourier analysis. 93
6.5 (a) Stack of line-outs through the center of experimental images (10 shot average). (b) Stack of line-outs through the center of experimental images (single-shot). Left: unperturbed section of the jet. Middle: perturbed center section of the jet. Right: fit to interface displacement velocity. 94
6.6 (a) Phase-contrast X-ray images (10 shot average) displayed with Meijering filter [120] showing a clear growth of the fluid perturbations' amplitude through the RM process. (b) 3D waterfall plot showing ripple magnitude growth with time. (c) Plot of experimentally calculated growth rate and comparison with the theoretical prediction. . 96

7.1 (a) Experimental setup for relativistic electron beam probing of dynamic electromagnetic fields using an LWFA. (b) Electron beam characterization showing its spectrum and charge density for 200 consecutive shots. The mean momentum is plotted as well as its standard deviation. (c) Scatter plot for the beam characteristics including mean momentum, charge, and divergence. 101
7.2 Workflow for background removal and approximation of unperturbed beam profile image I_0. (a) The original measured image is masked to remove the fields at the edges of a logical mask. (b) A low-pass filter is applied to the measured image to find an initial approximation for the unperturbed beam. The inverse of the mask is similarly applied to section out the region with the fields. (c) Both masked images are blended together to obtain a first-order approximation of the unperturbed beam I_0. 104
7.3 Workflow for the recovery of electromagnetic fields from an experimentally taken electron beam image (~ 1 J laser energy deposition). (a) Approximation of the unperturbed reference beam I_0. (b) Comparison between the original electron image and the image obtained from the reconstruction of the deflection potential field Φ. (c) Recovered potential field Φ as well as its gradients corresponding to the deflection angles α_x and α_y. (d) Electric field reconstruction from the deflection angles. The resulting deflection angles can be interpreted as either an electric or a magnetic field. 105
7.4 Workflow for the recovery of electromagnetic fields from an experimentally taken electron beam image (~ 0.5 J laser energy deposition). (a) Approximation of the unperturbed reference beam I_0. (b) Comparison between the original electron image and the image obtained from the reconstruction of the deflection potential field Φ. (c) Recovered potential field Φ as well as its gradients corresponding to the deflection angles α_x and α_y. (d) Electric field reconstruction from the deflection angles. The resulting deflection angles can be interpreted as either an electric or a magnetic field . 107
7.5 Workflow for the recovery of electromagnetic fields from an experimentally taken electron beam image (~ 0.1 J laser energy deposition). (a) Approximation of the unperturbed reference beam I_0. (b) Comparison between the original electron image and the image obtained from the reconstruction of the deflection potential field Φ. (c) Recovered potential field Φ as well as its gradients corresponding to the deflection angles α_x and α_y. (d) Electric field reconstruction from the deflection angles. The resulting deflection angles can be interpreted as either an electric or a magnetic field . 108
7.6 Workflow for the recovery of electromagnetic fields from an experimentally taken electron beam image (~ 0.5 J laser energy deposition with quadrupole). (a) Approximation of the unperturbed reference beam I_0. (b) Comparison between the original electron image and the image obtained from the reconstruction of the deflection potential field Φ. (c) Recovered potential field Φ as well as its gradients corresponding to the deflection angles α_x and α_y. (d) Electric field reconstruction from the deflection angles. The resulting deflection angles can be interpreted as either an electric or a magnetic field 109
7.7 3D FLASH radiation hydrodynamic simulation of the laser-water interaction. The resulting electric fields are derived and projected. (a) Time evolution of projected number density. (b) Time evolution of projected pressure. (c) Time evolution of projected electric field x-component. (d) Time evolution of projected electric field y-component. (e) Time evolution of projected electric field magnitude. 111

7.8 Relativistic electron beam probing of electromagnetic field evolution (~ 0.1 J laser energy deposition). (a) Shows I/I_0 to display the perturbation field and its evolution in time. (b) Path-integrated (projected) electric field (x-component) recovered with iterative algorithm. (c) Path-integrated (projected) electric field (y-component) recovered with iterative algorithm. (d) Path-integrated (projected) electric field magnitude recovered with iterative algorithm. (e) Synthetic electron beam radiography image using the predicted field configuration in order to compare with the original measurement. 112

7.9 Relativistic electron beam probing of electromagnetic field evolution (~ 0.5 J laser energy deposition). (a) Shows I/I_0 to display the perturbation field and its evolution in time. (b) Path-integrated (projected) electric field (x-component) recovered with iterative algorithm. (c) Path-integrated (projected) electric field (y-component) recovered with iterative algorithm. (d) Path-integrated (projected) electric field magnitude recovered with iterative algorithm. (e) Synthetic electron beam radiography image using the predicted field configuration in order to compare with the original measurement. 114

7.10 Relativistic electron beam probing of electromagnetic field evolution (~ 1 J laser energy deposition). (a) Shows I/I_0 to display the perturbation field and its evolution in time. (b) Path-integrated (projected) electric field (x-component) recovered with iterative algorithm. (c) Path-integrated (projected) electric field (y-component) recovered with iterative algorithm. (d) Path-integrated (projected) electric field magnitude recovered with iterative algorithm. (e) Synthetic electron beam radiography image using the predicted field configuration in order to compare with the original measurement. 115

7.11 Synthetic electron beam radiography maps given the electric field topology derived from 3D FLASH simulations. The radiographs are performed for different time delays and multiple regimes are displayed for comparison which vary on the strength of the imposed electric field. (a) $E_0 \times 10^0$, (b) $E_0 \times 10^1$, (c) $E_0 \times 10^2$, (d) $E_0 \times 10^3$, (e) $E_0 \times 10^4$. 117

7.12 Relativistic electron beam probing of electromagnetic field evolution with quadrupole lens (~ 0.5 J laser energy deposition). (a) Shows I/I_0 to display the perturbation field and its evolution in time. (b) Path-integrated (projected) electric field (x-component) recovered with iterative algorithm. (c) Path-integrated (projected) electric field (y-component) recovered with iterative algorithm. (d) Path-integrated (projected) electric field magnitude recovered with iterative algorithm. (e) Synthetic electron beam radiography image using the predicted field configuration in order to compare with the original measurement. 119

B.1 Technical drawing of target assembly including overall height, width, and depth. All dimensions are in millimeters. The height of the target is typically changed to match focus of experimental probe. 129

LIST OF APPENDICES

A Useful Shock Relations **125**

B Technical Drawing of Water Target **128**

LIST OF ACRONYMS

HEDP High-Energy-Density Physics

ICF Inertial Confinement Fusion

MCF Magnetic Confinement Fusion

LWFA Laser Wakefield Acceleration

SM-LWFA Self-Modulated Laser Wakefield Acceleration

PCXI Phase-Contrast X-ray Imaging

NIF National Ignition Facility

XFEL X-ray Free Electron Laser

HTT Hundred-Terawatt-Thomson

BELLA Berkeley Lab Laser Accelerator

LBNL Lawrence Berkeley National Laboratory

CUOS Center for Ultrafast Optical Science

CW Continuous-Wave

PIC Particle-In-Cell

RHS Right-Hand Side

LHS Left-Hand Side

EE Euler Equations

EOS Equation of State

1D One-Dimension

3D Three-Dimensions

RT Rayleigh-Taylor

KH Kelvin-Helmholtz

RM Richtmyer-Meshkov

PSL Photon-Stimulated Luminescence

PSF Point Spread Function

FFT Fast Fourier Transform

TIE Transport-of-Intensity

3T Three-Temperature

ABSTRACT

This dissertation demonstrates the potential of laser wakefield acceleration (LWFA)-generated relativistic electron beams and X-rays as advanced diagnostics in the realm of high-energy-density physics (HEDP) interactions. The high-quality electron beams produced by LWFA provide an ultrafast, bright, and spatially coherent betatron X-ray source with a small size suitable for high-resolution imaging. When coupled with high-repetition-rate laser systems, this lays the foundation for capturing the intricate dynamics of submicron-scale structures, such as hydrodynamic instabilities, with unprecedented spatio-temporal resolution. Diagnosing plasma instabilities is particularly important in order to progress the development of critical technologies such as inertial confinement fusion, promising sustainable energy solutions.

The dissertation features an innovative bulk liquid (water) target operational within high-vacuum environments and under extreme conditions, which is pivotal in achieving the experimental goals. This adaptable target ensures clean and replenishable interactions at high-repetition rates, thus overcoming challenges associated with conventional solid targets in HEDP experiments.

First, betatron X-rays have been used to dynamically capture the interaction of a long laser pulse with the liquid target, observing the generation and evolution of a shock wave in water. Through a combination of experimental results and FLASH hydrodynamic simulations, insights into unique 3D hydrodynamic effects are obtained.

The second core element in this work is hydrodynamic instabilities. Using betatron X-rays, this work illuminates unstable plasma processes at scales that were previously inaccessible. While these insights entail elements of speculation, compelling arguments point toward the Richtmyer-Meshkov process as an underlying mechanism for the instabilities observed in the experiments.

Finally, LWFA-generated relativistic electron beams are used for charged-particle deflectometry of electromagnetic fields. Focusing on the laser-water interplay at ultrafast timescales, results are presented for the observation of time-evolving fields produced from the aftermath of the laser energy deposition into the dense plasma. The experimental measurements have been compared with electron beam radiographs synthetically generated from 3D hydrodynamic simulations.

The measurements carried out in this dissertation pave the way to improved plasma diagnostic systems in HEDP experiments. The utilization of both X-ray photons and relativistic electron beams provides a dual perspective into plasma dynamics that is rarely found.

CHAPTER 1

Introduction

1.1 Motivation

The wish to understand the nature of matter and its properties under different conditions has driven human curiosity for centuries. This pursuit has allowed humans to not only better understand our own biology but also allowed the development of new technologies in medicine, chemistry, and industry. During the beginning of the 20th century, this quest took on new dimensions as the research community began to question what stars are made of, and how they are able to power themselves. High-Energy-Density Physics (HEDP), is a rapidly evolving field that focuses on the study of plasma and matter under extreme conditions, as found in the interiors of stars, the cores of giant planets, and advanced laboratory experiments of the kind performed during this dissertation work. The knowledge gained in this field has widespread implications for astrophysics, materials science, nuclear physics, and other related disciplines. Among the most promising applications of HEDP is the pursuit of practical fusion energy, which has the potential to provide a virtually limitless and clean energy source for humanity. In this sense, gaining insights into the behavior of matter at extreme pressures, temperatures, and densities has the potential to revolutionize our energy landscape, particularly through the development of fusion technologies.

Many different approaches to fusion have been proposed in the past decades, each with its own advantages and technical difficulties. In the absence of a strong gravitational field (the natural plasma confinement method for the universe), the main efforts can be crudely summarized into two groups which differ by the confinement method for the fusion plasma - Magnetic Confinement Fusion (MCF), and Inertial Confinement Fusion (ICF). The MCF machines including Tokamaks or Stellarators rely on strong magnetic fields to confine the hot plasma, and multiple groups are currently pursuing research around the world, steadily making progress towards practical fusion energy. In particular, ITER will be starting operation this decade [70] as the largest fusion experiment to date and a worldwide effort towards fusion. Alternatively, the ICF approach relies on the compression and heating of a small fuel capsule to extreme conditions using powerful lasers

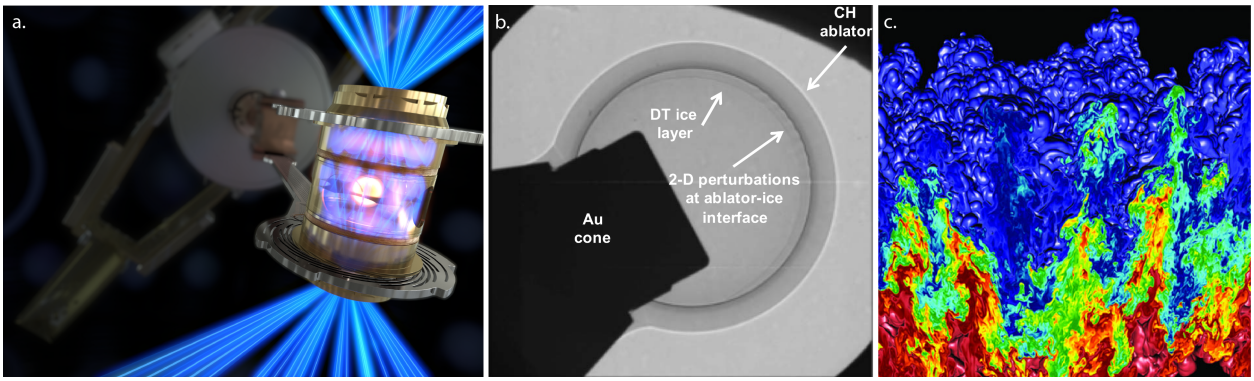

Figure 1.1: (a) Multiple laser beams are focused inside an ICF hohlraum [140] and their energy is converted into X-rays, which then compress a fuel capsule until it implodes to create fusion plasma. Figure reproduced from [100]. (b) An X-ray radiograph of the plastic capsule and inner Deuterium-Tritium ice layer showing plastic ablator, DT ice layer, and re-entrant Au cone for the layered HGR platform. Figure reproduced from [158]. (c) Simulation of Rayleigh-Taylor hydrodynamic instability created on LLNL's BlueGene/L supercomputer using Miranda code. Figure reproduced from [99].

or other methods, such as heavy ion beams or Z-pinches. The National Ignition Facility (NIF), the world's largest and most powerful laser facility, has made significant strides in ICF research, achieving notable results that have garnered widespread attention this year, by demonstrating a burning plasma for the first time in history [90, 194, 193]. These experiments have shown that releasing energy through fusion is achievable under laboratory conditions, raising hopes for the eventual development of viable fusion power plants.

Despite these successes, fusion technologies face considerable challenges. One of the primary hurdles is the presence of various instabilities in the plasma, which can develop during the compression and heating of the fuel capsule as shown in Fig. 1.1. These instabilities have a profound impact on the performance and efficiency of fusion experiments, making their study and control a crucial aspect of advancing fusion science [138, 157, 94]. In order to study and diagnose plasmas under extreme conditions, a wide range of diagnostic systems has been developed, including optical and X-ray techniques [156, 158, 82]. These diagnostic tools are essential for probing the properties of matter and understanding the underlying physics in high-energy-density experiments. However, current diagnostic systems have limitations, particularly with respect to spatial and temporal resolution, as well as signal-to-noise ratio [65, 123, 96, 171, 12, 41, 132, 66]. These limitations can impede our ability to fully characterize and understand the complex dynamics of matter at extreme conditions, ultimately hindering the advancement of fusion technology.

High-resolution imaging is essential for capturing the intricate details of plasma behavior and instability growth, as well as studying turbulent length scales. However, conventional diagnostic systems often suffer from limited spatial and temporal resolution, which can obscure critical infor-

mation about plasma dynamics. For example, X-ray radiography, a common diagnostic technique, relies on the penetration of X-rays through matter to produce images. However, the resolution of these images is often limited to tens or hundreds of microns, given by the brightness and spot size of the X-ray source as well as the detector's sensitivity.

A high signal-to-noise ratio is also crucial for accurately measuring the properties of high-energy-density plasmas, but current diagnostic systems can struggle to achieve sufficient sensitivity under challenging experimental conditions. The detection of weak signals in the presence of noise can be particularly problematic for X-ray diagnostics, as high-energy electrons and photons can produce background noise that interferes with the measurements.

Furthermore, the ability to perform experiments at a high repetition rate is essential for rapid progress in HEDP and fusion research [67]. Many diagnostic systems, however, are limited by their slow data acquisition and processing capabilities. This can be particularly challenging for X-ray diagnostics, which often require complex and time-consuming procedures for data analysis, such as phase recovery, or reconstruction of tomographic images. Given these challenges, there is a pressing need to improve and advance diagnostic systems for HEDP experiments as well as for fusion technologies. This has been the motivation for the development of high-repetition-rate targets, as well as imaging techniques with higher spatial and temporal resolution and better signal-to-noise throughout this dissertation. These techniques not only pave the way to better diagnostic systems in HEDP experiments but also have the potential to inform on the physics of plasma instabilities during laser interactions and thus greatly benefit ICF science in the future.

1.2 High-intensity lasers and plasma wakefield acceleration

High-intensity lasers have revolutionized the field of HEDP by providing a powerful tool for generating and probing extreme states of matter. The story of high-intensity lasers arguably began with the invention of the laser itself in 1960 by Theodore H. Maiman using a ruby crystal as a gain medium for light amplification. The laser, an acronym for "Light Amplification by Stimulated Emission of Radiation", was a groundbreaking technology for producing spatially and temporally coherent light, which opened the doors to a multitude of scientific and technological applications, revolutionizing fields such as medicine, manufacturing, telecommunications, and experimental physics.

In the early days of laser development, most lasers were Continuous-Wave (CW) lasers, having a unique frequency and average power. Given their monochromatic nature (nominally infinite pulse duration), CW lasers are inefficient in increasing their peak power for all time. Alternatively, it is much more efficient to increase the laser peak power in a burst during a short period of time. This motivated the development of broadband short pulse lasers with higher peak powers and high field

intensities, which allowed for producing higher electron quiver velocities during their interaction with matter.

In the late 1960s, a number of new technologies were developed that revolutionized our capacity to generate short-pulse higher-intensity lasers including Q-switching and mode-locking. First, Q-switching is a technique that involves modulating the quality factor (Q) of a laser resonator to produce high-power output pulses. It uses a shutter to periodically block the output coupler of a laser, causing the laser energy to build up, and then release it in a short pulse when the shutter opens. Shortly afterward, mode-locking was developed to produce even shorter pulses. In mode-locking, the phases of different cavity modes of the optical resonator are locked together, resulting in the constructive interference of these modes to produce an even shorter pulse of light. The development of short-pulse lasers once again opened up a wide range of new applications for lasers including micromachining, material processing, additive manufacturing, and medical applications, among others [63, 154, 106, 133, 183, 155]. Nevertheless, the pursuit to keep increasing laser peak power soon encountered an obstacle that would last for more than a decade.

Given a finite beam, as the length of the pulse becomes shorter and shorter its intensity can become so high that it can damage the material that the laser is passing through. In other words, this can limit the peak intensity of the laser pulse that can be generated before damaging the amplifier components themselves. Moreover, there is also a power limit for the pulse before self-focusing occurs [24], and subsequently filamentation of the beam [15]. This bottleneck seemed unconquerable until the advent of Chirped Pulse Amplification (CPA) in the mid-1980s [166].

CPA is a technique that earned Gérard Mourou and Donna Strickland the 2018 Nobel Prize in Physics and ingeniously circumvents the optical damage problem. The technique uses a series of optical elements to stretch, amplify, and then compress a pulse of light. The chirping process changes the shape of the pulse so that different frequency components are linearly distributed in time. This process modifies the pulse so that it is longer in time with a lower peak intensity before amplification, which consequently reduces the risk of optical damage. After amplification, the pulse is then compressed back to its original state by removing the chirp using a grating compressor, thus yielding an ultra-short, high-intensity laser pulse. This advent in technology revolutionized the field of laser physics and led to a redefinition of "high-intensity" lasers with pulse durations of picoseconds and peak powers exceeding terawatts.

Following further CPA development in the mid-1990s, Nd:Glass and CO_2 lasers were available with high enough intensities $I\lambda^2 \gg 10^{18}$ Wcm$^{-2}\mu$m^2 to allow the birth of one of the most promising applications of ultra high-intensity lasers - their ability to produce relativistic electron beams and X-ray radiation through a process known as Laser Wakefield Acceleration (LWFA). In LWFA, an ultra-high-intensity laser ionizes a gas target and produces a plasma in which electrons are expelled away from high-intensity regions, thus leaving an ion cavity in the wake of the light pulse.

This process is mediated through the ponderomotive force, which will be discussed in Chapter 2. Trapped electrons in the ion cavity can then be accelerated to relativistic velocities and oscillate to generate X-rays bursts. Theoretical work on LWFA began in the 1970s by Tajima and Dawson [168], but practical realization became possible with the development of high-intensity laser technology.

At the beginning of LWFA research, the laser pulses were still too long in time to couple with the plasma efficiently and they experienced strong non-linear optical self-focusing. For efficient LWFA, the length of the pulse should be less than a plasma period as will be discussed in Chapter 2. Nevertheless, even though ideal lasers were not available, researchers were still producing LWFA electrons through a process known as Self-Modulated Laser Wakefield Acceleration (SM-LWFA) [30, 62, 122], with the first experimental evidence of electron trapping and acceleration to 44 MeV energies with SM-LWFA [121], as well as many other afterwards [145, 34, 124]. Alternatively, direct-laser acceleration [55, 113, 137, 6] is another known technique that works in a similar manner to SM-LWFA, in which the laser pulse is sufficiently intense but long so that it creates a plasma channel void of electrons.

Moreover, electron beams from LWFA initially had a broad Maxwellian spectrum. This was caused by the electron beam outrunning the laser pulse, which has a group velocity that depends on the plasma density. High densities caused the electrons to outrun the pulse and reach the decelerating portion of the potential, thus gaining energy spread. Then in the early 2000s, an important achievement has obtained in the LWFA community; the observation of self-trapped quasi-monoenergetic electron beams [111, 50, 58, 51]. With the advent of more advanced lasers ($t < 50$ fs, $P > 10$ TW) it was possible to maintain the same focused intensity but with a larger spot size, which caused electrons to self-trap at lower densities than before, and thus prevent them from reaching the dephasing limit while having a mono-energetic beam [110]. Since then, LWFA has been a groundbreaking research field for utilizing intense laser pulses to drive plasma waves and produce monoenergetic electron beams with many successful experiments reaching energy levels in the GeV range [102, 64, 29, 76, 182, 101, 152].

Furthermore, trapped energetic electrons in LWFA experience the channel and laser electric fields and oscillate inside the ion channel in response. These electron oscillations emit X-ray radiation through a process analogous to undulator oscillations in conventional synchrotrons. In this sense, LWFA is an exciting new table-top source of electrons that is capable of accelerating beams to highly relativistic energies in distances of only centimeters at a fraction of the cost compared to conventional accelerators extending over kilometers in size. In these regimes, LWFA electron beams are comparable in energy with those used in 3rd generation synchrotron sources, thus making them promising candidates for X-ray photon light source applications.

The X-ray bursts from LWFA, so-called betatron X-rays, exhibit unique properties, such as

ultrafast pulse durations (on the order of femtoseconds), small source sizes (on the order of a few microns), and a broad energy spectrum, extending up to several tens of keV. These characteristics make LWFA X-ray sources particularly suitable for high-resolution imaging applications in HEDP research and ICF diagnostics. The ultrafast pulse duration of betatron X-rays enables time-resolved studies of transient phenomena, while the small source sizes and broad energy spectrum allow for high spatial and temporal resolution, respectively. Moreover, traditional X-ray sources, such as X-ray tubes, synchrotrons, and the X-ray Free Electron Laser (XFEL), may have limitations in terms of size, cost, and versatility. The compact nature of LWFA-based X-ray sources can help overcome these challenges for both, national-scale facilities and university-scale laboratories, having some remarkable results already published in the literature [186, 71, 83, 31, 52, 53, 2]. The research and development of LWFA-based betatron X-ray sources over the past decades have been discussed in research topical reviews [4, 3].

Within this context, the objective of this dissertation is to utilize LWFA electron beams and betatron X-ray pulses at high repetition rates to study matter under extreme conditions. The dissertation will focus on describing both, betatron X-ray imaging and electron beam probing, analysis techniques as well as presenting original results. In combination with simulation work, the experimental results attempt to contribute to the understanding of sub-micron scale time-dependent HEDP systems such as those found in ICF experiments.

1.3 Dissertation outline

The work in this dissertation comprises a series of three experiments conducted at the Hundred-Terawatt-Thomson (HTT) laser system, as part of the Berkeley Lab Laser Accelerator (BELLA) Center located at the Lawrence Berkeley National Laboratory (LBNL). The experiments were supported by LaserNetUS and led by the Center for Ultrafast Optical Science (CUOS) at the University of Michigan. The outline of the dissertation is as follows:

- **Chapter II:** The second chapter is an introduction to the most important theoretical concepts needed as a background for this dissertation work. Some of the topics discussed include high-intensity lasers, the motion of electrons in a laser field, laser-driven plasma waves and electron acceleration, the generation of betatron radiation in a plasma channel, and some pertinent concepts in HEDP.

- **Chapter III:** The third chapter focuses on describing the experimental methods, among them the characteristics of the laser system, the experimental chamber configuration, optical, electron beam, and X-ray beam characterization, as well as the analysis techniques used in the dissertation and simulation methods.

- **Chapter IV:** The fourth chapter describes the development of a cylindrical liquid jet target capable of flowing in a vacuum and undergoing laser heating at high-repetition-rate. This target is a crucial part of performing the HEDP pump-probe experiments in later chapters.
- **Chapter V:** The fifth chapter presents the first experimental results using high-repetition-rate betatron X-rays to capture the dynamic evolution of laser-driven shock waves in water. Some of the analyses displayed in this chapter include the generation of synthetic phase-contrast X-ray images, and density recovery techniques from X-ray measurements, shock velocity measurements, and pressure calculations.
- **Chapter VI:** The sixth chapter describes the observation of plasma instabilities within a shocked liquid target. In particular, it focuses on the observation of the Richtmyer-Meshkov process with state-of-the-art level spatial scales, as well the experimental determination of the growth-rate for multiple unstable processes and multi-wave generation along the jet.
- **Chapter VII:** The seventh chapter describes a series of experiments that use the relativistic LWFA electron beam as a probe to capture time-dependent ultrafast plasma dynamics. The experimental results obtained from this innovative method include the recovery of electric and magnetic fields and plasma temperature estimations from the electron beam radiography images as well as their comparison to 3D hydrodynamic simulations.
- **Chapter VIII:** The eighth and final chapter focuses on bringing a short summary, drawing conclusions, and providing an outlook for the future of LWFA-based diagnostic sources in HEDP.

CHAPTER 2

Background

2.1 Laser wakefield acceleration

2.1.1 Introduction

The advent of ultra-high-intensity lasers opened the doors to the generation of relativistic electron beams through LWFA. During the laser-plasma interaction, the ponderomotive force from the light pulse is responsible for deflecting plasma electrons from their equilibrium positions thus leaving a channel of heavy ions in the wake of the pulse. This structure is termed the "wakefield", in which the space-charge forces exhibit over four orders of magnitude higher acceleration gradients than conventional accelerators, while simultaneously inducing electron oscillations analogous to those from magnetic undulators. The production of high-quality monoenergetic beams [111, 50, 58, 51], as discussed previously in Chapter 1, was a pivotal point in the field. It marked the transition from a linear regime to a relativistic non-linear regime regarding the characteristics of the wakefield, also known as the "bubble" or "blow-out" regime as predicted by simulations [136].

LWFA electron beams first reached the 1 GeV milestone by increasing the acceleration distance utilizing a laser driven capillary channel that served as a guiding structure [102, 75, 178, 101]. Nowadays, higher energies at the GeV-level have successfully been achieved by a variety of methods that aim to control the electron bunch injection and manipulation of its phase space. Specifically, wakefield injection [74, 147] consists of electrons crossing the separatrix between trapped and untrapped orbits in the phase-space diagram. These electrons must not only be injected in the correct phase of the plasma wave to be accelerated, but also they must be of sufficiently short duration. The reason for this is that ideally all electrons in the beam bunch experience similar magnitudes of the electric field, and thus be accelerated uniformly.

If the wakefield amplitude is sufficiently large so that their velocities exceed the wake phase velocity then electrons in the plasma can be self-injected, or self-trapped, and different self-injection mechanisms have been used to increase its effectiveness [74, 147]. Alternatively, different methods for injection have been explored in the literature including optical injection using a second

laser pulse [51, 45, 172, 89, 73, 170], or shock-injection using modulated density gradients [20]. All these methods have advantages and disadvantages which allow to control of the phase-space distribution of the beam, or its stability during experimental campaigns [57, 146, 60, 68, 19].

Of particular relevance for the experiments performed in this thesis is the technique known as *ionization injection*. In ionization injection, a small amount of higher-Z gas is added to the target so that it interacts with the peak of the laser intensity. As inner shell electrons are ionized they will disturb the electron orbits from the fluid motion thus causing a more controlled injection scheme [29, 26, 131, 119, 135, 105, 25]. Given the ability to decouple the ionization process with a second laser pulse [69], ionization injection has shown great promise for controlling the phase-space distribution of the electron beam as well as decent stability in gas cell targets [175]. The ability to control the injection process during experiments is crucial for developing LWFA-based radiation sources.

LWFA research is now concerned with overcoming the dephasing limit for maximum electron energy gain, among tackling other challenges for improving the beam instability, and energy distribution, as well as efforts for creating LWFA-based X-ray free electron lasers. Additionally, the concept of "staging" including multiple phases of acceleration has been conceptually demonstrated where an electron beam is coupled into and gained energy in a second LWFA [164]. Other experiments have utilized a driver-witness approach in which the wakefield is driven by a first LWFA bunch, while a witness gains energy from the wake, thus overcoming the dephasing limit [28]. In the rest of this subsection, the most fundamental concepts behind LWFA will be introduced.

2.1.2 The relativistic ponderomotive force

When an electron encounters a high-intensity laser field its motion is influenced by the electric and magnetic fields that comprise the laser light and can be described by the Lorentz force [59, 184],

$$\frac{d\mathbf{p}}{dt} = -e\left[\mathbf{E} + (\mathbf{v} \times \mathbf{B})\right] \ , \tag{2.1}$$

with an energy equation,

$$\frac{d}{dt}\left(\gamma m c^2\right) = -e\left(\mathbf{v} \cdot \mathbf{E}\right) \ , \tag{2.2}$$

where $\gamma = \sqrt{1 + p^2/\left(m_e^2 c^2\right)}$ is the relativistic factor and $\mathbf{p} = m_e \gamma \mathbf{v}$ is the electron momentum with velocity $\mathbf{v}_e$, mass m_e, and charge $q = -e$. The electric and magnetic fields of the laser can be expressed as $\mathbf{E} = -\partial \mathbf{A}/\partial t$ and $\mathbf{B} = \nabla \times \mathbf{A}$, having a vector potential $\mathbf{A}$. To start, we may gain an understanding of the basic behavior by considering a non-relativistic case where $\mathbf{v}_e \ll c$ and $|\mathbf{B}| = |\mathbf{E}|/c$ and a transversely polarized laser plane wave with $\mathbf{E} = -e\mathbf{E_0} \cos\left(\omega_L t - \mathbf{k} \cdot \mathbf{x} + \phi_L\right)$

the magnetic cross-product term can be ignored. This simplifies the Lorentz force equation to

$$m_e \frac{d\mathbf{v_e}}{dt} = -e\mathbf{E}_0 \cos\left(\omega_L t - \mathbf{k}\cdot\mathbf{x} + \phi_L\right) \ , \tag{2.3}$$

for which integration over time gives the electron quiver velocity v_e having a maximum value of

$$v_{e,max} = \frac{e|\mathbf{E}_0|}{m_e \omega_L} \ . \tag{2.4}$$

Then, by averaging the quiver velocity over one laser cycle it is possible to define an average ponderomotive energy W_{pond} and ponderomotive potential ϕ_{pond} as

$$W_{\text{pond}} = \frac{1}{2} m_e \langle \mathbf{v}_e^2 \rangle_T = \frac{e^2 \mathbf{E}^2}{4 m_e \omega_L^2} = e\Phi_{\text{pond}} \ . \tag{2.5}$$

In this sense, the ratio between the work done by the electric field of the laser pulse over one wavelength to the rest mass of the electron is defined as the normalized vector potential a_0

$$a_0 = \frac{e|\mathbf{E}_0|}{m_e \omega_L c} = \frac{e|\mathbf{A}|}{m_e c} = 0.85\sqrt{I_0\left[10^{18}\text{W/cm}^2\right]} \cdot \lambda_L\left[\mu m\right] \ . \tag{2.6}$$

This parameter is typically used to characterize the difference between the non-relativistic ($a_0 \ll 1$) and the relativistic (blow-out) regime ($a_0 \geq 1$). For instance, in a Ti:Sapph-based laser system like the ones used for the experiments in this thesis, operating at a wavelength of $\lambda_0 = 800$ nm then the relativistic regime $a_0 = 1$ is reached for laser intensities in the order of $I_0 \approx 2.2 \times 10^{18}$ W/cm^2. At these intensities $|\mathbf{v}_e| \longrightarrow c$ the cross magnetic term in Eq. 2.1 can no longer be neglected, so both the electric and magnetic fields are responsible for the motion of the electron.

The electron motion in this case can be quite complex depending on the laser field's polarization, but it generally follows an oscillatory pattern in phase with the electric field of the laser light as well as net forward drift motion. In particular, for a focused laser pulse, the electron experiences a quasi-static force known as the ponderomotive force [91], which tends to expel electrons out of regions of high laser intensity $\mathbf{F}_P = -e\nabla\Phi_{\text{pond}}$. This phenomenon, which is a non-linear effect of the laser field, can result in the formation of an electron "sheath" around the high-intensity region and is responsible for many phenomena in LWFA. In the linear regime, the ponderomotive force can be conveniently described by the normalized vector potential a averaged over one laser cycle, so for a Gaussian beam in time with $a(t) = \langle a \rangle_T = a_0 \text{exp}\left[-\left(t/\tau_0\right)^2\right]$,

$$\mathbf{F}_p = -m_e c^2 \nabla \frac{a^2}{2} \ . \tag{2.7}$$

Nevertheless, for the non-linear relativistic regime, the ponderomotive force is typically defined

by the gradient of the cycle-averaged relativistic gamma factor $\langle\gamma\rangle$ as described in Ref. [163, 46]. Therefore, let us then make use of multiple timescale perturbation theory letting $\mathbf{p} = \mathbf{p}_q + \delta\mathbf{p}$ such that for the linear limit, the zeroth order motion is equivalent to the quiver momentum $\mathbf{p}_\perp = m_e c\mathbf{a}_\perp$, directly obtained from the conservation of canonical momentum $d\left(\mathbf{p}_\perp - e\mathbf{A}_\perp\right) = 0$. Then, assuming that the laser is propagating in an underdense plasma with a sufficiently broad spot size, and taking a slowly varying envelope approximation so that $k_0 w_0 \gg 1$ and $\omega_0 \tau_p \gg 1$, the first order motion yields the relativistic ponderomotive force when cycled averaged,

$$\mathbf{F}_{p,rel} = -\frac{mc^2}{\langle\gamma\rangle}\nabla\left\langle\frac{a^2}{2}\right\rangle \ . \tag{2.8}$$

Overall, the ponderomotive force is a key factor in the dynamics of electrons in the interaction of high-intensity lasers with matter. The motion of an electron in a high-intensity laser field can vary from simple oscillations to highly complex, relativistic trajectories depending on the laser intensity. Understanding this motion is fundamental for many applications in modern physics, including high-harmonic generation, electron acceleration, attosecond science, and X-ray generation via LWFA. The ponderomotive force also takes an important role during the initial "injection" of electrons into the plasma wake and subsequent acceleration in LWFA.

2.1.3 Electron acceleration in a wakefield

LWFA electron beams are produced by focusing an ultrashort short high-intensity laser pulse of wavelength λ_0 into an underdense plasma, typically a gas, with electron number densities of $n_e \approx 10^{18}$–10^{19} cm^{-3}. The strong electric field of the laser will almost immediately ionize the gas, and the electron acceleration process is mediated through the interaction of the electromagnetic wave (laser) with the plasma. Since it would be impossible to describe each particle individually, the equations normally used to describe the motion of plasma electrons in electromagnetic waves include the Lorentz equation, the continuity equation, and Poisson's equation given by,

$$\frac{d\mathbf{p}}{dt} = \left(\frac{\partial}{\partial t} + \mathbf{v}\cdot\nabla\right)\mathbf{p} = -e\left[\mathbf{E} + \mathbf{v}\times\mathbf{B}\right] \ , \tag{2.9}$$

$$\frac{n_e}{\partial t} + \nabla\left(n_e\mathbf{v}\right) = 0 \ , \tag{2.10}$$

$$\nabla^2\Phi = -\frac{\rho}{\epsilon_0} = e\frac{\delta n_e}{\epsilon_0} \ , \tag{2.11}$$

where $\delta n_e - n_{e,0}$ is the local density perturbation and $\rho = -e\delta n_e$ is the charge density.

As the electrons are ionized by the laser and expelled away by the ponderomotive force they will simultaneously experience the restoring electrostatic force from the ions. Therefore, they will

naturally oscillate from their initial position with a resonant frequency ω_p which can be derived from Eq. 2.9. By assuming small wave amplitudes in a cold plasma fluid, the equation of motion reads

$$n_{e,0} m_e \frac{\partial \mathbf{v}}{\partial t} = -n_{e,0}\mathbf{E} \, . \tag{2.12}$$

For which the initial thermal energy of the electrons as well as any quadratic terms have been ignored. The vector identity $\nabla \times (\nabla \times \mathbf{a}) = \nabla (\nabla \cdot \mathbf{a}) - \nabla^2 \mathbf{a}$ can be used to reformulate the wave equation to,

$$-\nabla (\nabla \cdot \mathbf{E}) + \nabla^2 \mathbf{E} = \mu_0 n_{e,0} \frac{e^2}{m_e}\mathbf{E} + \mu_0 \epsilon_0 \frac{\partial^2 \mathbf{E}}{\partial^2 t} \, . \tag{2.13}$$

Therefore assuming a laser pulse with an electric field in the form of a plane wave $\mathbf{E} \propto \exp(ik_L x - \omega_L t)$ propagating in a uniform medium (cold neutral plasma) with $\nabla \cdot \mathbf{E} = 0$ the resulting dispersion relation is,

$$\omega_L^2 = \omega_p^2 + c^2 k_L^2 \, , \tag{2.14}$$

it will subsequently launch longitudinal plasma oscillations with a characteristic cold electron plasma frequency ω_p given by

$$\omega_p = \sqrt{\frac{e^2 n_{e,0}}{m_e \varepsilon_0}} \, . \tag{2.15}$$

For the 1D non-linear regime, the laser group velocity is given by $v_g = \sqrt{1 - n_e/n_c}$, where n_c is the critical plasma density given by,

$$n_{e,c} = \frac{\epsilon_0 m_e}{e^2}\omega_L^2 = \frac{1.1}{\lambda_L^2[\mu\mathrm{m}]} 10^{21} \mathrm{cm}^{-3} \, , \tag{2.16}$$

for $\omega_L = \omega_p$. When $n_e < n_c$ the medium is underdense and the electromagnetic wave can propagate through the plasma. However, when $n_e \geq n_c$ the medium is overdense and the electrons can follow the laser field oscillation thus shielding the plasma and reflecting the pulse instead. For an electromagnetic wave propagating through an underdense plasma the corresponding phase velocity v_{ph} and group velocity v_g are

$$v_{ph} = \frac{\omega_L}{k_L} \, , \tag{2.17}$$

$$v_g = \frac{\partial \omega_L}{\partial k_L} = \eta c \, . \tag{2.18}$$

Here the refractive index η for a cold plasma medium is given by

$$\eta = \sqrt{1 - \frac{\omega_p^2}{\omega_L^2}} < 1 \, . \tag{2.19}$$

Therefore the wake phase velocity is dictated to the first order by the laser group velocity and the corresponding relativistic gamma factor of the plasma wave results in

$$\gamma_p = \frac{1}{\sqrt{1-(v_g/c)^2}} \approx \frac{\omega_L}{\omega_p} \ . \tag{2.20}$$

Furthermore, for a plasma wave excited by a laser pulse in a Coulomb gauge ($\nabla \cdot A = 0$) the Lorentz force can be expressed in terms of the vector potential so that

$$\left(\frac{\partial}{\partial t} + \mathbf{v}\cdot\nabla\right)\mathbf{p} = e\left[\frac{\partial}{\partial t}\mathbf{A} + \nabla\Phi - \mathbf{v}\times\nabla\times\mathbf{A}\right] \ , \tag{2.21}$$

and by taking $\nabla p^2 = m_e^2 c^2 2\gamma\nabla\gamma$ and using the vector identity $\nabla p^2 = 2\left[(\mathbf{p}\cdot\nabla)\,\mathbf{p} + \mathbf{p}\times(\nabla\times\mathbf{p})\right]$ this leads to

$$m_e c^2 \nabla\gamma = (\mathbf{v}\cdot\nabla)\,\mathbf{p} + \mathbf{v}\times(\nabla\times\mathbf{p}) \ . \tag{2.22}$$

Here the LHS represents the ponderomotive force as described before, which can be inserted into Eq. 2.21 to obtain the following equation of motion,

$$\frac{\partial\mathbf{p}}{\partial t} = e\nabla\Phi + e\frac{\partial\mathbf{A}}{\partial t} - m_e c^2\nabla\gamma \ , \tag{2.23}$$

where $\mathbf{v}\times\nabla\times(\mathbf{p} - e\mathbf{A}) = 0$ indicating that the electrons are exclusively driven by the vector potential and the canonical momentum is conserved $\mathbf{p} - e\mathbf{A} = 0$ for all times if there is no initial perturbation in the plasma [27]. This equation is the starting point to obtain solutions for linear and non-linear laser-driven plasma waves.

For the following derivations, it is convenient to introduce a coordinate transformation to the wake rest frame for a non-evolving wake with $\xi = z - v_g t$ and $\tau = t$ with partial derivatives,

$$\frac{\partial}{\partial z} = \frac{\partial}{\partial\xi} \qquad \text{and} \qquad \frac{\partial}{\partial t} = \frac{\partial}{\partial\tau} = -v_g\frac{\partial}{\partial\xi} \approx -c\frac{\partial}{d\xi} \ , \tag{2.24}$$

and it is convenient to normalize the relevant quantities,

$$\beta = \mathbf{v}/c, \qquad \mathbf{a}_0 = \frac{e\mathbf{A}}{m_e c}, \qquad \phi = \frac{e\Phi}{m_e c^2}, \qquad \gamma = \frac{E}{m_e c^2}, \qquad \mathbf{u} = \frac{\mathbf{p}}{m_e c} \ . \tag{2.25}$$

It is possible to find analytical solutions to Eq. 2.23 by assuming small laser intensities $a_0 \ll 1$ and small plasma density perturbations $\delta n_e \ll n_{e,0}$ and using Poisson's equation Eq. 2.11. Then for a Gaussian laser beam envelope with $a = a_0 \exp\left(-\xi^2/\left(c\tau_0\right)^2\right)\exp\left(-r^2/w_0^2\right)$ the resulting solution

for a scalar wakefield potential $\phi(\mathbf{r}, \xi)$ is

$$\begin{aligned} &\phi(\mathbf{r}, \xi) = -f(\mathbf{r}) \sin(k_p \xi) \ , \\ \text{where} \qquad &f(\mathbf{r}) = a_0^2 \sqrt{\frac{\pi}{2}} \frac{k_p}{4} c\tau_0 \text{exp}\left(-\frac{2r^2}{w_0^2}\right) \text{exp}\left(-\frac{(k_p c\tau_0)^2}{8}\right) \ . \end{aligned} \tag{2.26}$$

Based on the definition of ϕ the resulting electric field and electron density are,

$$\frac{\mathbf{E}_\parallel}{\mathbf{E}_{p,0}} = -\frac{1}{k_p}\frac{\partial \phi}{\partial \xi}, \qquad \frac{\mathbf{E}_\perp}{\mathbf{E}_{p,0}} = -\frac{1}{k_p}\frac{\partial \phi}{\partial r}, \qquad \frac{\delta n_e}{n_{e,0}} = \frac{1}{k_p^2}\frac{\partial^2 \phi}{\partial \xi^2} \ , \tag{2.27}$$

where $\mathbf{E}_{p,0}$ is the so-called relativistic wavebreaking field - dictating the field strength at which breakdown of the wakefield structure occurs. The radius of the wake (assuming a spherical shape) is dictated by the plasma frequency ω_p, as well as the laser focal spot size. Analytical solutions can be obtained for the 1-D spatial case [45, 161] that are helpful in giving an insight into understanding the plasma behavior. Assuming a 1-D case, the 3-D electron momentum can be described by parallel (z-direction and longitudinal (x-y direction) components. In this case, the equation of motion can be derived with Eq. 2.1 and Eq. 2.2 and following [59, 184] as,

$$\frac{d\mathbf{p}_\perp}{dt} = e\left(\mathbf{E}_\perp + \mathbf{v}_\parallel \times \mathbf{B}_\parallel\right) = e\frac{d\mathbf{A}_\perp}{dt} \ , \tag{2.28}$$

$$\frac{d\mathbf{E}_\parallel}{dt} = c\frac{d\mathbf{p}_\parallel}{dt} \ , \tag{2.29}$$

where the integration for an electron initially at rest gives the longitudinal and transverse momenta as,

$$\mathbf{p}_\perp = e\mathbf{A}_\perp \implies \mathbf{u}_\perp = \gamma\beta_\perp = \mathbf{a} \ , \tag{2.30}$$

$$E - c\mathbf{p}_\parallel = m_e c^2 \implies \gamma - 1 = \mathbf{u}_\parallel \ . \tag{2.31}$$

Then following the solution for the wake potential ϕ can be derived from Eq. 2.23, Eq. 2.10, and Eq. 2.11 to be

$$\frac{\partial^2 \phi}{\partial \xi^2} = k_p^2 \gamma_p^2 \left(\beta_p \left(1 - \frac{1 + a^2}{\gamma_p^2 (1+\phi)^2}\right)^{-1/2} - 1\right) \ , \tag{2.32}$$

describing a nonlinear ordinary differential equation that can be solved for wake potential ϕ. If a linearly polarized square pulse is assumed with $v_g \longrightarrow c$, then the scalar potential $\phi_{0,max}$ and peak

electric field $E_{0,max}$ can be obtained [14],

$$\phi_{0,max} \approx a_0^2/2, \qquad E_{0,max} = E_{p,0}\frac{a_0^2/2}{\sqrt{1+a_0^2/2}} \ . \tag{2.33}$$

Alternatively, for the 3-D non-linear regime ($a_0 > 1$) with an arbitrary pulse envelope $a(\xi)$ the wakefield is not easily defined and neither is the laser group velocity. Therefore 3-D Particle-In-Cell (PIC) simulations are typically performed [61, 108] in order to obtain scaling laws for 3D LWFA, as well as the wake potentials, fields, and density profiles.

When a particle is initiated in a wakefield it will gain energy as long as it stays in phase with the accelerating section of the wake. Since the laser group velocity in the linear regime is $v_g < c$ the accelerating particles with $v_e \sim c$ will eventually outrun the wake. This means that there is a maximum energy gain that can be extracted from a wakefield given a laser wavelength λ_0 and plasma density n_e. The phenomenon of an accelerating particle outrunning the wakefield is also known as dephasing, and the distance over which this occurs is known as the dephasing length L_{deph}. It has been shown in [46, 168] that the maximum achievable energy (in the 1D linear regime) is given by,

$$E_{max} \approx \left(\frac{n_c}{n_e}\right) m_e c^2 \ , \tag{2.34}$$

while the corresponding dephasing length is approximately,

$$L_{deph} \approx \left(\frac{n_c}{n_e}\right)\frac{\lambda_p}{2} \propto \left(\frac{n_e}{n_e}\right)^{3/2} \ . \tag{2.35}$$

In order to obtain scalings for the maximum energy gain and the accelerator length let us once again assume that wakefield (regardless of its structure) has a potential $\phi(\xi, \vec{r})$. This implies that in the wake rest frame the new potential, indicated by a prime notation, becomes

$$\phi' = \gamma_p\left(\phi - v_g A_z\right) = \gamma_p \phi \ , \tag{2.36}$$

when using a Lorenz gauge and the Lorentz boost factor γ_p. Then, to find scalings for maximum energy gain, the first assumption is that the difference between the speed of light in a vacuum and the laser group velocity $c - v_g$ is proportional to the plasma density. This implies that

$$\gamma_p = \sqrt{\eta\frac{n_c}{n_e}} \ , \tag{2.37}$$

where η is a constant. Therefore, the maximum energy gain in the wake rest frame is given by,

$$\Delta T' = e\Delta\phi' = e\left(\phi'_{max} - \phi'_{min}\right) \ . \tag{2.38}$$

Next, we can use the limit $\gamma_p \Delta\phi \gg 1$, so that $\Delta p'c \approx \Delta T'$ to transform this expression so that to obtain the energy gain of an electron in the laboratory frame

$$\Delta T = 2\gamma_p^2 e\Delta\phi \tag{2.39}$$

and it, therefore, scales as,

$$\Delta T \approx C_1 \left(\frac{n_c}{n_e} m_e c^2\right) \ , \tag{2.40}$$

where $C_1 = 2\eta\left(e\Delta\phi/m_e c^2\right)$ is a scaling factor dependent on the wakefield structure.

Following dimensional analysis it can be concluded that the longitudinal electric field has a magnitude of order $E_0 = mc\omega_p/e$ thus it follows that the dephasing length approximately scales as

$$L_{deph} \approx C_2 \left(\frac{n_c}{n_e}\right)^{3/2} \lambda_0 \ , \tag{2.41}$$

where $C_2 = C_1/2\pi\eta$ is another scaling factor and α is obtained from averaging between the maximum and minimum potentials in the electric field so that $\langle \mathbf{E}_\parallel \rangle = \eta \mathbf{E}_0$.

To obtain an accurate value for C_1 and C_2 scaling factors in the 3D non-linear regime, it is necessary to run numerical simulations. It is important to remember that this analysis is only valid for non-evolving wakefields, non-evolving laser pulse, and uniform plasma densities. For more realistic scenarios, these scalings will certainly change and there have been studies on this subject [109] using a variety of analysis and simulation tools, obtaining the results

$$\Delta T \approx \frac{2a_0}{3} \left(\frac{n_c}{n_e}\right) m_e c^2 \tag{2.42}$$

and

$$L_{deph} \approx \frac{2\sqrt{a_0}}{3\pi} \left(\frac{n_e}{n_e}\right)^{3/2} \lambda_0 \ . \tag{2.43}$$

describing the energy gain and the dephasing length, which have also been tested experimentally obtaining accurate results [112, 118].

2.1.4 Generation of betatron radiation in a plasma channel

When electrons are trapped in a wake they can be injected off-center from the laser propagation axis and then undergo betatron oscillations. As electrons oscillate inside the wake they produce radiation bursts in the form of a collimated beam of broadband X-rays. This phenomenon gives the name to betatron X-rays from relativistic electrons oscillating inside the plasma bubble in LWFA. In this section, the fundamental equations for betatron radiation are introduced.

The first observation of betatron radiation was at SLAC national laboratory from a ~ 28 GeV electron beam from a conventional linear accelerator undergoing oscillations inside a lithium plasma [181]. Later on, betatron radiation was observed from a laser-driven wake having a broadband spectrum in the range of 1–10 keV and approximately $\sim 10^8$ photons [142]. Since then, multiple experiments have successfully used betatron X-rays for synchrotron-like photon source applications with reviews available in the literature [33, 47].

In order to obtain the equation of motion for electrons undergoing transverse betatron oscillations while simultaneously being accelerated in the longitudinal direction in the non-linear relativistic regime, let us first assume a spherical ion cavity following the derivation in [88, 107]. Assuming a frame of reference with the wakefield at rest, the transverse electric fields inside the ion bubble are given by

$$E_x = \frac{m_e \omega_p^2 x}{4e} \tag{2.44}$$

and

$$E_y = \frac{m_e \omega_p^2 y}{4e} \ , \tag{2.45}$$

having an exclusively azimuthal magnetic field given by

$$B_x = \frac{m_e \omega_p^2 y}{4e} \tag{2.46}$$

and

$$B_y = -\frac{m_e \omega_p^2 x}{4e} \ . \tag{2.47}$$

Furthermore, the accelerating field in the longitudinal direction is given by

$$E_z = m_e \omega_p^2 \xi / 2e \ . \tag{2.48}$$

Here the wake coordinate is $\xi = z - v_g t$ has once again been used. In this case, the longitudinal field will have a maximum amplitude $|E_z|_{max} = \sqrt{a_0} m_e c \omega_p / e$ at the bubble edge with radius $r_b = 2\sqrt{a_0} c/\omega_p$ and it will be equal to zero $|E_z| = 0$ at the center of the bubble with $\xi = 0$. The

field will then have an average strength given by

$$\langle E_z \rangle = \frac{1}{2}|E_z|_{max} = (\sqrt{a_0}/2)\, m_e c\omega_p/e \ . \tag{2.49}$$

We can therefore write all force components an electron would experience inside the wake as,

$$F_z = -eE_z \ , \tag{2.50}$$

$$F_x = -e\left(E_x - v_z B_y\right) \ , \tag{2.51}$$

$$F_y = -e\left(E_y - v_z B_x\right) \ , \tag{2.52}$$

which can be expressed in a compact form by taking $v_z \approx c$ then,

$$\frac{d\mathbf{p}}{dt} \simeq -\frac{1}{2} m_e \omega_p^2 \mathbf{s} \tag{2.53}$$

where $\mathbf{s} = (x, y, \xi) = \mathbf{r} - v_g t\hat{z}$ as the coordinates co-moving with the bubble at the group velocity v_g. This equation of motion can be integrated by assuming the longitudinal momentum is slowly varying to give,

$$p_z \approx \gamma_p^2 a_0 m_e c \left(1 - \frac{\xi^2}{r_b^2}\right) \tag{2.54}$$

Moreover, for the transverse direction, the equation of motion can be obtained by modeling the electron as a slowly varying oscillator with betatron frequency

$$\omega_b = \frac{\omega_p}{\sqrt{2p_z}} \ , \tag{2.55}$$

and resulting in WKB solutions following [88],

$$p_x = \frac{p_{x0}}{\sqrt{p_z(\xi)}} \cos\left[\int \omega_b(\xi) d\xi\right] \ . \tag{2.56}$$

According to the text on classical electrodynamics by Jackson [72] it is then possible to calculate the intensity emitted by the electron per unit frequency $d\omega$ and solid angle $d\Omega$ as,

$$\frac{d^2 I}{d\omega d\omega} = \frac{e^2\omega^2}{4\pi c}\left[\int_{-\infty}^{\infty} \mathbf{n} \times (\mathbf{n} \times \beta)\, e^{i\omega\left(t - \frac{\mathbf{n}\cdot\mathbf{r}}{c}\right)} dt\right]^2 \ , \tag{2.57}$$

where $\mathbf{n}$ is the vector in the observation direction and $\beta = v/c$ is the normalized electron velocity.

This expression can be simplified in the so-called asymptotic limit for strong electron oscillations. In this regime, the betatron oscillations are comparable to those from a traditional magnetic wiggler with its characteristic strength parameter only dependent on the strength of the imposed magnetic field. For the plasma wiggler, the corresponding strength parameter is

$$a_\beta = \gamma k_\beta r_\beta \gg 1 \ , \tag{2.58}$$

where γ is the electron relativistic factor, $r_\beta \approx r_b$ is the oscillation radius, and $k_\beta = k_p/\sqrt{2\gamma}$ is wave number dependent on the plasma frequency. When $a_\beta \gg 1$, in the asymptotic limit, the radiation spectrum can then be described as observed at an angle θ from the plane of the electron oscillations and it is given by [47, 72] as

$$\frac{d^2I}{d\Omega d\omega} \propto \frac{\gamma^2\xi^2}{1+\gamma^2\theta^2}\left[K_{2/3}^2(\xi) + \frac{\gamma^2\theta^2}{1+\gamma^2\theta^2}K_{1/3}^2(\xi)\right] \tag{2.59}$$

where in this case $K_{2/3}$ and $K_{1/3}$ are modified Bessel functions and

$$\xi = \frac{\omega}{\omega_c}\left(1+\gamma^2\theta^2\right)^{3/2} \ , \tag{2.60}$$

with a critical frequency $\omega_c \approx 3a_\beta\gamma^2\omega_\beta$, and betatron frequency $\omega_\beta = \omega_p/\sqrt{2\gamma}$.

For $\theta = 0$ the expression can then be simplified even further to approximate a synchrotron spectrum given by

$$\frac{d^2I}{d\Omega d\omega} \propto \gamma^2\xi^2K_{2/3}^2(\xi) \ , \tag{2.61}$$

with $\xi = \omega/\omega_c$. This expression leads to a synchrotron-like spectrum which can be integrated over the full spatial extent of the betatron beam to obtain

$$\frac{dI}{d\omega} = \sqrt{3}\frac{e^2}{c}\gamma\xi\int_\xi^\infty K_{5/3}(x)dx \ . \tag{2.62}$$

The equations in this section for betatron radiation spectra and electron equation of motion have been extensively used to study LWFA dynamics. In the literature, we can observe multiple analytical studies which compare these expressions to results obtained from PIC simulations [87, 126, 81]. Although it is important to note that these apply to specifically imposed initial conditions. Moreover, in the 3D blowout regime electrons undergo betatron oscillations in multiple planes, and they are affected by the time-evolution of the wakefield as well as the laser field itself. Nowadays, techniques exist for post-processing PIC simulations and track the electron trajectories, thus being able to estimate a radiation spectrum and power with accuracy [115, 116, 117].

2.2 High-energy-density physics

2.2.1 Introduction

High-energy-density science is concerned with the state of matter at high pressures, defined as having pressures above one million atmospheres, or 1 Mbar. This definition is given in reference to the internal energy density of a hydrogen molecule. In other words, if the pressure applied to ordinary solid matter exceeds 1 Mbar it often ionizes, compresses, and becomes a plasma with high-energy-density (very hot and very dense), such as that found in stellar medium with fusion conditions. It has become obvious over the past century that matter exhibits distinct behavior under the presence of free electrons when it is ionized to a plasma, which starts occurring at pressures above ~ 0.1 MBar. One way to characterize plasmas is by its Debye length λ_D given by

$$\lambda_D^2 = \frac{\epsilon_0 k_B T_e}{n_e q} \ . \tag{2.63}$$

Where T_e is the electron plasma temperature, n_e its number density, k_B is the Boltzmann constant, ϵ_0 is the vacuum permittivity, and q the elemental charge. It is possible to compare the high-energy-density regime to physical and astrophysical systems by considering their respective density and pressure. For example, common solid, liquid, and gaseous systems lie in the range of temperatures below 10^4 K and densities within a few orders or magnitude from that of water 10^{-3}–10^1 g/cm^3. Most ideal and dusty plasmas in the universe are found at lower densities and higher temperatures such as solar wind, or nebulae with $\lambda_D \approx 10$ m, while the solar core or planetary systems are of significantly higher densities and lower temperatures with $\lambda_D \approx 10^{-11}$ m.

In general terms, any ionized medium may, by some definitions, be considered plasma so in this sense high-energy-density matter is plasma. However classical plasma theory is only applicable to space plasmas and low-pressure plasma sources, the so-called "ideal plasmas" which have many assumptions built into them. High-energy-density plasmas are not typically ideal plasmas as they normally have high density and characterizing features which makes them behave like a non-ideal gas. High-energy-density plasmas also encompass conditions at which the density is low but at really high temperatures so that the pressure is higher than 0.1 MBar. For example, air density at a temperature above 1 keV. If the density decreases even further but the temperature keeps increasing then plasmas where relativistic effects are important arise, which also fall outside traditional plasma theory.

Overall, all of these plasmas share in common that their collective behavior dominates their properties. In high-energy-density plasmas, their behavior is more correlated, relativistic, and radiative while ionization and Coulomb interactions are not necessarily essential. In this sense, one way to characterize plasmas is to compare the magnitude of the energies associated with Coulomb

forces to the kinetic energy of a thermal particle. A commonly used coupling parameter is therefore defined as

$$\Gamma = \frac{Ze^2}{4\pi\epsilon_0 a k_B T_e} \ , \tag{2.64}$$

where $a = 3/(4\pi n)^{1/3}$ is the Wigner-Seitz radius. Then, for $\Gamma \gg 1$ the system would be a strongly coupled plasma, while $\Gamma \ll 1$ it would be a weakly coupled (ideal) plasma. Lastly, when higher-Z plasmas are heated to hundreds of eV then they will emit radiation, and the radiation transport effects can become important in the collective behavior of the plasma system. This regime is also known as radiative plasma and radiation hydrodynamics, which mostly falls outside the scope of this thesis. Alternatively, for accessing relativistic plasmas at hundreds of keV it is typically needed to use ultrafast lasers and particle accelerators. An important consideration is that plasmas are typically described in equilibrium conditions, while most interesting HEDP phenomena are dynamic in nature, which is a core element in this thesis. Some of these include shock waves, radiation waves, matter ablation, or hydrodynamic instabilities. Therefore, this section will focus on introducing some of the fundamental concepts in high-energy-density dynamic systems.

2.2.2 Hydrodynamic fluid equations

Plasmas have two key descriptions: kinetic and fluid. The description used depends on the plasma system in question and the statistical distribution of its particle velocities $f(\mathbf{v}, \mathbf{r}, t)$. For plasmas with non-Maxwellian particles distributions a kinetic description is typically required. In order to describe the particles' behavior statistically the Boltzmann equation is used which is given by,

$$\left.\frac{df}{dt}\right|_C = \frac{\partial f_s}{\partial t} + \mathbf{v} \cdot \nabla f_s + \frac{\mathbf{F}}{m_s} \cdot \nabla_v f_s \ . \tag{2.65}$$

In the Right-Hand Side (RHS) of Eq. 2.65, the $\mathbf{F}$ term is the sum over all forces acting on the particles typically referring to the Lorentz force $\mathbf{F} = q(\mathbf{E} + \mathbf{v} \times \mathbf{B})$, then ∇_v is the grad operator in velocity space, $df/dt|_C$ indicates the time rate of change of f due to collisions. When the Left-Hand Side (LHS) of Eq. 2.65 is equal to zero the equation is known as the Vlasov equation for collisionless plasma. Furthermore, when $f(\mathbf{v}, \mathbf{r}, t)$ is Maxwellian then a fluid description can be applied. The Maxwellian particle velocities distribution is of the form,

$$f_s(\mathbf{v}) = n(\mathbf{r}) \left(\frac{m_s}{2\pi k_B T_s}\right)^{3/2} e^{-\frac{m_s \mathbf{v}^2}{2k_B T_s}} \ , \tag{2.66}$$

where m_s and T_s are the particle's mass and temperature, respectively, and it is typically normalized so that $\iiint f_s(\mathbf{v}, \mathbf{r}, t) d^3\mathbf{v} = n(\mathbf{r})$. Then, by taking the moments of the Boltzmann equation

and assuming a polytropic gas one gets the fluid description for plasmas,

$$\frac{\partial \rho}{\partial t} + \nabla \cdot \rho \mathbf{u} = 0 \ , \tag{2.67}$$

$$\rho \left(\frac{\partial \mathbf{u}}{\partial t} + \mathbf{u} \cdot \nabla \mathbf{u} \right) = -\nabla p \ , \tag{2.68}$$

$$\frac{\partial p}{\partial t} + \mathbf{u} \cdot \nabla p = -\gamma p \left(\nabla \cdot \mathbf{u} \right) \ . \tag{2.69}$$

Here $\mathbf{u}, \rho, p$ are the velocities, density, and pressure respectively, while γ is the polytropic index (ratio of specific heats). In this set of equations Eq. 2.67 is the continuity equation describing the conservation of mass, Eq. 2.68 is the equation of motion derived from the conservation of momentum, and Eq. 2.69 is the energy equation obtained from conservation of energy. From the EE one will notice that there are three equations and four unknowns. This has to do with the fact that an Equation of State (EOS) is required which relates state variables including pressure, temperature, and density to one another. For a polytropic gas, the EOS is

$$p \propto \rho^{\gamma} \ . \tag{2.70}$$

The Euler Equations (EE) can also be written in a more general form such as to include any other forces such as electromagnetic fields or gravity. Therefore, not accounting for mass sources the continuity equation Eq. 2.67 would remain unchanged, while the momentum equation (non-relativistic) Eq. 2.68 would read

$$\rho \left(\frac{\partial \mathbf{u}}{\partial t} + \mathbf{u} \cdot \nabla \mathbf{u} \right) = -\nabla P + \mathbf{F}_{EM} + \nabla \cdot \sigma_v + \mathbf{F}_{other} \ . \tag{2.71}$$

The term $\mathbf{F}_{\text{EM}}$ is to account for the interaction of particles with electromagnetic fields, σ_v is the viscous stress tensor, and $\mathbf{F}_{\text{other}}$ is to account for any other forces such as gravity. The term involving viscosity with σ_v can be analyzed by approximating it with the scalar viscosity ν so that $\sigma_v \sim \rho\nu \left(\nabla \cdot \mathbf{u} \right)$, therefore the viscosity term can be approximated as,

$$\begin{aligned} \nabla \cdot \sigma_v &\approx \nabla \cdot \left(\rho\nu \left(\nabla \cdot \mathbf{u} \right) \right) \\ &\approx \rho\nu \nabla^2 \mathbf{u} \\ &\approx \frac{\rho\nu U}{L^2} \ . \end{aligned} \tag{2.72}$$

Where L is the characteristic length and which divides by $\rho U^2/L$ to find the normalized amplitude,

$$\frac{\left[\frac{\rho\nu U}{L^2}\right]}{\left[\frac{\rho U^2}{L}\right]} = \frac{1}{R_e} \ , \tag{2.73}$$

then,

$$R_e = \frac{UL}{\nu} \ . \tag{2.74}$$

Here R_e is the Reynold's number which describes the ratio of inertial forces to viscous forces in a fluid. When R_e is large and ν is small, then the term $\nabla \cdot \sigma_v$ in Eq. 2.68 would be small and can be dropped. Alternatively, when R_e is small and ν is large then $\nabla \cdot \sigma_v$ must be included and accounted for in the momentum equation.

In order to solve the EE one technique that can be used is "linearization", which consists of decomposing (approximating) a variable into a zeroth order average value denoted with the subscript 0, and a small perturbation/deviation from the average as the first order quantity denoted with a subscript 1 such as

$$\rho \approx \rho_0 + \rho_1 \ , \tag{2.75}$$

$$p \approx p_0 + p_1 \ , \tag{2.76}$$

$$\mathbf{u} \approx \mathbf{u}_0 + \mathbf{u}_1 \ . \tag{2.77}$$

With $\mathbf{u} = \mathbf{u}_1$ when $\mathbf{u}_0 = 0$. For small wavelength perturbations, we neglect higher-order terms. Therefore it follows that the linearized continuity and momentum equations become

$$\frac{\partial \rho_1}{\partial} + \rho_0 \nabla \cdot \mathbf{u}_1 + \mathbf{u}_1 \cdot \nabla \rho_1 + \rho_1 \nabla \cdot \mathbf{u}_1 = 0 \ , \tag{2.78}$$

$$\rho_0 \left(\frac{\partial \mathbf{u}_1}{\partial t} + \mathbf{u}_1 \cdot \nabla \mathbf{u}_1 \right) + \rho_1 \left(\frac{\partial \mathbf{u}_1}{\partial t} + \mathbf{u}_1 \cdot \nabla \mathbf{u}_1 \right) = -\frac{\partial p}{\partial \rho} \nabla \rho_1 \ . \tag{2.79}$$

From these expressions, all terms that have a multiple of two small quantities with subscript 1 will result in a second-order term that is small enough to be dropped. Therefore this leads to the linearized EE

$$\frac{\partial \rho_1}{\partial t} + \rho_0 \nabla \cdot \mathbf{u}_1 = 0 \ , \tag{2.80}$$

$$\rho_0 \frac{\partial \mathbf{u}_1}{\partial t} = -\frac{\partial p}{\partial \rho} \nabla \rho_1 \ . \tag{2.81}$$

One can then use these two equations and take the second derivative in time followed by substitu-

tion and some algebra to obtain the result

$$\frac{\partial^2 \rho_1}{\partial t^2} - \frac{\partial p}{\partial \rho} \nabla^2 \rho_1 = 0 \ , \tag{2.82}$$

which describes the acoustic wave equation in which $\partial p / \partial \rho = c_s^2 = \gamma p / \rho$ is the speed of sound for a polytropic gas.

2.2.3 Multi-fluid model

Many high-energy-density phenomena occur at timescales at which the single fluid description for plasma is no longer valid. For these situations, a multi-fluid description is more appropriate, a model in which the motion of electrons and ions are considered separately. This kind of description is more complex than the single fluid, but it is more accurate in describing high-energy-density systems in which the electrons' motion has an influence on the behavior. A particularly relevant example in this context is the case for direct laser irradiation of a target and the laser-plasma interaction thereafter, a subject that is a core element in this thesis. In this sense, electrons and ions start acting independently when the density decreases or the temperature increases significantly so that the collisional coupling between electrons and ions becomes smaller.

Within this context, one can utilize the EE independently for every fluid species j, so that

$$\frac{\partial n_j}{\partial t} + \nabla \cdot (n_j \mathbf{u}_j) = 0 \tag{2.83}$$

for the continuity equation, and for the momentum equation

$$m_j n_j \frac{\partial \mathbf{u}_j}{\partial t} + m_j n_j \mathbf{u}_j \cdot \nabla \mathbf{u}_j = n_j q_j \left(\mathbf{E} + \frac{\mathbf{u}_j}{c} \times \mathbf{B} \right) - \nabla p_j + \sum_l R_{j,l} \ , \tag{2.84}$$

where the subscript $j = e$ is typically used for electrons, and $j = i$ for ions, and $R_{j,l}$ is the rate of momentum density change between species j and l. Just as in the single fluid description, the three multi-fluid EE have four unknowns and thus an EOS is necessary. At high enough temperatures, any material can be approximately described as a polytropic gas with an EOS describing an ideal gas. This is,

$$p = \rho R T = N k_B T = \frac{\rho \left(1 + Z\right) k_B T}{A m_p} \ , \tag{2.85}$$

where N is the total number density of particles, k_B is the Boltzmann constant, and T is the temperature. For a high-energy-density plasma one can take the average level of ionization Z (number of electrons), the average mass of the ions A, as well as the proton mass m_p to estimate the pressure for a polytropic gas. Moreover, the internal energy for a system of particles with n

degrees of freedom is

$$\rho\epsilon = \frac{n}{2} N k_B T = \frac{n}{2} \frac{\rho\,(1+Z)\,k_B T}{A m_p} \,. \tag{2.86}$$

This leads to the commonly seen result from statistical physics for the internal energy of a particle given by $1/2K_BT$ per degree of freedom so that $\epsilon = \frac{3}{2}k_BT$ for three degrees of freedom. From the internal energy, it follows that the specific heat (energy required to raise a unit of mass to a unit degree in temperature) at constant volume is

$$C_v = \left.\frac{\partial \epsilon}{\partial T}\right|_\rho = \frac{n}{2} R \,, \tag{2.87}$$

and the specific heat at constant pressure (assuming $Z(R)$ is independent of T) is

$$C_p = \left.\frac{\partial \epsilon}{\partial T}\right|_P = \left(\frac{n}{2} + 1\right) R \,. \tag{2.88}$$

Directly from these results and using thermodynamic principles for a constant entropy, once again one obtains that the speed of sound is given by

$$c_s^2 = \left(\frac{\partial p}{\partial \rho}\right)_s = \frac{C_p}{C_v}\left(\frac{\partial p}{\partial \rho}\right)_T = \frac{C_p}{C_v}\frac{p}{\rho} = \frac{\gamma p}{\rho} \,. \tag{2.89}$$

From this result, a definition for the polytropic index can be obtained as the ratio of specific heats

$$\gamma = \frac{C_p}{C_v} = 1 + \frac{2}{n} \,. \tag{2.90}$$

Notice that for $n = 3$ this implies that $\gamma = 5/3$, which is typically used for a polytropic (ideal) gas. However as the degrees of freedom increase then an isothermal system is approached and γ decreases towards 1. Another consequence would be the previously stated result: $p \propto \rho^\gamma$ for adiabatic changes over pressure in which γ is constant, and furthermore these results imply that the internal energy is

$$\rho\epsilon = \frac{p}{(\gamma - 1)} \,. \tag{2.91}$$

Calculations using polytropic models are not straightforward. For an isothermal system, the result would be $p \propto \rho$ and therefore $\gamma = 1$. However, in this limit, Eq. 2.91 would imply that the internal energy is infinite, which is not physical. Typically, for only kinetic degrees of freedom one would expect to have $\gamma = 5/3$ and the above equation applies to an adiabatic system that is not isothermal. In contrast, isothermal systems are those with very fast heat transport which change compression while maintaining a constant temperature. In an isothermal system, acoustic phenomena can be described with $\gamma = 1$, while the internal energy of the system can be evaluated

using $\gamma = 5/3$. This variation in the polytropic index is a more realistic and complex scenario during high-energy-density experiments, which partly motivates some of the results discussed later in this dissertation.

2.2.4 Shock waves and jump conditions

Shock waves are a fundamental phenomenon in HEDP and a protagonist in this dissertation work. Nearly all experiments in HEDP involve at least one kind of shock wave, if not many. On a fundamental level, shocks are "strong" discontinuities in the state variables carrying disturbances in a medium with high compression and expansion. In high-energy-density experiments, high-compression systems might be created by pistons or high-intensity lasers, while in astrophysical systems such as in sonic booms in the magnetosphere from solar wind, or a supernova expansion from the passing of a star. Most interesting astrophysical phenomena are sudden and typically include one kind of shock wave.

To analyze shock waves one can start by comparing them to normal sound waves, in which energy is transported at the sound speed $c_s^2 = \partial p/\partial \rho$, then the maximum energy than can be carried by the wave is in the order of the internal pressure $\sim c_s^2 \rho$ with a maximum in the order of $\sim \rho c_s^3$. If one is to increase the pressure in the medium even further then a discontinuity (shock) is created at its boundary. The fluid cannot respond to such higher pressures by radiating sound waves and so a shock is launched. For instance, when a plasma of density $1\mathrm{g/cm}^3$ is rapidly heated by a laser, say to 1eV in temperature, the resulting pressure would be in the order of one million atmospheres (1Mbar), and even higher pressures are relatively easily obtained in high-energy-density experiments. At those high-energy-density conditions fluids cannot sustain the amount of pressure generated and shock waves are generated as a result.

If a perturbation in a medium moves at a speed u then the ratio of this quantity to the speed of sound in the medium c_s is known as the Mach number $M_u = u/c_s$. Therefore if $u < c_s$ and $M_u < 1$ then the flow is said to be subsonic, while for $u > c_s$ and $M_u > 1$ the wave is supersonic in nature. Within this context, a shock wave will have three effects on the medium. First, it will carry forward the energy deposited at a shock speed $u_s > c_s$. Second, it will heat and accelerate the upstream (ahead of shock, unshocked) medium, thus depositing kinetic energy in the post-shocked fluid with velocity u_p. Lastly, it will continue heating the downstream (behind the shock, shocked) fluid so that the motion of the shock wave relative to the heated fluid is subsonic. For the following analysis the upstream fluid will be denoted with a subscript 1 and the downstream fluid with a subscript 2.

By utilizing the shock frame of reference it is possible to derive equations that describe the physical conditions in the shocked material. Regardless of the presence of a discontinuity in the

medium, the laws for conservation of mass, conservation of momentum, and conservation of energy still hold. Therefore, starting once again from the Euler equations in conservative form:

$$\frac{\partial \rho}{\partial t} = -\nabla \cdot (\rho \mathbf{u}) \ , \tag{2.92}$$

$$\frac{\partial}{\partial t}(\rho \mathbf{u}) = -\nabla \cdot (\rho \mathbf{u}\mathbf{u}) - \nabla p \ , \tag{2.93}$$

$$\frac{\partial}{\partial t}\left(\frac{\rho u^2}{2} + \rho\epsilon\right) = -\nabla \cdot \left[\rho \mathbf{u}\left(\epsilon + \frac{u^2}{2}\right) + p\mathbf{u}\right] \ . \tag{2.94}$$

Then for a general conservative type equation with a state variable ρ_Q and its corresponding flux Γ_Q having the form

$$\frac{\partial \rho_Q}{\partial t} = -\nabla \cdot \Gamma_Q \tag{2.95}$$

, it is possible to introduce a small planar disturbance $\nabla \to \partial/\partial x$ and integrate over a small region so,

$$\begin{aligned} \frac{\partial \rho_Q}{\partial t} &= -\frac{\partial}{\partial x}\Gamma_Q \\ \int_{x1}^{x_2} \frac{\partial \rho_Q}{\partial t} dx' &= -\int_{x1}^{x_2} \frac{\partial}{\partial x}\Gamma_Q(x')dx' \end{aligned} \tag{2.96}$$

As the region becomes infinitesimally small $x_2 - x_1 \to 0$ then the LHS of Eq. 2.96 approaches zero but the RHS does not, implying that the fluxes at each side of the discontinuity are conserved this is,

$$\begin{aligned} 0 &= \Gamma_Q(x_2) - \Gamma_Q(x_1) \\ \Gamma_Q(x_q) &= \Gamma_Q(x_2) \end{aligned} \tag{2.97}$$

This is an important result that applies for an infinitesimally small region dx that is fixed, which highlights the significance of using the shock frame of reference in this analysis. Applying the flux conservation result to the three EE in conservative form one finds the shock relations, also known as the (one-dimensional) Rankine-Hugoniot *jump conditions*,

$$\rho_1 u_1 = \rho_2 u_2 \ , \tag{2.98}$$

$$\rho_1 u_1^2 + p_1 = \rho_2 u_2^2 + p_2 \ , \tag{2.99}$$

$$\left[\rho_1 u_1\left(\epsilon_1 + \frac{u_1^2}{u}\right) + p_1 u_1\right] = \left[\rho_2 u_2\left(\epsilon_2 + \frac{u_2^2}{u}\right) + p_2 u_2\right] \ , \tag{2.100}$$

which imply that the mass, momentum, and energy flux across a shock front are conserved. As in the previous analysis, an equation of state is needed to complete these jump conditions. In this sense, equation of state measurements are commonly carried out by taking measurements of shocks and plotting the Rankine-Hugoniot relation or *shock Hugoniot* function $p\left(p_1, 1/\rho_1, 1/\rho_2\right)$.

To obtain these relations in the laboratory one is often able to measure the shock velocity u_s and post-shock fluid velocity u_p for example by using X-ray imaging techniques, such as those used during later chapters in this thesis, to measure the time it takes a shock to cross a given thickness. These measurements are typically obtained in the lab frame of reference where the shock is not at rest, but rather the shock velocity corresponds to the upstream velocity $u_s = |u_1|$ and the post-shock particle velocity is $u_p = u_1 - u_2$ which can be substituted in the jump condition equations to obtain expressions for the density jump and pressure difference across the shock this is,

$$\begin{aligned} \frac{\rho_2}{\rho_1} &= 1 + \frac{u_p}{u_1 - u_p} \ , \\ p_2 - p_1 &= \rho_1 u_1 \left(u_1 - u_2\right) = \rho_1 u_1 u_p \ , \end{aligned} \tag{2.101}$$

which allows one to determine the thermodynamic state of a system from the measurements of u_s, and u_p, albeit this is not always straightforward. The jump conditions introduced in Eq. 2.92, Eq. 2.93, and Eq. 2.94 describe the fundamental concept of mass, momentum, and energy conservation across the shock front, however, these can be manipulated further to obtain other, sometimes more practical, shock relations. Some of these useful expressions are found in Appendix A and in later chapters in this dissertation.

2.2.5 Overview of hydrodynamic instabilities

Up to this point, the Euler equations have been used for giving a fluid description of hydrodynamic phenomena such as shock waves. Nevertheless, this analysis has been conducted for a One-Dimension (1D) system, which is a function of linear or radial distance. The physical world really operates in Three-Dimensions (3D), and the increase in dimensionality certainly affects the overall behavior of the system. In daily activities it is possible to observe some rather intriguing and fascinating hydrodynamic phenomena such as turbulent clouds, droplet formation in a faucet, or eddies in a cup of coffee with some milk. One might expect that these well-observed hydrodynamic instabilities including, but not limited to, the Rayleigh-Taylor (RT) instability, the Kelvin-Helmholtz (KH) instability, or the Richtmyer-Meshkov (RM) process are well understood, as they have been studied for centuries. Nonetheless, regardless of highly talented scientists, advanced mathematics, and supercomputers running fluid simulations, hydrodynamic instabilities and turbulent flows still hold many mysteries, still being one of the subfields of physics with less progress over the past century.

To understand why a full description of 3D hydrodynamic instabilities has proved to be so difficult for physicist includes the fact that the EE contain terms including the divergence of the product of two parameters, say $\nabla \cdot \rho \mathbf{u}$. This leads to a non-linear equation assuming both quantities

are a function of space (which they are in real 3D scenarios). Therefore, to deal with such a problem it is typically assumed that one of the two variables is constant for a specific situation, or alternatively, by linearizing the equation and dropping second-order terms. Even then, much has been learned on hydrodynamic instabilities, and much is still being studied. This is one of the fundamental motivations in this dissertation work, the need to improve our understanding of such hydrodynamic systems, and how electron beams and X-rays from LWFA can be a step forward in the direction to advance our diagnostic systems and consequently expand our knowledge of hydrodynamic instabilities and their effect on HEDP and ICF experiments.

There is no doubt that these approaches can lead to a useful understanding of how hydrodynamic instabilities behave at the 1D fundamental level. However, these models fail to capture all the intricacies in the plasma dynamics found in real 3D experimental conditions. For instance, some of the second-order non-linear terms dropped during linearization analysis might be large during strong density and pressure perturbations and are capable of driving waves of their own. These effects are not tractable in the analysis and, depending on the spatio-temporal scale, its behavior is not followed in computer simulations—constrained by the analytical models as well as their computing capacity for resolving the dynamics. Regardless, of these limitations, acquiring some understanding of hydrodynamic instabilities is certainly feasible. In particular, analysis and simulations can help in understanding the conditions that might lead to unstable behavior, from which many of the well-known instabilities acquired their name.

In this sense, linearization could be used to find an initial approximation for the growth rate in an unstable system when its perturbation amplitude is relatively small. In real experiments, as the modulation/perturbation amplitude grows in amplitude then a 1D or 2D approximation will no longer be valid, and 3D effects will start to influence the dynamics of the instability. This is common for real fluids in HEDP experiments where structures can develop in 3D as a consequence of strong 2D perturbations, such as in turbulent flow, which set the stage for secondary instabilities to develop. It is important to note that even though 2D instabilities have thoroughly been studied, 3D instabilities are typically specific and geometry dependent. Some of the consequences of geometry will become apparent later in this thesis.

CHAPTER 3

Methods

3.1 Introduction

This chapter introduces the experimental, analytical, and simulation methods that were used to carry out the experiments described in Chapter 5, Chapter 6, and Chapter 7. For the experiment, the optical characterization of both long pulse and ultrashort pulse laser foci was important, as well as diagnosing the quality of the generated electron beam in terms of its energy distribution, charge, and divergence. The X-ray beam was also characterized in order to recover its spectrum and source size. The characterization of the electron and X-ray beams are accompanied by analysis techniques described in this chapter, including synthetic phase-contrast X-ray imaging generation, density retrieval from experimentally measured phase-contrast X-ray images, and electromagnetic field recovery from radiography images taken with a LWFA electron beam probe. These are relevant to each of the results shown in Chapter 5, Chapter 6, and Chapter 7, respectively. Additionally, an introduction to the FLASH radiation hydrodynamics code is given, where the fundamental equations under which it operates are discussed. Simulations using the FLASH code have been a pertinent part in complementing the experimental results obtained during the experimental campaigns.

3.2 BELLA HTT laser system

The experiments conducted for this dissertation were performed at the BELLA Center located at the Lawrence Berkeley National Laboratory. The experiments utilized the HTT dual-beam laser system, which is the focus of this section. The HTT laser system front-end starts with the Coherent Vitara oscillator, which generates a train of femtosecond pulses at a rate of ~ 80MHz having ~ 100 μJ of pulse energy at central wavelength $\lambda_0 = 800$ nm. Then, the Coherent Legend Elite containing a Pockel cell downsamples the frequency from MHz to kHz, meanwhile stretching and amplifying the beam from microjoules to millijoules through an initial regenerative amplifier process. Next, a homemade pulse-cleaning system treats the pre-pulses of the kHz beam, obtaining an

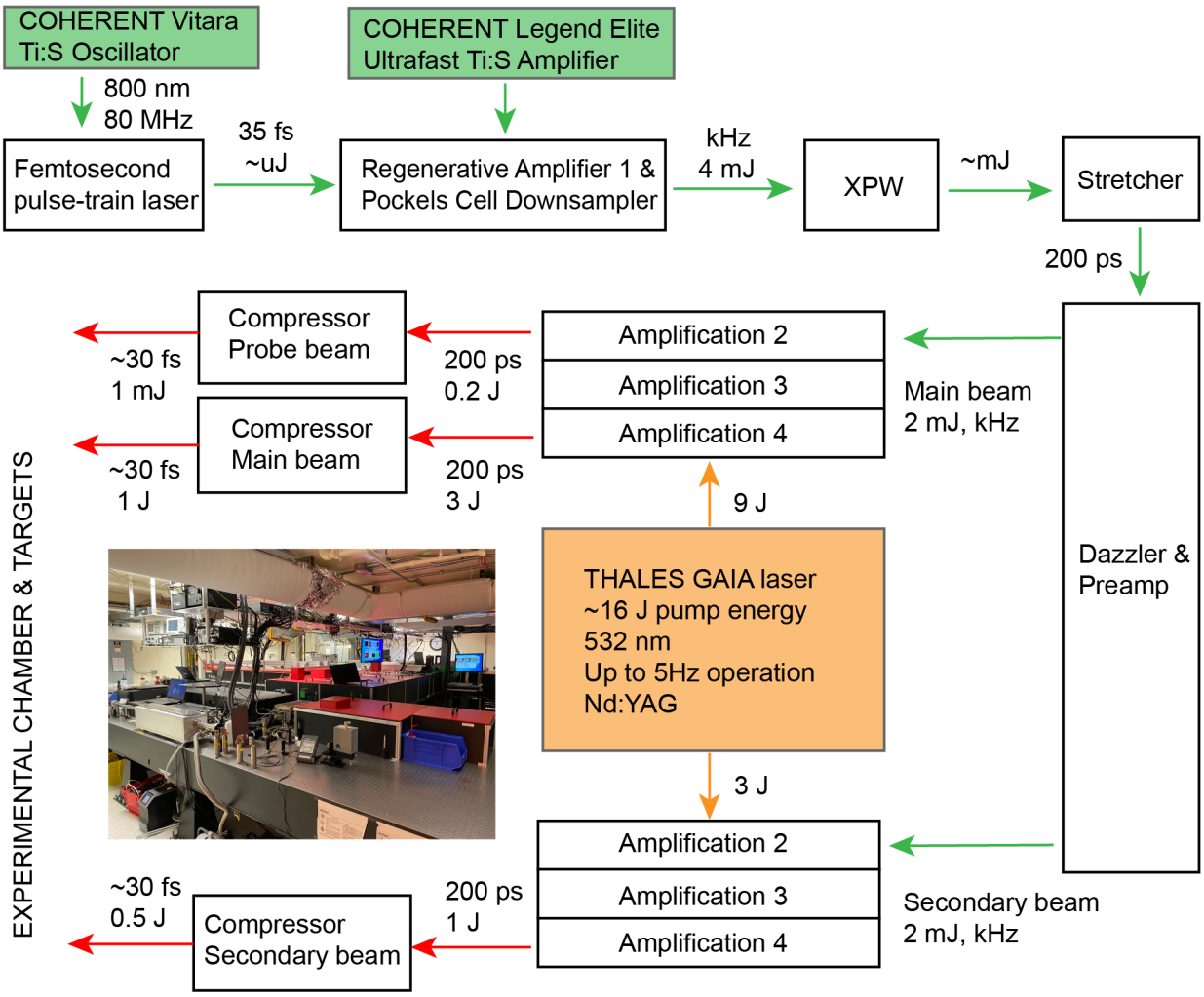

Figure 3.1: Block diagram showing the BELLA HTT dual-beam laser system architecture. The BELLA HTT system is designed for the generation of ultrafast laser pulses capable of producing LWFA electron beams for Thomson scattering and pump-probe experiments.

intensity contrast ratio of order 10^{-7}, which is sufficient for generating LWFA electron beams. The laser pulses are next guided to cross-polarized wave (XPW) apparatus as shown in Fig. 3.1. Clean pulses then are guided through a home-built stretcher which stretches the beam from femtoseconds to around ~ 200 ps. Inside the stretcher, a dazzler is used, which manipulates the chirp (color distribution) inside the pulse. This is available to control the focus and pulse duration in the target area. After the dazzler and pre-amplifier, the beam is then split into two: a main beamline and a secondary beamline. Both of these beamlines are guided through independent regenerative amplifiers which are based on a GAIA (Amplitude) pump laser with nominally 16 J of pump energy, operating at a repetition rate of 1 Hz used for the experiments described in this thesis (maximum 5 Hz).

The GAIA laser amplifies both the main beam as well as the secondary line through a series of three-crystal regenerative amplifiers. The main seed beam is amplified by ~ 9 J of energy from the GAIA to a net output of 3 J before compression (1 J on target). This main arm of amplification is also responsible for generating a probe beam, which is used to interrogate the plasma density through interferometric techniques. The probe has ~ 0.2 J out of the main amplifier. Then, the secondary beamline is amplified by ~ 3 J of energy from the GAIA, destined for the so-called heater line, reaching an output energy of ~ 1 J before compression and ~ 600 mJ on target. After amplification, a pair of two-grating compressors are responsible for individually compressing the beams from 200 ps to 30 fs. The compressed beams are then guided to the experimental chamber. During the experiments conducted for this thesis, the heater line was not actually compressed after amplification, instead, the compressor was bypassed and the amplified long pulse was guided directly to the experimental chamber to act as a long-pulse shock-driver beam.

3.2.1 Experimental chamber setup

Following amplification from CPA, the BELLA HTW beams are guided into the experimental chamber. The LWFA main beam has a 3-inch diameter out of the compressor and into the chamber and a duration of 40 fs. It is later focused by an $f/20$ off-axis parabolic mirror (1.5 m focal length) onto the front of a gas plume from the supersonic nozzle, reaching on-target intensities of order $I \sim 10^{18}$ Wcm^{-2}. After bypassing the compressor, the shock-driver (scatter) beam has a diameter of 1.6 inches and a pulse duration of ~ 200 ps. It is then focused by an $f/27$ off-axis parabolic mirror (focal distance of 1.1 m), reaching intensities of order $I \sim 10^{14}$ Wcm^{-2}, sufficient to generate large amplitude shock-waves in low-Z targets. The long pulse laser was focused perpendicularly to the LWFA driver pulse beamline and approximately ~ 20 cm behind the gas jet. See Fig. 3.2 for a diagram of the experimental chamber configuration. A 1.2 m long variable delay-stage was also used in the heater line, which allowed for precise control of timing

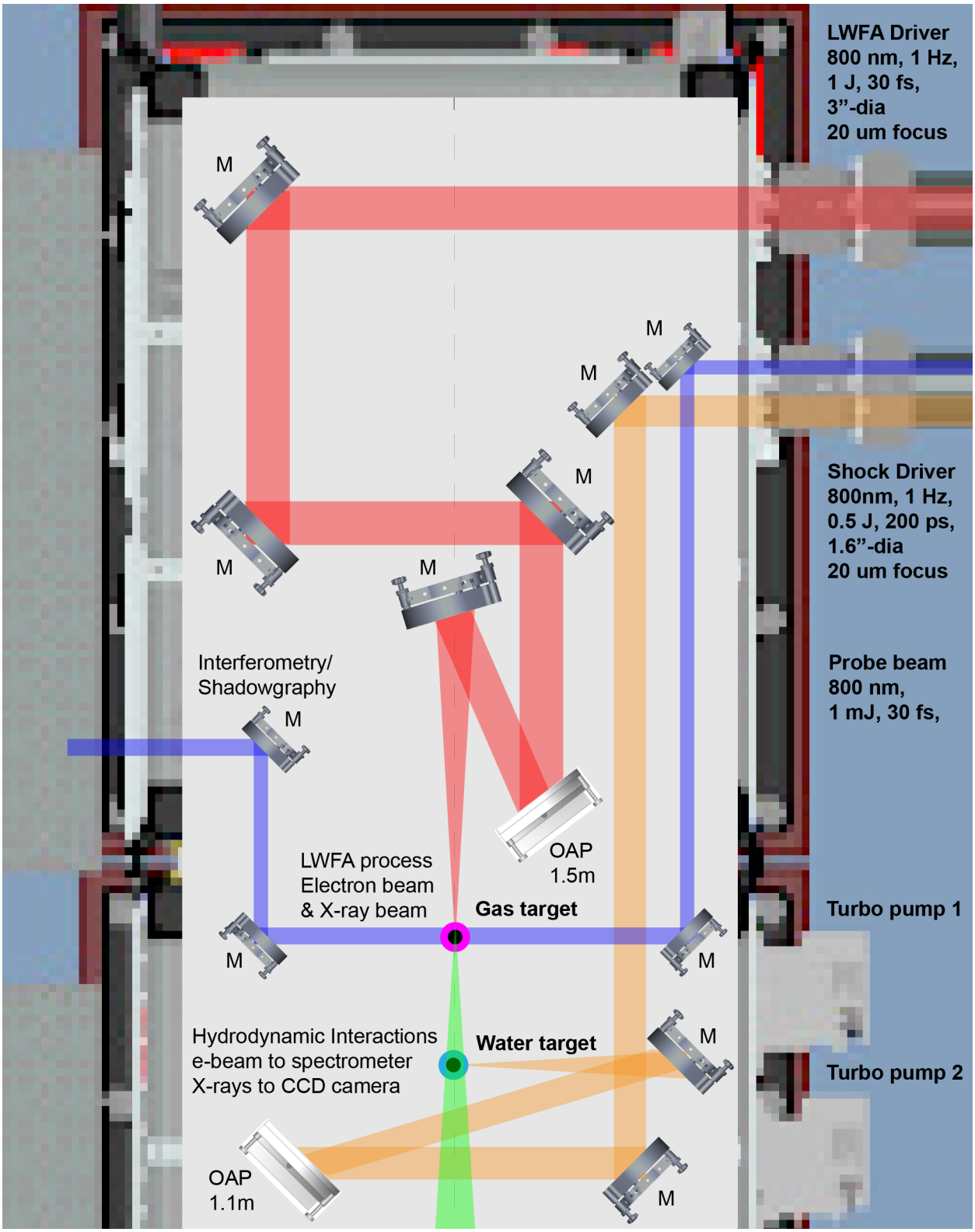

Figure 3.2: Diagram of the BELLA HTT experimental chamber configuration for the pump-probe experiments performed in this dissertation.

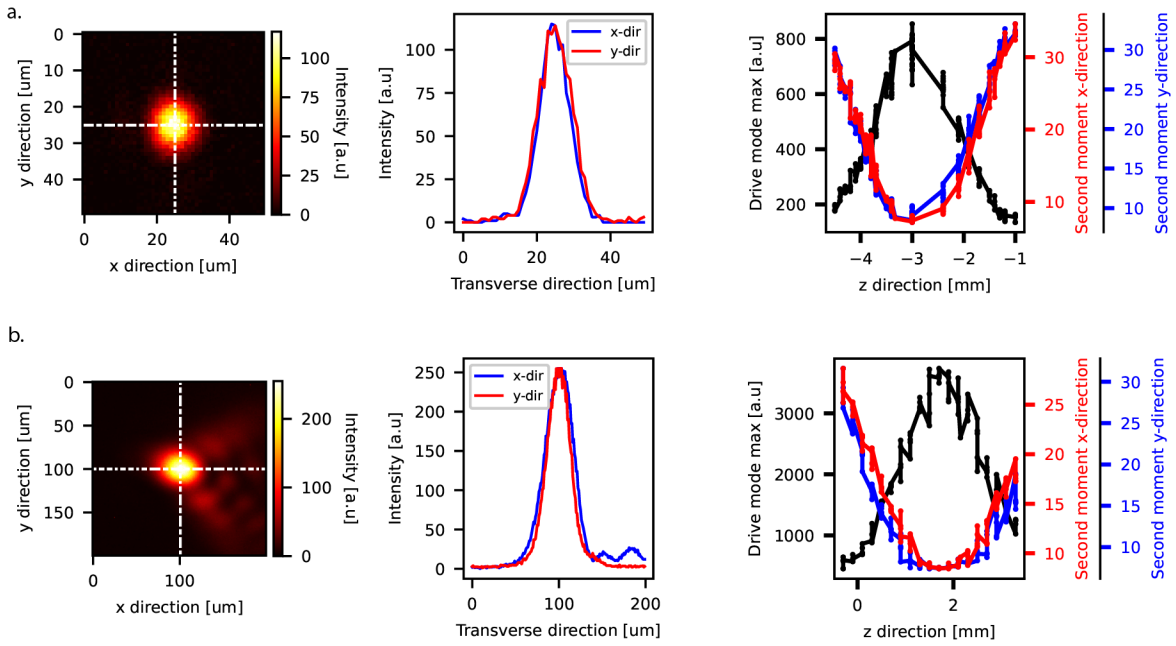

Figure 3.3: Images of focal spots, profiles of focal spots in the transverse direction at focus position, and plots of the laser spots mode maxima and second moments as a function of the longitudinal direction: z-scan. (a) LWFA driver laser and (b) shock heater laser.

for the shock-driver with respect to the LWFA X-rays from hundreds of femtoseconds to up to 8 ns within the interaction. Additionally, an optical probe beam with $\lambda = 800$ nm and 40 fs is also available, which was utilized to analyze the plasma density during laser-gas target interactions through interferometric techniques.

3.3 Diagnostics

3.3.1 Optical characterization

For the experiments performed in Chapter 5, Chapter 6 and Chapter 7, the focal spots of the laser beams were characterized by using off-axis parabolas to focus the beam, aligned by correcting astigmatic aberrations, and a camera to capture the focal spots. The far fields of the beams were imaged using a lens and a Basler camera. The measurement of the focal spot waist can be calculated by taking into account the geometrical magnification and pixel size of the camera. An image of the laser spot at the focus position can be found in Fig. 3.3 as well as a z-position scan through focus, where the maximum mode is plotted as a function distance, as well as the second-moments in the x-direction and y-direction in order to visualize the change in the beam waist size.

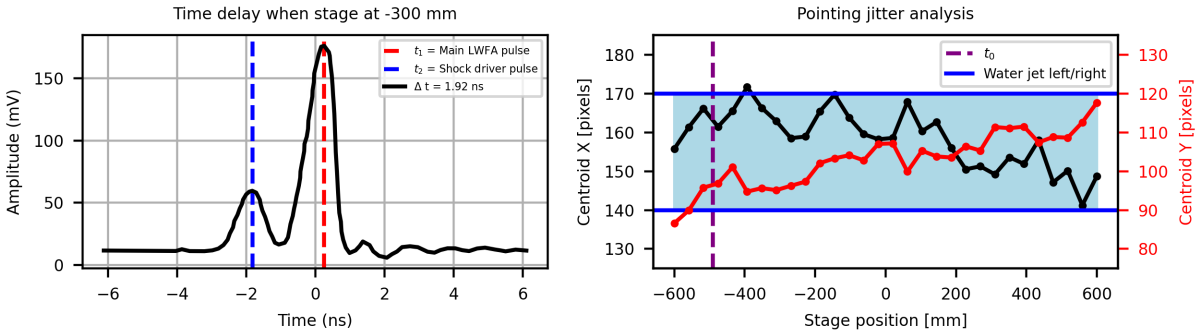

Figure 3.4: (left) Measurement of t_0 from both HTT beams for a given delay stage position taken with a photodiode and oscilloscope. (right) Tracking measurement of heater laser spot x and y centroids as a function of delay stage position.

The experiments in later chapters are concerned with using two laser pulses to perform dynamic imaging based on pump-probe delay scans. One pulse will drive the electron beam and X-ray source, while the second pulse will heat, ablate, and generate a shock wave in a (liquid) target for examination. In order to probe different moments in time, two mirrors on top of a 1.2 m long delay stage were used. Within this context, characterizing the drifting of the focal spot along the delay line is crucially important to ensure an effective laser-target interaction. Focal spot drifting occurs due to imperfections in delay stage flatness and mirror alignment. After some optimization, the drifting effect along the delay line was minimized to ensure the "shock driver" pulse always interacts with the target. The centroid of the "shock driver" pulse was tracked in the x and y directions and plotted along the delay stage as shown in Fig. 3.4. Additionally, a photodiode measurement was used to examine the time difference between the two pulses at a given delay stage position. With this measurement it was possible to calculate at which delay position both pulses should overlap, i.e. an indication of the t_0 position. The photodiode measurement of both pulses at a given delay stage position is shown in Fig. 3.4.

3.3.2 Description of gas target

In the experiments described in this thesis, ionization injection of electrons into the laser wakefield accelerator was achieved by focusing the laser pulse into a plume gas mixture (99.5% Helium and 0.5% Nitrogen). The supersonic flow was generated from a 3 mm diameter conical nozzle, which was synchronized and triggered along with the high-power beam line that provided the laser wakefield driver pulse and provided an approximately flat-top gas profile [192]. A voltage-controlled regulator was available to tune the backing pressure of the gas jet resulting in modifying the density of the gas plume ranging from 2.1–2.8×10^{18} cm^{-3}. The laser-plasma interaction was

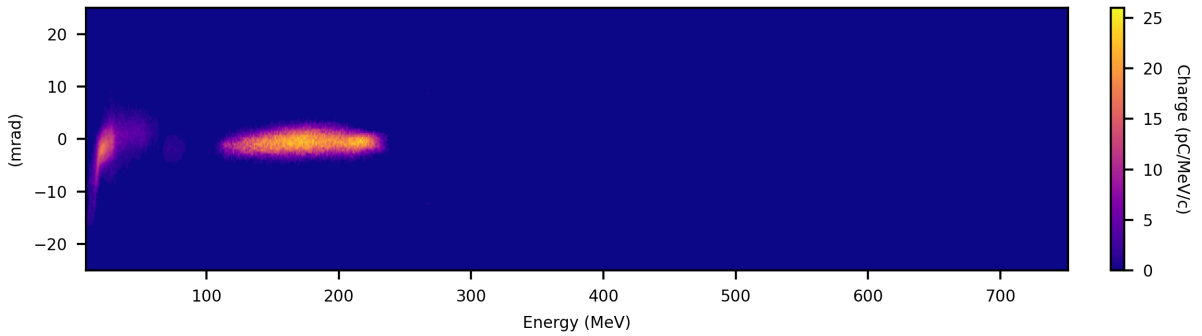

Figure 3.5: Image of scintillating lanex screen from magnetic spectrometer showing a typical shot with the resulting electron energy (MeV) vs angle (mrad).

later characterized by a Mach-Zehnder interferometer including a frequency-doubled probe line running perpendicular to the jet as well as the high-power line.

3.3.3 Electron beam characterization

The electron beam is characterized using a magnetic spectrometer and a scintillating imaging screen. The spectrometer operates by setting a dipole magnet (in this case electromagnet) along the electron beam path, thus influencing its direction and curving its trajectory. Lower energy electrons will be more affected by the magnetic field and curve more, while higher energy electrons will be less affected by the magnetic field and curve less. This energy-dependent curvature allows for discriminating electrons based on their energy, as they may be imaged after the magnet on scintillating Lanex screens and the measured angular deflection may be converted into an energy scale. An example of a spectrum measurement with the lanex screen is shown in Fig. 3.5. To the lowest order, the angular deflection is inversely proportional to the particle energy, as can be seen from the Lorentz force equation. The scintillating light from the screens is captured by a CCD camera, which has a known distance and magnification.

In order to recover momentum and beam charge from the magnetic spectrometer images, the system must be well calibrated so that the field of the magnet is known, as well as the signal-to-charge relation for the Lanex screen. After properly taking these calibrations into consideration it is possible to independently analyze each magnetic spectrometer image and extract the corresponding momentum distribution, charge, density and, from the scintillating screen, beam divergence, as shown in Fig. 3.6 for 400 consecutive shots. For more details on the magnetic spectrometer and its calibration at the BELLA HTT system see Ref. [125]. For the particular run shown in Fig. 3.6, the high-intensity pulse accelerated electrons to 167 ± 13.4 MeV mean energy with divergences $x : 7.8 \pm 1$ mrad, $y : 3.4 \pm 0.8$ mrad and mean charge 32.5 pC.

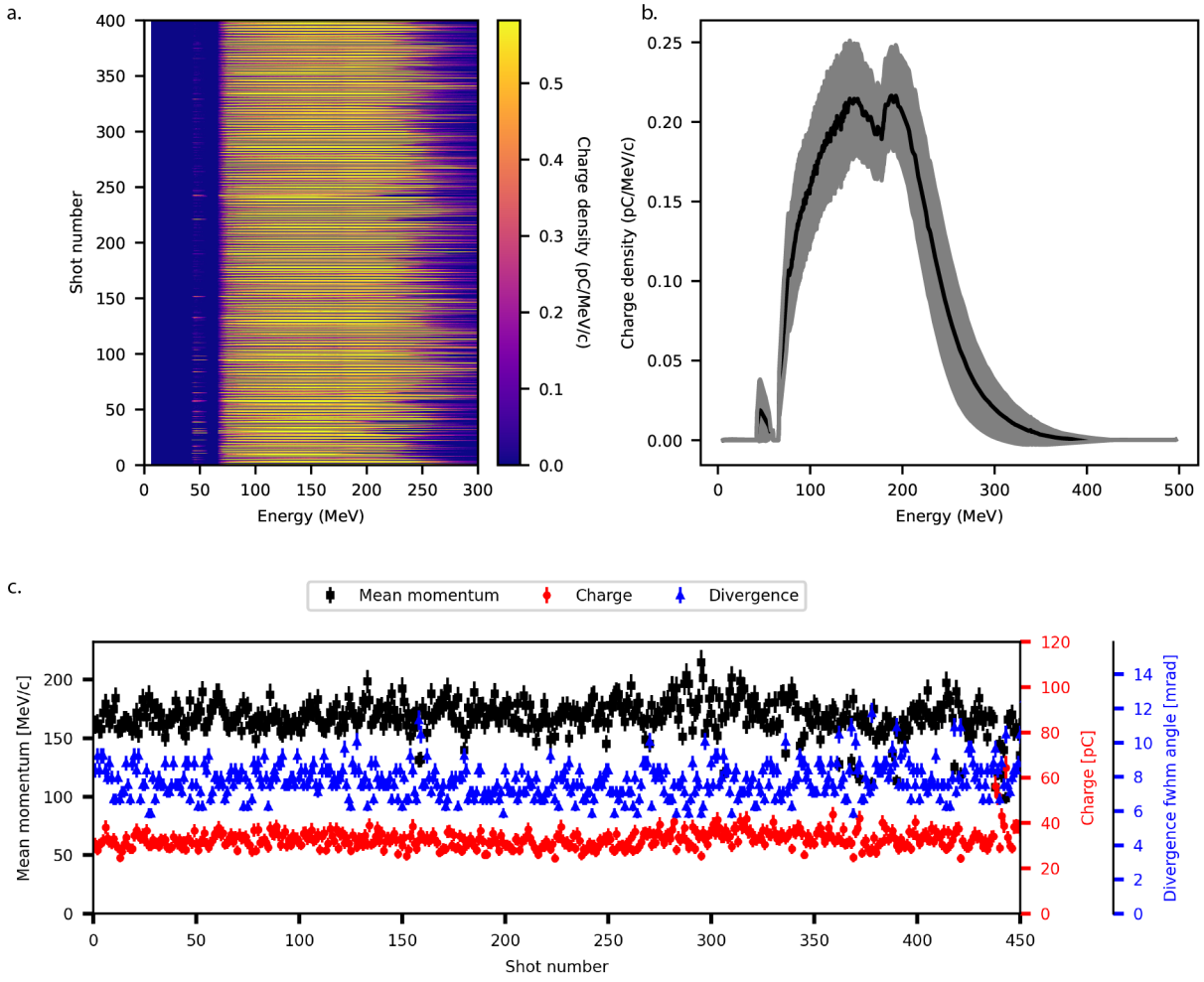

Figure 3.6: (a) Plot of electron beam spectrometer screens for 400 consecutive shots. Displaying the energy range for the beams as well as the calculated charge density. (b) Energy spectrum for the electron beam averaging over 400 shots. The standard deviation on the charge density is also displayed. (c) Scatter plot for 400 shots measuring mean momentum, charge, and divergence of the beam.

3.3.4 X-ray beam characterization

Electron beams from a LWFA will produce X-ray bursts through the oscillation of electrons inside the plasma bubble, so-called betatron oscillations. This section describes the techniques used for the characterization of the betatron X-ray beam, including its spectrum and source size. Naturally, due to energy conservation, the X-ray beam from LWFA will have significantly less energy than the electron beam. A common technique in experimental physics is to recover the X-ray spectrum by using dispersive Bragg crystals, however, for broadband betatron X-ray sources a crystal-based spectrometer would not have enough spectral range. Therefore, a series of foils with different material and thickness and a CCD camera (or an image plate) is typically used to measure the X-rays. Given that CCDs are sensitive to electrons as well as photons, the first step in the characterization of the X-rays is to ensure that the electron beam is deflected from the detector, typically accomplished using a dipole magnet as described in Sec. 3.3.3. Next, additional radiation sources, such as bremsstrahlung generation from the interaction of electrons with chamber walls, must also be discriminated against before proceeding with X-ray analysis.

The X-ray spectrum may be recovered using the techniques described in [84, 78]. The method starts by using a Ross filter wheel, as shown in Fig. 3.7, which has slices of different materials and thicknesses. Each material sample has a different X-ray transmission curve, and the X-ray CCD camera has a quantum efficiency (sensitivity) dependent on photon energy as well, shown in Fig. 3.7.

To recover the spectrum of the betatron X-ray source an image is first taken on the CCD of a filter design with multiple materials for interrogating. The first step is to calculate the synthetic Photon-Stimulated Luminescence (PSL) value for each material sample i by using their respective X-ray transmission T_i and the CCD camera quantum efficiency response Q_{CCD} defined as,

$$PSL_i = \int Y_i(\omega) f(\omega) d\omega_i \times \theta \ , \tag{3.1}$$

where

$$Y_i(\omega) = T_i \times Q_{CCD} \ . \tag{3.2}$$

Here θ is the angle subtended by each pixel from the source. The first variant of the spectrum recovery technique is based on pairs of Ross filters [141, 79, 80]. This method uses pairs of filters and takes advantage of the K-edges of the materials. Each Ross pair has the same X-ray transmission curve, but a different energy range between their K-edges, in such a way that by subtracting the curves it is possible to obtain an energy bin or bandpass filter-like window for counting, as shown in Fig. 3.7. The absolute number of photons per energy bin $W_i(\text{keV})$ and solid angle can be calculated by subtracting the measured signals $S(\text{PSL/rad})$ and taking into account

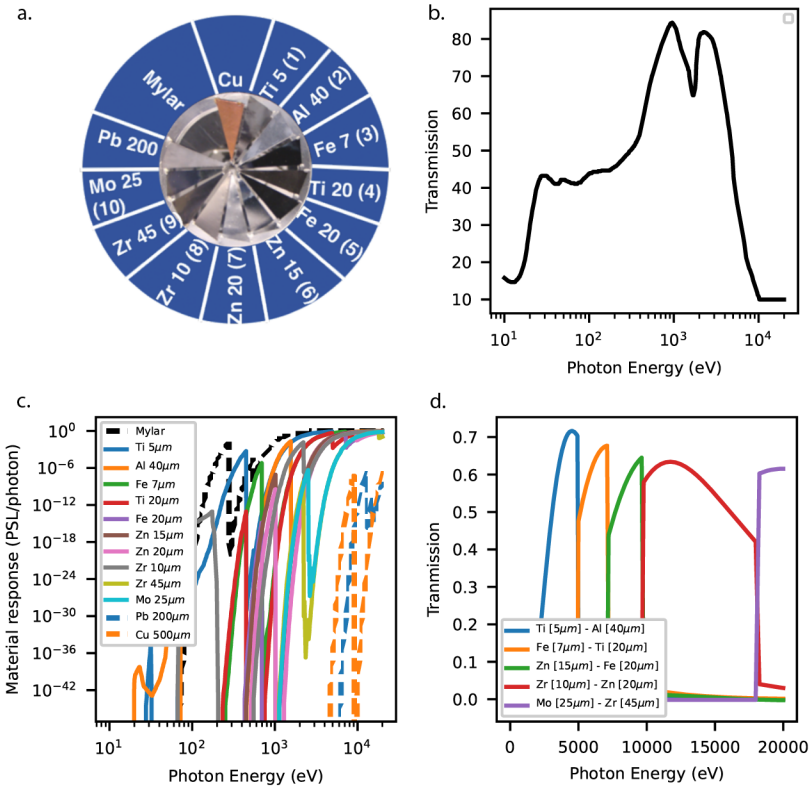

Figure 3.7: (a) Picture of the Ross filter wheel retrieved from Ref. [78] displaying all different channels, materials, and thicknesses in micrometers. (b) Quantum efficiency curve of the Princeton Instruments PI-MTE X-ray CCD camera displaying transmission percentage as a function of photon energy. (c) Material response curves for all channels in the filter wheel as a function of X-ray photon energy. (d) Energy bins from the subtracting of Ross filter pair response curves. The bins are created by the difference in K-edges from two materials that have the same response curve but a different energy range.

the mean transmission of the pair and detector response Y_i^{mean}

$$\frac{d^2N}{dEd\Omega}\,[\text{photons/keV/srad}] = \frac{PSL_i}{Y_i^{\text{mean}} \times \theta \times W_i^{\text{bin}}} \tag{3.3}$$

Ideally, for the Ross method, both filters in a pair are exposed to the same background and thus when they are subtracted from one another the background is also subtracted. Nevertheless, this might not be necessarily true in practice for non-uniform backgrounds. Additionally, some specific materials and thicknesses can be hard to obtain, which in turn would lead to filter pairs that either do not cover the full energy range in question, leave energy bin gaps in between, or the energy outside their bin is not exactly zero which leads to errors in the counting.

Alternatively, the forward fit analysis method is fundamentally based on the X-ray attenuation properties the beam experiences with the filter. Each material wedge is analyzed by counting the average signal transmitted and fitting an assumed analytical distribution to the measured data set so as to extrapolate the critical energy [1, 85, 103]. The assumed (guessed) analytical function for the betatron source, in this case, is a synchrotron-like spectrum following [47] with the given form in the asymptotic limit,

$$f_{\text{guess}}(\omega) = A\left(\frac{\omega}{\omega_{\text{crit}}}\right)^2 K_{2/3}^2\left(\frac{\omega}{\omega_{\text{crit}}}\right)\ , \tag{3.4}$$

where ω_{crit} is the critical frequency after which the spectrum amplitude falls off exponentially. This guessed function $f_{guess}(\omega)$ is then multiplied by each one of the materials transmission curves $T_i(\omega_i)$ as well as the quantum efficiency of the camera. The resulting curves are integrated to obtain the expected relative signal counts compared to the unfiltered signal in PSL values,

$$S_{\text{predicted},i} = \int_0^\infty f_{\text{guess}}(E) Y_i(E) dE\ . \tag{3.5}$$

Then, the calculated PSL values are compared to those values measured from the data by performing the least squares subtraction,

$$\chi^2 = \sum_i \left(S_{\text{predicted},i} - S_{\text{measured},i}\right)^2\ . \tag{3.6}$$

By varying the critical energy value of the initial analytical expression f it is possible to minimize χ^2 to obtain a best-fit spectrum, as shown in Fig. 3.8. For the given run, the resulting fit results in a critical energy for the $E_{crit} = 4.88 \pm 1.33$ keV for the BELLA HTT betatron source.

It is also worth mentioning that for this analysis local background subtraction was performed on the measured image by subtracting the signal level from the Cu and Pb filter in case of a uniform beam distribution, or by considering the surrounding background signal for non-uniform beams.

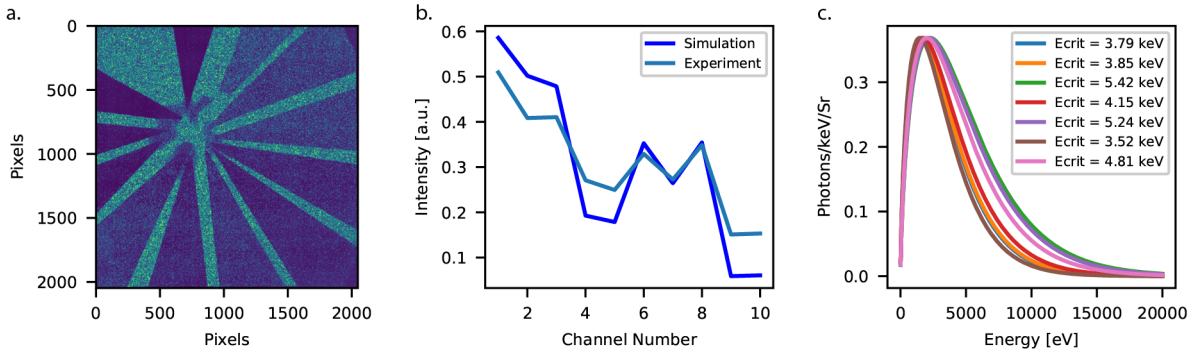

Figure 3.8: (a) Image of Ross filter wheel taken with the HTT betatron X-rays. (b) Comparison of photon counting for all channels in the filter wheel between synthetic best fit and measured data. (c) Estimated synchrotron spectrum given a best-fit critical energy for seven shots.

For non-uniform backgrounds, a mask must be created by selecting the perimeter of each filter in the image and removing the mask from the original image. The background is then smoothed so that an unperturbed beam can be estimated. Such unperturbed beam is then subtracted from the data before analysis, thus vastly improving the results.

Next, the size of the radiation source was estimated by making use of Kirchoff-Fresnel formalism on the diffraction of light. The theory fundamentally consists of the idea that disturbances in a wavefront at a point P arise from the superposition of secondary waves generated at a surface between this point and the light source. Mathematically, the Huygens-Fresnel principle is an approximation for expressing the solution of a homogeneous wave equation from disturbances at an arbitrary point in the field. If P_0 is located at (x_0, y_0, z_0), P is located at (x, y, z), and (ξ, η) are coordinates for a point Q in the aperture plane for the disturbance in between P_0 and P, then the solution to this problem is obtained by solving the diffraction integral following [17],

$$U(P) = \frac{i\cos\delta}{\lambda}\frac{Ae^{ik(r'+s')}}{r's'}\iint_{\mathscr{A}} e^{ikf(\xi,\eta)}d\xi d\eta\ , \tag{3.7}$$

where $r'^2 = x_0^2 + y_0^2 + z_0^2$, $s'^2 = x^2 + y^2 + z^2$, and δ is the angle between the observation direction and the normal to the aperture plane $\mathscr{A}$. By assuming the size of the aperture is small compared to both r' and s' it is possible to expand r and s as a power series so that

$$f(\xi,\eta) = -\frac{x_0\xi + y_0\eta}{r'} - \frac{x\xi + y\eta}{s'} + \frac{\xi^2+\eta^2}{2r'} + \frac{\xi^2+\eta^2}{2s'} - \frac{(x_0\xi + y_0\eta)^2}{2r'^3} - \frac{(x\xi + y\eta)^2}{2s'^3} + \ldots \tag{3.8}$$

It becomes clear that this expression can be simplified when the higher-order terms for ξ and η can be ignored in f. Indeed, this is known as *Fraunhofer diffraction*, while for those cases in which the

higher-order terms cannot be ignored, it is known as *Fresnel diffraction*. In this section, in order to recover the size of the X-ray radiation source, the general form of the Fresnel formalism will be used. First, the basic diffraction integral from Eq. 3.7 can be expressed in complex form as,

$$U(P) = B\,(C + iS) \tag{3.9}$$

where,

$$B = -A\frac{i}{\lambda}\cos\delta\frac{e^{ik(r'+s')}}{r's'}\ , \tag{3.10}$$

$$C = \iint_A \cos\left[kf(\xi,\eta)\right] d\xi d\eta\ , \tag{3.11}$$

$$S = \iint_A \sin\left[kf(\xi,\eta)\right] d\xi d\eta\ . \tag{3.12}$$

Then, the intensity of the wave at the point P in the detector is given by

$$I(P) = |U(P)|^2 = |B|^2\left(C^2 + S^2\right)\ . \tag{3.13}$$

In order to solve the integrals of Eq. 3.11 and Eq. 3.12 it is helpful to make some assumptions. Let us first keep the second-order terms in ξ and η of f in Eq. 3.8 and ignore third and higher-order terms. Then, following the text by Born and Wolf [17], defining

$$b = \frac{\lambda}{2\left(\frac{1}{r'} + \frac{1}{s'}\right)\cos\delta}\ , \tag{3.14}$$

it is possible to make a change of variables of integration to u and v via $u = \xi\sqrt{b\cos\delta}$ and $v = \eta\sqrt{b/\cos\delta}$, thus simplifying the expression even further to yield

$$C = b\iint_{\mathscr{A}} \cos\left[\frac{\pi}{2}\left(u^2 + v^2\right)\right] dudv \tag{3.15}$$

and

$$S = b\iint_{\mathscr{A}} \sin\left[\frac{\pi}{2}\left(u^2 + v^2\right)\right] dudv\ . \tag{3.16}$$

Additionally, let us further assume that the area of integration $\mathscr{A}$ at the perturbation plane is perpendicular to the incident wavefront and rectangular with sides parallel to u and v, thus simplifying the integrals even more through trigonometric identities. This means we may make use of the well-known *Fresnel's integrals*

$$\mathcal{C}(w) = \int_0^w \cos\left(\frac{\pi}{2}\tau^2\right) d\tau \tag{3.17}$$

and

$$\mathcal{S}(w) = \int_0^w \sin\left(\frac{\pi}{2}\tau^2\right) d\tau \tag{3.18}$$

where,

$$w = \sqrt{\frac{2}{\lambda}\left(\frac{1}{r'} + \frac{1}{s'}\right)} x \cos\delta \tag{3.19}$$

Which have been extensively studied and are of great importance to a variety of diffraction problems. These integrals have relevant properties which go beyond the scope of this thesis but have been described in detail in Ref. [17]. The Fresnel's diffraction integrals can indeed be used to recover the size of the radiation source by solving them for a given interference pattern. In particular, one can consider the Fresnel diffraction pattern for a straight-edge disturbance. In particular, let us restrict our attention to the case in which the source-to-detector line PP_0 is perpendicular to the straight edge located at a plane Q in between. If x is the distance of the straight edge from the origin at Q, the Fresnel's integrals extend over the following region of integration,

$$-\infty < \xi < x \quad -\infty < \eta < \infty \tag{3.20}$$

Or,

$$-\infty < u < w \quad -\infty < v < \infty \tag{3.21}$$

Keeping in mind that the dimensions of the domain of integration A must be small compared to the dimensions of PP_0. Further algebra and use of Fresnel identities lead to the following expressions for the real and complex components of the intensity distribution $U(P)$ in terms of $\mathcal{C}(w)$ and $\mathcal{S}(w)$ this is,

$$C = b\left[\left(\frac{1}{2} + \mathcal{C}(w)\right) - \left(\frac{1}{2} + \mathcal{S}(w)\right)\right] \tag{3.22}$$

$$S = b\left[\left(\frac{1}{2} + \mathcal{C}(w)\right) + \left(\frac{1}{2} + \mathcal{S}(w)\right)\right] \ . \tag{3.23}$$

When plugged into Eq. 3.13, these equations lead to the following final expression to calculate the intensity distribution,

$$I = \frac{1}{2}\left[\left(\frac{1}{2} + \mathcal{C}(w)\right)^2 + \left(\frac{1}{2} + \mathcal{S}(w)\right)^2\right] I_0 \tag{3.24}$$

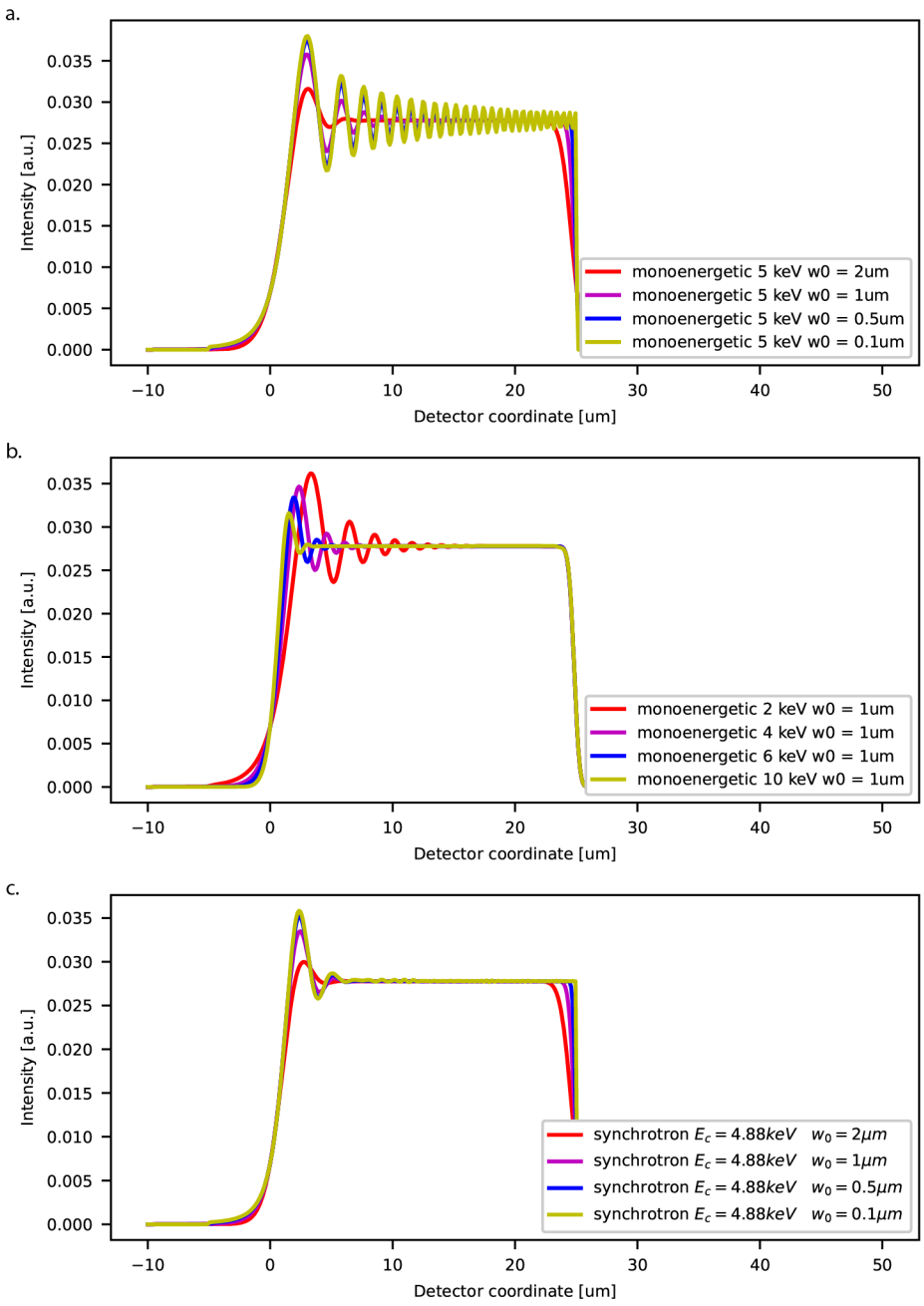

Figure 3.9: (a) Expected Fresnel diffraction pattern of a monoenergetic radiation source interfering with a half-plane straight edge as a function of source size. (b) Expected Fresnel diffraction pattern of a monoenergetic radiation source interfering with a half-plane straight edge as a function of source energy. (c) Expected Fresnel diffraction pattern of a polychromatic radiation source interfering with a half-plane straight edge as a function of source size.

where,

$$I_0 = 4|B|^2 b^2 = \frac{|A|^2}{\left(r' + s'\right)^2} \tag{3.25}$$

Therefore, Eq. 3.24 can be used to calculate the intensity distribution expected at the detector for the interference pattern between a beam with initial distribution I_0 and a sharp straight edge. This calculation is made for a point-like radiation source, however here the goal is to obtain the intensity pattern for a finite-size source. Thus, in order to obtain the real intensity distribution one must convolve the electric field given by $E = B\left(C + iS\right)$ with a source distribution such as,

$$E^*(\omega) = E(\omega) * \sigma \tag{3.26}$$

then,

$$I^*(\omega) = |E^*(\omega)|^2 \tag{3.27}$$

Additionally, the polychromaticity of the radiation source can be taken into account by performing a weighted superposition of the electric fields according to the spectrum. For a Gaussian source with FWHM given by σ as,

$$I = \int_0^{\omega_{\max}} \left(\frac{f(\omega)}{\int f(\omega) d\omega} \right) * I^*(\omega) d\omega \tag{3.28}$$

where $f(\omega)$ represents the radiation spectrum. It is then possible to calculate the expected diffraction pattern for a monoenergetic source with different energies, with different source sizes, as well as for a polychromatic source (synchrotron spectrum) along with different source sizes, as displayed in Fig. 3.9.

Within this context, by imaging a sharp knife edge with the betatron X-rays and fitting the data to the expected Fresnel diffraction pattern of a Gaussian source interfering with a half-plane, it is possible to recover the best-fit for the radiation source size. The fitting of the data for this particular run results in the size of the X-ray source for the BELLA HTT system being $\sigma \leq 1\mu$m as shown in Fig. 3.10.

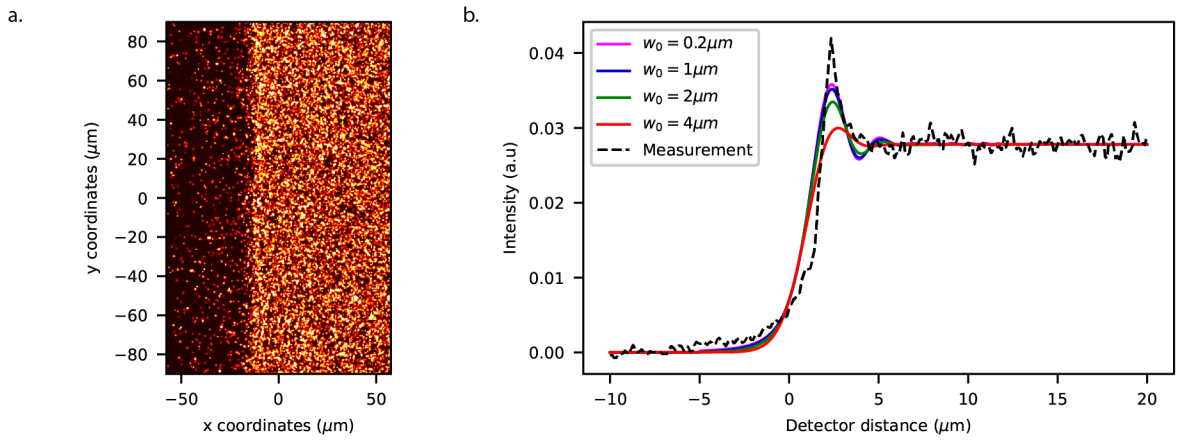

Figure 3.10: (a) Betatron X-ray image of a sharp edge. (b) Lineouts for multiple images and fit of the Fresnel diffraction pattern for a synchrotron spectrum with multiple source sizes.

3.4 Analysis

3.4.1 Phase-contrast X-ray imaging

Traditional X-ray radiography-based techniques are based on the absorption of X-rays as they travel through a sample. The resulting image is then based on the density of the object and its absorption coefficient. Alternatively, Phase-Contrast X-ray Imaging (PCXI) is a technique that is based on the accumulation of phase as X-rays travel through an object. In this sense, X-rays will experience deflections based on the variations in the index of refraction of the sample, which then translates to the accumulation of phase. Such a phase-contrast technique offers higher contrast and resolution of imaging weakly absorbing objects which might also include variations in density and index of refraction. Some phase-contrast imaging techniques require a highly monochromatic source, or complex X-ray optics, which makes them challenging for practical applications. Nevertheless, this thesis will focus on the so-called propagation-based PCXI. This kind of scheme is based on the free-space propagation of X-rays and their interference pattern after they accumulate phase by traveling through a sample. This kind of scheme is suitable for conventional polychromatic sources [185], such as those found in this dissertation work. A free-space propagation method also appears to be the most suitable for a seamless transition to clinical applications.

A key requirement for a propagation-based technique is ensuring the source has high spatial coherence in the transverse direction, meaning that the wave amplitudes are laterally correlated. In order to ensure this requirement is met one must choose the imaging geometry carefully, paying close attention to the source-to-object distance l and object-to-detector distance L. It is then possible to estimate a coherence length for a collection of uncorrelated emitters of wavenumber k

and source size σ, which is given by $d_\perp \sim l/k\sigma$ [185, 84]. Therefore, lateral spatial coherence can be achieved by having a small effective source size, or by imaging at a large distance from the source. In general, the smaller the source the better as long as the photon flux is sufficiently high. As stated before, variations in the sample density, thickness, and refractive index, will have the effect of accumulating phase and changing the shape of the X-ray wavefront traversing the target.

In order to model the expected image pattern from a phase-contrast imaging system a common approach is given in the text by Born and Wolf [17] which utilizes Fresnel/Kirchoff diffraction integrals. This approach is also followed in work by Snigrev *et al* [159] and Arfelli *et al* [7]. This method allows to precisely predict the "pure" phase contrast pattern I assuming a monochromatic point source and infinite detector spatial resolution. In order to obtain the "real" image pattern J the pure pattern must be convolved with the detector Point Spread Function (PSF) and rescaled by the source/magnification distribution, as it is followed by Olivo *et al* [127, 128], and Peterzol *et al* [134]. The convolutions have the effect of blurring the image by a finite source size and can be described as

$$J = I * \text{PSF} * \left[S\left(\frac{R_1}{R_0}\right) \right] \tag{3.29}$$

$$= I * \text{PSF} * s \tag{3.30}$$

$$= I * f \ . \tag{3.31}$$

Where $*$ is the convolution operator, S and s are the source distribution and rescaled source distribution respectively, and $f = \text{PSF} * s$ is a function that can be computed first before convolving it with the pure image for simplicity. Then the real image pattern is given by

$$J = \mathcal{F}^{-1}\left[\mathcal{F}(I)\mathcal{F}(f)\right] \ . \tag{3.32}$$

An alternative to the Fresnel/Kirchoff formalism is based on simpler ray tracing techniques. In this case, the X-rays are tracked as they pass through the sample and the corresponding deflection angles are calculated via the gradient of the projected phase-shift in the sample (see Davis et al [35]). In most practical cases the ray-tracing approach is sufficient in order to capture the effect of the maximum and minima of the source and detector convolutions, although they fail to capture secondary fringes. The transition between Fresnel/Kirchoff to ray tracing techniques is also discussed in Peterzol *et al* [134].

The work in this dissertation utilizes the Fresnel/Kirchoff method which allows the decoupling of the phase-contrast intensity pattern obtained from a sample with the effects of the source size, detector PSF and beam polychromaticity on the image. The technique consists of solving the Fresnel/Kirchoff integrals numerically to obtain the expected complex wave distribution and

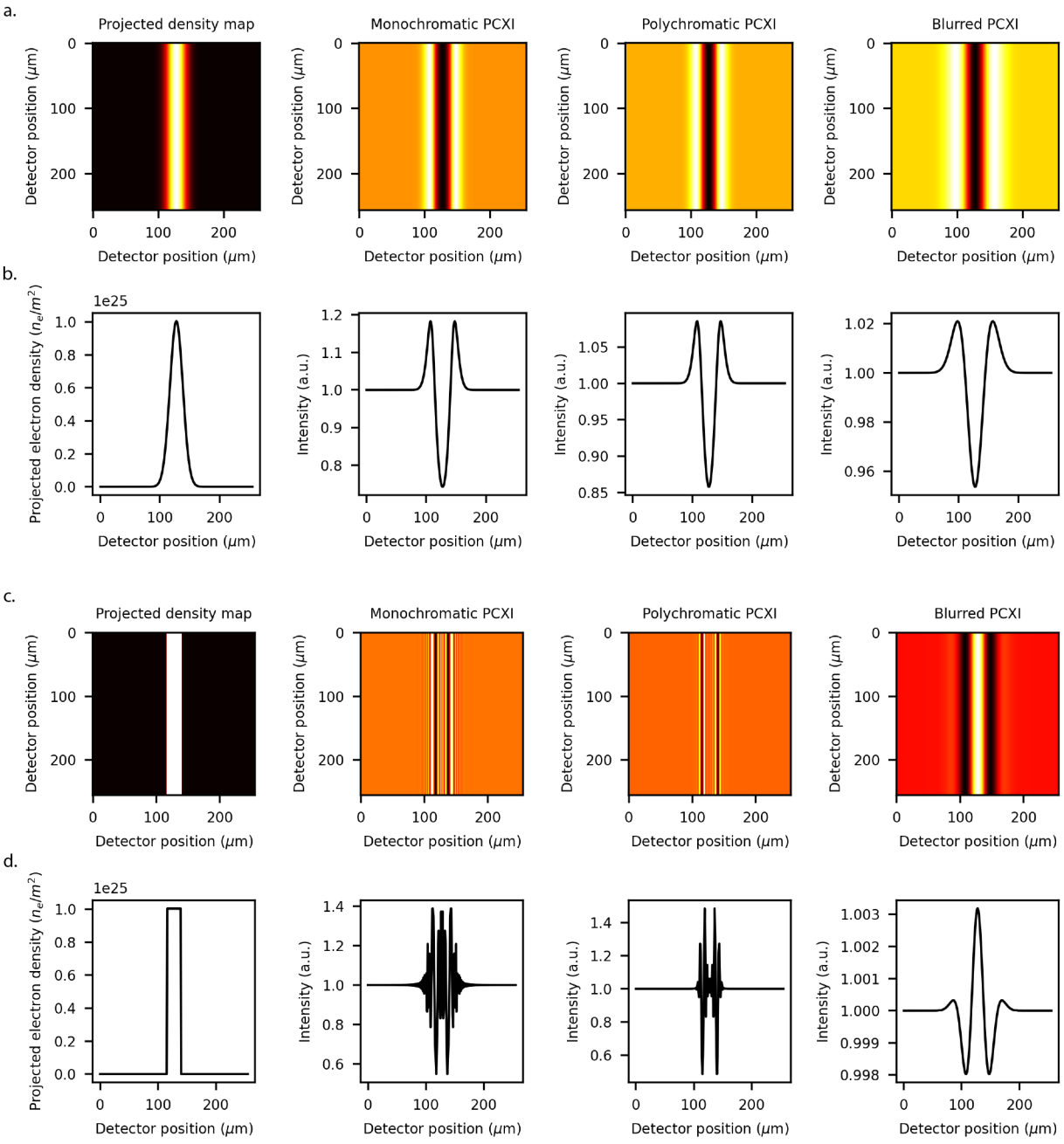

Figure 3.11: Synthetic density map projected along the imaging direction. Synthetic phase-contrast X-ray image (ideal) for a monochromatic radiation source. Synthetic phase-contrast X-ray image (ideal) for a polychromatic radiation source. Synthetic phase-contrast X-ray image (real) for a polychromatic radiation source and finite source size. (a) Images for Gaussian function and (b) corresponding lineouts. (c) Images for top-hat function and (d) corresponding lineouts.

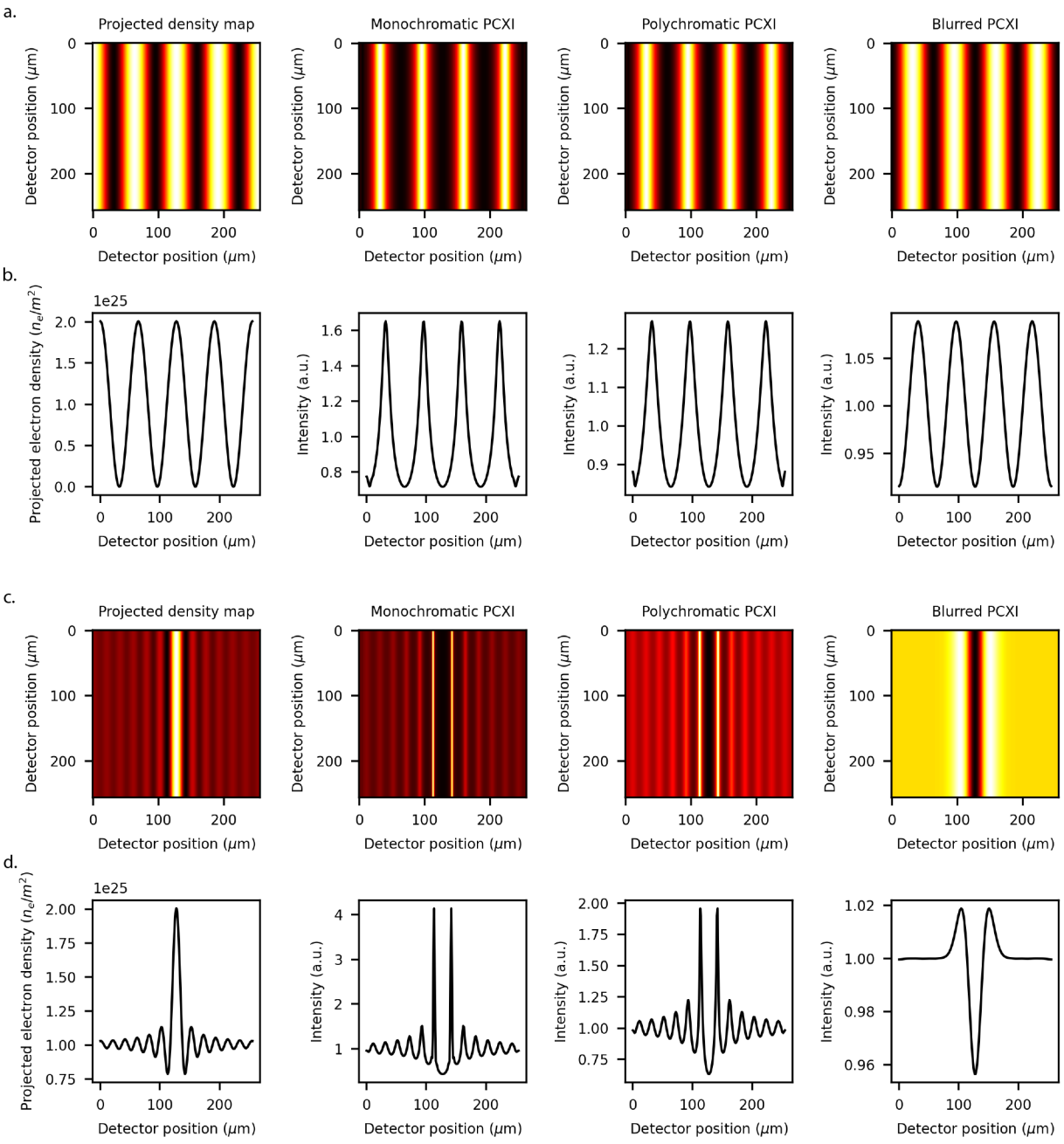

Figure 3.12: Synthetic density map projected along the imaging direction. Synthetic phase-contrast X-ray image (ideal) for a monochromatic radiation source. Synthetic phase-contrast X-ray image (ideal) for a polychromatic radiation source. Synthetic phase-contrast X-ray image (real) for a polychromatic radiation source and finite source size. (a) Images for cosine function and (b) corresponding lineouts. (c) Images for sinc function and (d) corresponding lineouts.

consequently the induced phase-shift for the material and geometry. Within this context, the real pattern I is given by

$$I = I_0||\tilde{u}(P_1)||^2 \,, \tag{3.33}$$

where I_0 is the incoming intensity distribution in the sample, and $\tilde{u}(P_1)$ is the complex-valued wave-field distribution in the detector plane given by

$$\tilde{u}(P_1) = -\frac{i}{2\lambda} r e^{-ikr} \iint_{\mathbb{R}^2} \left[\frac{R_0}{r_0} + \frac{R_1}{r_1}\right] \frac{t(P_1) e^{ik(r_0+r_1)}}{r_0 r_1} dxdy \,, \tag{3.34}$$

where r is the length of the vector from the source S to the point P_1 on the detector plane, k is the wave number, R_0 and R_1 are the source-to-object SP planes and object-to-detector planes PP_1 projection distances respectively. Correspondingly r_0 and r_1 are the lengths of the vectors connecting two points from SP and PP_1, and $t(P_1)$ is the object transfer matrix given by

$$t(P) = \exp\left[i\phi\right] \tag{3.35}$$

$$= \exp\left[i\left(iD(P) - B(P)\right)\right] \tag{3.36}$$

where the phase induced ϕ is complex-valued and its form depends on material properties. Particularly, for a given material sample the index of refraction for X-rays is less than unity and of the form,

$$n = 1 - \delta - i\beta \tag{3.37}$$

with

$$\delta = \frac{r_e N_A \lambda^2 \rho}{2\pi} \sum_j \frac{w_j \left[Z_j + f_j'\right]}{A_j} \tag{3.38}$$

and,

$$\beta = \frac{\nu}{\omega_p} \delta \tag{3.39}$$

where r_e is the classical electron radius, N_A is the Avogadro number, ρ is the mass density of the compound, A_j are the atomic number and the atomic weight of the jth element of the compound, f_j' is the real part of the dispersion factor, ω_p the previously discussed plasma frequency, and ν is the collisions rate factor. Taking all these considerations into account the phase map for X-rays crossing a sample can be obtained using the transfer function of Eq. 3.36 and the following projected distributions

$$D(P) = \frac{-2\pi}{\lambda} \int \delta(x,y,z) dr \tag{3.40}$$

and

$$B(P) = \frac{-2\pi}{\lambda} \int \beta(x,y,z) dr \,. \tag{3.41}$$

Therefore, Eq. 3.34 is sufficient for producing a synthetic phase-contrast X-ray image given a projected density map and assuming a point-like source. As stated previously the pure image must be convolved with the source distribution to obtain the real blurred image. Furthermore, Eq. 3.34 can be simplified by utilizing the Fresnel (paraxial) approximation for long propagation distances relative to the transverse size of the sample. In such approximation $R_0/r_0 \approx R_1/r_1 \approx 1$ as long as the so-called effective Fresnel number is larger than unity $N_{eff} > 1$ where

$$N_{eff} = \left(R\bar{\lambda}\right)^{-1} \frac{M}{M-1}\sigma_{obj}\sqrt{M^2\sigma_{obj}^2 + (M-1)^2\,\sigma_{src}^2 + \text{PSF}^2}\ . \tag{3.42}$$

Here $R = R_0 + R_1$, $\bar{\lambda}$ is the weighted sum of the source spectrum wavelength, $M = (R_0 + R_1)/R_0$ is the magnification, σ_{obj} is the size of the smallest object feature, and σ_{src} is the source width. Therefore, as long as $N_{eff} > 1$ the Fresnel approximation can be used to simplify Eq. 3.34 and reach the final expression in Fourier space,

$$\tilde{U}(u,v) = M^2 T(Mu, Mv)\text{exp}\left[-\pi i\lambda R_1 M(u^2+v^2)\right]\text{exp}\left[2\pi i(R_1/R_0)(x_0u + y_0v)\right]\ , \tag{3.43}$$

where u and v are the transverse spatial frequencies corresponding to x and y, and $T(Mu, Mv)$ is the Fourier transform of the object transfer function $t(P)$. Therefore, Eq. 3.43 can be readily solved using a Fast Fourier Transform (FFT) algorithm. To obtain the pure pattern I, and later convolve it with s to obtain the real phase-contrast pattern one would obtain in the detector.

Finally, this routine would produce a real image from a finite-size monochromatic source, in order to account for polychromaticity of the source, the resulting image can be weighted and summed according to the spectrum distribution of the source so that

$$I_{poly} = \sum_{\lambda} w(E) I_{mono}(\lambda)\ , \tag{3.44}$$

where $w(E)$ is the energy-dependent weighting factor. The effect of the full algorithm can be observed in Fig. 3.11 and Fig. 3.12 for both a monochromatic source and a polychromatic source evaluated for different 2D projected density maps.

3.4.2 Density retrieval

In the previous section, we explored a Fresnel-based propagation technique to generate synthetic PCXI images from a given density map. This method is advantageous to others since it doesn't depend on additional optical elements which can induce aberrations. The free space propagation nature indicates that the achievable resolution is highly dependent on the source size, and its applicability using polychromatic sources was discussed in the previous section. In this section, we do

the inverse and describe an algorithm used for quantitative phase extraction from an image taken using propagation-based projection microscopy. This method can be utilized to analyze data obtained from X-ray phase-contrast imaging [159, 185] or electron microscropy, as well as other point-projection microscopy techniques using visible light [13], electron beams [37, 9, 36], an even neutrons [5]. For review articles on this technique see [130, 129].

The algorithm starts with the so-called transport-of-intensity Transport-of-Intensity (TIE) equation, which describes the evolution of a paraxial monochromatic electromagnetic or matter wave [169, 144]:

$$\nabla_\perp \cdot [I(\mathbf{r}_\perp, z)\nabla_\perp \phi(\mathbf{r}_\perp, z)] = -\frac{2\pi}{\lambda}\frac{\partial}{\partial z} I(\mathbf{r}_\perp, z) \ . \tag{3.45}$$

Where $I(\mathbf{r}_\perp, z)$ is the beam intensity, $\phi(\mathbf{r}_\perp, z)$ is the beam phase, $\mathbf{r}_\perp$ denotes the position vector in the plane perpendicular to the optical axis z, and λ is the radiation wavelength. In general, for a normally incident plane wave of radiation the evolution of its intensity is well approximated by Beer's law of absorption as it travels through the sample,

$$I(\mathbf{r}_\perp, z = R_1) = I^{in} e^{(-\mu T(\mathbf{r}_\perp))} \ , \tag{3.46}$$

where I^{in} is the uniform intensity of the incident beam, $z = R_1$ indicates the plane at the exit surface of the object, μ is the linear attenuation coefficient, and $T(\mathbf{r}_\perp)$ is the projected thickness of the homogeneous object along the optical axis onto the plane over which the image is taken. Most of the aforementioned work using this equation has been directed towards finding a solution of the TIE for the phase of the wave, and the full derivation of the algorithm can be found in Ref. [129]. The final result can be summarized in the following equations to simultaneously extract the phase and amplitude from a single defocused image of a homogeneous object [129, 11]. Then, assuming $N_{eff} > 1$ and a polychromatic radiation source the recovered transfer function $T(\mathbf{r}_\perp)$ is given by

$$T(\mathbf{r}_\perp) = -\left(\frac{1}{\bar{\mu}}\right) \ln\left(\mathcal{F}^{-1}\left[\frac{\mathcal{F}\left(M^2 I(M\mathbf{r}_\perp, z = R_1)\right)/I_{in}}{1 + 4\pi^2\left(\frac{R_1}{M}\right)\left(\frac{\bar{\delta}}{\bar{\mu}}\right)[\mathbf{u}^2 + \mathbf{v}^2]}\right]\right) \ . \tag{3.47}$$

Where M is the magnification of the imaging system, u and v correspond to the spatial frequencies in Fourier space, and $\bar{\delta}, \bar{\mu}$ are the spectral averaged deviation of the refractive index and linear attenuation coefficient factors respectively. Then, if the object is sufficiently thin, the phase of the beam at $z = R_1$ is then proportional to the projected thickness such that

$$\phi(\mathbf{r}_\perp, z = R_1) = -\frac{2\pi}{\bar{\lambda}}\bar{\delta} T(\mathbf{r}_\perp) \ . \tag{3.48}$$

The extracted phase can then be related to the projected electron number density n_e/m^2 of the

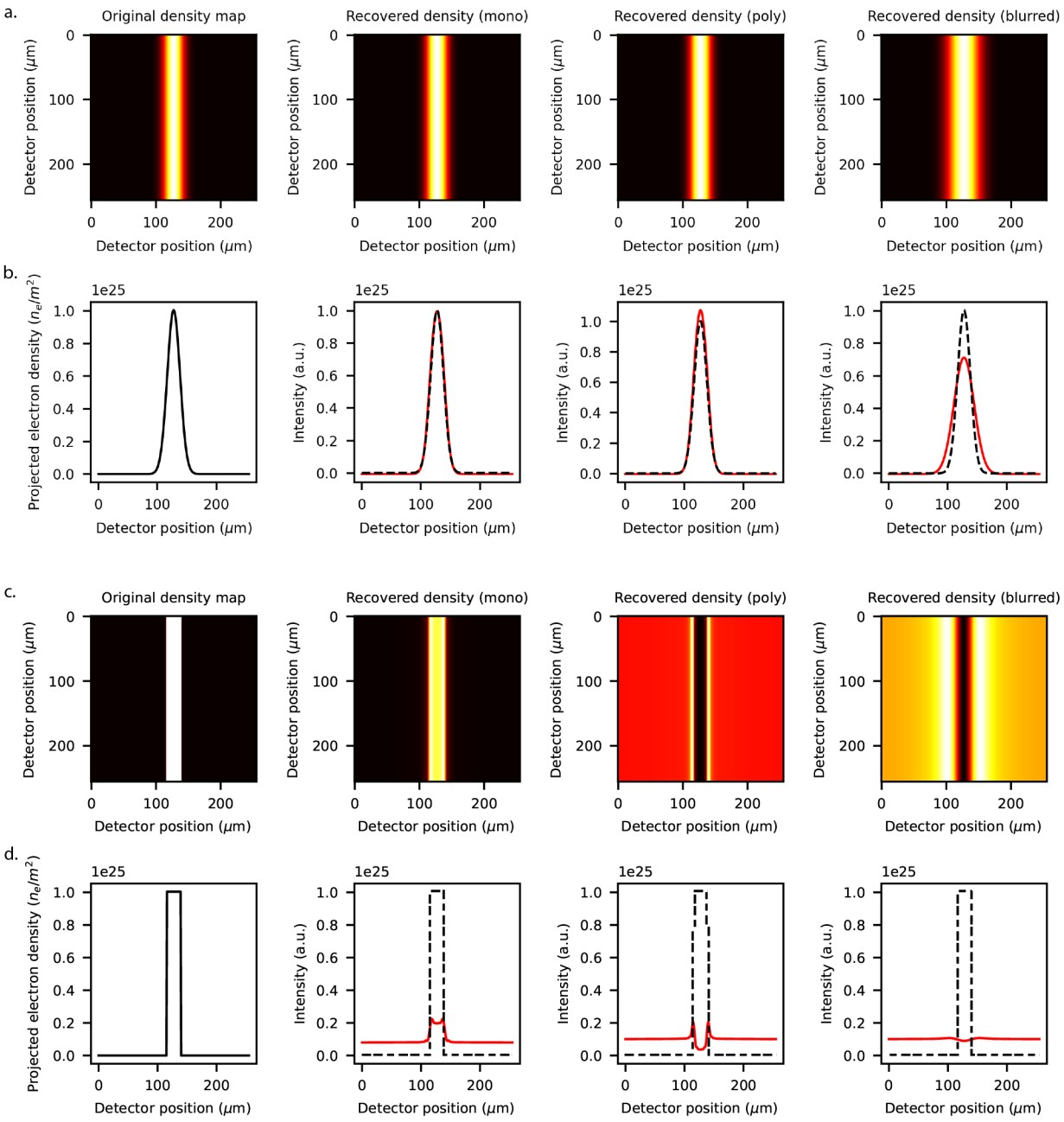

Figure 3.13: Synthetic density map projected along the imaging direction. Recovered density map from the synthetic phase-contrast X-ray image with a monochromatic radiation source. Recovered density map from the synthetic phase-contrast X-ray image with polychromatic radiation source. Recovered density map from the synthetic phase-contrast X-ray image with polychromatic radiation source and finite source size. (a) Images for Gaussian function and (b) corresponding lineouts. (c) Images for top-hat function and (d) corresponding lineouts.

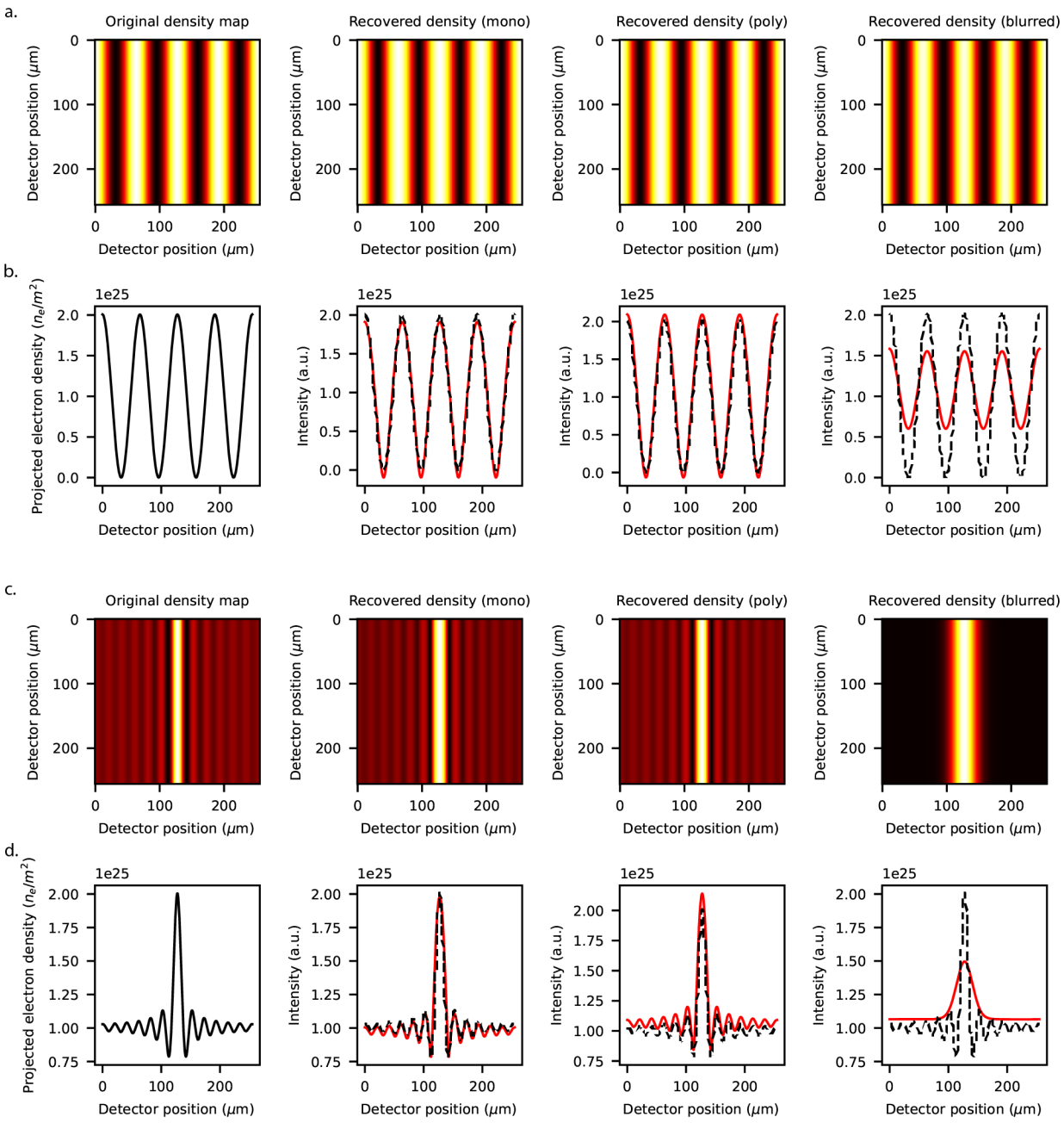

Figure 3.14: Synthetic density map projected along the imaging direction. Recovered density map from the synthetic phase-contrast X-ray image with a monochromatic radiation source. Recovered density map from the synthetic phase-contrast X-ray image with polychromatic radiation source. Recovered density map from the synthetic phase-contrast X-ray image with polychromatic radiation source and finite source size. (a) Images for cosine function and (b) corresponding lineouts. (c) Images for sinc function and (d) corresponding lineouts.

homogeneous object following [185] and solving the following equation,

$$\phi(\mathbf{r}_\perp, z) = -\bar{\lambda} r_e \int_z n_e(\mathbf{r}_\perp, z) dz \tag{3.49}$$

and so,

$$\int_z n_e(\mathbf{r}_\perp, z) dz = -\frac{\phi(\mathbf{r}_\perp, z)}{\bar{\lambda} r_e} \ , \tag{3.50}$$

where r_e is the classical electron radius. In order to successfully apply the algorithm the polychromaticity of the source needs to be taken into account with the weighted averages $\bar{\lambda}, \bar{\delta}, \bar{\mu}$ over the energy spectrum. These can be calculated using the following equations,

$$\bar{\lambda} = \frac{\int \lambda D(\lambda) I(\lambda) d\lambda}{\int D(\lambda) I(\lambda) d\lambda} \ , \tag{3.51}$$

$$\bar{\delta} = \frac{\int \delta(\lambda) D(\lambda) I(\lambda) d\lambda}{\int D(\lambda) I(\lambda) d\lambda} \ , \tag{3.52}$$

$$\bar{\beta} = \frac{\int \beta(\lambda) D(\lambda) I(\lambda) d\lambda}{\int D(\lambda) I(\lambda) d\lambda} \ , \tag{3.53}$$

$$\bar{\mu} = \frac{\int \mu(\lambda) D(\lambda) I(\lambda) d\lambda}{\int D(\lambda) I(\lambda) d\lambda} \ . \tag{3.54}$$

Here, $\delta(\lambda)$ and $\beta(\lambda) = \delta(\lambda)\,(\nu/\omega_p)$ correspond to the real and imaginary parts of the X-ray refractive index as a function of wavelength $n(\lambda) = 1 - \delta(\lambda) - i\beta(\lambda)$. And $\mu(\lambda) = 4\pi\beta(\lambda)/\lambda$ is the corresponding wavelength dependent attenuation factor. Note that β is δ multiplied by ν/ω_p which accounts for collisions in the plasma. Finally, in order to obtain the mass density ρ from the electron number density the following equation can be applied,

$$\delta = \frac{r_e N_A \lambda^2 \rho}{2\pi} \sum_j \frac{w_j \left(Z_j + f'_j\right)}{A_j} \ . \tag{3.55}$$

Where N_A is the Avogadro's number, Z_j and A_j are the atomic number and atomic weight of the compound respectively, and f'_j is the real part of the dispersion correction factor. This technique can be successfully applied to recover the phase and projected density for data taken with propagation-based phase-contrast X-ray imaging, as it will be shown in later chapters.

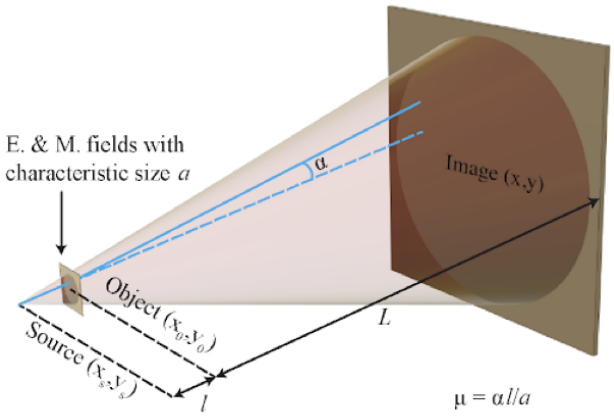

Figure 3.15: Diagram depicting the geometry for electron beam deflectometry.

3.4.3 Electron beam probing and field recovery

An emerging area of research, relativistic electron deflectometry, consists on the probing of electromagnetic fields using relativistic electrons from an LWFA as a probe [149, 180, 191, 190]. This technique can be used to examine electric and magnetic fields that might be generated during laser-plasma interactions in HEDP experiments. Any generated fields will then have the effect of deflecting the trajectories of the electrons by a certain angle that depends on both the electron beam energy and the field magnitude as well as direction. The deflected electron beam is then captured on a scintillating phosphore screen for analysis. This section consists of describing the background material and key steps for recovering the magnitude of electromagnetic fields that have been captured by a relativistic LWFA electron beam probe following the technique and notation described by [92].

The recovery method starts by assuming that the object (fields) is located at a distance l from the particle (electron) source, and the detection screen is situated at a distance L from the object as shown in Fig. 3.15. Generally, $L \gg l$, and $l \gg a$, where a is a characteristic spatial scale of the field in question. In a cartesian geometry, the object plane is described by the coordinates (x_0, y_0), while the ideal image in the detector is described by the coordinates (x, y), such that $x = x_0 \times M$ and $y = y_0 \times M$, where $M = (1 + L/l)$ is the geometric magnification. After the electrons traverse the electromagnetic fields they will be deflected by an angle α_x, α_y such that the coordinates of the real image described by the electron trajectories can be described in the following way,

$$x = x_0 + \frac{L}{l} x_0 + \alpha_x L \ , \tag{3.56}$$

$$y = y_0 + \frac{L}{l} y_0 + \alpha_y L \ , \tag{3.57}$$

where $\tan\alpha \approx \alpha$. When α is small, the last term can simply be dropped and use the approximations above. However, when α is large, indicating strong deflections, then the relationship between image and object coordinates is nonlinear, which introduces issues discussed below. The deflection angles are the key to this technique as they can be related to the path-integrated electric or magnetic fields by the following expressions for a relativistic electron beam

$$\alpha_x = \frac{q}{\gamma m_e v_z^2} \int E_x dz \quad \text{or} \quad \alpha_x = \frac{q}{\gamma m_e v_z} \int B_y dz \ , \tag{3.58}$$

$$\alpha_y = \frac{q}{\gamma m_e v_z^2} \int E_y dz \quad \text{or} \quad \alpha_y = \frac{q}{\gamma m_e v_z} \int B_x dz \ . \tag{3.59}$$

Within this context, the objective of the following algorithm is to obtain solutions for the deflection angles α_x and α_y and thus reconstruct the electromagnetic fields present at the interaction (object) plane. Following Kugland *et al.* [92], the undisturbed electron beam at the object plane is described by the image $I_0(x_0, y_0)$, while the image of the disturbed beam at the detector plane $I(x, y)$ can be obtained by the following relation,

$$I(x, y) = \frac{I_0(x_0, y_0)}{\left| \frac{\partial(x,y)}{\partial(x_0,y_0} \right|} \ , \tag{3.60}$$

where $|\frac{\partial(x,y)}{\partial(x_0,y_0}|$ is the absolute value of the determinant of the Jacobian matrix relating the object and image planes and can be described by

$$\left| \frac{\partial(x, y)}{\partial(x_0, y_0)} \right| = \left| \left(1 + \frac{L}{l} + \frac{\partial \alpha_x}{\partial x_0} L \right) \left(1 + \frac{L}{l} + \frac{\partial \alpha_y}{\partial y_0} L \right) - L^2 \frac{\partial \alpha_x}{\partial y_0} \frac{\partial \alpha_y}{\partial x_0} \right| \ . \tag{3.61}$$

In order to solve this equation let us assume that $\boldsymbol{\alpha} = [\alpha_x, \alpha_y, 0]$ is small and that the object-to-image coordinates follow a linear mapping. Additionally, all electron trajectories are assumed to be rotation-less such that $\nabla \times \boldsymbol{\alpha} = 0$. For this regime, the deflection angles can be obtained from a potential field ϕ so that

$$\boldsymbol{\alpha} = \nabla \Phi \ . \tag{3.62}$$

For convenience let us introduce the normalization $\tilde{x} = x/w_x$, $\tilde{y} = y/w_y$, $\tilde{\alpha_i} = \alpha_i L/w_i$, $\tilde{\boldsymbol{\alpha}} = \tilde{\nabla}\tilde{\Phi}$, and $\tilde{I_0} = I_0/M^2$ where w_i is width of the beam at the image plane. The Jacobian

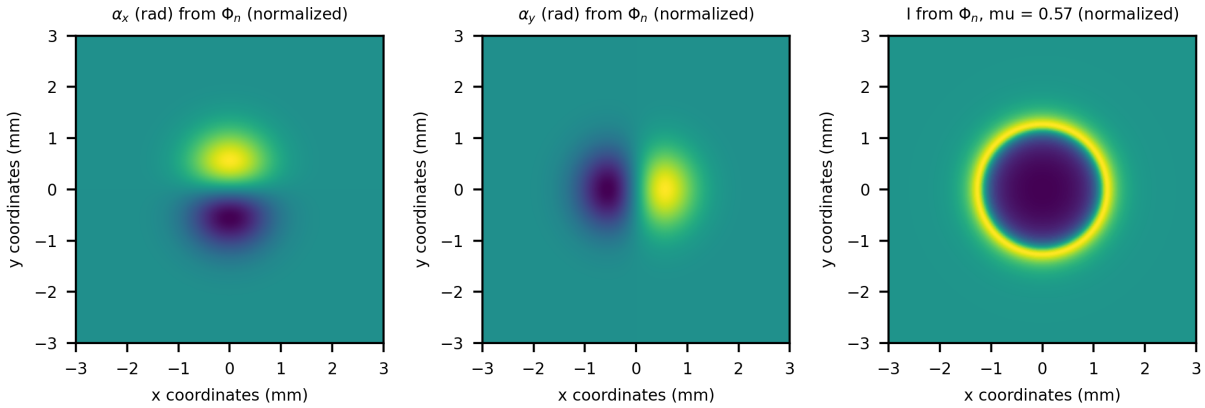

Figure 3.16: Map of user-defined deviation angles α_x and α_y as well as the resulting image I obtained from the calculated potential field $\mathbf{\Phi}$.

described by Kugland *et. al* [92] can then be rewritten in the following form,

$$\frac{1}{M^2}\left|\frac{\partial(x,y)}{\partial(x_0,y_0)}\right| = \left|1+\tilde{\nabla}^2\tilde{\Phi}+\frac{\partial^2\tilde{\Phi}}{\partial\tilde{x}^2}\frac{\partial^2\tilde{\Phi}}{\partial\tilde{y}^2}-\left(\frac{\partial^2\tilde{\Phi}}{\partial\tilde{x}\partial\tilde{y}}\right)^2\right| . \tag{3.63}$$

Which leads to the final expression being solved numerically,

$$\tilde{\nabla}^2\tilde{\Phi} = \frac{\tilde{I}_0+\epsilon}{I+\epsilon}-1-\frac{\partial^2\tilde{\Phi}}{\partial\tilde{x}^2}\frac{\partial^2\tilde{\Phi}}{\partial\tilde{y}^2}+\left(\frac{\partial^2\tilde{\Phi}}{\partial\tilde{x}\partial\tilde{y}}\right)^2 . \tag{3.64}$$

This has an important assumption, which is that $\boldsymbol{\alpha}$ was assumed to be small. In the regime where $\boldsymbol{\alpha}$ is large, the fields are too strong, and *particle crossing* occurs along the trajectories. This results in the formation of caustics, and implies that the relationship between x_0 and x is highly nonlinear, for which there is no unique solution to Φ, and thus the relationship between I_0 and I is no longer unique, imposing limitations on the applicability of this algorithm for inversing radiographs where strong fields are present. To evaluate such a scenario, it is useful to introduce the variable μ which parametrizes the non-linearity of the projection,

$$\mu = \frac{l\alpha}{a} . \tag{3.65}$$

So that when $\mu \ll 1$ the mapping is linear and the approximation $x \approx M \times x_0$ and $y \approx M \times y_0$ can be made. Nevertheless, as $\mu \longrightarrow 1$ the mapping becomes non-linear, and therefore second-order terms with α must be included. Finally, when $\mu > 1$ caustics (particle-crossing trajectories)

are present in the image. For the non-linear regime without caustics, electromagnetic fields can recovered using this inversion technique and they can be compared to synthetic radiography images based on hydrodynamic simulations as it will be shown in Chapter 7.

For the purpose of demonstration, the algorithm was used along with synthetic data to analyze its performance in recovering ϕ, α_x, α_y and μ as shown in Fig. 3.17. The algorithm starts by the user defining the initial conditions, such as the geometry of the problem—source-to-object l and object-to-detector L distances—beam energy W, and the test field values and magnitudes. In this case a user-defined potential field Φ_{test} was provided in the form,

$$\Phi_{\text{test}} = -\frac{e}{\sqrt{2m_e W}} B_0 \frac{a \cdot b}{2} \sqrt{\pi} \exp\left[-\left(\frac{r}{a}\right)^2 \right] , \tag{3.66}$$

where W is the beam energy, a and b are constants, $r = \sqrt{x^2 + y^2}$ is the position vector, and B_0 is the peak magnetic field value. Then everything follows, and α_x, α_y can be calculated by taking the gradient of the potential so $\nabla \Phi_{\text{test},i} = \alpha_i$ as shown in Fig. 3.16. Having defined the potential field and calculated the deflection angles an image can be generated from them I_{test}. The deflection potential can be reconstructed using an iterative algorithm.

The iterative algorithm operates by taking two images as an input: the original image I, in which field deflections are present, as well as an image corresponding to the unperturbed beam profile $\tilde{I}_0$ before the deflections. The process to obtain the background (unpertubed) image $\tilde{I}_0$ from an experimental measurement will be highlighted in Chapter 7. The algorithm then starts by initializing the normalized spatial coordinates $(\tilde{x}, \tilde{y})$ and solving for $\tilde{\Phi}_1$. Next, the iterative solution will be solved including a correction for the non-linear terms of $\tilde{\Phi}$. A description of the algorithm reads as follows,

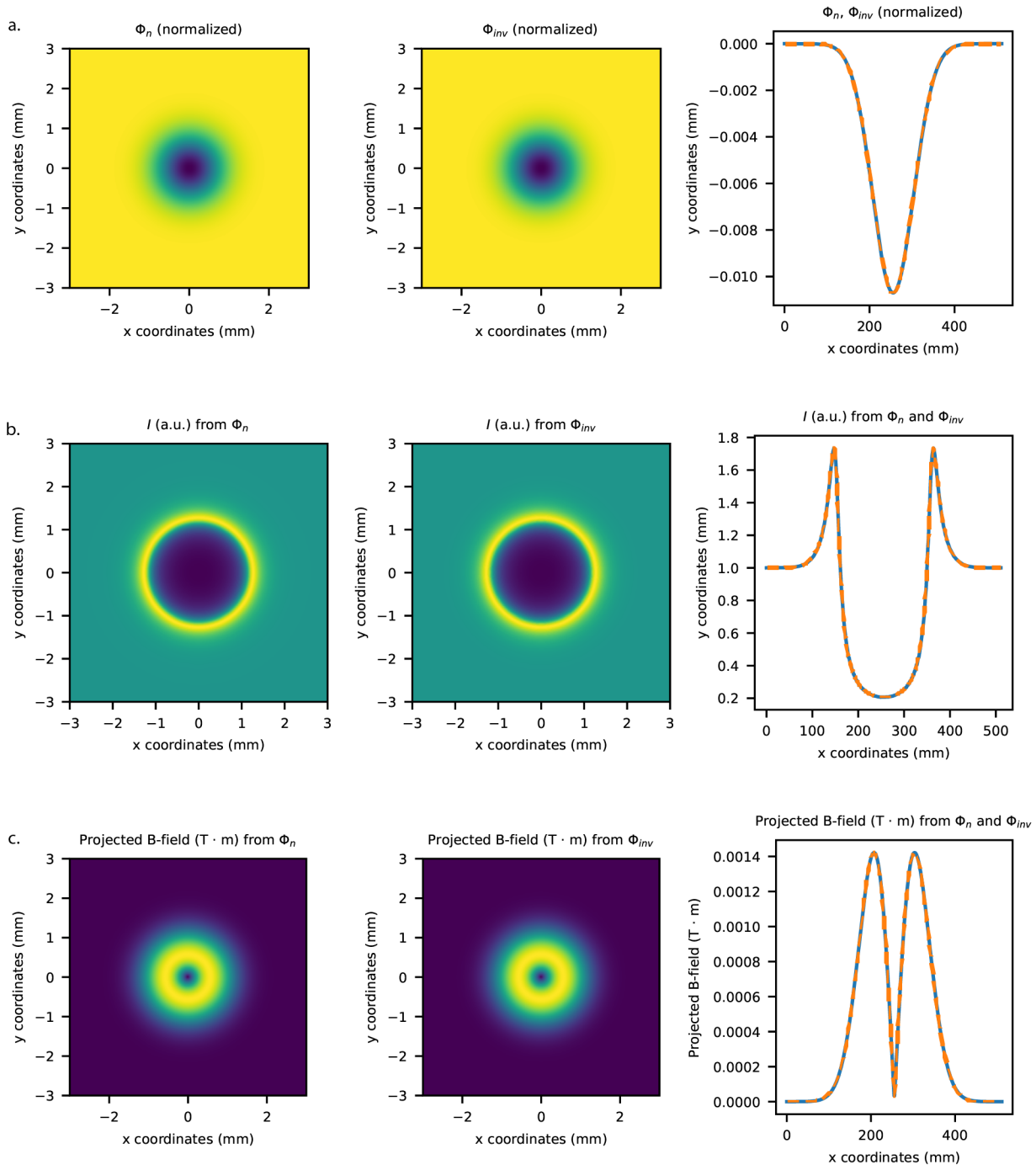

Figure 3.17: (a) Map of deflection potential field Φ as well as a map of the iteratively recovered potential field. (b) Image obtained from the user-defined potential field Φ as well as a calculated image from recovered potential field. (c) Image of magnetic field defined by the user as well as magnetic field recovered by the algorithm. Plots of their corresponding lineouts are displayed for comparison.

Iterative reconstruction of the deflection potential

Input: $I, \tilde{I}_0$

Output: $\tilde{\Phi}$ and $(\tilde{x}, \tilde{y})$

Initialize normalized spatial coordinates $(\tilde{x}, \tilde{y})$

% Solve for $\tilde{\Phi}_1$:

$\tilde{\nabla}_1^2 = \frac{\tilde{I}_0+\epsilon}{I+\epsilon} - 1$

% Begin iterative solution including nonlinear terms

while difference(I_{interp}, I_{calc}) or difference($\tilde{\Phi}_n, \tilde{\Phi}_{n-1}$) $>$ tolerance **do**

Use $\tilde{\Phi}_n$ and $\tilde{I}_0$ to calculate (x_n, y_n) and I_{calc}

Calculate I_{interp} by interpolating I onto (x_n, y_n)

$I^* =$ average(I_{interp}, I_{calc}) *% Improves stability and converge*

% Use full expression from Eq. (8) to solve for $\tilde{\Phi}_{n+1}$

$\tilde{\nabla}^2\tilde{\Phi}_{n+1} = \frac{\tilde{I}_0+\epsilon}{I^*+\epsilon} - 1 - \frac{\partial^2\tilde{\Phi}_n}{\partial\tilde{x}^2}\frac{\partial^2\tilde{\Phi}_n}{\partial\tilde{y}^2} + \left(\frac{\partial^2\tilde{\Phi}_n}{\partial\tilde{x}\partial\tilde{y}}\right)^2$

end while

This iterative algorithm is capable of reconstructing the deflection potential Φ_{inv} and consequently it is possible to reconstruct I_{inv} with great accuracy and has been demonstrated for the test benchmarking problem shown in Fig. 3.17

3.4.4 Computational modeling: FLASH 4.0

The computational code FLASH 4.0 [22] is capable of simulating HEDP experiments using what is known as Three-Temperature (3T) capabilities. It is often found in HED plasmas that the electron temperature T_e and ion temperature T_i are not necessarily the same. Additionally, if radiation is emitted during the interaction it will also have an independent temperature $T_{rad} = (u_{rad}/a)^{1/4}$ for a radiation field with total energy density $u_{rad}(\mathbf{x}, t)$. The radiation field is not in equilibrium with the plasma thus normally $T_e \neq T_i \neq T_{rad}$, thus it is desired to have a 3T plasma treatment. FLASH treats the radiation field using frequency-dependent multi-group diffusion. The radiation temperature T_{rad} does not directly enter the calculations, but the 3T treatment implies that there are three components being modeled: electrons, ions, and radiation. This section is meant to describe the 3T capabilities of the FLASH code and the equations it uses for its treatment and evolution of 3T HED plasmas. For a more detailed description see the FLASH code User's guide [22]. Starting

with the equations for conservation of mass, momentum, and energy:

$$\frac{\partial \rho}{\partial t} + \nabla \cdot (\rho \mathbf{v}) = 0 \ , \tag{3.67}$$

$$\frac{\partial \rho}{\partial t} + \nabla \cdot (\rho \mathbf{v}) = 0 \ , \tag{3.68}$$

$$\frac{\partial}{\partial t}(\rho E_{tot}) + \nabla \cdot [(\rho E_{tot} + P_{tot})\,\mathbf{v}] = Q_{\text{laser}} - \nabla \cdot \mathbf{q} \ . \tag{3.69}$$

Where ρ is the total mass density, $\mathbf{v}$ is the average fluid velocity, P_{tot} is the total pressure defined as the sum of the ion, electron, and radiation pressure so,

$$P_{tot} = P_{ele} + P_{ion} + P_{rad} \ . \tag{3.70}$$

Then E_{tot} is the total specific energy which includes the specific internal energies of the electrons, ions, and radiation field as well as the specific kinetic energy, therefore,

$$E_{tot} = e_{ion} + e_{ele} + e_{rad} + \frac{1}{2}\mathbf{v} \cdot \mathbf{v} \ . \tag{3.71}$$

Moreover, $\mathbf{q}$ is the total heat flux which includes a radiation and electron conductivity component,

$$\mathbf{q} = \mathbf{q}_{ele} + \mathbf{q}_{rad} \ . \tag{3.72}$$

Finally Q_{laser} represents the energy source due to laser heating. Given that FLASH utilizes a 3T approach, the internal energy of electrons, ions, and radiation must be evolved using a different set of equations as shown below,

$$\frac{\partial}{\partial t}(\rho e_{\text{ion}}) + \nabla \cdot (\rho e_{\text{ion}} \mathbf{v}) + P_{\text{ion}} \nabla \cdot \mathbf{v} = \rho \frac{c_{v,\text{ele}}}{\tau_{ei}} (T_{\text{ele}} - T_{\text{ion}}) \ , \tag{3.73}$$

$$\frac{\partial}{\partial t}(\rho e_{\text{ele}}) + \nabla \cdot (\rho e_{\text{ele}} \mathbf{v}) + P_{\text{ele}} \nabla \cdot \mathbf{v} = \rho \frac{c_{v,\text{ele}}}{\tau_{ei}} (T_{\text{ion}} - T_{\text{ele}}) - \nabla \cdot \mathbf{q}_{\text{ele}} + Q_{\text{abs}} - Q_{\text{emis}} + Q_{\text{laser}} \ , \tag{3.74}$$

$$\frac{\partial}{\partial t}(\rho e_{\text{rad}}) + \nabla \cdot (\rho e_{\text{rad}} \mathbf{v}) + P_{\text{rad}} \nabla \cdot \mathbf{v} = \nabla \cdot \mathbf{q}_{\text{rad}} - Q_{\text{abs}} + Q_{\text{emis}} \ . \tag{3.75}$$

Where $c_{v,\text{ele}}$ is the electron specific heat, and τ_{ei} is the ion/electron equilibration time, Q_{abs} and Q_{emis} represent the increase in electron internal energy due to the total absorption or radiation, or decrease in electron internal energy due to the total emission of radiation, respectively.

Next the 3T equation of state in FLASH is what connects the internal energy of the components to their temperatures and pressures. FLASH offers a variety of equations of state which are described in the User's guide [22]. During a full physics HED simulation, FLASH will use the 3T

equation of state to complete the system and solve Eq. 3.67, Eq. 3.68, Eq. 3.69, Eq. 3.73, Eq. 3.74, and Eq. 3.75. The method for FLASH to do this starts by a series of operator splits which split off all of the terms on the left-hand side of the equations and solve them in different code units. Therefore the equations that remain describe the effect of work and the advection of conserved quantities described as,

$$\frac{\partial \rho}{\partial t} + \nabla \cdot (\rho \mathbf{v}) = 0 \ , \tag{3.76}$$

$$\frac{\partial}{\partial t}(\rho \mathbf{v}) + \nabla \cdot (\rho \mathbf{v}\mathbf{v}) + \nabla P_{\text{tot}} = 0 \ , \tag{3.77}$$

$$\frac{\partial}{\partial t}(\rho E_{\text{tot}}) + \nabla \cdot [(\rho E + P_{\text{tot}})\,\mathbf{v}] = 0 \ , \tag{3.78}$$

$$\frac{\partial}{\partial t}(\rho e_{\text{ion}}) + \nabla \cdot (\rho e_{\text{ion}} \mathbf{v}) + P_{\text{ion}} \nabla \cdot \mathbf{v} = 0 \ , \tag{3.79}$$

$$\frac{\partial}{\partial t}(\rho e_{\text{ele}}) + \nabla \cdot (\rho e_{\text{ele}} \mathbf{v}) + P_{\text{ele}} \nabla \cdot \mathbf{v} = 0 \ , \tag{3.80}$$

$$\frac{\partial}{\partial t}(\rho e_{\text{rad}}) + \nabla \cdot (\rho e_{\text{rad}} \mathbf{v}) + P_{\text{rad}} \nabla \cdot \mathbf{v} = 0 \ . \tag{3.81}$$

These sets of equations are solved by the *Hydro* unit in FLASH. The *Hydro* unit utilizes general hydrodynamic solvers only with only conservation of energy, momentum, and mass. Notice how Eq. 3.79, Eq. 3.80, and Eq. 3.81 are not in conservative form given that there work terms present that diverge under the presence of shocks and cannot be solved directly. More specific information on the hydro unit, as well as other units, can be found in the FLASH code User's guide as well [22].

Without taking into account hydrodynamic terms, the remaining equations that describe the evolution of electron, ion, and radiation internal energies are the following,

$$\rho \frac{\partial e_{ion}}{\partial t} = \rho \frac{c_{v,\text{ele}}}{\tau_{ei}} (T_{\text{ele}} - T_{\text{ion}}) \ , \tag{3.82}$$

$$\rho \frac{\partial e_{ele}}{\partial t} = \rho \frac{c_{v,\text{ele}}}{\partial t} = \rho \frac{c_{v,\text{ele}}}{\tau_{ei}} (T_{\text{ion}} - T_{\text{ele}}) - \nabla \cdot \mathbf{q}_{\text{ele}} + Q_{\text{abs}} - Q_{\text{emis}} + Q_{\text{laser}} \ , \tag{3.83}$$

$$\rho \frac{\partial e_{\text{rad}}}{\partial t} = \nabla \cdot \mathbf{q}_{\text{rad}} - Q_{\text{abs}} + Q_{\text{emis}} \ . \tag{3.84}$$

These sets of equations are solved by the *Heatexchange* unit. The first term on the right-hand side of Eq. 3.82 represents collisions between electrons and ions and is responsible for the exchange of internal energy between them. This term will equilibrate the electron and ion temperatures over

time. The *Heatexchange* unit will therefore update the electron and ion temperatures following,

$$\frac{\partial e_{\text{ion}}}{\partial t} = \frac{c_{v,\text{ele}}}{\tau_{ei}} \left(T_{\text{ele}} - T_{\text{ion}}\right) \ , \tag{3.85}$$

$$\frac{\partial e_{\text{ele}}}{\partial t} = \frac{c_{v,\text{ele}}}{\tau_{ei}} \left(T_{\text{ion}} - T_{\text{ele}}\right) \ , \tag{3.86}$$

$$\tag{3.87}$$

where the specific heat of the electron $c_{v,\text{ele}}$ is calculated through the equation of state. Next, the second term of the right-hand side in Eq. 3.83 is responsible for electron energy transport through the conduction of heat, where the heat flux is defined as

$$\mathbf{q}_{\text{ele}} = -K_{\text{ele}} \nabla T_{\text{ele}} \ , \tag{3.88}$$

where K_{ele} is the electron thermal conductivity and is calculated in the *Conductivity* unit, while the *Diffuse* unit is in charge of including the effect of conduction in FLASH by using operator splitting and solving the following equation each time step, which can be solved implicitly,

$$\rho \frac{e_{\text{ele}}}{\partial t} = \nabla \cdot K_{\text{ele}} \nabla T_{\text{ele}} \ . \tag{3.89}$$

FLASH also utilizes an electron diffusion flux limiter parameter $0 < f < 1$ to give the electron heat transport a more physically realistic behavior in regions with high-temperature gradients. Finally, the radiation transport is treated through multi-group diffusion theory. Each energy group contributes to the total radiation flux, emission, and absorption terms in Eq. 3.82, Eq. 3.83, and Eq. 3.84. Then for a given energy group g with $1 < g \leq N_g$ the total flux can be calculated as a summation over each group as,

$$Q_{\text{abs}} = \sum_{g=1}^{N_g} Q_{\text{ele},g}, \quad Q_{\text{emis}} = \sum_{g=1}^{N_g} Q_{\text{emis},g} \tag{3.90}$$

$$\mathbf{q}_{\text{rad}} = \sum_{g=1}^{N_g} \mathbf{q}_g \ . \tag{3.91}$$

And the change of each group's radiation energy density u_g is calculated through

$$\frac{\partial u_g}{\partial t} + \nabla \cdot (u_g \mathbf{v}) + \left(\frac{u_g}{e_{\text{rad}} \rho} P_{\text{rad}} \nabla \cdot \mathbf{v} = -\nabla \cdot \mathbf{q}_g + Q_{\text{emis},g} - Q_{\text{abs},g} \right) \ , \tag{3.92}$$

where the total specific radiation energy is related to the energy density u_g by,

$$\rho e_{\text{rad}} = \sum_{g=1}^{N_g} u_g \tag{3.93}$$

In this regard, the *RadTrans* unit will solve the radiation diffusion equations for each energy group and calculate its values in conjunction with the *Diffuse* unit. The multigroup diffusion package used in FLASH depends on the radiation flux, emission, and absorption which are all functions of the material opacity, calculated in turn by the *Opacity* unit.

The last remaining flux term is Q_{laser}, which represents the deposition of energy by a laser source into the electrons, and is highly relevant in the work in this thesis. The Q_{laser} term is computed by the *EnergyDeposition* unit in FLASH, which utilizes the geometrics optics approximation to laser energy deposition in the form of a laser ray-tracing model. The current implementation of ray-tracing in FLASH consists of setting up a beam made of a number of rays whose paths are traced through the simulation domain, then their trajectories are updated according to the local refractive index of each cell. The *EnergyDeposition* unit in FLASH is responsible for calculating this process through the geometric optics approximation. Moreover, the laser power that is deposited into a cell is calculated based on the process of inverse bremsstrahlung power in each cell, which depends on the gradient of the local electron number density and the local gradient of the electron temperature. At the moment of writing, in the FLASH 4.7 distribution, two implementations of ray tracing are available - one is based on the average quantities for each cell, and the other one is more refined and is based on cubic interpolation for the calculation. Modeling laser energy deposition with ray-tracing is rather complex and requires a large number of input parameters, for a more detailed description of these two implementations see the FLASH User's Guide Chapter 17.4 [22].

The FLASH simulation allows the user to define multiple laser pulses when modeling a HED interaction. Each laser pulse is first defined by sections (piecewise linear function), for each section of the pulse a pair of time-power parameters are given as shown in Fig. 3.18. The time-power pairs ensure that by integrating over all sections the total energy in the pulse is obtained. The user is also capable of setting the spot size of the laser beam, as well as the direction and angle of incidence into the simulation domain.

Additionally, the user must also define the spatial variation of the intensity transversely across the beam. If the FLASH variable *ed_crossSectionFunctionType_1* is set to "gaussian2D", the transverse spatial intensity profile is defined by a supergaussian function of the form

$$I(r) = I_0 \left(- \left[\left(\frac{x}{R_x} \right)^2 + \left(\frac{y}{R_y} \right)^2 \right]^{\gamma} \right) , \tag{3.94}$$

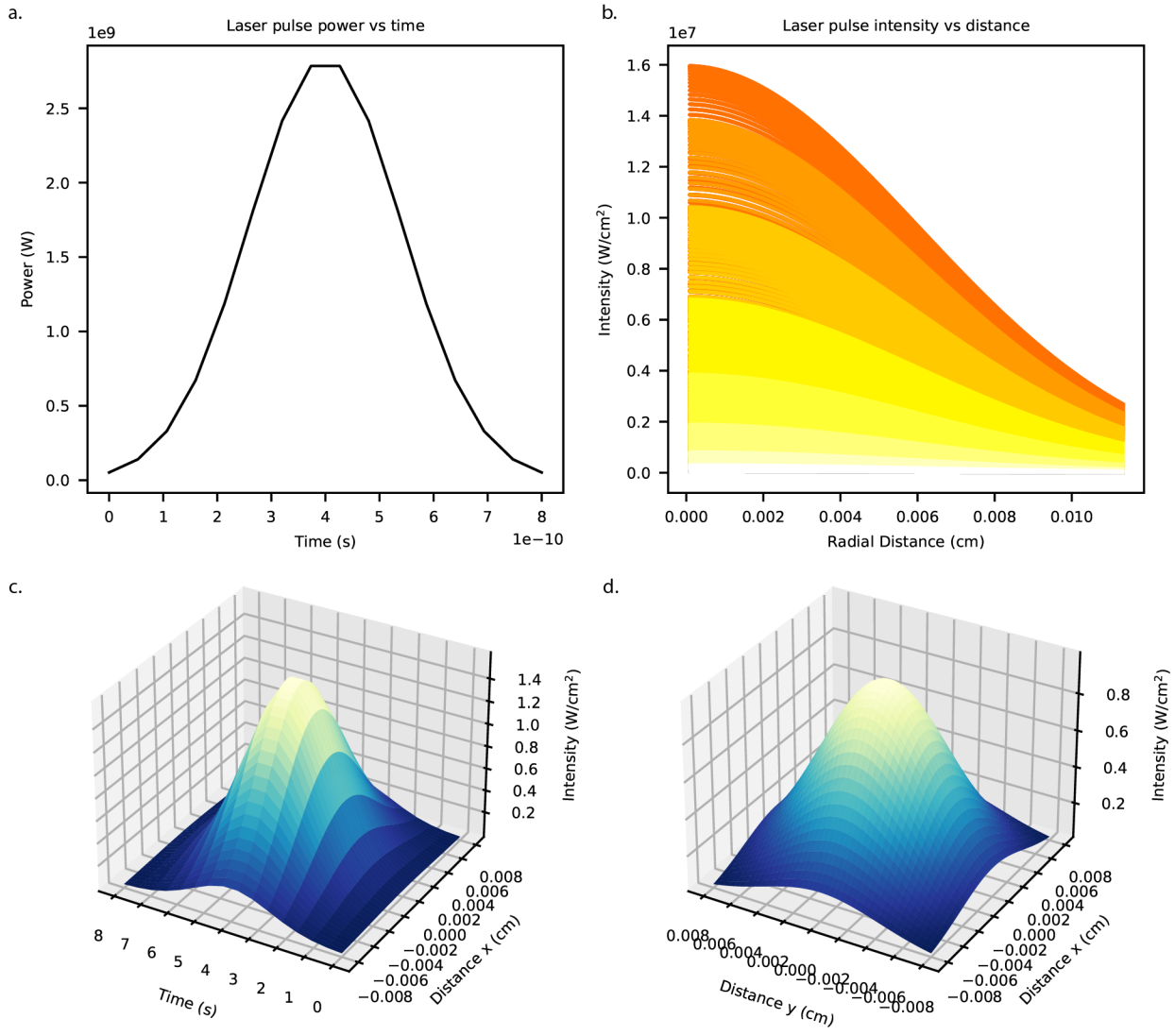

Figure 3.18: (a) Plot of time-power pairs which define the evolution of the laser pulse in FLASH. (b) Spatial intensity profile for $x > 0$. Colors displayed represent time evolution. (c) 3D representation of the FLASH laser pulse constructed from the spatial intensity profile and time-power pairs evolution. (d) Intensity profile of laser pulse in the transverse x and y directions.

where R_x and R_y define the e-folding length of the intensity distribution in x and y direction respectively, and γ sets the power of the supergaussian function desired. An example of a spatial intensity distribution for $x > 0$ is shown in Fig. 3.18 where the colormap represents its evolution in time longitudinally along the pulse. Finally, the user does not directly specify I_0. Instead, the total beam power P is calculated and I_0 is calculated through the relation

$$P = 2\pi \int_0^R rI(r)dr \ . \tag{3.95}$$

Finally, the user needs to specify how many rays to use in the simulation as well as how the rays will be spatially distributed across the beam. Typically the configuration used is one such that the rays are laid out on the circular cross-section of the beam with some radial and angular spacing. In other words, the beam is divided into regions of equal radius and angle, the total number of rays is divided by the number of regions, and an equal number of rays is assigned to each angular slice.

CHAPTER 4

Liquid Targets for High-Repetition-Rate Experiments

4.1 Motivation

In the realm of high-energy-density physics HEDP experiments, the quest for innovative and efficient target designs has been a topic of constant interest and development. The advent of high-intensity, high-repetition-rate lasers has broadened the scope of these experiments, paving the way for numerous new applications and discoveries. One particular area of development that warrants attention is the implementation of liquid targets, for example, water, that can operate in a vacuum environment. The prospect of employing liquid targets offers several advantages in terms of data acquisition rates, time-varying hydrodynamic systems, and increased experimental adaptability compared to traditional solid targets.

Furthermore, high-repetition-rate lasers operating at high intensities have the potential to generate vast amounts of data, crucial for enhancing the understanding of HEDP phenomena [67]. However, the current reliance on solid targets presents a limitation in terms of data acquisition rates. Solid targets require regular replacement and alignment, leading to longer experimental times and reduced overall efficiency. By introducing a liquid target, such as water, that can withstand the vacuum environment, this issue can be effectively mitigated. Liquid targets can regenerate at much faster rates, enabling rapid, continuous interaction with the laser and resulting in significantly increased data acquisition rates. The ability to collect data at a faster pace will enhance the depth of analysis, offering invaluable insights into the underlying processes of HEDP.

Beyond the increase in data acquisition rates, liquid targets present new opportunities for time-varying hydrodynamic systems in pump-probe experiments. As water flows in a vacuum, its hydrodynamic properties and interactions with the laser can be closely examined in real-time. This ability to investigate the behavior of the target material over a continuous time period opens the door for the study of dynamic and transient phenomena that were previously inaccessible using

solid targets. The application of liquid targets in this context will offer a more comprehensive understanding of the material behavior and energy coupling under extreme conditions, providing an essential platform for the development of novel applications and technologies.

This section will serve as a description to the most important concepts regarding liquid targets flowing in a vacuum, as well as highlight relevant work on liquid targets for laser-plasma experiments. Starting with liquid sheet targets, which have been studied for plasma mirror applications [56, 173]. Next, single micron diameter liquid jet targets have been designed specifically for ion acceleration research [77, 86]. Most relevant to the studies in this thesis is the work by Faubel et al. on bulk liquid jet targets [48, 49, 23, 54]. Bulk targets with diameters $D > 10$ μm are desired in HEDP pump-probe imaging experiments [162], given that a larger liquid interaction region equals more space for evolution of the interaction. This implies that for high-repetition-rate experiments a larger window of the hydrodynamic evolution in time and space can be captured. For the experiments carried out in this thesis, the designed cylindrical liquid microjet had $D \leq 50$ μm and was capable of operating in a vacuum $p = 10^{-5}$ torr for extended periods of time, limited by the water intake capacity of the roughing and turbo pumps in the chamber as well as the inclusion of an LN_2 cold trap as described in the next section.

4.2 Experiment

The cylindrical liquid microjet is composed of two main components: a fused silica nozzle with 20–50 μm aperture diameter and a catcher with 300–600 μm opening diameter. The alignment of both components is achieved through the use of 5$\times$ translation stages (or 2$\times$ translation stages and 3$\times$ picomotors), which ensure the jet nozzle remains in alignment with the catcher and the whole target structure is in focus with the experimental probe. One in-vacuum (USB) camera is necessary to assist in the alignment procedure of nozzle and catcher. Alternatively, two cameras closely monitoring the target through viewports outside the chamber can also be used. Once alignment is complete the liquid is delivered to the chamber and vacuum pressures as low as to 10^{-5} Torr can be achieved, provided a $\sim$1000 L/min turbo pump and LN_2 cold trap are included.

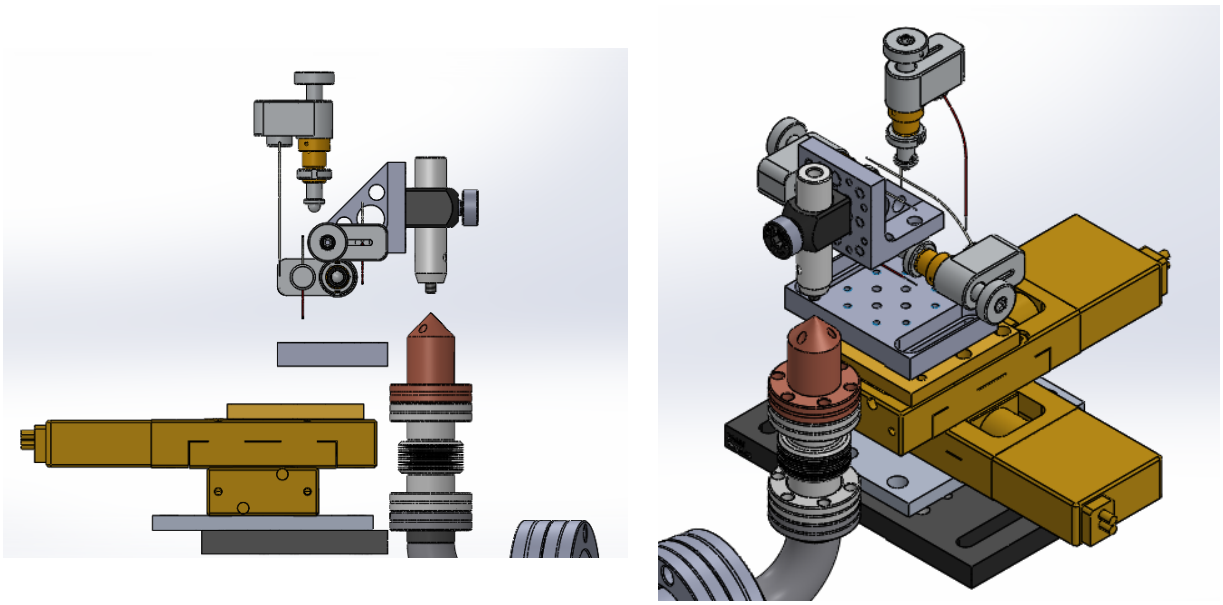

Figure 4.1: Cylindrical jet target CAD assembly. (left) Side view and (right) isometric view. The design includes 3× picomotors controlling the nozzle in the x, y, z directions and 2× translation stages for aligning the target to the experimental probe.

A schematic design of the target assembly is shown in Figure 4.1 and a technical drawing with its dimensions in the Appendices in Figure B.1. The liquid target is usually modified to satisfy the chamber and experimental requirements. Some modifications include changing the height to match that of the probe, incorporating a larger liquid reservoir to increase the operation time, or varying the jet diameter to match the vacuum level requirements. The cylindrical liquid microjet parameters are summarized in Table 4.1.

Cylindrical microjet parameters	**Range**
Jet diameter (μm)	10–50
Jet length (cylindrical section) (mm)	1–20
Jet velocity (ms^{-1})	10–100
Liquid viscosity (mPa·s)	1–10
Operation time (hrs.)	1–12
Chamber pressure (mTorr)	0.01–100

Table 4.1: Table of parameter for the cylindrical microjet.

The jet nozzle is made of cleaved capillary tubing (30 μm ID Polymicro capillary tubing — Molex) and similarly connected to the chamber via 1/16” (0.03” inner diameter) stainless steel

tubing and fittings. The liquid is delivered to the nozzle by a High-Performance Liquid Chromatography (HPLC) pump similarly connected to the chamber via a 1/16" outer diameter stainless steel tubing feed-through. The liquid flow rate in the experiment is variable reaching up to 10 ml/min with jet velocities up to 100 m/s. The liquid jet is subsequently captured at the bottom by a custom made conical-shaped copper catcher with a top aperture of 300–600 μm where the liquid falls into. This is shown in Figure 4.2.

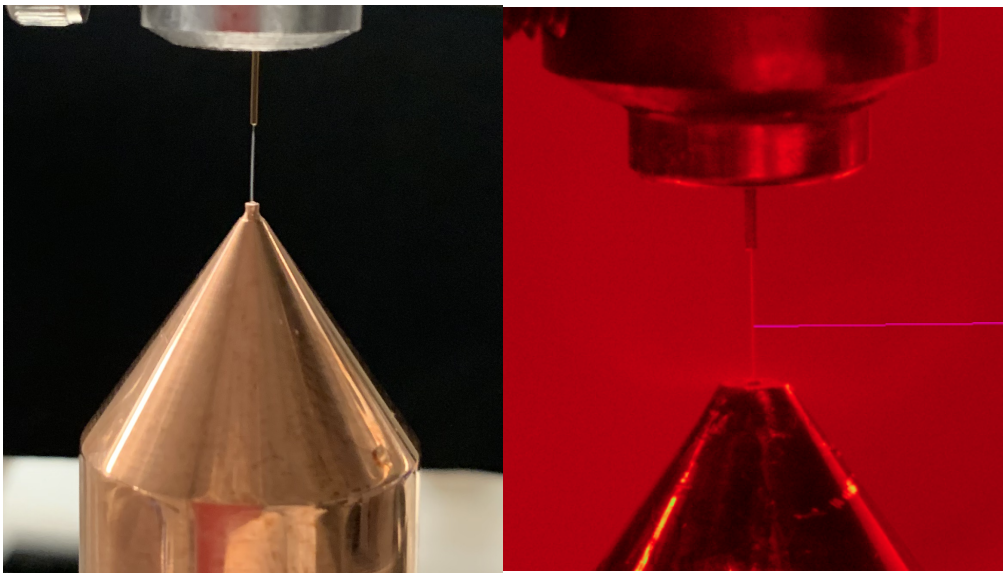

Figure 4.2: Close-up pictures of a cylindrical water target. (left) A water jet diameter of ~ 100 μm and (right) photo taken inside the vacuum chamber with alignment cameras and a jet diameter of ~ 50 μm.

The copper head of the catcher is linked with standard DN16CF flanges and connected directly to a liquid reservoir through a metal tube. The catcher is simultaneously heated by direct contact with miniature cartridge heaters (3×15 W, Thorlabs) in order to avoid ice formation during the alignment procedure. This configuration is better appreciated in Figure 4.3.

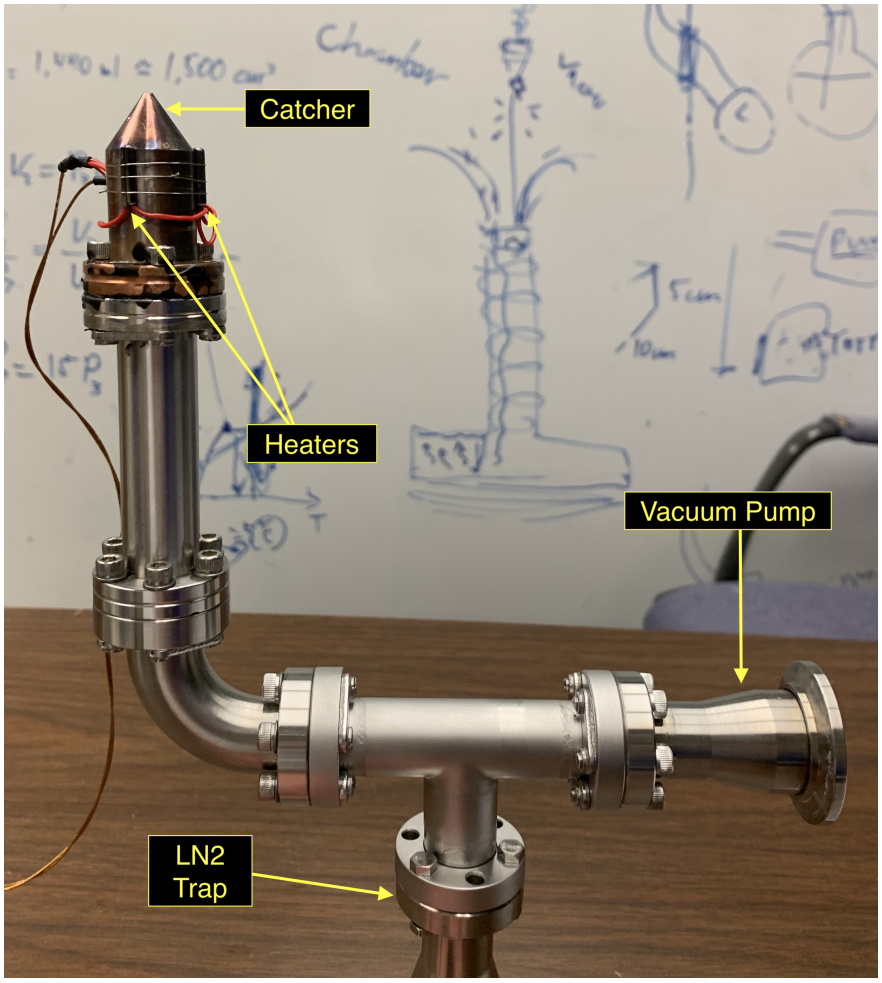

Figure 4.3: Photograph showing the configuration of the liquid microjet catcher.

An experimental setup including the cylindrical microjet target is shown in Figure 4.4. In this configuration a 30 μm water jet is installed along the optical axis 10 cm past the focus of the high power laser at the gas jet. This particular liquid target setup includes a nozzle, a catcher, 5$\times$ manipulators for alignment, heating elements, and a reservoir connected to an additional vacuum pump as well as a liquid nitrogen cold trap.

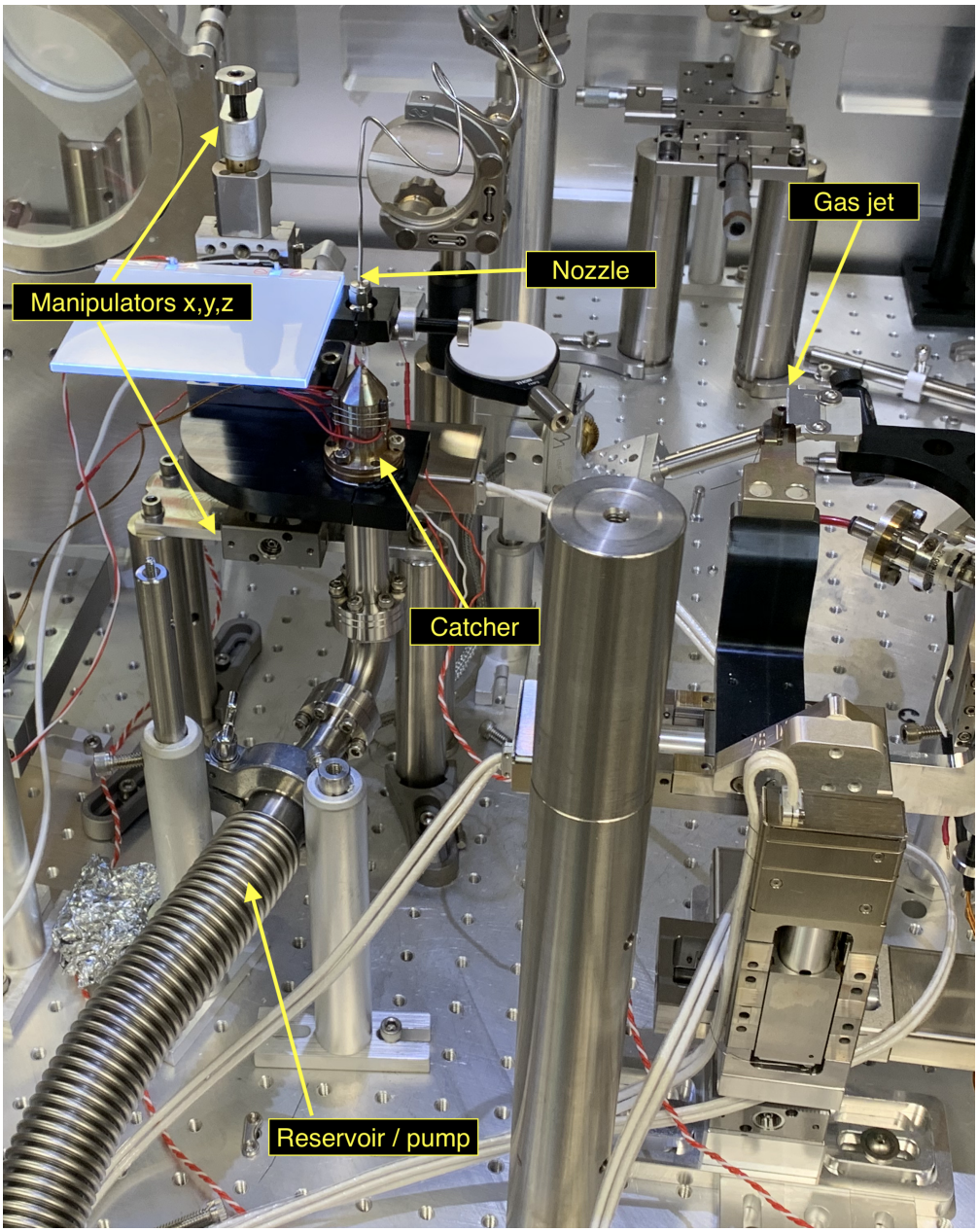

Figure 4.4: Example photo showing a $\sim$ 30 μm cylindrical water jet target configured in a laser wakefield accelerator pump-probe experiment setup.

4.3 Discussion

The use of liquid targets affords increased adaptability in experimental design. With the option to easily vary target thickness, composition, and flow rate, researchers can fine-tune their experiments to explore different facets of HEDP. This flexibility in target manipulation allows for the study of a diverse range of phenomena, spanning from laser-plasma interactions to inertial confinement fusion and more. By incorporating liquid targets, the range of potential experimental parameters and research avenues is expanded, fostering a more thorough understanding of HEDP.

Furthermore, the integration of betatron X-ray imaging from a laser wakefield accelerator presents a unique opportunity for observing hydrodynamic interactions with unmatched spatio-temporal resolution. The integration of liquid targets with this imaging technique permits visualizing and characterizing the complex interplay between the high-intensity laser pulses and hydrodynamic systems, revealing intricate details of plasma formation and energy deposition processes. Having a replenishing target implies that *movies* can be quickly captured with the X-rays during pump-probe experiments in high-energy-density conditions.

In conclusion, the development of liquid targets for high-repetition-rate high-energy-density physics experiments in vacuum environments represents a significant stride forward in the field. With faster data acquisition rates, the ability to investigate time-varying hydrodynamic systems, and increased experimental adaptability, liquid targets offer a promising alternative to their solid counterparts.

CHAPTER 5

Dynamic Ultrafast X-Ray Imaging of Shocks in Water

5.1 Introduction

Matter at extreme conditions, such as those found when heated by a high-intensity laser, remains difficult to study in the laboratory due to the high field intensities present, limited control of the experimental environment, and poor resolution of diagnostic systems. Within this context, X-ray radiography is an important tool in HEDP and has been used successfully over the past decades to study the dynamics of matter during high-energy-density interactions [43, 93, 95, 40, 179, 97]. Nevertheless, X-ray radiography presents many limitations regarding the contrast, signal-to-noise ratio, and imaging resolution it can provide given complex target configurations such as those found in ICF experiments. Even at NIF, the images are based on absorption from a laser backlighter X-ray source and can be limited to ~ 20 μm resolution [21] and, in some cases, this may be reduced to ~ 10 μm [165]. It is therefore imperative to improve on new systems with higher-quality images to better diagnose turbulent length scales in HEDP experiments.

As an alternative approach, laser wakefield acceleration (LWFA) [168], has emerged [111, 58, 50, 102, 64, 29, 182, 76] as a table-top source of ultrafast [167], bright, and spatially-coherent [151] X-ray pulses with a small source size [84] that allows for high spatial resolution imaging [4]. As the ultrashort laser pulse travels through the plasma the ponderomotive force $F_P = -(e^2/2\gamma m_e)\nabla \mathbf{A}^2$ expels electrons away from high-intensity regions leaving an ion channel and launching plasma waves in the wake of the pulse [109]. The oscillation of electrons inside the ion bubble generates radiation bursts with broadband spectrum [47] typically in the keV range [2]. Importantly, the betatron X-rays proceed from a small source size (a few microns) such that after propagation of a few cm the photons develop spatial coherence, making them suitable for phase-contrast X-ray imaging (PCXI) [159, 185]. Propagation based PCXI technique is based on the phase-shift induced as the spatially-coherent X-ray beam crosses a sample and its contrast

enhancement is entirely geometry dependent [129]. The small X-ray deflections induced by gradients in the refractive index $n = 1 - \delta - i\beta$ result in the deflection of rays out of regions of high density. It is particularly sensitive and may detect relatively small density gradients, thus making it an excellent candidate for probing weakly absorbing objects with low atomic number. This has been demonstrated in recent work conducting PCXI of bubbles, capsules, and insects [174, 52, 53], 3D reconstruction of bone structure [32], and imaging of laser-driven shocks in solid targets [186, 187, 148], among others [3]. Nevertheless, previous experiments have been limited to a single-shot configuration and many have not been able to exploit the high-repetition-rate capabilities to image time-dependent dynamic phenomena.

Within this context, imaging the evolution of hydrodynamic shock waves in a pump-probe configuration is a particularly relevant first step towards better imaging diagnostic systems in high-energy-density experiments, where shock waves are largely common. Previous studies have been limited thus far by the repetition rate of both the laser and target systems, and have only recorded static single-shot images. In this sense, a liquid target improves on previous work by providing orders of magnitude more data in less amount of time, while also making possible to image hydrodynamic phenomena in situ. In this work we demonstrate a platform for studying laser-driven shock waves with unprecedented spatio-temporal resolution by using the betatron X-rays from a high-repetition-rate LWFA in combination with a liquid (water) jet target. A high-repetition-rate scheme, small source size, and ultrashort pulse duration permit studying sub-micron scale hydrodynamic systems in regimes unreachable until now.

5.2 Experiment

The experiments were performed at the LBNL BELLA Center, where the HTW dual beam laser system (20–30 TW, $\lambda_0 = 800$ nm) was used to drive both the laser wakefield accelerator and generate the shock wave in the liquid target as shown in Fig. 5.1. The main LWFA beam consisted of a linearly-polarized high-energy (1.5 ± 0.2) J, high-repetition-rate (1 Hz), ultrafast (40 ± 5 fs FWHM) laser pulse focused by an f/20 off-axis parabola into a gas jet (see Methods, chapter 3) reaching on-target intensities in the order of $I \approx 10^{18}$ Wcm^{-2}. The high-intensity pulse accelerated electrons to 167 ± 13.4 MeV mean energy with $x : 7.8 \pm 1$ mrad, $y : 3.4 \pm 0.8$ mrad pointing divergence and mean charge of 32.5 pC. The relativistic electrons generated radiation bursts with sub-micron source size and synchrotron-like spectrum. The X-rays were recorded using a cooled, in-vacuum, CCD camera (PI-MTE). The characterization of the radiation spectrum was performed following Ref. [78] by imaging a Ross filter wheel with wedges of different materials and thicknesses. The resulting fit gives a critical energy of $E_{\text{crit}} = 4.88 \pm 1.33$ keV. The size of the source was estimated by imaging a sharp "knife edge" and fitting the data to the expected Fresnel diffraction pattern of a

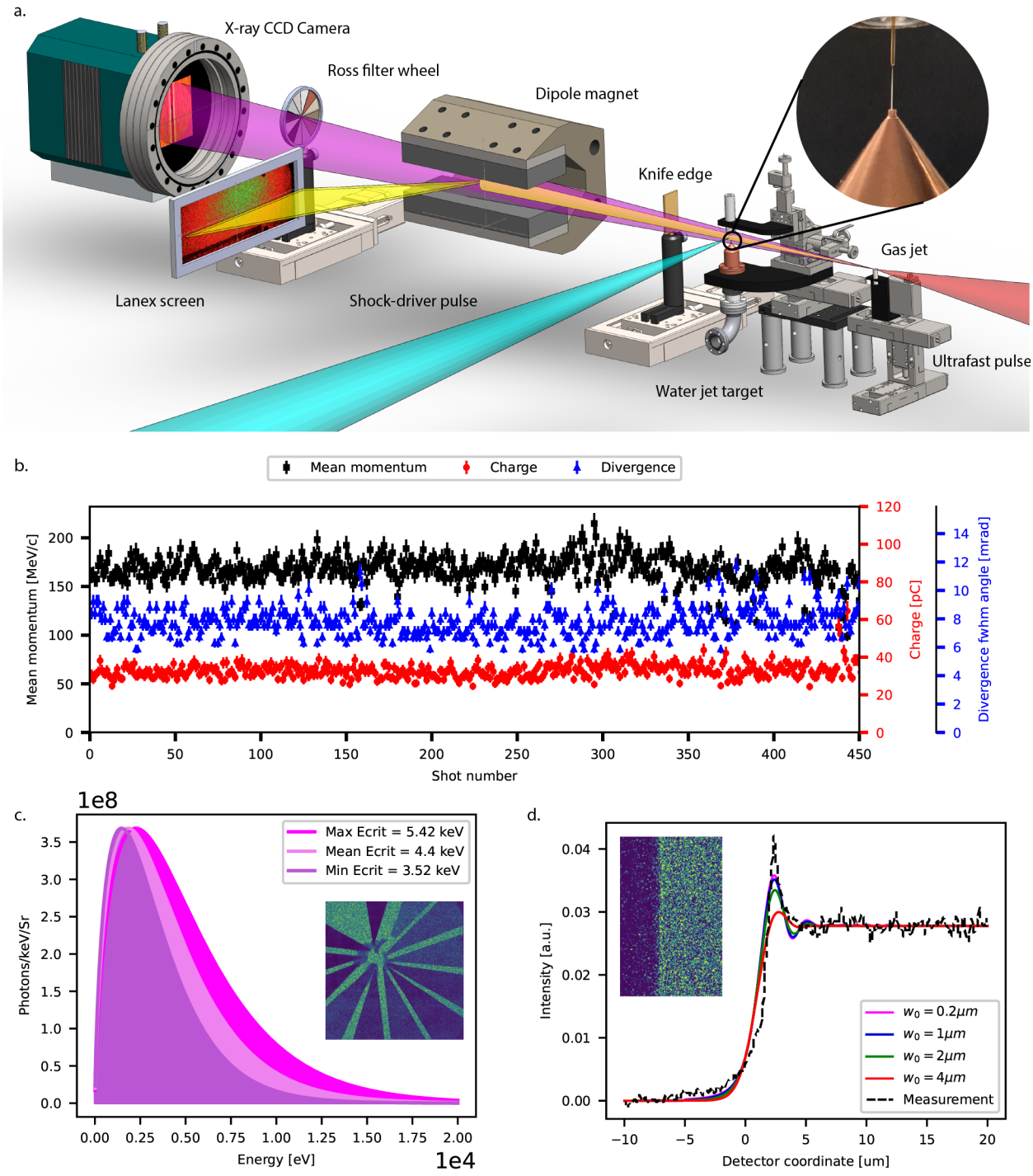

Figure 5.1: (a) Experimental configuration for pump-probe ultrafast X-ray imaging of shocks in water. (b) Characterization of the electron beam, 460 shots were taken continuously measuring the mean momentum, charge, and FWHM divergence angle. (c) Energy spectrum of the betatron X-ray source, measured by imaging a filter wheel with samples of different materials and thicknesses and fitting a synthetic spectrum to the data. (d) Betatron X-ray source size is measured by imaging a sharp knife-edge and fitting the expected Fresnel diffraction pattern for different source sizes.

Gaussian source interfering with a half-plane. The fitting of the data results in the size of the X-ray source being predicted to be $\sigma \leq 1\mu$m, as shown in Fig. 5.1.

The geometry of the experimental setup was carefully considered as the phase-contrast effect is sensitive to spatial coherence i.e. phase correlation across the wavefront. To properly choose source-to-object distance l and object-to-detector distance L we can estimate the coherence length. For a collection of uncorrelated emitters of wavenumber k and source size σ the coherence length is given by $L_\perp = l/k\sigma$ [84]. Since we expect to be able to resolve features of order σ at the image plane, therefore the coherence length should be longer than the source size, $L_\perp > \sigma$, so we can reverse this equation to estimate the required source-object distance to be $l \approx L_\perp \sigma k > k\sigma^2$, which in terms of the photon energy in units of keV and microns is

$$l[m] > 5.1 \times 10^{-3} \left(\sigma[\mu\text{m}]\right)^2 \left(\hbar\omega[keV]\right) \ . \tag{5.1}$$

For example, for 5 keV X-rays with a 2 μm source size, the coherence length is at least the source size when the source-to-object distance is 10 cm. The broadband polychromatic spectrum of a betatron source is still suitable for a propagation-based geometry as the phase-contrast pattern is independent of wavelength to first order in the Fresnel or paraxial approximation ($R_0/r_0 \approx R_1/r_1 \approx 1$. For this approximation to be valid the Fresnel effective number must be larger than unity $N_{F,eff} > 1$. This condition holds true given the present experimental setup with source-to-object distance $R_0 = 20$ cm, object-to-detector distance $R_1 = 580$ cm, and beam divergence of a few tens of mrad.

The shock driver laser was obtained by splitting the main BELLA HTW beam and subsequently bypassing the compressor, thus generating a long high-energy pulse (200 ps, 1.2 ± 0.2 J). The laser was focused perpendicularly to the main beam into the water target plane to a FWHM spot size of 60 ± 5 μm reaching intensities of order $I \approx 10^{14}$ W/cm^2. A variable delay line allowed for precise control of timing with respect to the X-rays up to 8 ns within the interaction. It is also worth noting that the pulse waist at the target plane is $w_0 \approx 60$ μm to ensure its interaction with the 30 μm jet when subject to horizontal jitter of the focus spot along the delay line. Moreover, the focal spot of the shock driver laser pulse at the water jet plane was optimized and its centroid was tracked along the delay line to guarantee the interaction of the pulse with the target.

To complement the experimental results, 3D FLASH simulations have been performed to predict the fluid dynamics of the interaction. The simulation radiography maps were coupled to a phase-contrast X-ray imaging algorithm following the Fresnel-Kirchoff formalism [128, 17, 11, 134] on propagation of the wave distribution (described in Chapter 3) in order to have a more direct comparison to experimental images.

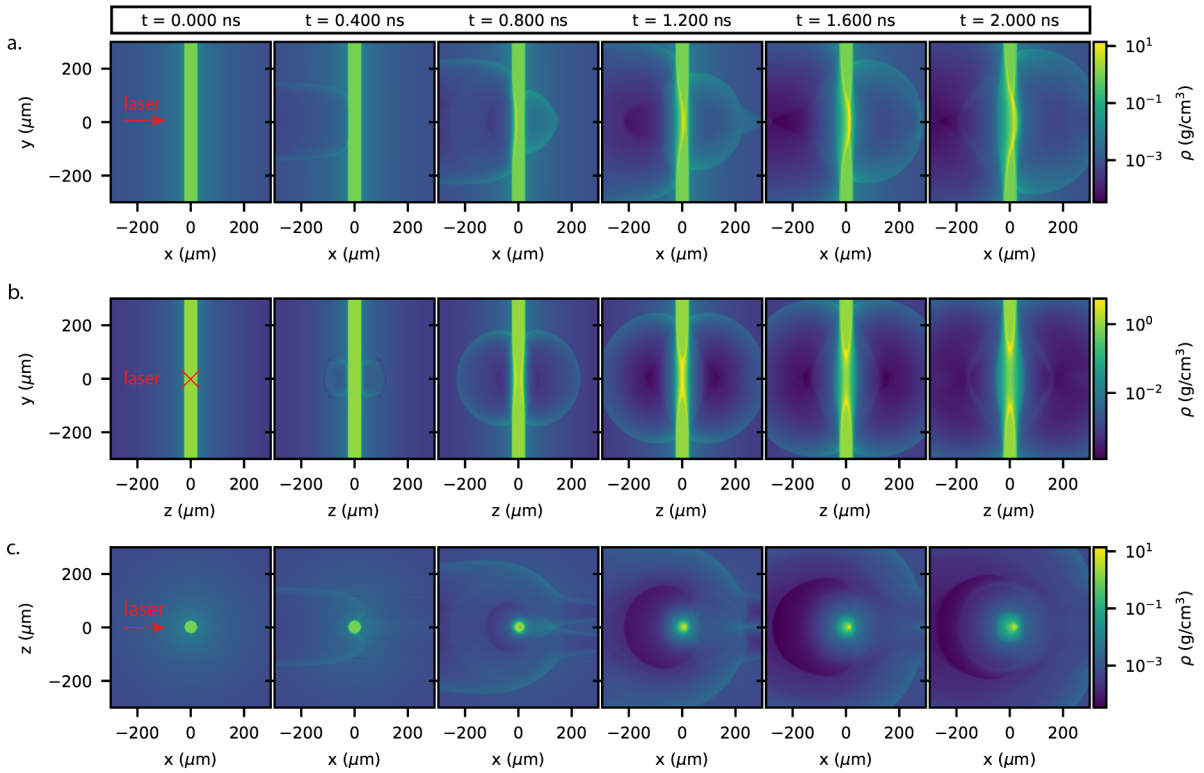

Figure 5.2: Time evolution plots for 3D FLASH simulations of laser-water interaction. (a) x-y plane shows a laser-driven shock propagating through the target. (b) y-z plane displays the high-density wrapping around the cylindrical target. (c) x-z plane showing the 3D effects of shock generation from the top, compressing the target symmetrically from around the surface.

5.3 Results & Simulations

In order to predict the characteristics and evolution of the laser-water interaction, 3D radiation hydrodynamic simulations were performed using the FLASH code, as described in Sec. 3.4. The simulation results are presented in Fig. 5.2 with slices from all three perspectives (directions) of the interaction in order for the reader to better understand the overall three-dimensional evolution. Looking at the water jet from the betatron X-rays point-of-view, a shock can be observed being generated from the front ablation surface and propagating throughout the water target. Once the shock reaches the back surface it expands adiabatically by releasing the pressure into the vacuum. Looking at the interaction from the top plane down, as well as from the perspective of the long pulse into the screen, it becomes clear that in three dimensions the high-density shock is not planar but rather has a curvature that wraps around the cylindrical target. In this sense, the shocked fluid is capable of propagating not only through the target but also around the target.

Within this context, Fig. 5.3 shows a time series of a laser-driven shock wave propagating

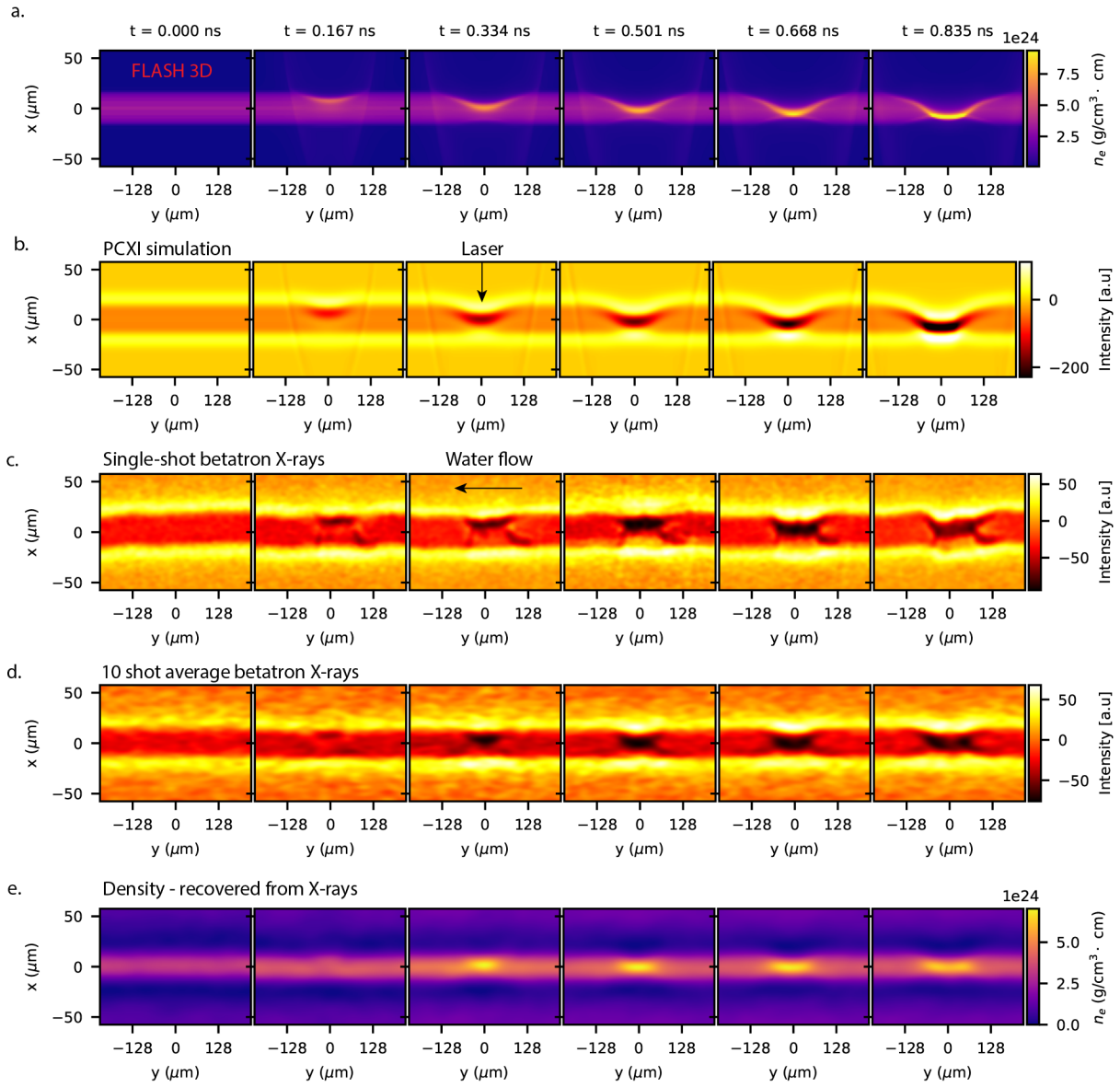

Figure 5.3: (a) Projected density from 3D FLASH radiation hydrodynamic simulation of the interaction of a 200 ps long laser pulse with a 30 μm cylindrical water jet target for $0 < t < 1$ ns. (b) Synthethic phase-contrast X-ray images of laser-driven shock waves using FLASH simulations and solving the Fresnel-Kirchoff integrals for a complex wave distribution. Experimental (c) single-shot and (d) ten-shot average betatron phase-contrast X-ray images of the laser-water interaction. (e) Density map recovered from experimental phase-contrast X-ray images. The water stream flows from left to right, while the long laser pulse propagates from the top.

through the cylindrical water target, comparing both simulation and experimental results for $0 < t < 1$ ns. The projected density maps obtained from FLASH simulations were treated with a Fresnel-Kirchoff-based algorithm to generate synthetic phase-contrast X-ray images that can directly be compared with experimental measurements. In this sense, Fig. 5.3 presents the formation and evolution of a hydrodynamic shock captured with ultrafast betatron X-rays. The time evolution of the shock is captured for single-shot images as well as for a ten-shot average. The experimental images have been pre-processed by applying a filter in Fourier space reducing undesired high spatial frequencies and thereby increasing the signal-to-noise ratio. The phase-contrast enhancement at the interfaces of the target is clearly visible, as well as the blurring effect on the image due to the finite source size. For both simulation and experiment it can be observed how the ablation of material by the laser generates a hydrodynamic shock that propagates from one end of the water target to the other. This allows for measuring the shock velocity in situ, which is approximately $u_s \approx 20\ \mu\text{m/ns} = 20$ km/s.

Shock velocity is important because it provides information regarding the thermodynamic state of the material. To see how this is true let us work in the shock frame of reference and introduce once again the conservation of mass, momentum, and energy through the Rankine-Hugoniot jump conditions discussed in Chapter 2,

$$\rho_1 u_1 = \rho_2 u_2 \ , \tag{5.2}$$

$$\rho_1 u_1^2 + p_1 = \rho_2 u_2^2 + p_2 \ , \tag{5.3}$$

$$\left[\rho_1 u_1 \left(\epsilon_1 + \frac{u_1^2}{2}\right) + p_1 u_1\right] = \left[\rho_2 u_2 \left(\epsilon_2 + \frac{u_2^2}{2}\right) + p_2 u_2\right] \ . \tag{5.4}$$

Where ρ is the mass density, u is the fluid velocity, p is the pressure, and ϵ the specific internal energy. Here the subscript 1 denotes the upstream unshocked fluid and subscript 2 is the downstream post-shock fluid. Note that in the laboratory frame of reference, $u_s = |u_1|$ when the upstream fluid is at rest. This helps us define an upstream shock Mach number for a polytropic gas as,

$$M_u = \frac{-u_1}{c_{s1}} = u_s \sqrt{\frac{\rho_1}{(\gamma_1 p_1)}} \ . \tag{5.5}$$

Where the index $\gamma = 5/3$ is commonly used for materials with low atomic number. This leads to obtaining $M_u \approx 2 \times 10^4$ for the present parameters, a clear indication of *strong shock* generation. We can then introduce M_u in the jump conditions of Equation (5.4) and solve for useful expressions to calculate the post-shock pressure and density using the measured shock velocity, this is

$$\frac{\rho_2}{\rho_1} = \frac{M_u^2(\gamma+1)}{M_u^2(\gamma-1)+2} \ , \tag{5.6}$$

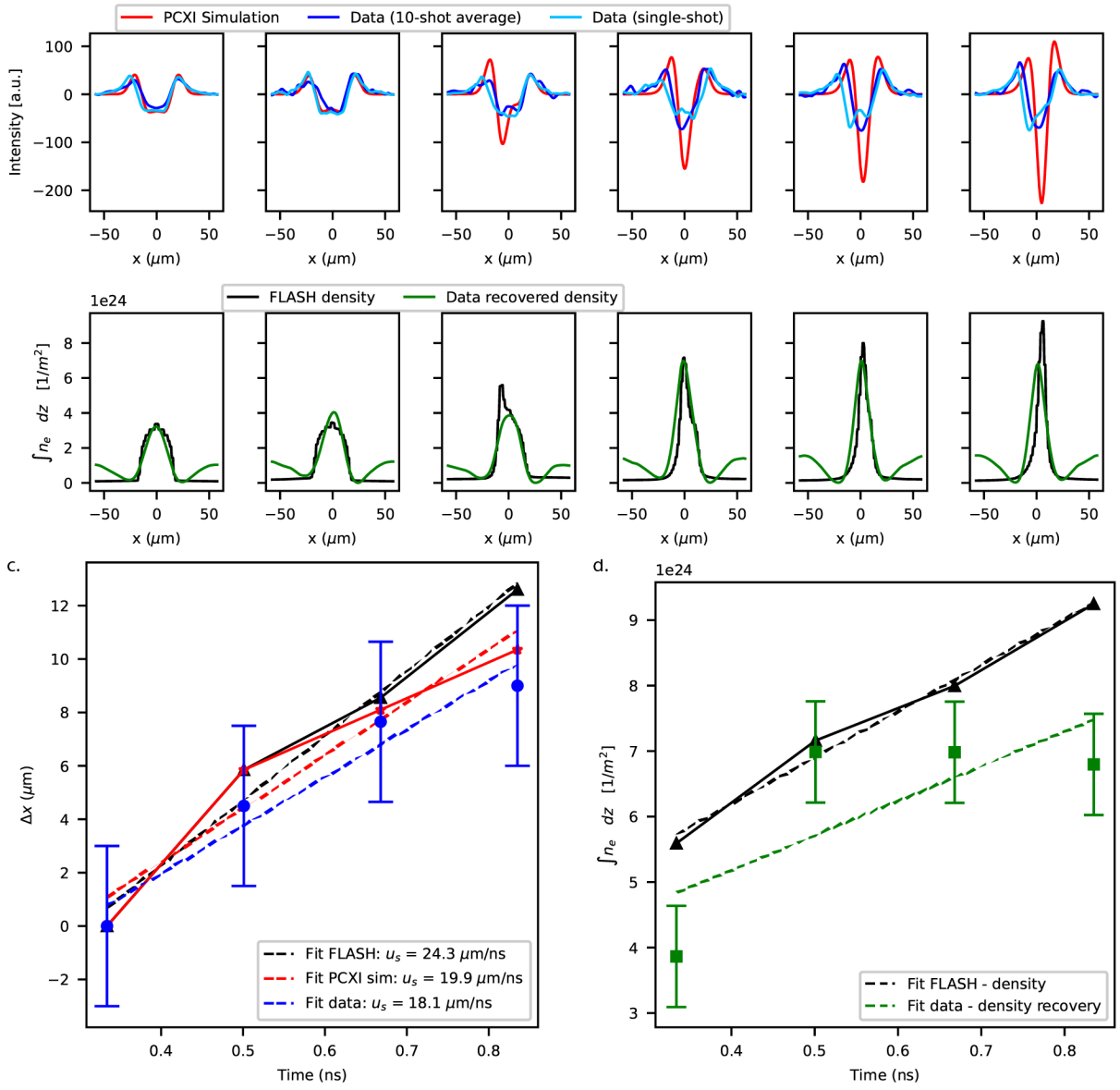

Figure 5.4: (a) Center lineouts for phase-contrast X-ray images of the shocked target, both for simulation and experiment. (b) Center lineouts for projected density of the shocked target, both from FLASH 3D simulation and recovered from experimental phase-contrast X-ray images. (c) Plot of shock velocity across the target. Measured by tracking the point of highest density in FLASH, and point of darkest signal in phase-contrast X-ray images. (d) Plot of shock magnitude (density jump) as a function of time. Measured by tracking the magnitude of the projected density as a function of time, both in FLASH simulations as well as from the density recovery analysis of the experimental images.

and

$$\frac{p_2}{p_1} = \frac{2\gamma M_u^2 - (\gamma - 1)}{(\gamma + 1)} \,. \tag{5.7}$$

We notice that in the strong shock regime when M_u becomes large, the physical limit for density jump in a polytropic gas is $\rho_2/\rho_1 = (\gamma+1)/(\gamma-1) \sim 4$, while the pressure grows infinitely, and is strongly dependent on the shock velocity measured experimentally. For the present analysis shown in Fig. 5.4 with $u_s \approx 20$ km/s, the resulting pressure is $p_2 \sim 3.3$ Mbar which falls within the range and order of magnitude of the ablation pressure predicted by FLASH and can be compared with a theoretically calculated ablation pressure [42].

$$P_{abl} = n_{\text{crit}}(1 + 1/Z)k_B T_e = 7.63 \text{ Mbar} \tag{5.8}$$

Where n_c is the critical density, Z is the effective ionization state, and T_e is the electron temperature. This results in an ablation pressure that closely matches the value calculated using the experimentally obtained shock velocity indicating simulation and experiment agree qualitatively well.

The evolution of the shock past 1 ns can be appreciated in Fig. 5.5, in which discrepancies between simulation and experiments start to emerge. One interesting result is that the experimental measurements show evidence of the liquid jet being compressed from multiple directions. Even though initial 2D and 3D FLASH simulations do not show such strong multi-direction compression. It was found that the compression in part occurs due to higher electron heat transport around the surface of the target, mediated by collisions in a liquid-vapor blanket present from the evaporation of the water jet in a vacuum. When such vapor blanket around the jet was introduced in the 3D simulation, in order to approximate the evaporative process, a clear observation of multi-direction compression was observed in the 3D simulations as shown in Fig. 5.5. The experimental images were processed using a Meijering filter, which calculates the eigenvectors of the Hessian to compute the similarity of an image region to neurites, according to the method described in [120].

Furthermore, the X-ray measurements go beyond compression to show evidence of shock reflection at the liquid-vacuum interface. Sound wave reflections at interfaces have been well documented from the mismatch in acoustic impedance. Nevertheless, the FLASH simulations do not display such behavior. One possible explanation is concerned with an increase in surrounding pressure. In the same way that increasing the vapor density surrounding the leads to multi-directional compression, it is possible that at high enough densities and temperatures, the pressure surrounding the jet is sufficient to avoid isothermal expansion and produce a *shock reflection*, or backward propagating shock as shown in Fig. 5.5.

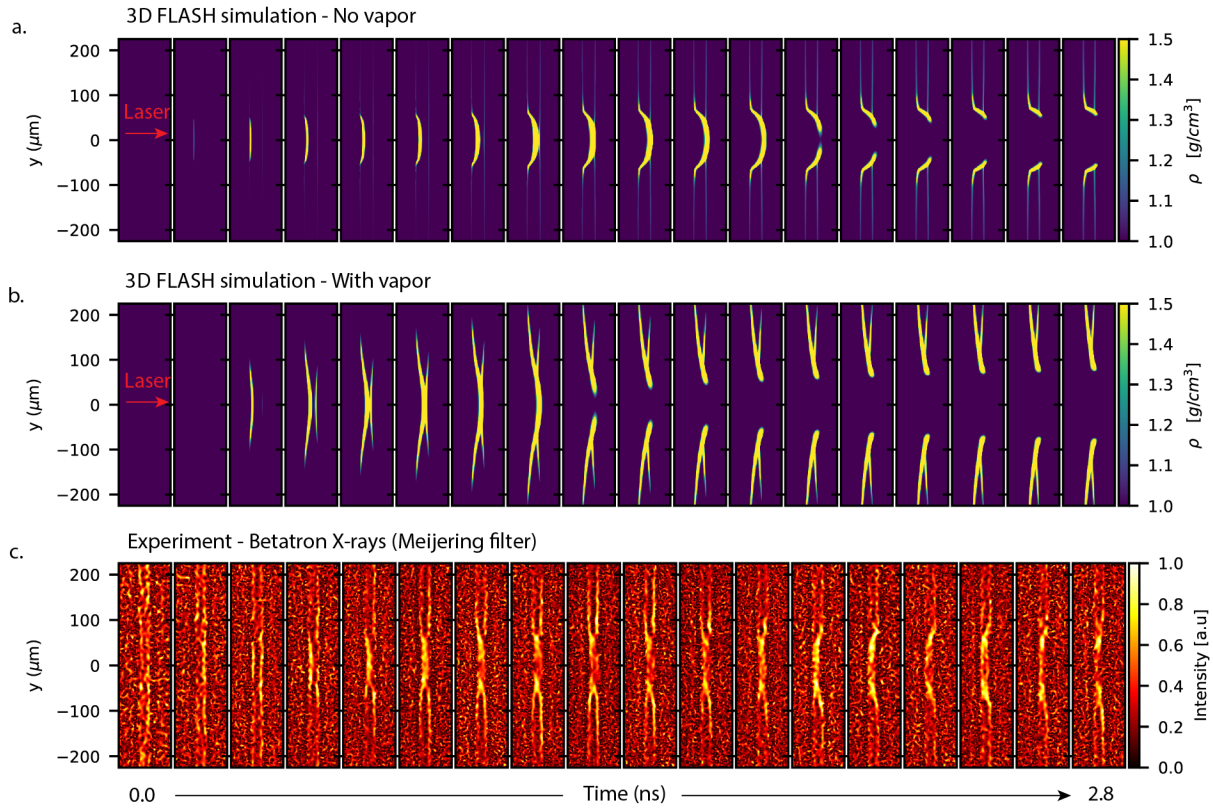

Figure 5.5: (a) 2D slice from 3D FLASH simulation of laser water interaction with no surrounding vapor density. (b) 2D slice from 3D FLASH simulation of laser water interaction with a surrounding vapor profile. (c) Experimentally measured data of laser water interaction displayed with Meijering filter, showing compression of the cylindrical target from multiple directions.

5.4 Discussion

We can attempt to model the laser-water interaction analytically following texts by Lindl and Drake [104, 42], and obtain some useful estimates for the electron temperatures and ablation pressures expected for the experiment. Initially the front tail of the long pulse will quickly produce plasma and the laser energy of the peak of the pulse is deposited in the ionized water electrons below the critical density n_c [38]. This creates a high-temperature region from which the electrons transport heat above n_c into the dense matter. The heated material flies away from the ablation surface and a strong shock is launched into the target through a rocket-like acceleration process. The energy deposited by the laser is responsible for sustaining both, the electron heat transport and the expansion of material away from the irradiated surface. Even though these laser conditions are different from what is typically used on Omega or NIF to generate flows to study hydrodynamic instabilities, for an initial calculation following texts by [104] and [42] let us treat the electron heating above critical density as a flux-limited transport model [39] and approximate the expansion of material as an isothermal rarefaction (given the good thermal conductivity and low density of the corona) with polytropic index γ and energy flux given by $\rho_s c_s^3 (5\gamma - 3)/\left(2\left(\gamma - 1\right)\right)$. The energy flux conservation equation then becomes

$$I_L = f n_c k_B T_e \sqrt{k_B T_e / m_e} + \rho_s c_s^3 \frac{(5\gamma - 3)}{2\left(\gamma - 1\right)} \,. \tag{5.9}$$

Here $\rho_s = g n_c$ is the density at the sonic point (critical surface), given as a fraction g of the critical density, $c_s^2 = \left(Z k_B T_e + 3 k_B T_i\right)/M \approx 224$ μm/ns is the effective ion sound velocity, and f is the flux-limiter number. To match the heat flux given by the Fokker-Planck equation typically requires $f \approx 0.1$, yet experimental observations suggests that the reported heat transport is even lower than predicted and could only be explained by using f as small as $f \sim 0.01$. This could be due to the fact that these models do not include non-local heat transport effects or magnetization of the electrons. For this analysis let us take $f = 0.05$ and radiation hydrodynamic simulations often find $T_i \approx T_e/3$ in the corona below n_c. Therefore, solving for T_e,

$$k_B T_e = \left(\frac{I_L}{n_c}\right)^{2/3} \left(\frac{f}{\sqrt{m_e}} + \frac{g(1+Z)^{3/2}(5\gamma - 3)}{2\sqrt{A m_p} Z\left(\gamma - 1\right)}\right)^{-2/3} \,. \tag{5.10}$$

In practical units we have,

$$T_e = 4.19 \left(I_{14} \lambda_u^2\right)^{2/3} \left(20 f + \frac{0.23 g \left(1 + Z\right)^{3/2} \left(5\gamma - 3\right)}{\sqrt{A} Z \left(\gamma - 1\right)}\right)^{-2/3} \quad \text{keV} \,, \tag{5.11}$$

where I_{14} is the laser irradiance in units of 10^{14} W/cm^2, and λ_u is the laser wavelength in μm. For the present experimental parameters, the predicted electron temperature is $T_e \approx 2.41$ keV. The calculation of electron temperature is relevant as it allows one to estimate important parameters regarding the thermodynamic state of the material.

First, it has been demonstrated that the electron temperature in the shocked fluid can be effectively used to calculate the time-scale for the thermal electron-ion equilibration time [143, 114]. In this sense, the calculation of the electron temperature through the Rankine-Hugoniot jump conditions presents a unique opportunity to estimate the time it takes for electrons and ions to reach equilibrium after the passage of the shock. As the shock propagates through a collisional plasma it will dissipate energy into the ions. The electrons, having a much higher thermal velocity, are adiabatically compressed and subsequently reach thermal equilibrium with the ions in time-scales according to Coulomb collisions [160]. This is, for electrons and ions reaching $T_e \approx T_i = T$ then,

$$\bar{\nu}^{e|i}/n_i = \bar{\nu}^{i|e}/n_e = 3.2 \times 10^{-9} Z^2 \lambda / \mu T^{3/2} \text{ cm}^3\text{sec}^{-1} \ . \tag{5.12}$$

Here the atomic Z can be effectively calculated for a molecule in a compound. An alternative expression for the thermal equilibration time is based on the post-shock electron temperature giving

$$t_{\text{eq}}(e,p) \approx 19.5 \times 10^{15} \left(\frac{T_e}{10^8 \text{K}} \right)^{3/2} \left(\frac{n_e}{10^{-3}\text{cm}^{-3}} \right)^{-1} \text{ sec.} \tag{5.13}$$

Where T_e is the electron temperature and n_e is the electron number density. Therefore, using the calculated electron temperature, and Eq. 5.13 the estimated electron-ion thermal equilibration time-scale is $t_{\text{eq}}(e,p) \sim 1 - 10$ ps. Nevertheless, this estimation is only considering Coulomb collisions. When particles couple to electric and magnetic fields the dissipation scale lengths are much shorter compared to the typical collisional mean free path. Additionally, the coupling of charged particles to electromagnetic fields mediated by plasma waves inherently affects electrons and ions differently due their significant difference in mass. For these reasons, and based on the fact that traditional radiation hydrodynamic simulations do not include such charge-separation effects, we might expect that the electron heating rate is shorter compared to the Coulomb collisional time-scales predicted above. Some of these charge separation effects are studied further in 7.

Next, using the value of T_e it is also possible to obtain an approximation for the ablation pressure at the critical surface,

$$P_{abl} = n_c \left(1 + 1/Z_{eff}\right) k_B T_e = a I_{14}^{2/3} \lambda_u^{-2/3} \quad \text{Mbar} \ . \tag{5.14}$$

In this case a is a constant that depends on the material. Using the obtained value for temperature the predicted ablation pressure is in the order of $P_{abl} \sim 5.82$–7.63 Mbar, directly dependent on I_L.

This is about twice the pressure found at the Earth's core [16]. The exact values for a still need to be firmly grounded through more experimental measurements.

The hypothesis of multi-directional compression, or pinching, is based on the idea that free electrons in the low-density region below n_c are not able to fully escape from the electrostatic forces imposed by the ions, but are free to move around the surface of the target traveling a significant distance before depositing their energy. For instance, let us take the mean free path λ_{mfp} of an electron in the plasma region below n_c and an electron above n_c. For the low density let us use a value slightly lower than critical $n_l = n_c/2 \approx 1 \times 10^{21}\text{cm}^{-3}$ and approximate $T_e \sim 2$ keV and $T_i \sim 50$ eV from our model in the previous section. Using a ionization state $Z = 3.5$ we obtain $\lambda_{mfp} \sim 21$ μm. On the contrary, for the high-density region with $n_h = n_0/2 \approx 1.5 \times 10^{23}$ cm^{-3} and the same T_e, T_i, and Z we obtain $\lambda_{mfp} \sim 0.2$ μm, which is clearly an overestimation given than the temperatures at high densities are much lower as well as their ionization state.

Ultimately, wave reflection is an inherent process whenever a propagating wave encounters an interface. Whether it's light bouncing off a mirror or sound echoing off a canyon, it's because of boundary conditions. When the signal in a line meets a change in impedance, that's an interface. At any interface, certain conditions need to be met. In the case of electric signals, these conditions are delineated by Maxwell's equations, which in turn impose restrictions on distinct features of the electric and magnetic fields at the interface. For shock waves or strong hydrodynamic waves, the equations that describe their behavior at interfaces are Euler's equations. The equations predict the transmission of the shock and generation of a reflected rarefaction. The strength of the rarefaction depends on a variety of experimental conditions including the specific polytropic index of the plasma.

In this work, we have created a platform and a systematic study for observing the generation of laser-driven hydrodynamic shocks in water with unprecedented spatio-temporal resolution. Through direct measurement of shock velocity using the betatron X-rays, it was possible to estimate the ablation pressure and ion temperature through Rankine-Hugoniot calculations. Additionally, interesting hydrodynamic phenomena outlining the importance of 3D effects on the evolution of high-energy-density systems have been observed such as multi-direction pinching of the target and wave reflection. In this sense, this work hopes to move a step closer to improving high-repetition-rate diagnostic systems in HEDP experiments that can help to better understand the electron heat transport dynamics, which are crucial for developing laser-driven fusion technologies.

CHAPTER 6

Hydrodynamic Instabilities in Shocked Liquid Jets

6.1 Introduction

Hydrodynamic instabilities such as Rayleigh-Taylor, and Kelvin-Helmholtz are ubiquitous in the universe and found in many exotic astrophysical events including solar flares, supernova remnants, or plasma nebulae. Similar environments can be found in HEDP experiments such as those pursuing inertial confinement fusion with high-energy lasers such as NIF and OMEGA, in which hydrodynamic instabilities are the primary cause for degradation in the thermonuclear yield [156, 8, 189]. In this sense, the diagnosis of hydrodynamic instabilities is imperative in order to continue progressing towards achievable fusion energy technologies.

In the preceding Chapter 5, high-repetition-rate betatron X-ray sources were introduced as a promising tool for imaging hydrodynamic phenomena. The pages ahead are a continuation of this narrative, focused on the evolution of the laser-shocked water at later stages, when the intricate tapestry of plasma instabilities may develop. This chapter hopes to push the limits of high-resolution imaging using LWFA betatron X-rays even further by providing first-of-their-kind X-ray images of the evolution of plasma instabilities in spatial and temporal resolutions unexplored until now. The experimental setup shown in Fig 6.1 is essentially the same as the one described in Chapter 5, with particular emphasis on probing the later phase of the laser-water interaction through a long delay stage and applying active correction for the shock driver laser focal pointing into the water target.

While this chapter embraces some elements of speculation, it stands as a testament to our quest for understanding. Through thoughtful analysis, arguments are presented to suggest that the instabilities observed with the X-rays are originated from the Richtmyer-Meshkov (RM) process. This phenomenon arises when a shock wave collides with the interface between different media, imprinting vorticity into the liquid. An increase in vorticity subsequently leads to the amplification of small perturbations and waves that might develop at the shock interface. This chapter not only presents some results that show the incredible high-resolution imaging capacities of betatron

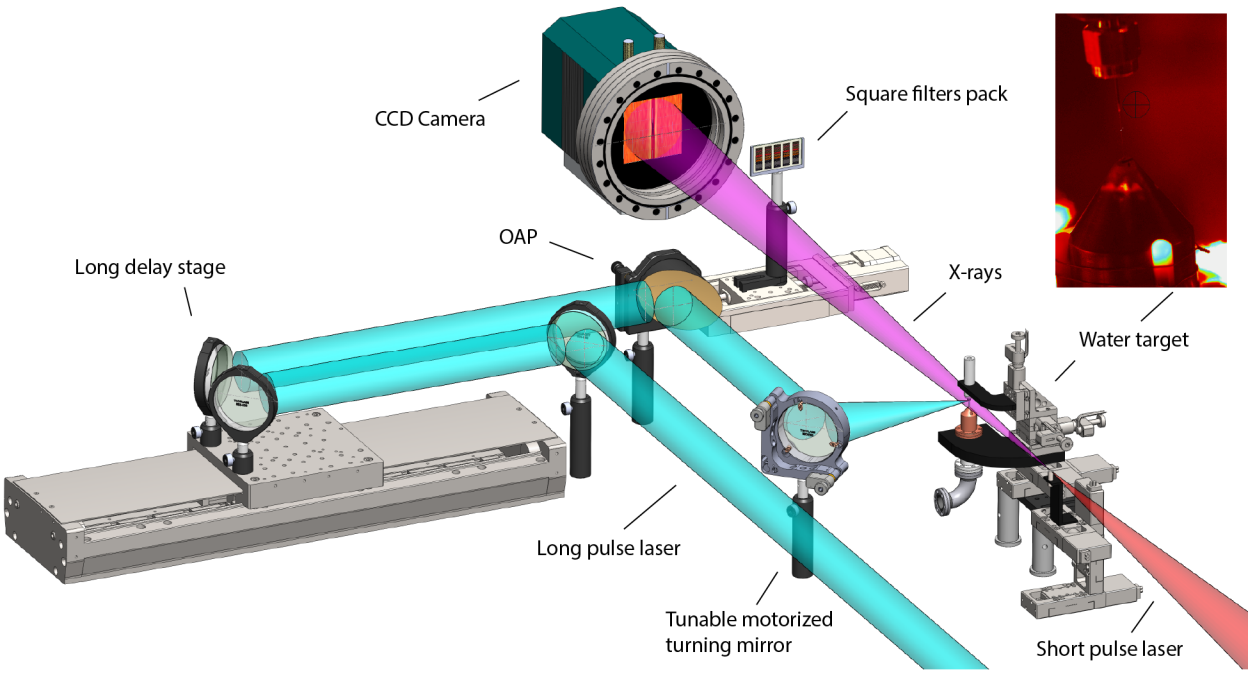

Figure 6.1: Experimental setup used for LWFA betatron X-ray imaging of laser-shocked water at later times $+2 < t < +8$ ns. Particular emphasis is placed on the active correction of the pointing of the shock driver laser to ensure proper alignment with the target as the delay line is varied.

X-rays, but also serves as proof that the platform developed as part of this thesis can be used to conduct analytical studies and compare them with theory, and simulation.

6.2 Results & Simulations

A laser-generated shock is by nature not an ideal shock. It is driven by the ablation of mass from a surface and thus it is not perfectly planar. The images obtained in Fig. 5.3 from the previous Chapter 5 display this by presenting a hydrodynamic shock with a bow shape - having a center head, and trailing wings at the sides. When a *rippled* shock with such lateral structure interacts with an interface that is also rippled (water to vapor-vacuum in this case) it affects the post-shock fluid flow with velocity $\mathbf{u}$ by depositing *vorticity* within the subsequently shocked fluid as described in Fig. 6.2. Vorticity can be defined as a vector field that describes the curl or local spinning motion of a continuum flow with velocity $\mathbf{u}$, mathematically this is $\nabla \times \mathbf{u}$. Next, the post-shock fluid velocity slows causing the fluid to flow away from the shock normal plane and introducing fluid velocity components in the directions transverse to the shock propagation direction. The sketch of this phenomenon in Fig. 6.2 shows how the post-shock fluid deflects away from the shock's normal direction while moving along both sides of the interface in opposite directions. The vorticity

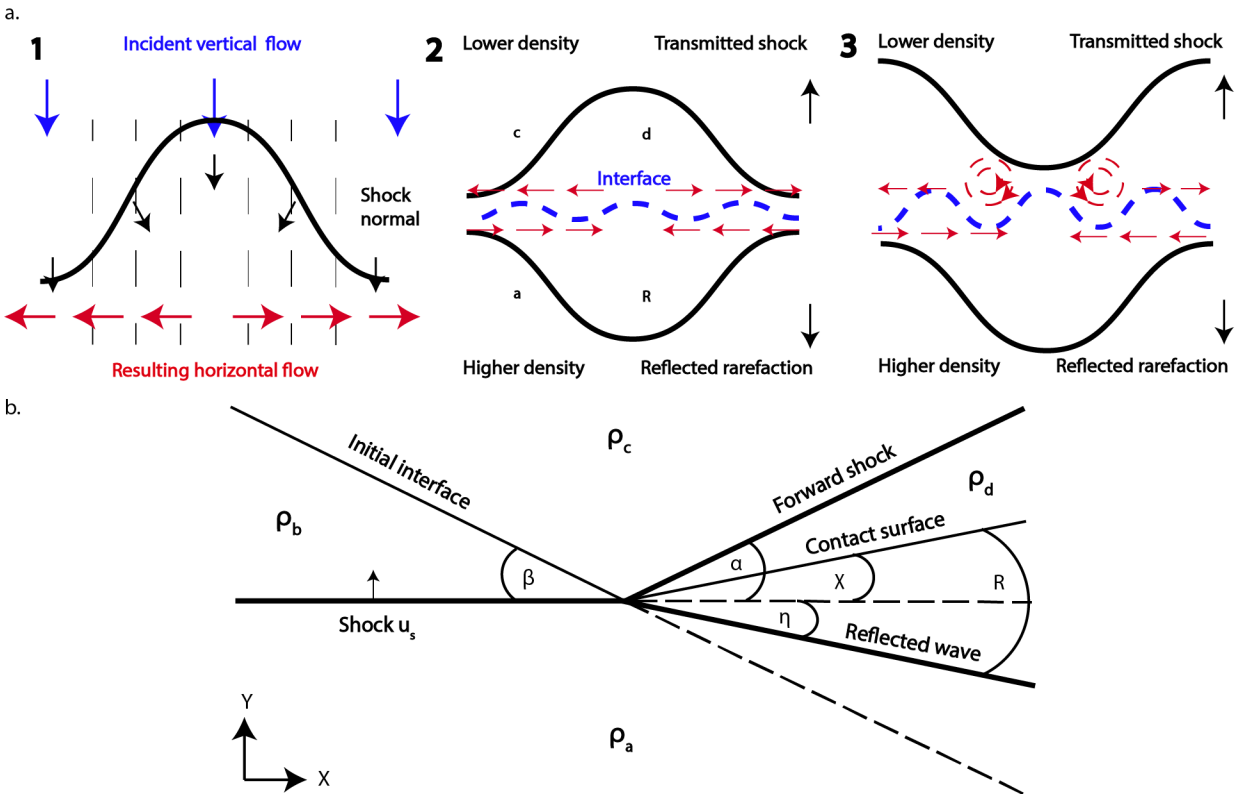

Figure 6.2: (a) Sketch of the Richtmyer-Meshkov process describing 1: deflection of post-shock fluid from shock normal, 2: introduction of vorticity at the interface, and 3: amplification of structure by the introduced vorticity (b) Sketch used for analyzing the behavior when an oblique shock encounters an interface using different components of the interaction. For convenience, η and β as shown are taken to be positive angles.

deposited in the post-shock fluid will reduce oscillations in the transmitted shock wave and grow small perturbations at the interface with time, thus amplifying any rippled structure present at the interface layer. This effect is also known as the *Richtmyer-Meshkov* (RM) process and has been studied previously [139, 176, 177, 188]. So long as the shock does not happen to be flat when it encounters the interface it will deposit vorticity at the interface and amplify any structure present.

Within this context, the evolution of a hydrodynamic instability captured with the betatron X-rays is shown in Fig. 6.3. The time-series shows a process that resembles the RM instability, in the sense that a strong shock crosses a rippled interface, the interface moves forward, and after the passage of the shock very distinctive ripples develop. A 3D hydrodynamic simulation was also performed in FLASH, in which a sinusoidal instability was imposed on the cylindrical jet radius, which later in time developed into a larger structure. The simulation and experimental measurements are not particularly the same, as it is expected. However, in both scenarios, the RM behavior is captured.

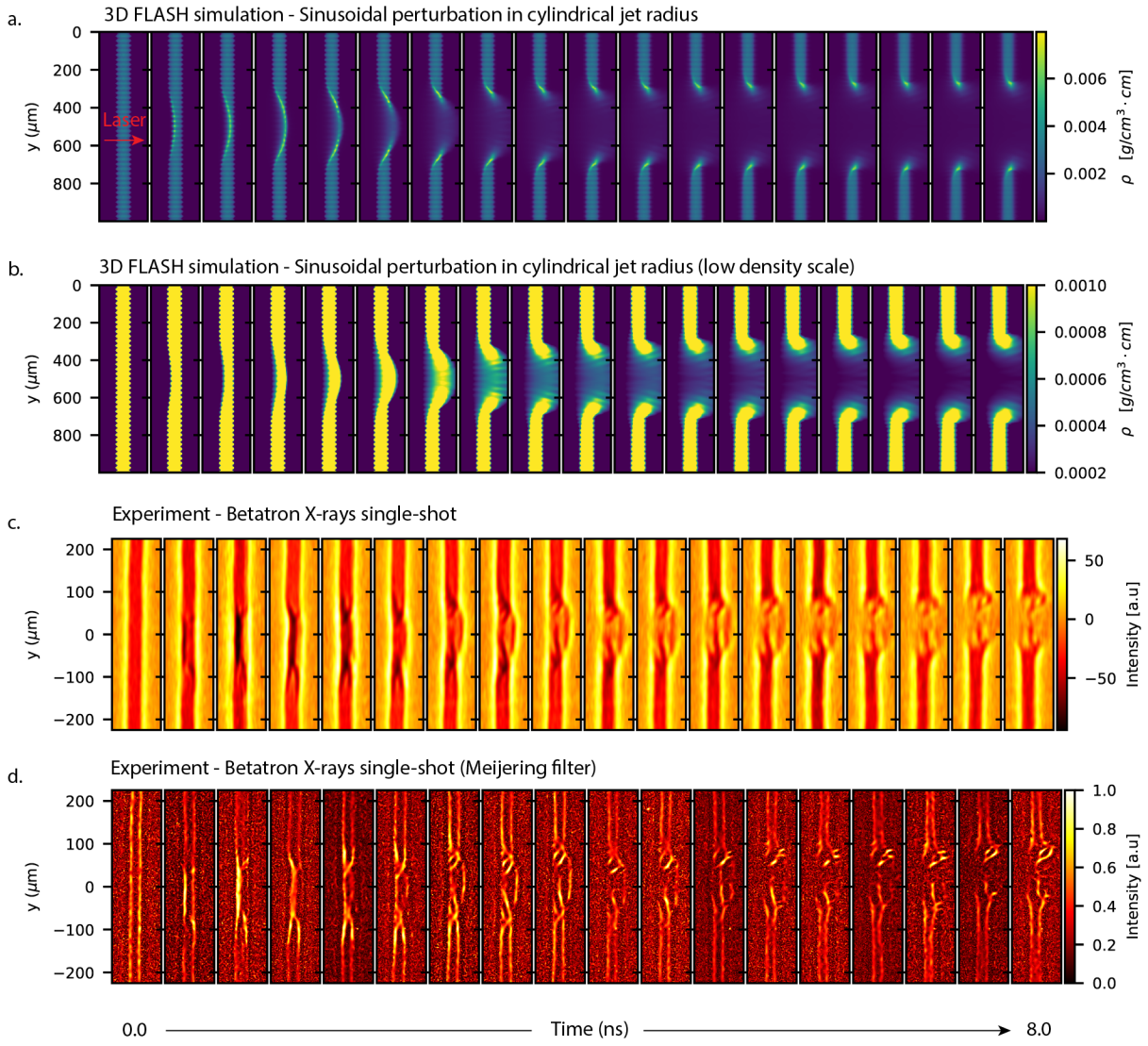

Figure 6.3: (a) Projected density from 3D FLASH simulation. A sinusoidal perturbation was introduced to the radius of the cylindrical water target to observe the evolution of the Richtmyer-Meshkov process. (b) The amplification of the perturbation structure can be observed in the simulations at lower densities. (c) Time delay scan of laser-water interaction captured experimentally using single-shot betatron X-ray imaging. The shock proceeds from left to right, resulting in the displacement of the back interface and subsequent instability formation, displaying the evolution of the Richtmyer-Meshkov process.

We can estimate how rapidly the modulations at the interface should grow using the equations for an oblique shock encountering an interface with a density decrease. Typically, a shock encountering an interface where the density decreases will produce a transmitted shock and a reflected rarefaction. Nevertheless, from our results in the previous section, we observed that the back surface of the target is also being compressed by pressure from 3D electron heat transport, thus we believe it is more reasonable to treat our description of the interface behavior *as if* a shock was reflected. Following texts by Landau [98] and Drake [42] on oblique shocks meeting interfaces, we will analyze the system by labeling shocked and unshocked regions with subscripts a, b, c, and d, and the region between the contact surface and the *reflected* wave as R as shown in Fig. 6.2. In this diagram, α indicates the angle between the initial shock normal and the transmitted shock front, β denotes the angle between the initial shock normal and the plane of the local interface, χ is the angle between the initial shock normal and the moving interface, and η represents the angle between the initial shock normal and the reflected wavefront. For simplification purposes, we will assume that the shock is driven by a constant pressure source and thus each of the waves has a constant velocity. Similarly, the entropy is assumed to be constant across all of the regions changing only at the shocks. To analyze the post-shock interface behavior this system can be thought of as stationary using cylindrical coordinates centered at the point where the shock meets the interface. Then a point on the shock moves radially inwards with time and a point on the reflected wave moves radially outwards as shown in Fig. 6.2. In this frame of reference, we also assume that u_z is constant everywhere ($du_z/dt = 0 = du_r/dt$) and the angle ϕ is defined relative to the x-axis. In this case, the momentum and continuity equations read

$$\begin{aligned} \frac{\partial u_r}{\partial \phi} - u_\phi &= 0 \ , \\ u_\phi \frac{\partial u_\phi}{\partial \phi} + u_r u_\phi &= -\frac{1}{\rho}\frac{\partial p}{\partial \phi} \ , \\ \left(u_r + \frac{\partial u_\phi}{\partial \phi}\right) + \frac{u_\phi}{\rho}\frac{\partial \rho}{\partial \phi} &\ . \end{aligned} \tag{6.1}$$

These equations can be combined and simplified to expressions for fluid velocities at each of the regions a, b, c, d, R and the solutions can then be translated to the lab frame of reference. In our case we are particularly interested in describing the effects on regions d and R, denoting the fluid at both sides of the interface. The lateral deviation of the flow can be described as the x-component in the velocity vectors u_d and u_R, which in the lab frame of reference and approximated for small angles are given by,

$$u_{d,\text{lab}} = \frac{-2\beta}{(\gamma+1)} u_s \left[\frac{\alpha}{\beta}\left(1+\frac{\alpha}{\beta}\right)\right]\hat{x} + \frac{2}{(\gamma+1)} u_s \left[1+\frac{\alpha}{\beta}\right]\hat{y} \ , \tag{6.2}$$

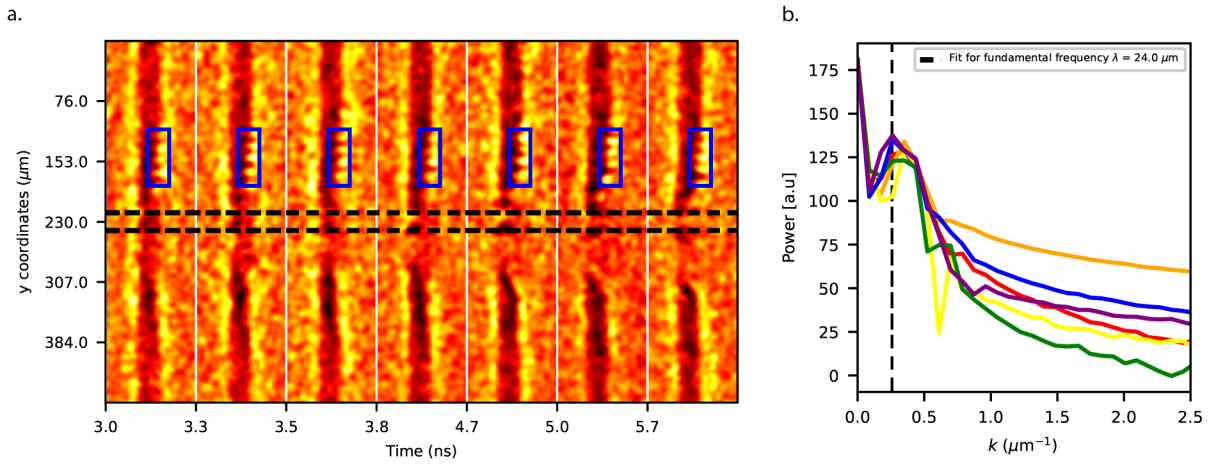

Figure 6.4: (a) Phase-contrast X-ray images of hydrodynamic instability (average of 5 shots per time-step) at $3 < t < 6$ ns. (b) The wavelength of the perturbations is relatively constant and recovered through Fourier analysis.

$$u_{R,\text{lab}} = \frac{2\beta}{(\gamma+1)^2} u_s \left[\frac{\eta}{\beta}\left((\gamma-1)+\frac{\eta}{\beta}(\gamma+1)\right)\right]\hat{x} + \frac{u_s}{(\gamma+1)^2}\left[4\gamma - 2\frac{\eta}{\beta}(\gamma+1)\right]\hat{y}\ . \tag{6.3}$$

We can then approximate the growth rate due to the RM process from the point of view that the increase in ripple amplitude is caused by the inward flow of material from the center toward the sides. Therefore, assuming the counter-propagating shock u_R deposits vorticity, and assuming small angles, $\eta = kL$ and $\eta/\beta \sim 0.9$ (typical for reflected shocks), then we obtain a perpendicular flow velocity,

$$u_\perp \approx \frac{3.4\gamma}{(\gamma+1)^2} k u_s x_{ps}\ , \tag{6.4}$$

and thus a growth rate is given by,

$$\frac{d}{dt}x_0 = \frac{1.7\gamma}{(\gamma+1)} k u_{ps} x_{ps}\ . \tag{6.5}$$

This implies that the ripples in the interface grow with time at a rate linearly proportional to the initial ripple amplitude x_0, wave-number k, and post-shock interface velocity u_{ps} in the lab frame. These features are also present in the formula described by Richtmyer [139], $\mathrm{d}x_0/\mathrm{dt} = kA^* u_{ps} x_{ps}$ which, in contrast, includes A^* the interface post-shock Atwood number. Therefore, by finding k, u_{ps}, and x_0 we can utilize Eq. 6.5 to calculate an expected growth rate for the interface perturbations and compare it to a growth rate obtained experimentally.

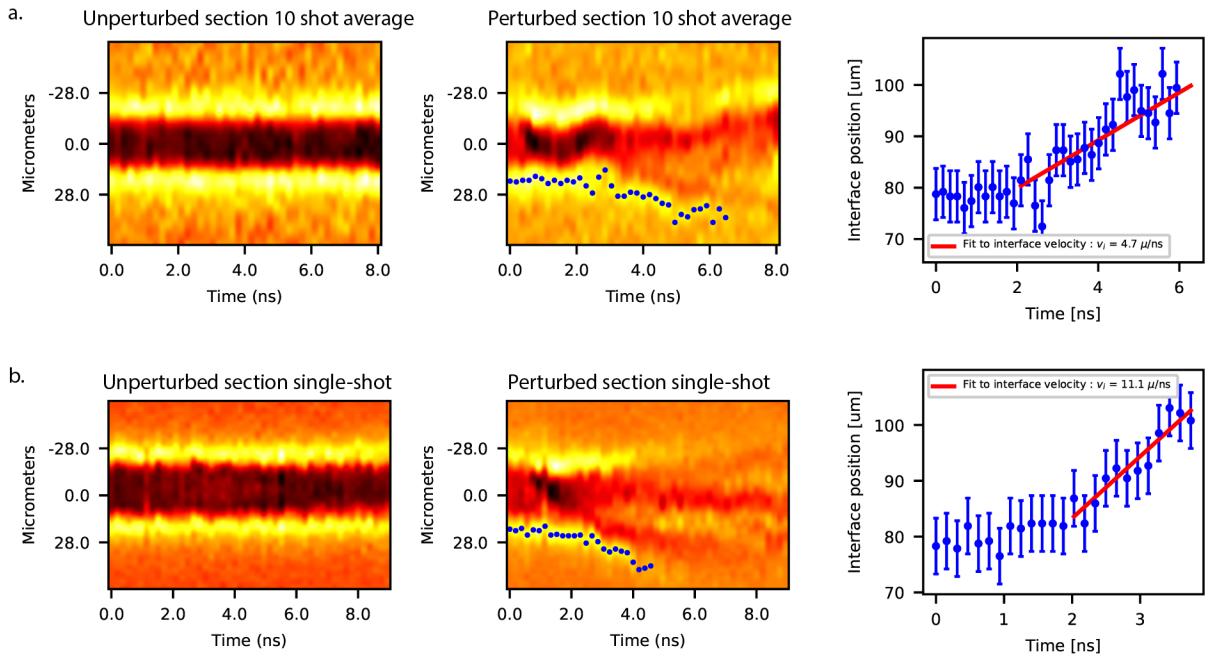

Figure 6.5: (a) Stack of line-outs through the center of experimental images (10 shot average). (b) Stack of line-outs through the center of experimental images (single-shot). Left: unperturbed section of the jet. Middle: perturbed center section of the jet. Right: fit to interface displacement velocity.

First, to obtain the wave number $k = 2\pi/\lambda$, the wavelength of the perturbations was recovered by performing Fourier analysis on the region enclosing the ripples found in the image observed with the betatron X-rays. Fig. 6.4 shows the results of the Fourier analysis indicating that $\lambda \sim 15$ μm.

Next, the post-shock velocity of the interface was obtained by taking a line-out through the center of the X-ray images at each time-step. In this case, we have stacked the line-outs next to each other in Fig. 6.5 to reveal the movement of the interface with time. The figure shows that at $t \sim 2.5$ ns the liquid-vacuum interface at the back of the target expands and moves forward with a velocity of $u_{ps} \sim 7$ μm/ns. The movement of the interface in the back side of the target is a consequence of the shock crossing the interface and therefore the interface moves in the laser propagation direction.

Finally, assuming an initial perturbation amplitude of size $x_{ps} = 1 - 3$ μm and using Eq. 6.5, we obtain a theoretically estimated growth rate to be,

$$\frac{d}{dt}a_0 = 2 - 20 \quad \mu\text{m/ns} \tag{6.6}$$

We can similarly obtain a growth rate experimentally, by analyzing how the amplitude grows in time for each peak in the rippled structure. This analysis is also plotted in Fig. 6.6, resulting in an experimental growth rate of $d/dt(a_0) \approx 10 - 20\mu$m/ns, which agrees very well with the analytical approximation.

6.3 Discussion

The exploration of plasma instabilities through the lens of high-resolution betatron X-ray imaging brings new possibilities of understanding within the realm of HEDP. This section provided the first-of-its-kind measurement of the Richtmyer-Meshkov-like plasma instabilities with unprecedented spatio-temporal resolution using a laser wakefield-based radiation source. At first sight, the observed waves present many mysteries including defined wavelengths, asymmetries, and complex structures. Multiple phenomena could be responsible for developing such structures, not only including the Richtmyer-Meshkov process but also the Rayleigh-Taylor or Kelvin-Helmholtz instabilities initially are potential candidates. The conclusions drawn in this chapter are based on the idea that the instabilities observed with the X-rays are primarily shock-driven and intrinsic to the interface between the liquid water and vacuum.

First, the RT instability is a phenomenon that materializes at the interface of two fluids of different densities—precisely the scenario characterizing this experimental setup. Two conceivable alternatives are possible at this interface; either the lighter fluid exerts force on the denser fluid,

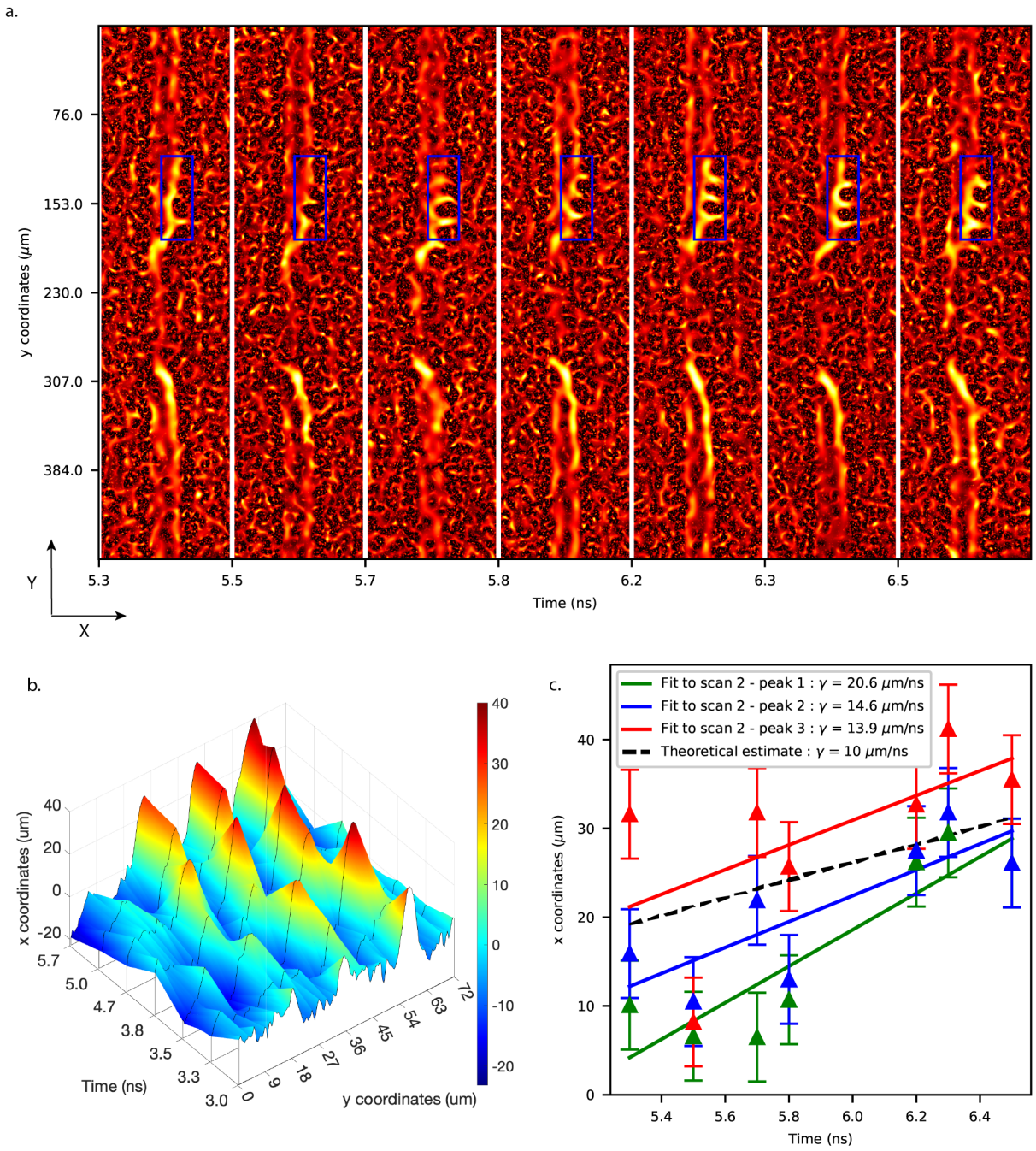

Figure 6.6: (a) Phase-contrast X-ray images (10 shot average) displayed with Meijering filter [120] showing a clear growth of the fluid perturbations' amplitude through the RM process. (b) 3D waterfall plot showing ripple magnitude growth with time. (c) Plot of experimentally calculated growth rate and comparison with the theoretical prediction.

establishing a stable equilibrium (e.g. the atmospheric air on top of the ocean's surface), or the heavier fluid imposes its force upon the lighter one, triggering the unstable process of Rayleigh-Taylor. When considering the case of the laser-water interaction at later phases, the conditions in the region of interest are those remaining from the aftermath of an adiabatic plasma expansion. During such a process, the expansion of the hot plasma exerts a force on the target surface similar to the rocket effect. This process is responsible for generating the hydrodynamic shocks observed in Chapter 5, however in this configuration, the low-density plasma fluid is exerting a force on the dense plasma core and not the opposite, hindering the likelihood of the RT instability developing at the surface.

Alternatively, the KH instability is based on the shear between two fluids of different densities which move in opposite directions. Even though fluids of different densities are certainly present at the interface (liquid water and vapor) their fluid velocities are practically negligible for the timescales captured with the X-rays. For instance, the liquid jet moves at a velocity of $u \approx 40$ m/s, which translates to a total displacement of only approximately 4 μm over the course of 10 ns. Given the fact that the observed perturbations in Fig. 6.6 cover a total distance in the order of tens of microns, it is unlikely that the fluids would have moved sufficiently fast from their own initial velocity to produce sufficient shear triggering the KH unstable processes.

Given the ultrashort timescales in which these plasma instabilities arise, other more exotic phenomena involving electron fluids-based KH processes have been theorized to explain the measurements presented in this chapter. In this scenario, some of the asymmetries observed are explained by introducing the fact that one of the ends of the water jet is connected to ground, while the other end is open-ended. If this is the case, strong positive fields near the interaction region could quickly generate a current running through the interface of the target. These innovative ideas while interesting and possible, but would require more involved hybrid simulation methods. Before venturing into the realm of charged-particle-based instabilities, this chapter has considered a simpler alternative that could be triggering such hydrodynamic phenomena and be responsible for the growth of the perturbations, such as the Richtmyer-Meshkov process.

The argument presented in this chapter is primarily based on pointing out the fact that the rippled structures grow soon after the shock crosses the interface. The RM process involves a non-ideal shock and/or a non-ideal interface. Both of these conditions are true in the experimental setup. Furthermore, based on the X-ray measurements it is certainly apparent that vorticity, to less or more extent, has been introduced into the fluid after the shock. Furthermore, the RM process predicts a moving interface triggering the growth of existing disturbances. In this sense, the analysis displayed in Fig. 6.5 of this chapter evidenced a clear displacement of the back liquid-vacuum interface after the crossing of the shock. The fact that the liquid water jet is inherently an unstable medium with minute disturbances present at all times and multiple wavelengths further

suggests that the RM process is likely to develop.

One important consideration in this argument is the initial seed of the instability which is an essential element in any perturbation theory. As previously mentioned, the water jet cylinder is inherently an unstable medium, so multiple minute waves run through its surface produced from a variety of environmental conditions including but not limited to, the evaporation at its surface, supersonic vapor emanating from the jet catcher, small vibrations in the chamber from the vacuum pumps, or most importantly, its interaction with a multitude of lasers. Not only is the shock driver laser interacting with the water jet, but also is the underlying kHz alignment laser which is of order mJ in energy and always present, as well the LWFA driver laser and its own kHz alignment laser. The variety of lasers involved in the experimental setup make them likely candidates to serve as a seed for plasma instabilities.

This consideration opens the door to a new avenue of investigation - the electromagnetic fields that are generated during the high-energy-density conditions from pressure gradients, and their potential influence on the overall interplay between shocks, plasmas, and the laser fields themselves. Certainly, for the interaction of high-intensity lasers and matter the presence of magnetic and electric fields is guaranteed. Nevertheless, while the photons from the betatron X-ray diagnostic that has been used thus far offer phenomenal imaging resolution, they are not sensitive to the presence of these fields. If any electromagnetic fields have an influence on the dense plasma their effect could be observed by the X-rays, but the mechanism and magnitude of the fields would be entirely missed. With the purpose of looking at the plasma dynamics from a completely different perspective, the next and final experimental chapter is focused on the probing of laser-generated electromagnetic fields using the relativistic electron beam as a probe.

CHAPTER 7

Relativistic Electron Beam Probing Using Laser Wakefield Accelerators

7.1 Introduction

The preceding chapters journeyed into the realm of high-resolution imaging using betatron X-rays, capturing ultrafast snapshots of matter under extreme conditions within the domain of HEDP. These images, although enlightening, are bound by the inherent limitations of photons. These imaging techniques primarily depend upon the deflection of X-rays by density gradients in the target sample, thereby revealing hydrodynamic shocks in regions with sharp density gradients and high pressures. While X-ray diagnostics serve as indispensable tools for imaging dense media, they often obscure the underlying electromagnetic fields that might be crucial to our understanding. This chapter is more than an exploration, it is a transformation of perspective.

It is universally acknowledged that in any laser-matter interaction within high-energy-density regimes, electric and magnetic fields emerge as intrinsic companions. The magnitude and topology of these fields varies depending on the experimental configuration, but their presence is ubiquitous. In the previous chapter it is hypothesized that some generated fields might potentially feed back into the hydrodynamic interactions and influence their behavior triggering instabilities. The degree at which electromagnetic fields could influence the plasma dynamics is not clearly defined, but their influence is guaranteed. Importantly, conventional radiation hydrodynamic simulations often fail to account for the charge separation between electrons and ions, a void that prevents a holistic portrayal of the interactions where magnetic fields may emerge and wield a significant influence. The pulse of innovation echoes loudly in the technique's core premise: the conversion of relativistic electron beams into field probes, unveiling an alternative perspective that goes beyond the scope of traditional X-ray photons. These beams respond to the fields they traverse, becoming living witnesses to electromagnetic phenomena.

The electromagnetic fields that orchestrate these intricate interactions might hold the key to unraveling their mysteries, yet they have remained largely elusive to direct observation. This chapter

embarks on a transformative direction of probing matter under extreme conditions, spotlighting an emerging technique that leverages the power of laser wakefield acceleration to use relativistic electron beams as dynamic probes for radiographic measurements of electromagnetic fields during HED encounters. As discussed in Section 3.4.3, any generated fields will have the effect of deflecting the trajectories of the electrons by a certain angle that depends on both the electron beam energy and the field magnitude as well as direction. Some previous measurements have been performed using LWFA electrons as a probe [149, 180, 191, 190], yet many of these do not capture the evolution of fields in time, and in some instances an estimation for the field magnitudes is not possible.

The investigation in this chapter once again revolves around the interaction of a long laser pulse with a water jet target, except from a completely different perspective that allow capturing nuances and intricacies inaccessible to their photon counterparts. Our journey unfolds through probing three distinct laser energy deposition regimes—low, medium, and high deposition. In each of these regimes, the relativistic electron beams traverse the interaction zones, capturing the electromagnetic signatures imprinted upon them. Subsequent analyses determine the magnitudes and orientations of these fields, emphasizing the stark difference between conventional focusing fields and robust fields that, while initially appearing defocusing, in truth exert an over-focusing influence. The transition between focusing and over-focusing regimes is captured as both, energy-dependent and time-dependent measurements of the fields. These measurements provide a fresh lens through which to diagnose the tapestry of high-energy-density interactions.

7.2 Experiment

The experimental investigations were conducted at the LBNL BELLA Center, where the HTW dual beam laser system (20–30 TW, $\lambda_0 = 800$ nm) played a dual role in driving the laser wakefield accelerator and generating the shock wave within the liquid target (depicted in Fig. 7.1). The intensity of the LWFA driver was in the order of $I \sim 10^{18}$ W/cm^2, while the intensity of the shock driver arm is in the order $I \sim 10^{14}$ W/cm^2. The short high intensity pulse was focused into a gas target [192] thus driving a wakefield and producing a relativistic electron beam. The electron beam obtained during this campaign had a mean energy of 137.9 ± 35.8 MeV with 128.7 ± 54.2 pC of charge, and a mean FWHM divergence of 5.7 ± 1.1 mrad. The electron beam was characterized with a beam profile monitor as well as with a magnetic spectrometer.

The beam profile monitor consists of a Phosphorous scintillating screen located at $z \approx 156$ cm from the gas jet nozzle. The screen is imaged onto a camera which records the light emitted from the phosphorous in the form an image of the electron beam transverse profile. For the magnetic spectrometer diagnostic a dipole electromagnet deflects the electron beam into a series of lanex

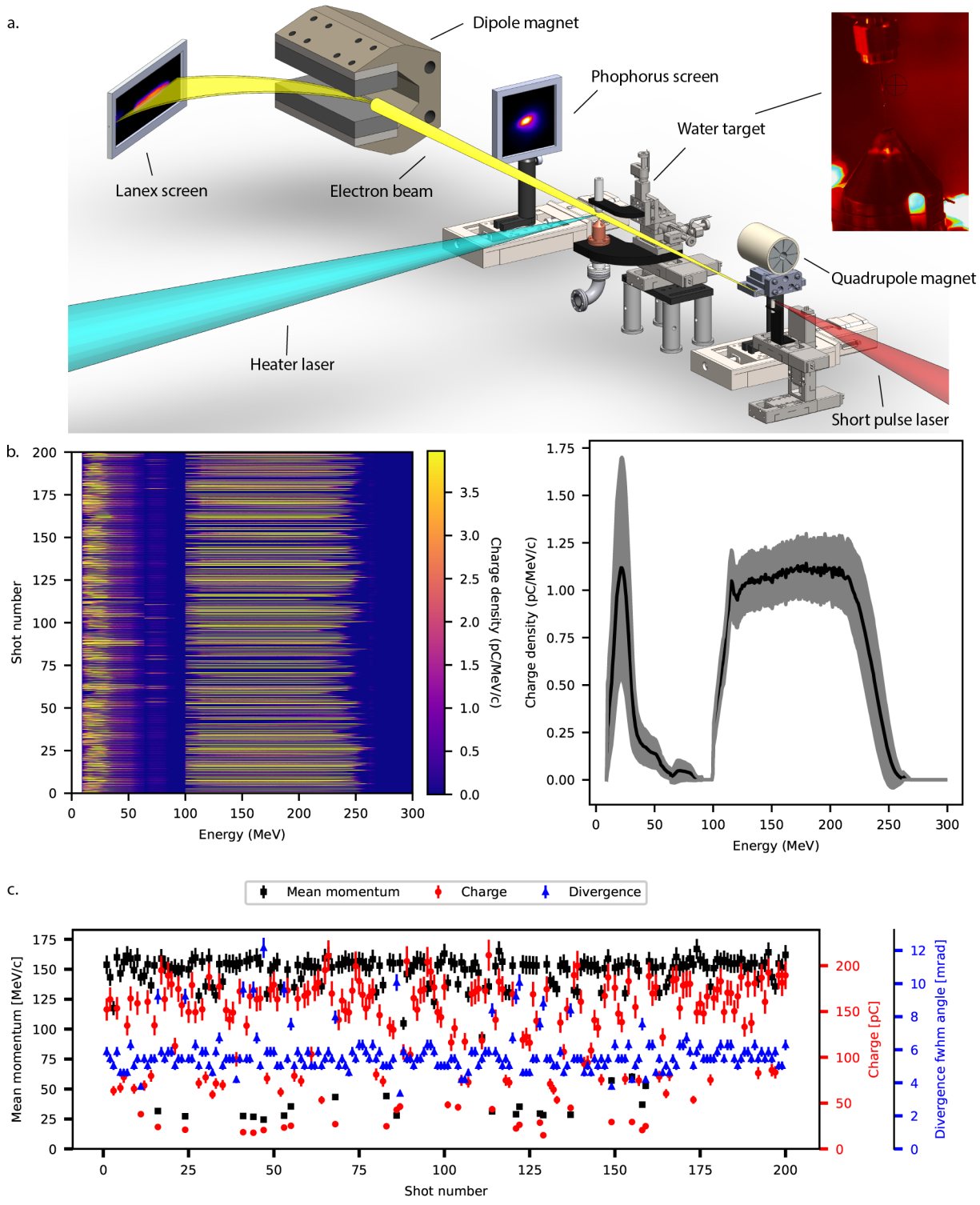

Figure 7.1: (a) Experimental setup for relativistic electron beam probing of dynamic electromagnetic fields using an LWFA. (b) Electron beam characterization showing its spectrum and charge density for 200 consecutive shots. The mean momentum is plotted as well as its standard deviation. (c) Scatter plot for the beam characteristics including mean momentum, charge, and divergence.

screens and, by doing so, differentiate the particles based on their momentum [125]. Less energetic particles will be deflected more by the imposed magnetic field, while higher energy particles will have a smaller deflection orbit. Through calibration of the trajectories with respect to the dipole field the electron beam spectrum was recovered successfully (Fig. 7.1).

The shock driver laser (200 ps) on the other hand, was obtained through the division of the main BELLA HTW beam. Typically, the secondary arm of the system is similarly amplified (1.2 ± 0.2 J) and compressed through chirped-pulse-amplification. Nevertheless, for this experimental configuration the desired shock driver laser has a long duration in time depositing its energy over 200 ps. In order to obtain the long pulse the compressor was bypassed after amplification of the secondary beam. This long pulse was perpendicularly focused onto the water target plane, having a FWHM spot size of $w_0 = 40 \pm 10$ μm. A flexible delay line furnished meticulous temporal synchronization of the long pulse with respect to the LWFA electron beam probe, permitting timing adjustments within the interaction of order tens of femtoseconds.

Notably, since the field recovery analysis technique described in Chapter 3 is highly sensitive to the *unperturbed* beam profile, the electron probe was optimized for improved stability and consistency before interacting with the high-energy-density fields. Additionally, the shock driver laser pulse's focal spot at the water jet plane was meticulously optimized, and its centroid constantly tracked along the delay line to secure the desired interaction with the target.

To enrich the empirical findings, 3D FLASH simulations (see FLASH simulations in Chapter 3) have been performed in order to observe the type of fields that radiation hydrodynamic codes predict for the interaction. The fields derived from the hydrodynamic simulations are then compared to those recovered from the measurements. Additionally, a synthetic electron beam radiography algorithm was employed to simulate the interaction of a fictitious relativistic electron beam with the fields obtained from FLASH.

7.3 Results & Simulations

The results consist of different datasets of electron radiography images taken using the LWFA relativistic electron beam as a probe. The charged-particle beam captured the evolution of electromagnetic fields generated during the laser-water interaction as a function of time. Multiple time-series were obtained, which primarily vary on the laser energy that was used for the shock driver laser.

The electron radiography images were analyzed with the iterative algorithm described in Chapter 3 in order to reconstruct the magnitude and direction of the fields that are captured. The first step in the analysis of the electron beam radiography images is the removal of the background; in other words, predict to some accuracy how the *unperturbed* electron beam I_0 looks like. This

is imperative for the application of the iterative algorithm in order to recover the magnitude and direction of the fields. In this sense, the reconstruction of I_0 does not follow a straightforward unique method, but rather it depends on different techniques which might lead to better or worse results depending on the dataset in question.

As it will be shown in this section, the background removal procedure needs to be adapted to match the measurements as best as possible. Fig. 7.2 displays an example measurement of electromagnetic fields captured with the electron beam probe, denoted as I *original*, as well the first-order technique to recover the unperturbed beam I_0. The method consists on first masking out the region where the fields are present in the measured image. Next, a low-pass filter is applied in Fourier space to the original image in order to obtain an initial approximation of I_0. Using this initial approximation an inverse mask is applied to set up apart the section where the fields reside. Both of these masked images are then blended together to obtain a prediction for I_0. The result is a blurred image in which the perturbations to the beam are smoothed out (see Fig. 7.2).

An important caveat with this method is that the blending should be done in such a way that the intensity of the signal is matched as closely as possible to the predicted background. One way of accomplishing this is by integrating the field-affected region before the mask and making sure that the substitute region has the same integral of intensity. This is a way of approximating charge conservation. The charge that is absent due to the fields must have moved in space to some other coordinates.

After the recovery of I_0 the calculation of any present electromagnetic fields proceeds following the method described in Sec 3.4.3. The iterative algorithm utilizes the original measured image as well as the predicted I_0 to obtain a resulting map of the deflection potential ϕ,

$$\nabla\phi = \boldsymbol{\alpha} \tag{7.1}$$

where $\boldsymbol{\alpha}$ are the deflection angles experienced by the relativistic electrons. Then, through the following relations,

$$\alpha_x = \frac{q}{\gamma m_e v_z^2}\int E_x dz \quad \text{or} \quad \alpha_x = \frac{q}{\gamma m_e v_z}\int B_y dz \tag{7.2}$$

$$\alpha_y = \frac{q}{\gamma m_e v_z^2}\int E_y dz \quad \text{or} \quad \alpha_y = \frac{q}{\gamma m_e v_z}\int B_x dz\ . \tag{7.3}$$

The electric or magnetic field can be reconstructed following the calculated deflection potential. Fig 7.3 shows an example of this field recovery calculation for the same example radiography image in Fig. 7.2.

Before venturing into discussing these fields in more detail, let us reiterate the fact that different

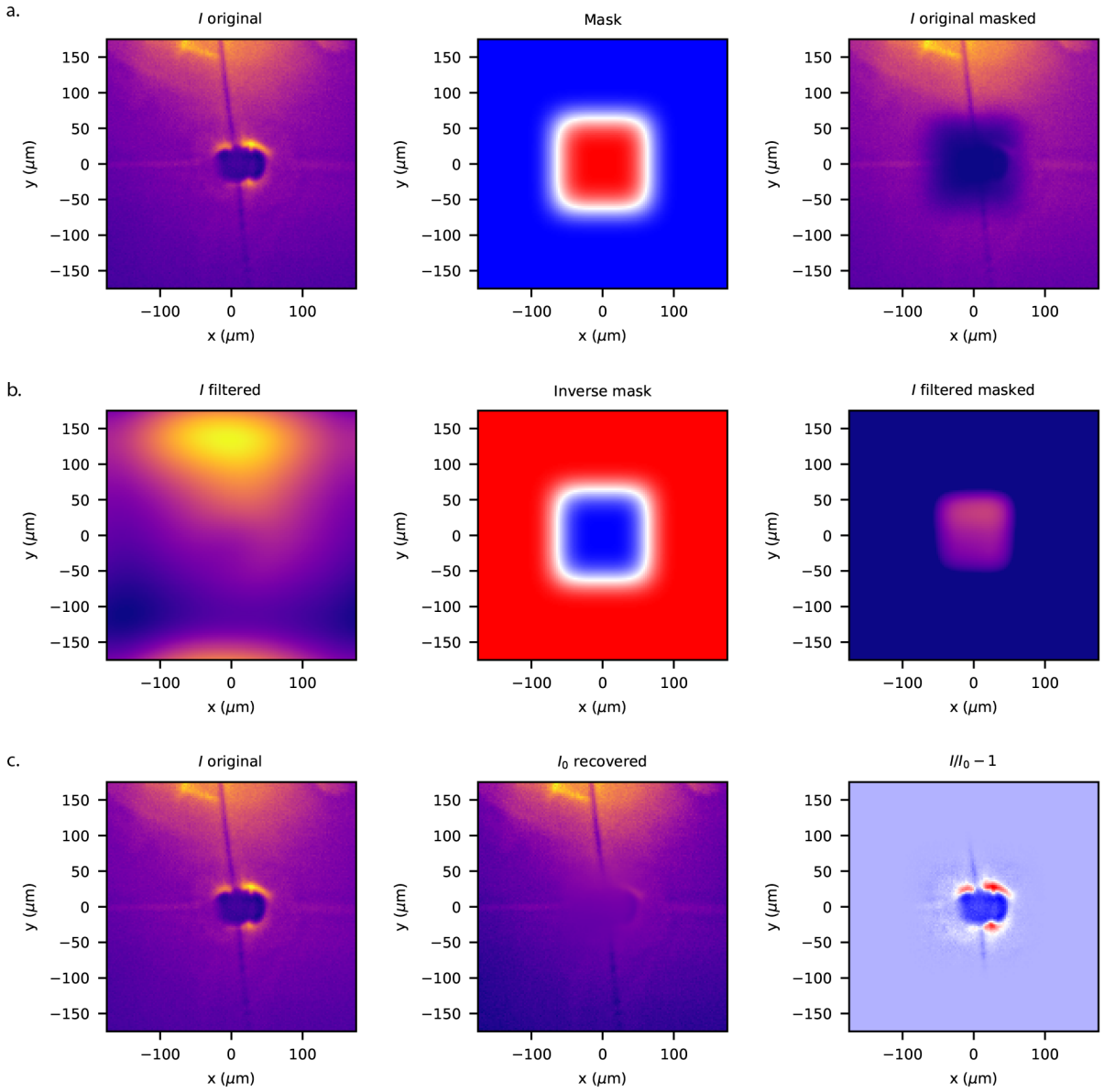

Figure 7.2: Workflow for background removal and approximation of unperturbed beam profile image I_0. (a) The original measured image is masked to remove the fields at the edges of a logical mask. (b) A low-pass filter is applied to the measured image to find an initial approximation for the unperturbed beam. The inverse of the mask is similarly applied to section out the region with the fields. (c) Both masked images are blended together to obtain a first-order approximation of the unperturbed beam I_0.

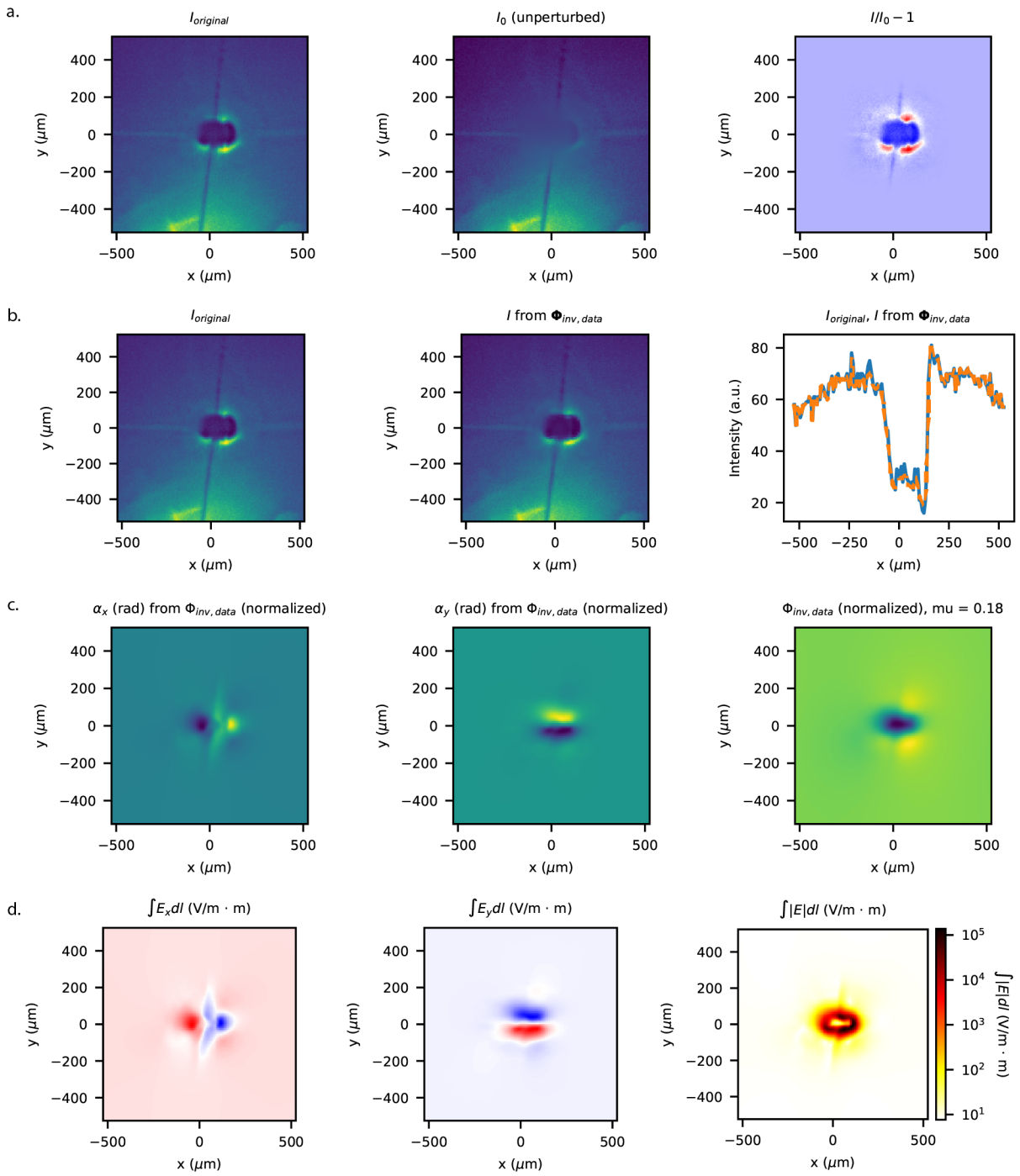

Figure 7.3: Workflow for the recovery of electromagnetic fields from an experimentally taken electron beam image ($\sim$ 1 J laser energy deposition). (a) Approximation of the unperturbed reference beam I_0. (b) Comparison between the original electron image and the image obtained from the reconstruction of the deflection potential field Φ. (c) Recovered potential field Φ as well as its gradients corresponding to the deflection angles α_x and α_y. (d) Electric field reconstruction from the deflection angles. The resulting deflection angles can be interpreted as either an electric or a magnetic field.

beam profiles and field configurations require an adaptation to the I_0 calculation process discussed above. When the fields are captured in a region away from the beam centroid then a simple filtered image might suffice to predict I_0. Nevertheless, for the kind of fields shown in Fig 7.4, Fig 7.5, and Fig 7.6, in which the electron beam is found rather centered on the perturbation (for the purpose repeatability), the background removal process to obtain I_0 is slightly more involved.

The adaptation to predict the unperturbed beam consists on precisely using a dataset of the electron beam profile without imposing a perturbation (no shock driver laser). In this sense, before imposing a field for the probe to go through and using the same experimental conditions, a dataseries (images) was taken to use as a reference stack for I_0. Following the background removal procedure of Fig. 7.2 the main difference consists on using a real unperturbed image that can be masked and blended, as opposed of using the same image with a Fourier filter. This technique can work better or worse than the Fourier filter approach, depending on how similar the chosen unperturbed image is to the perturbed image in question. In order to make a quantitative measurement of this discrepancy all the unperturbed images in the dataset stack were tested against the perturbed in image in question and the χ^2 difference between the images was calculated following

$$\chi^2 = \sum_i \left(S_{\text{predicted},i} - S_{\text{measured},i}\right)^2 . \tag{7.4}$$

This was done to better approximate the field-affected area based on how the surrounding beam looks like. The image that minimized χ^2 with respect to the perturbed image in question was chosen as the reference for I_0. An alternative approach would be to use all the images in the unperturbed data stack and calculate a mean that could be used for reference of I_0. Nevertheless, it was observed that using the mean of the images did not necessarily minimize χ^2. This modification of the background removal process was utilized to recover I_0 with acceptable accuracy in Fig. 7.4, Fig. 7.5, and Fig. 7.6. Each of these examples corresponds to a different regime in laser energy used on the heating laser, and each corresponds to a different regime of imaging for the electron beam probe. This variation in the way fields are imaged come accompanied by an adaptation to their background removal process in order to obtain an accurate representation of I_0 and therefore a more trustworthy recovery of the electromagnetic fields with this technique. Once a background removal and field recovery process is successfully tested for each electron beam imaging regime, their field evolution as a function of time can follow.

Before analyzing the recovered fields obtained from the measurements, it is certainly helpful to obtain a prediction from simulations for the kind of fields one might expect during the interaction. In this regard, 3D radiation hydrodynamic simulations were performed using FLASH (see Fig. 7.7), which allow the prediction of the expected density, temperature, and pressure distributions at these timescales, albeit using fluid equations. From these parameters it is possible to

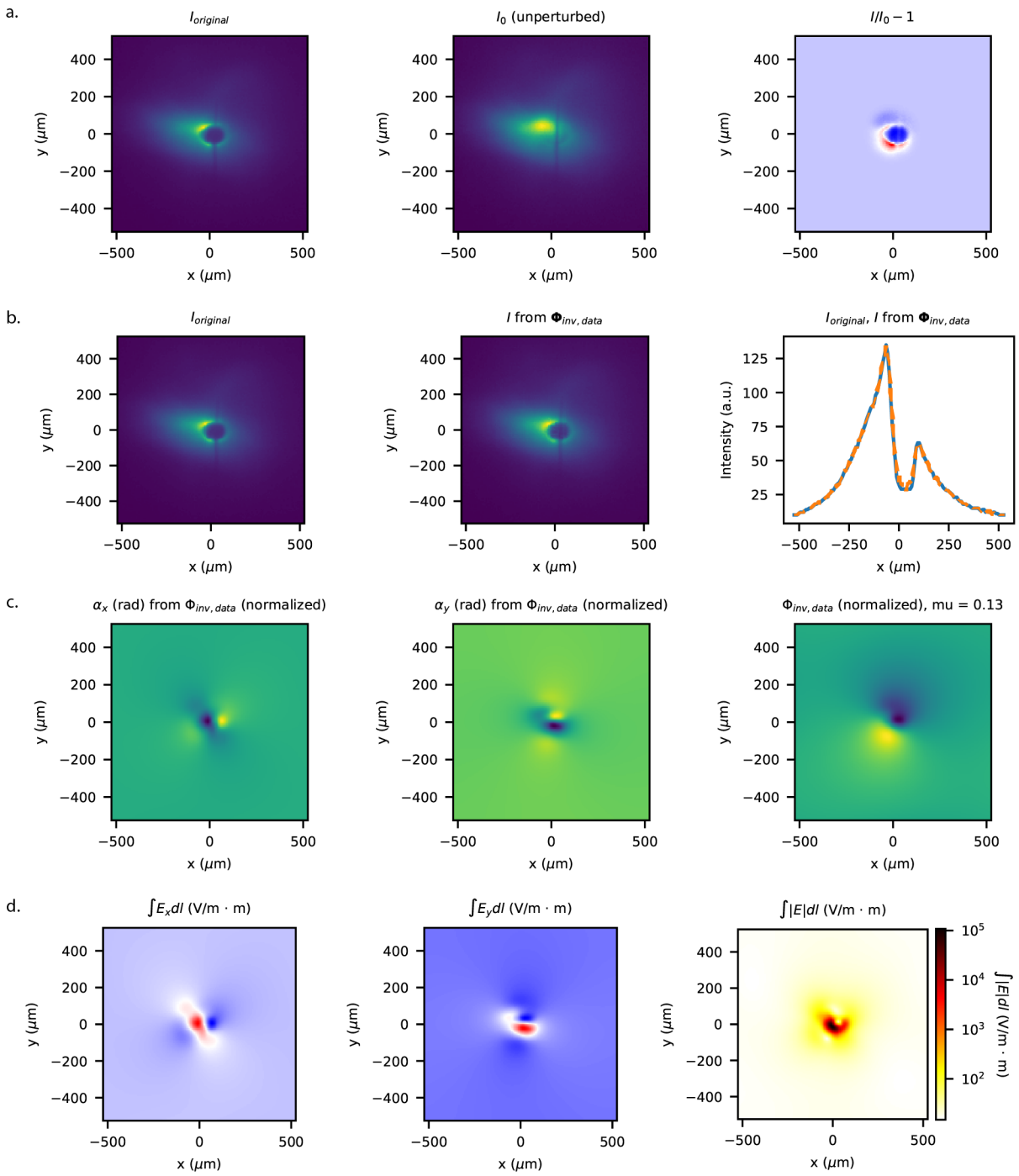

Figure 7.4: Workflow for the recovery of electromagnetic fields from an experimentally taken electron beam image ($\sim$ 0.5 J laser energy deposition). (a) Approximation of the unperturbed reference beam I_0. (b) Comparison between the original electron image and the image obtained from the reconstruction of the deflection potential field Φ. (c) Recovered potential field Φ as well as its gradients corresponding to the deflection angles α_x and α_y. (d) Electric field reconstruction from the deflection angles. The resulting deflection angles can be interpreted as either an electric or a magnetic field

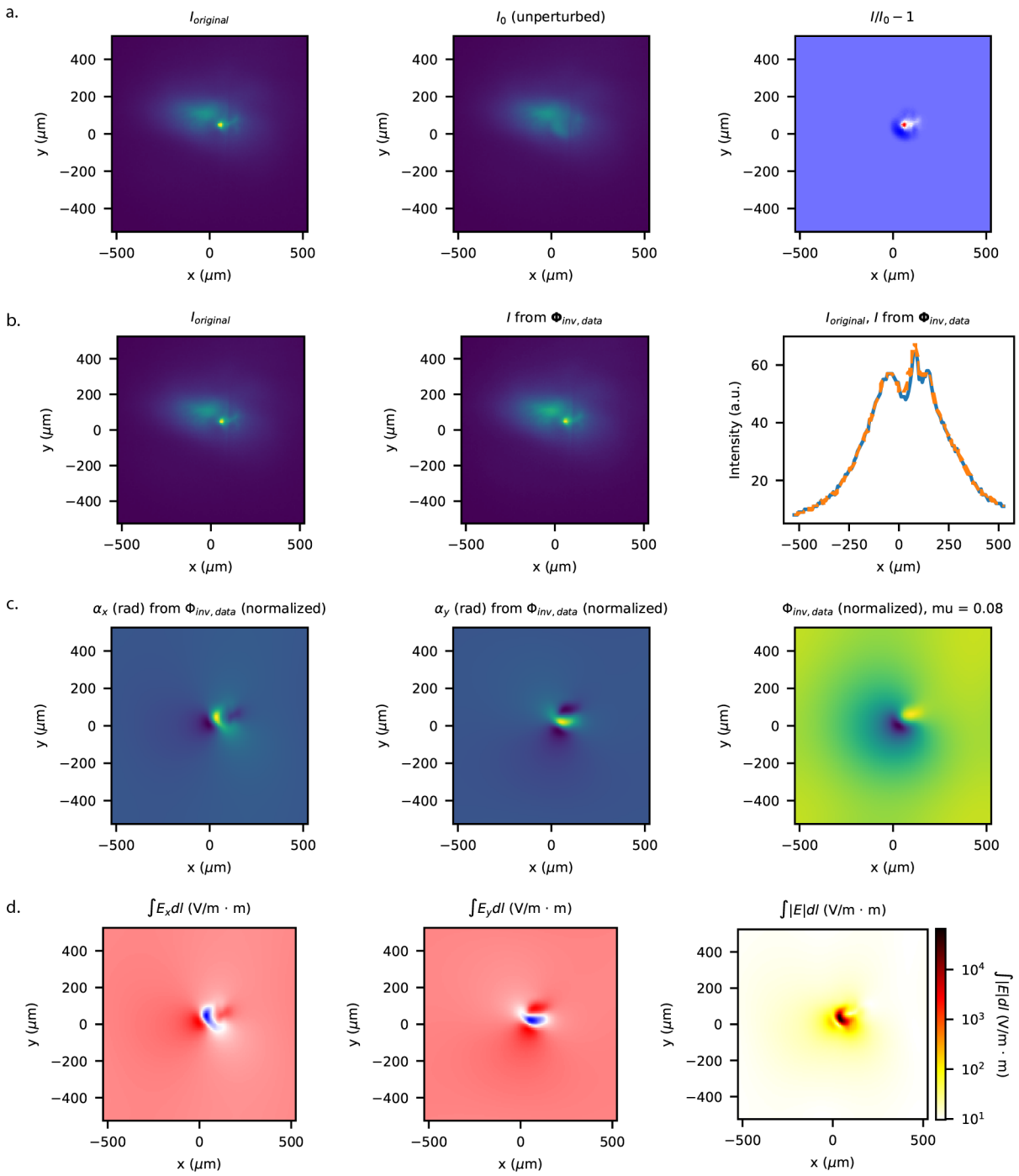

Figure 7.5: Workflow for the recovery of electromagnetic fields from an experimentally taken electron beam image ($\sim$ 0.1 J laser energy deposition). (a) Approximation of the unperturbed reference beam I_0. (b) Comparison between the original electron image and the image obtained from the reconstruction of the deflection potential field Φ. (c) Recovered potential field Φ as well as its gradients corresponding to the deflection angles α_x and α_y. (d) Electric field reconstruction from the deflection angles. The resulting deflection angles can be interpreted as either an electric or a magnetic field

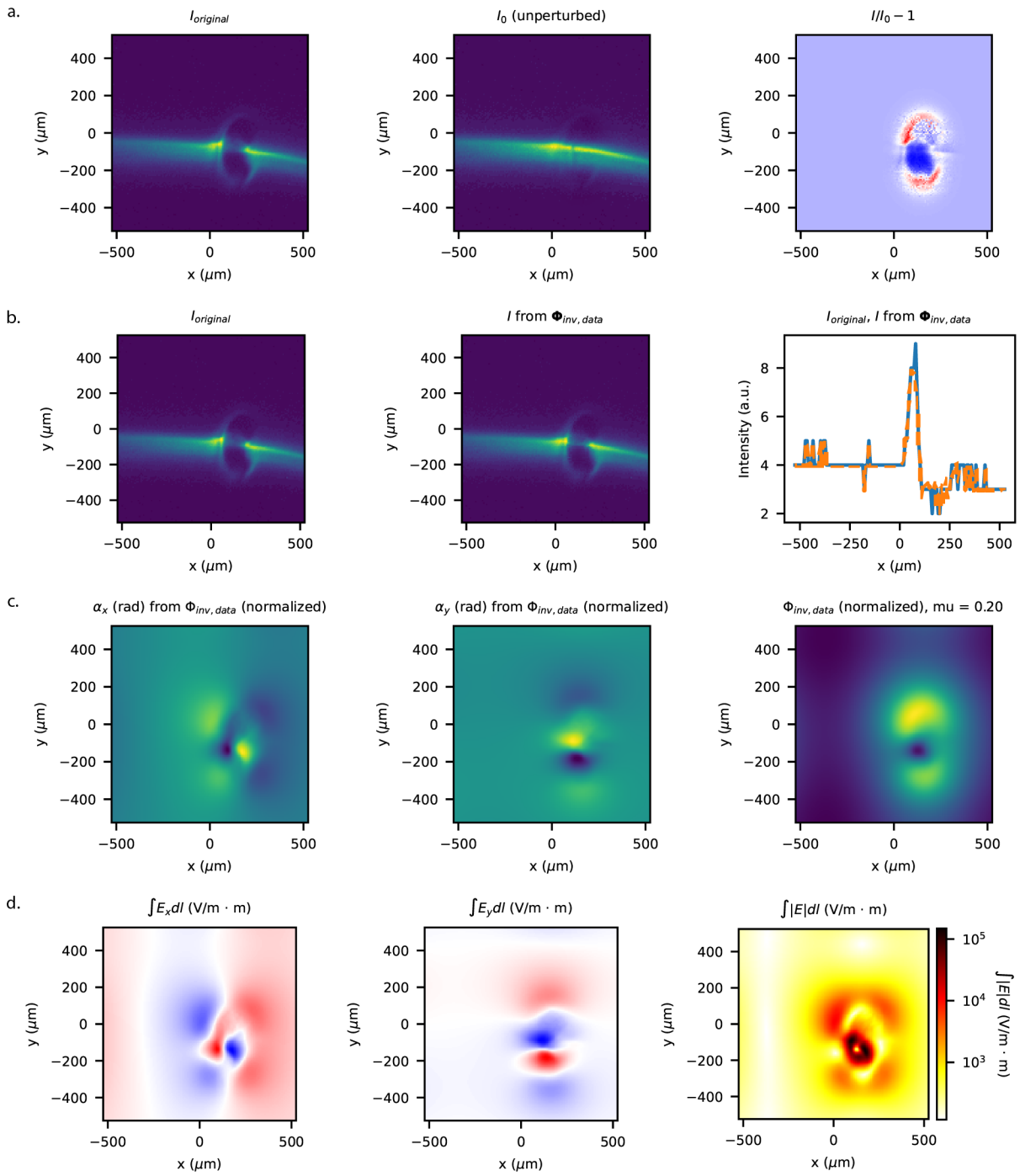

Figure 7.6: Workflow for the recovery of electromagnetic fields from an experimentally taken electron beam image ($\sim$ 0.5 J laser energy deposition with quadrupole). (a) Approximation of the unperturbed reference beam I_0. (b) Comparison between the original electron image and the image obtained from the reconstruction of the deflection potential field Φ. (c) Recovered potential field Φ as well as its gradients corresponding to the deflection angles α_x and α_y. (d) Electric field reconstruction from the deflection angles. The resulting deflection angles can be interpreted as either an electric or a magnetic field

calculate *derived fields* for the simulation results. Specifically, the generated electric field during the interaction was derived from the FLASH calculated pressure and number density following,

$$E = -\frac{\nabla p}{e n_e}. \tag{7.5}$$

By being 3D simulations, the fields are similarly calculated in all three dimensions. Nonetheless, the electron beam probing measurements are consistent with the deflection of particles due to path-integrated fields. In other words, the accumulation of field experienced by the electrons as they travel through the sample. For this purpose, the x and y components of the derived electric field displayed in Fig. 7.7 are projected fields. Finally, having calculated path-integrated fields from FLASH it is possible to combine them with a relativistic-electron deflectrometry code in order to produce synthetic electron beam radiographic images (see Fig. 7.7), that can later be directly compared with the measurements.

Following the laser-matter interaction, the FLASH simulations predict the expansion of low density plasma electrons heated by the laser, which creates a zone of high pressure gradients. The highest pressure point at the surface of the target is responsible for driving the hydrodynamic shock explored in Chapter 5. Following this topology, the simulations predict a strong focusing field that the electron beam will interact with.

Within this context, it is possible to examine the electron beam radiography measurements that were obtained during this experiment and compare them with simulation. Starting with Fig. 7.8, the time-series is obtained by probing the interaction of the long-pulse laser at low energies (~ 100 mJ) with the cylindrical water target. At this energy regime, the fields predicted by simulation are validated by the measurements not only in magnitude but also in direction. The recovered fields present a clear focusing effect on the electron beam probe as a result of the laser heating and ionization at the surface of the target, previously predicted by FLASH. The time-evolution can also be appreciated in the measurements, which clearly describe a field that quickly increases in magnitude and subsequently weakens and fades away with time.

Based on the preceding simulations and experimental measurements, one might expect that as the energy deposited by the laser increases, so does the magnitude of the focusing fields. The strength of the fields is directly dependent on the temperatures and pressure gradients that are present during the interaction, and having more energy available in the laser directly translates to higher energy-density conditions. Fig. 7.9 shows the time-series evolution of the laser-driven fields for an intermediate laser energy regime ($E_L \approx 500$ mJ). The experimental results obtained at this regime are immediately different than those previously measured for the focusing fields. To begin with, the relativistic electron beam probe appears to be increasingly defocusing with time, indicated by a void in the center of the beam that is continuously expanding. The recovered

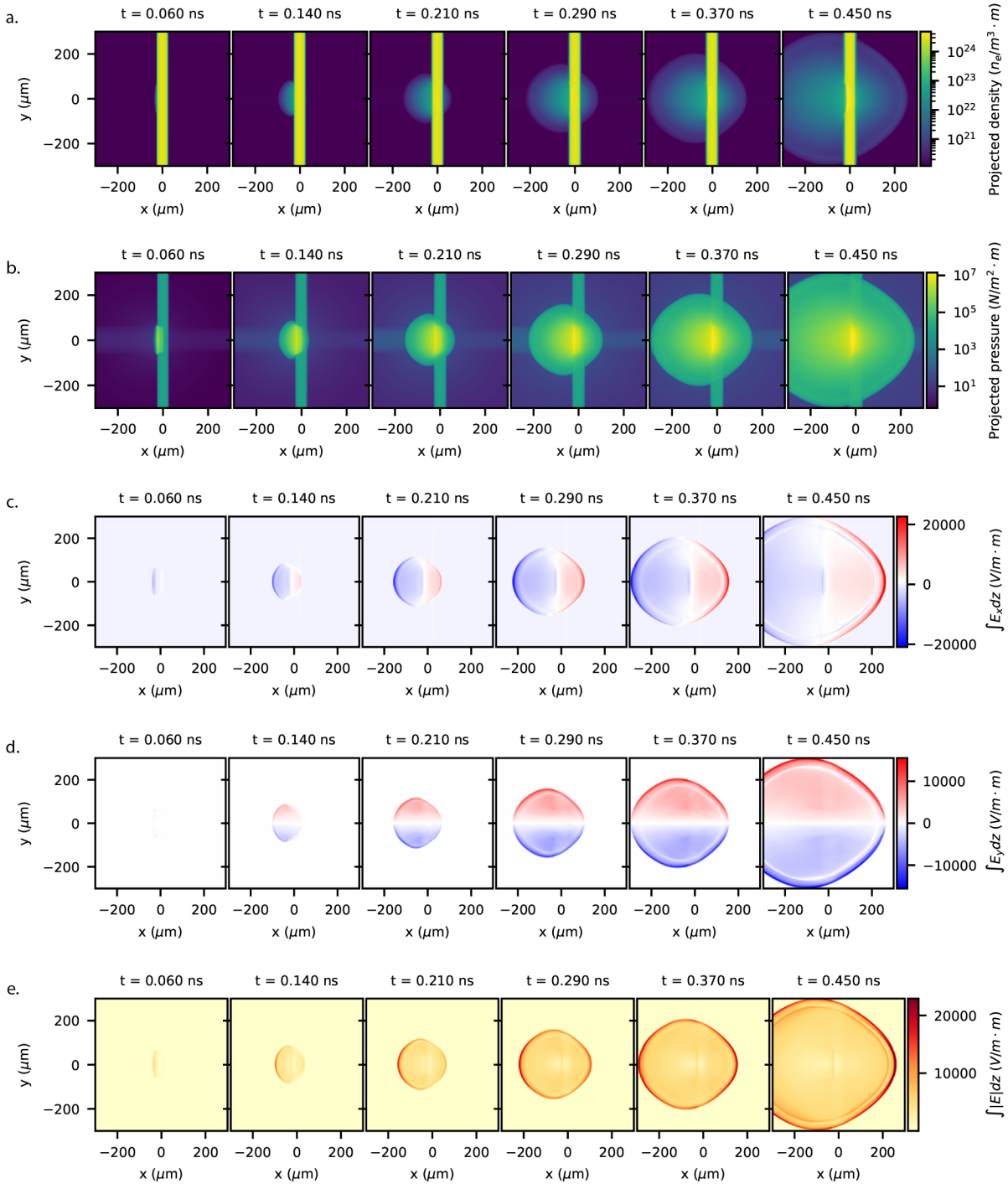

Figure 7.7: 3D FLASH radiation hydrodynamic simulation of the laser-water interaction. The resulting electric fields are derived and projected. (a) Time evolution of projected number density. (b) Time evolution of projected pressure. (c) Time evolution of projected electric field x-component. (d) Time evolution of projected electric field y-component. (e) Time evolution of projected electric field magnitude.

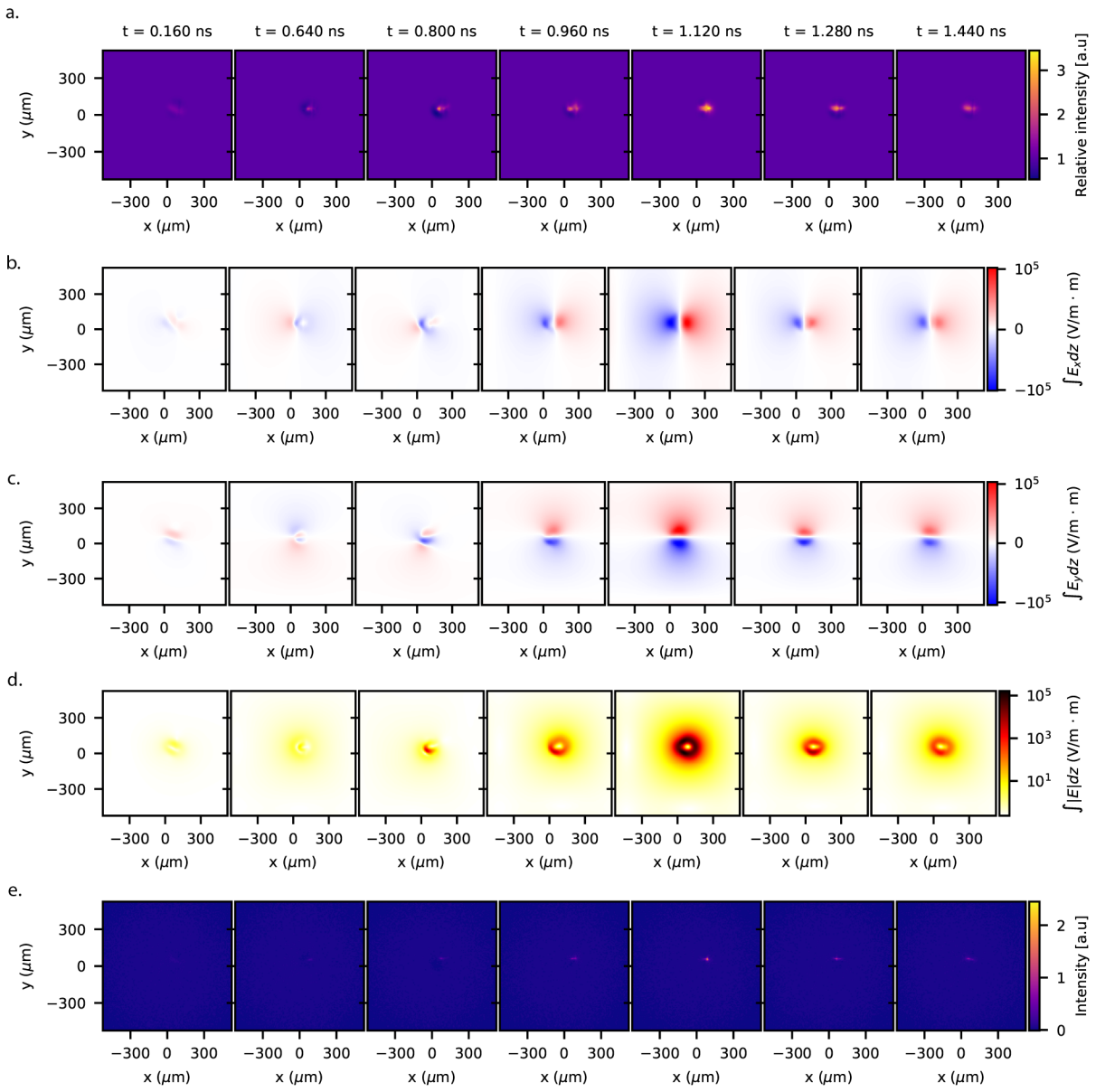

Figure 7.8: Relativistic electron beam probing of electromagnetic field evolution ($\sim$ 0.1 J laser energy deposition). (a) Shows I/I_0 to display the perturbation field and its evolution in time. (b) Path-integrated (projected) electric field (x-component) recovered with iterative algorithm. (c) Path-integrated (projected) electric field (y-component) recovered with iterative algorithm. (d) Path-integrated (projected) electric field magnitude recovered with iterative algorithm. (e) Synthetic electron beam radiography image using the predicted field configuration in order to compare with the original measurement.

electric fields from the iterative code predict a similar scenario, displaying x and y components that are, while similar in magnitude, exactly opposite in direction from those previously predicted in Fig. 7.8. The fields recovered in Fig. 7.9 would seem to indicate a defocusing effect that initially goes against natural intuition and is further discussed in the discussion section.

Lastly, the third time-series dataset in Fig. 7.10 consists on the highest laser energy ($E_L \approx 1$ J) deposited in the water target. At this regime, one can observe a defocusing an effect similar to the one present in Fig. 7.9. The strength of the fields is high enough to produce this effect even when probed with a less energetic region of the electron beam probe. The field responsible for the void in the electron radiographs of Fig. 7.10 is similarly evolving in time. From the results of the field reconstruction it can be appreciated that the fields are only short-lived. They increase in magnitude quickly, while diminish its effect with time. This measurement is particularly interesting because in the later frames of the time-series, as the magnitude of the field decreases, a reversal in the y field direction is observed. This observation goes in line with the field reversal previously observed between Fig. 7.8 and Fig. 7.8, except here it is occurring not as a function of energy but as a function of time. This field reversal mechanism is discussed in the next section.

7.4 Discussion

Early in time, before the peak of the main pulse arrives, the water target is transparent to laser light, a phenomenon also known as the shine-through effect in ICF research [10, 18, 39, 44], which will likely cause pre-heating of the target before plasma formation. After pre-heating the electrons continue getting hotter because they absorb the full laser energy and transfer this energy back to the ions. Nevertheless, the electron-ion energy transfer rate es very slow, much slower compared to the laser energy deposition occurring at much shorter timescales. This means that the rate of heat transfer for the ions is subsonic i.e. at the acoustic wave propagation velocity. However in the case of the electrons due to their small mass and higher heat conduction they will transport heat *supersonically*, having an average thermal velocity two orders of magnitude higher than the ion sound speed. This means that the internal heat of the target increases in isochoric conditions i.e. the target doesn't have time to expand and release the energy.

This increase in energy in turn causes pressure to increase and a rarefaction into vacuum proceeds. In a hydrodynamic picture, we immediately created a heated zone/ pressurized layer by supersonic electron heat conduction from the laser energy deposited into the plasma. This thermalization effect lasting a few tens of picoseconds can be observed in the first few frames of Fig. 7.7.

Within this context, the results obtained in the preceding section (Fig. 7.8) successfully demonstrate the application of the relativistic electrons from LWFA to capture the time evolution of a

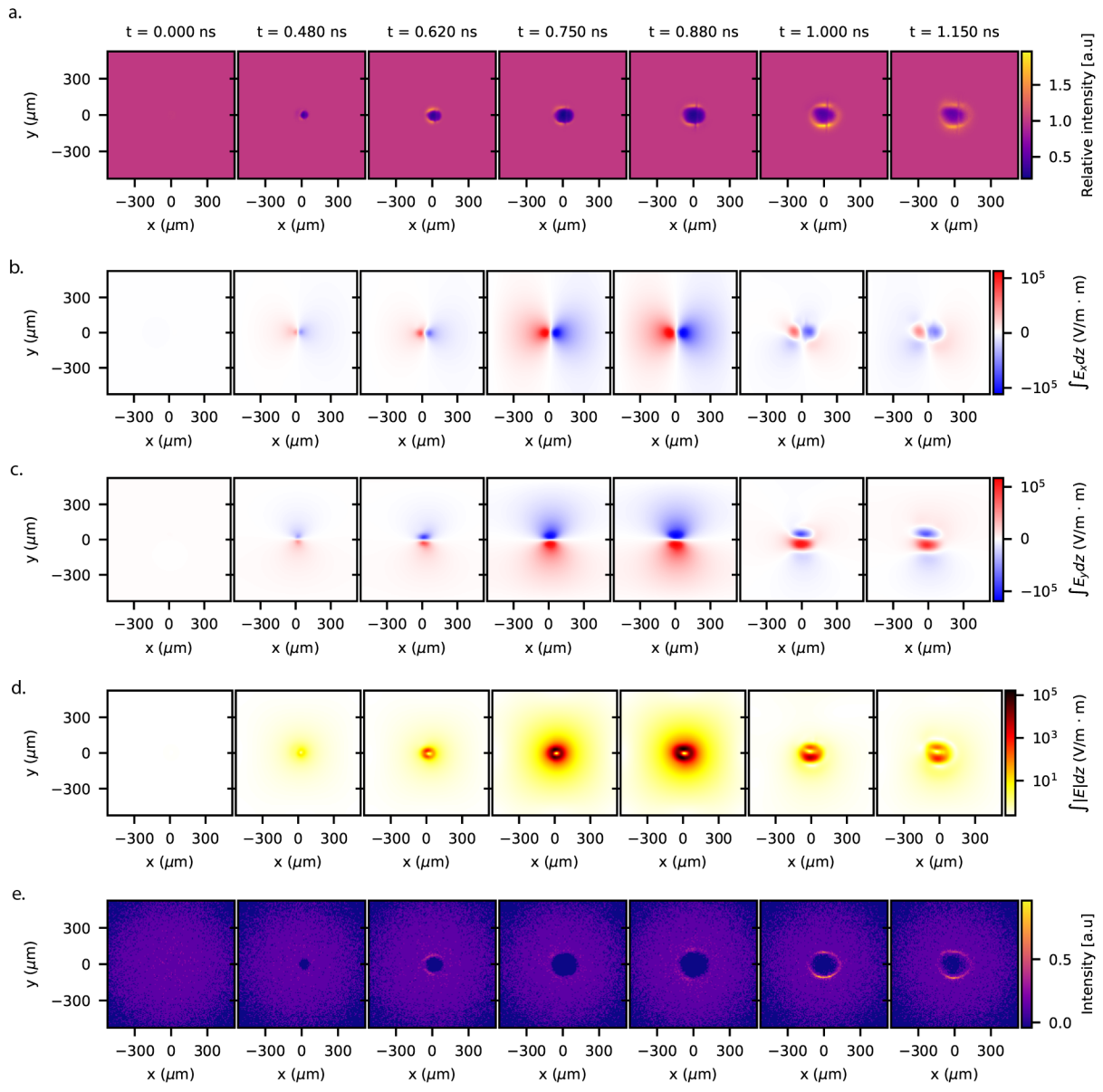

Figure 7.9: Relativistic electron beam probing of electromagnetic field evolution ($\sim$ 0.5 J laser energy deposition). (a) Shows I/I_0 to display the perturbation field and its evolution in time. (b) Path-integrated (projected) electric field (x-component) recovered with iterative algorithm. (c) Path-integrated (projected) electric field (y-component) recovered with iterative algorithm. (d) Path-integrated (projected) electric field magnitude recovered with iterative algorithm. (e) Synthetic electron beam radiography image using the predicted field configuration in order to compare with the original measurement.

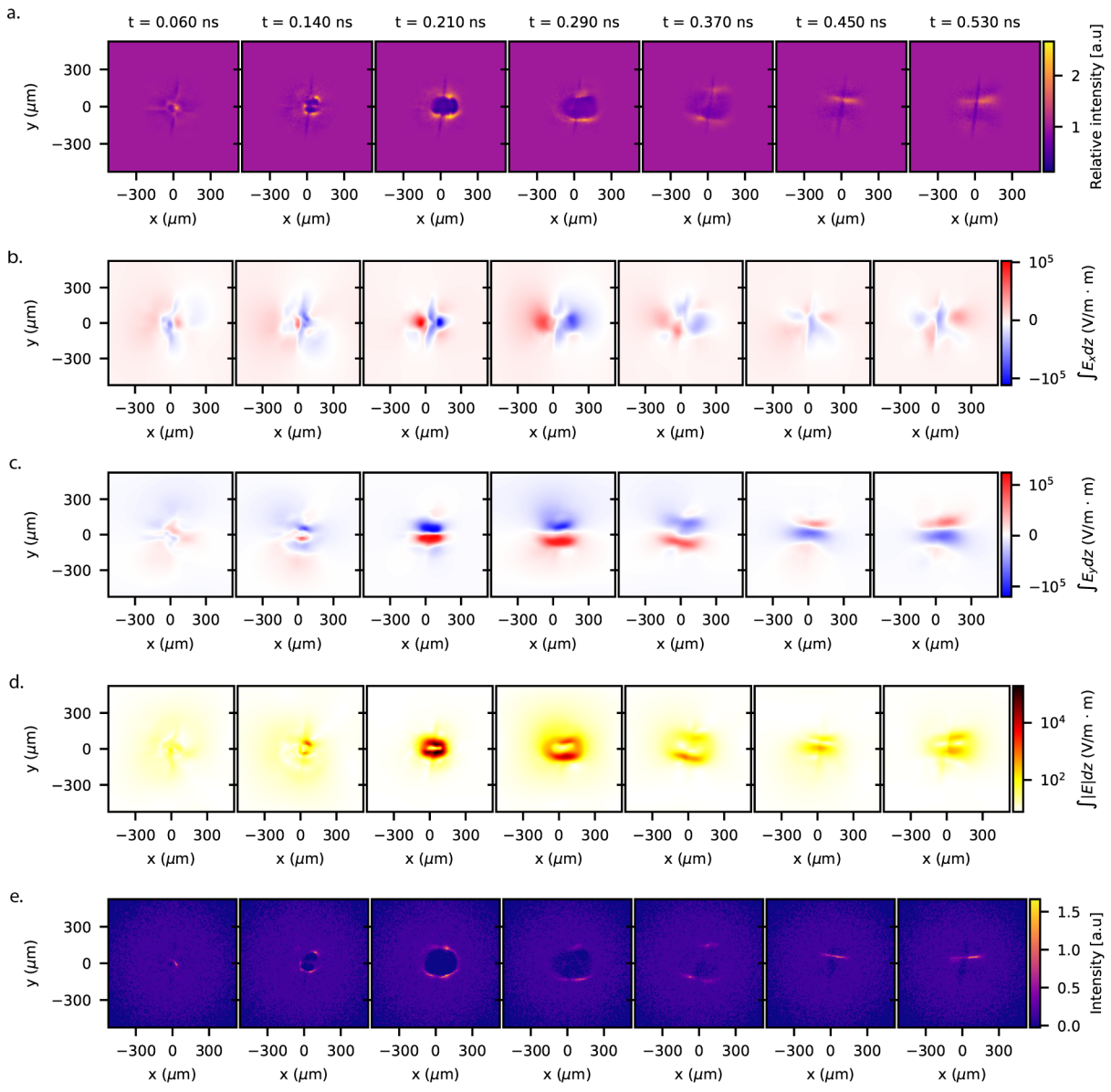

Figure 7.10: Relativistic electron beam probing of electromagnetic field evolution ($\sim$ 1 J laser energy deposition). (a) Shows I/I_0 to display the perturbation field and its evolution in time. (b) Path-integrated (projected) electric field (x-component) recovered with iterative algorithm. (c) Path-integrated (projected) electric field (y-component) recovered with iterative algorithm. (d) Path-integrated (projected) electric field magnitude recovered with iterative algorithm. (e) Synthetic electron beam radiography image using the predicted field configuration in order to compare with the original measurement.

thermoelectric field consistent with the expanded plasma predicted by simulation. Based on these fields topology, the expected effect on the electron beam probe is that of a focusing lens, is which correctly captured at low energy deposition.

Nevertheless, as the the energy in the heating laser increases and the field intensities become stronger what the experimental measurements reveal in Fig. 7.9 and Fig. 7.10 is that the relativistic electron beam is actually *overfocused*. The high field intensities exert a force on the beam sufficiently strong to focus it down to a point closer to the interaction coordinates and therefore projecting into the detector screen as a defocusing lens. This realization changes the perspective from which the high-field measurements are analyzed, and can give hints as to what extent the magnitude of fields prediced by simulation disagree with those obtained from experiment.

Of particular relevance is the fact that the high energy deposition results show evidence for heating and ionization breakdown on both sides of the target, followed by plasma expansion rather symmetrically around the interaction region as has been discussed in Chapter 5. The experimentally measured fields in Fig. 7.10 expand at a rate of $c \approx 284 \pm 3\mu$m/ns, which can be compared to the theoretically calculated plasma expansion velocity into vacuum using an isothermal rarefaction model along with temperatures obtained from a radiation hydrodynamic code such as FLASH giving $c_s = \sqrt{(ZT_e + 3T_i)/M} \approx 224\mu$m/ns.

Overall, the analysis suggests that the emergence and expansion of the observed dark voids during the interaction are explained by the creation of robust electric fields resulting from the rapid plasma heating and expansion. Consequently, these electric fields exert a strong focusing effect on the electron beam, leading to a regime of overfocusing that manifests as apparent defocusing in the detector plane. The manifestation of overfocused fields forms a void at the center of the electron beam probe, which evolves over time and can be quantified through measurements. Furthermore, this analysis aids in establishing a more accurate determination of the magnitude of the fields generated within high-energy-density experiments. To explore this notion further, a sequence of synthetic electron beam radiographs have been calculated in Fig. 7.11. These radiographs were created by imposing the electric fields anticipated by FLASH and varying their magnitude through scalar multiplication. The analysis is aimed at exploring the distinct imaging regimes enabled by the electron beam, contingent upon the strength of the fields applied.

What the synthetic radiographs reveal is in fact all regimes of imaging that have been captured by the experimental measurements. When lower electric field intensities are imposed the electron beam responds by focusing, while at higher field strengths a void is generated caused by the overfocusing of the charged particle probe. If the magnitude of the fields is increased even further, not only the overfocused void is present, but also the horizontal focusing field line that has been captured in Fig. 7.3 can be appreciated.

The differentiation between focusing and overfocusing regimes and their transition in time is

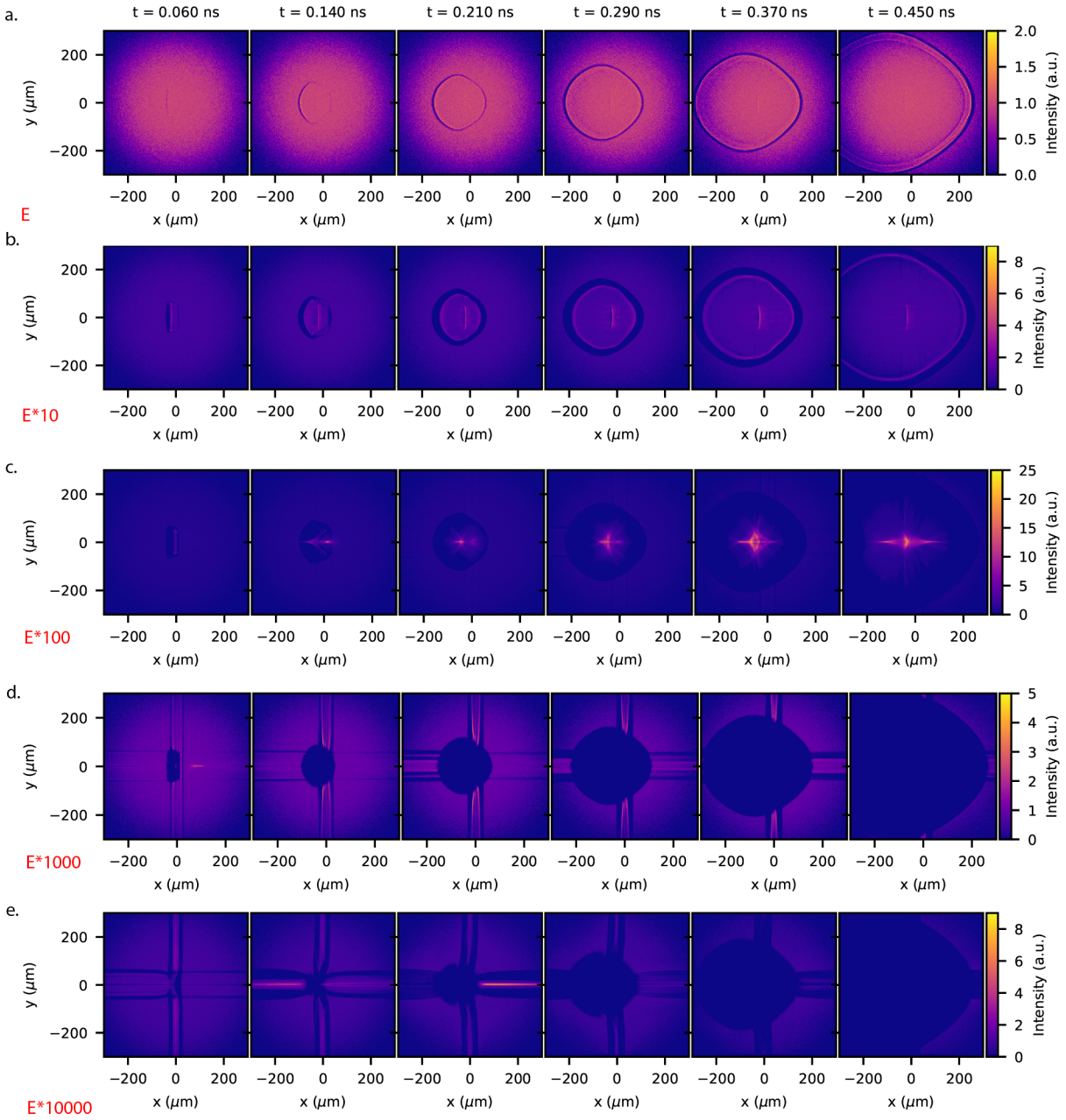

Figure 7.11: Synthetic electron beam radiography maps given the electric field topology derived from 3D FLASH simulations. The radiographs are performed for different time delays and multiple regimes are displayed for comparison which vary on the strength of the imposed electric field. (a) $E_0 \times 10^0$, (b) $E_0 \times 10^1$, (c) $E_0 \times 10^2$, (d) $E_0 \times 10^3$, (e) $E_0 \times 10^4$.

an interesting phenomenon. The work in this chapter captured the transition of these regimes both by varying the laser energy as well as their time delay. Nevertheless, there is potentially an alternative way of resolving this ambiguity. This innovative idea is based on the introduction of a quadrupole magnet. In order to make sense of this let us refer back to the field recovery method from Kugland et al. [92] introduced in Chapter 3. This charged particle deflectrometry method to recover electromagnetic fields relies on the important assumption that no particle crossings, or *caustics*, are present during the interaction. Assuming no particle crossing exist, the algorithm will have a unique solution for the recovery of the electromagnetic field. For this reason, the recovery results obtained in Fig. 7.3 and Fig. 7.4 which predict a defocusing field are not correct. The presence of particles crossing while overfocusing does not permit the algorithm to recover the correct topology of fields. Moreover, in order to reduce particles crossing one solution is to increase the beam's divergence. Larger beam divergence would allow for probing stronger fields before caustics occur. In this context, the quadrupole setup in Fig. 7.1 would have the advantage of increasing the divergence of the field in one direction, while reducing in the other direction. This configuration would allow for a potentially dual perspective when capturing the fields, by probing strong fields in the direction that the divergence was increase before they have an overfocusing effect.

This idea was tested as part of this experimental campaign by introducing a quadrupole magnet a few centimeters away from the electron accelerator and the results are shown in Fig. 7.6 and Fig. 7.12. Initially, the quadrupole has the expected effect of focusing the electron beam in one direction (reducing divergence), while defocusing in the other direction (increasing divergence). When the perturbation field is introduced into this imaging configuration the measurements display what looks like two defocusing fields (voids) on top and bottom of the electron beam. In order to make sense of this, one potential explanation is based on the fact that in the direction that the electron beam is focused by the quadrupole the expected measurement is a large parabola-like field from strong overfocusing. Alternatively, in the direction where the electron beam is defocused by the magnet the expected measurement would be the real focusing field predicted by simulations in the absense of particles crossings. If put together, both of these images would result in a bean-like parabolic shape which is focused in the center. This hypothesis resemble the experimental measurements obtained with the quadrupole in Fig. 7.6.

In the case of direct-laser irradiation, electron heat transport plays a key role in the evolution of the target and it is a major issue in ICF research. For low-Z targets that are fully ionized, the laser energy absorption opacity to inverse-Bremsstrahlung is close to that of the free-free value. However, as the effective nuclear charge Z of the irradiated material increases and more electrons are attached to the nuclei the ionization is less complete and the emitted thermal radiation plays an increasing role in the dynamics. For medium Z targets like the one in the present experiment with

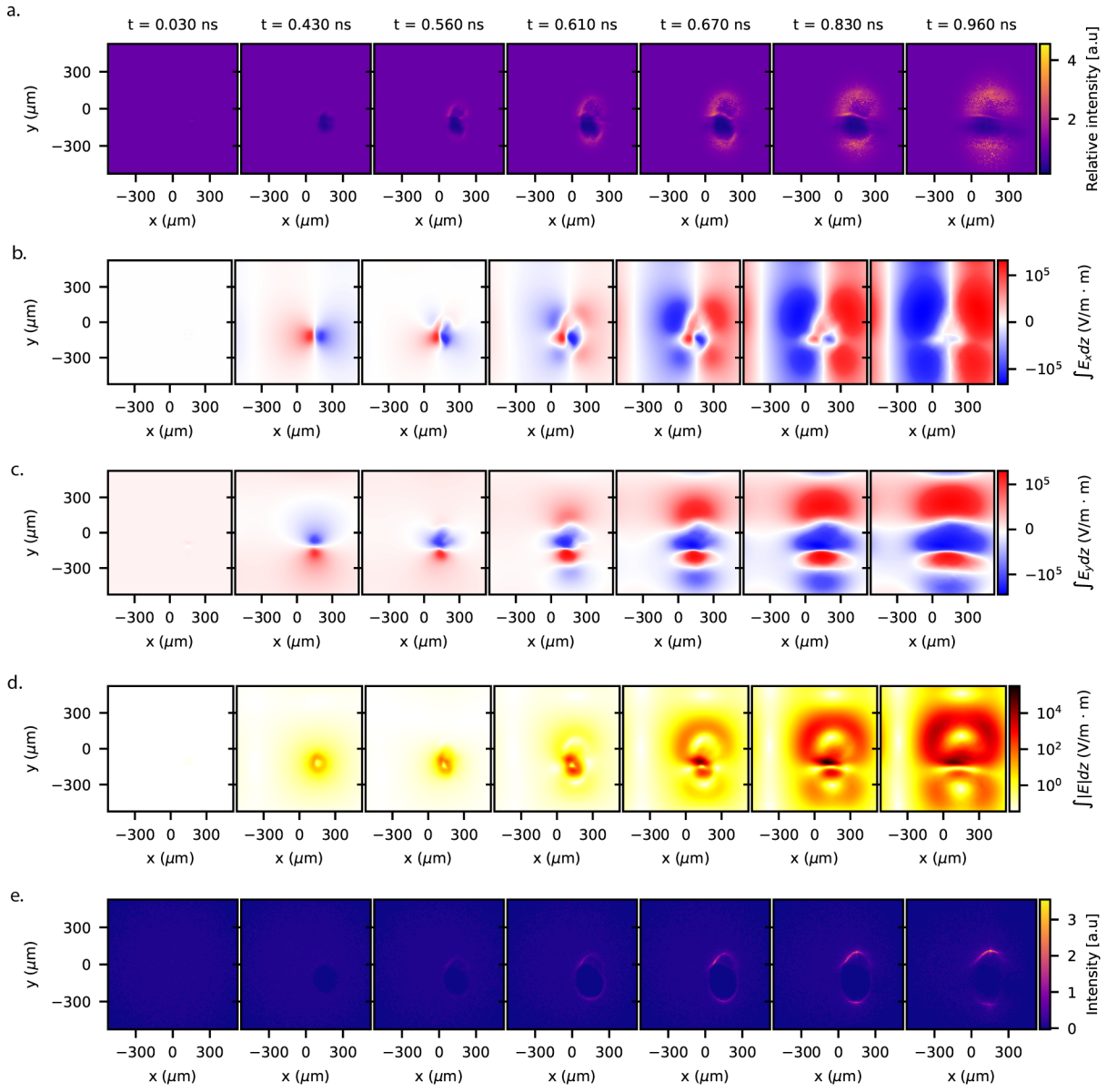

Figure 7.12: Relativistic electron beam probing of electromagnetic field evolution with quadrupole lens (~ 0.5 J laser energy deposition). (a) Shows I/I_0 to display the perturbation field and its evolution in time. (b) Path-integrated (projected) electric field (x-component) recovered with iterative algorithm. (c) Path-integrated (projected) electric field (y-component) recovered with iterative algorithm. (d) Path-integrated (projected) electric field magnitude recovered with iterative algorithm. (e) Synthetic electron beam radiography image using the predicted field configuration in order to compare with the original measurement.

$Z \approx 4$ and $n_0 > n_c$ the target evolution is complex, and the overall laser energy deposition depends on the interchange between electron and radiation heat transport, hydrodynamic expansion, and shock generation. Initially, the laser energy is deposited in the corona below n_c, mostly through inverse-bremsstrahlung. This creates a heat front from which electrons transport energy above n_c up to the ablation surface, sustaining the pressure that drives a shock forward into the matter as was observed in Fig. 5.3. In the case of direct-drive ICF experiments, the overall efficiency to compress the fuel is directly determined by the fraction of laser energy that is absorbed as electron thermal flux and transported to the ablation region. The excess energy that is not carried above n_c towards the dense plasma will heat and accelerate the corona outwards, and the heated low-density plasma will diminish the laser-energy absorption efficiency even further, as the opacity to inverse-bremsstrahlung absorption $K_{IB} \approx N_e^2/T_e^{3/2}$ is inversely dependent on electron temperature [38].

In practice, the electron heat-transport models are only an approximation and the electron temperatures are affected by several details including laser spectrum, intensity, and spatial profiles. For instance, the classical derivation by Spitzer and Harm to describe the dynamics of electron heat flux is governed by the equation $Q_{SH} = -\kappa_{th}\partial k_B T_e/\partial z$ with transport coefficient κ_{th}. It is a diffusive heat transport model and relies on the assumption of gentle temperature gradients $\lambda_{mfp} \ll T_e/|\nabla T_e| = L_T$. Any plasma configuration with large temperature gradients will not be accurately described by the model as the transport becomes too strong. Additionally, the derivation ignores electron-electron collision which would overestimate the transport as described by [91]. In general, the Spitzer and Harm model gives accurate results as long as $L_T/\lambda_{mfp} >> 30$. This condition is typically satisfied by UV lasers, rarely satisfied by 800nm lasers like the one in the present experiment, and never satisfied at infrared wavelengths [42]. A more accurate description of electron transport would include solving the Fokker-Planck equation, yet this must be done numerically and it cannot be practically included in a radiation-hydrodynamics code. These challenges have motivated the search for alternative simpler models that can be effectively implemented in simulations, as is the case of the commonly used flux-limited heat transport model. In such description, the thermal energy density in the plasma is transported at some limiting free-streaming thermal velocity. This results in a maximum heat flux that can be adjusted by multiplying a flux limiter parameter f so that $Q_{FS} = f \times n_e k_B T_e v_{th}$. The flux-limited heat transport description can be improved further by crude modeling the non-local effects as electron bunches streaming at different thermal velocities, also known as multi-group flux-limited diffusion (used in FLASH) These models can be useful for predicting ablation pressures and shock wave propagation velocities after tuning them to experimentally measured parameters, and adjusting f accordingly ($f \sim 0.05$ typical). However, these models do not accurately capture the kinetics of the interaction during laser energy absorption and deposition where strong temperature gradients are present. In reality, electron heat transport in laser-irradiated materials is not unidirectional diffusive and only affected

by the local surrounding particles. The transport is also affected by non-local effects including electric and magnetic field generation and super-thermal particles traveling from a range of distances which influence the overall heating dynamics. For all these reasons, the simulations of such electron heat transport physics use only crude models and may not give accurate results. In particular, these simulations will not give correct results for the detailed structure of the plasma near the irradiated surface where fast particles penetrate deep into the target. The larger mean free path of heated particles below n_c means they are capable of traveling larger distances along the critical surface of the target and their smaller Coulomb cross section allows them to penetrate deeper into the target. This can have the effect of producing an ionization front and leaving a warm foot ahead of the peak of the pulse. A great deal of effort has been carried out to create non-local electron heat transport models that are also feasible to implement in hydrodynamic codes including one by Schurtz [150]. These models have most recently been reviewed and compared by Sherlock [153]. It is evident that obtaining a better understanding of the electron heat transport dynamics is imperative for accurately modeling ICF and HEDP experiments. Additionally, the data supports the idea that non-local heating effects do come into play during the interaction, with the possibility of electric and magnetic fields contributing to the electron transport dynamics as well. Motivated by acquiring an insight into these effects and obtaining a better understanding of the target evolution, innovative electron beam radiography measurements have been performed using the laser wakefield relativistic beam.

Beyond the immediate horizons of this investigation lies a future rich with potential. This innovative technique not only augments our understanding of HEDP phenomena but also opens doors to a broader realm of applications. By embracing the advantages of charged particle imaging, we embark on a dual journey—complementing the radiant insights of X-ray photons with the dynamic revelations of relativistic electrons.

CHAPTER 8

Conclusion and Outlook

The work in this thesis is a first of its kind series of experimental campaigns aiming to demonstrate the potential application of electron beams and X-rays produced from laser wakefield accelerators for pump-probe studies of high-energy-density systems that are dynamically evolving with submicron scale features in space. Traditional diagnostic systems in high-energy-density experiments, such as those performed at NIF or OMEGA, often suffer from low resolution and poor signal-to-noise ratio. In this regard, it is imperative to develop higher-resolution diagnostic systems that advance our understanding of high-energy-density systems and leverage the progress on investigations such as those pursuing inertial confinement fusion.

Given their small source size ($\sigma \approx 1\mu$m), LWFA-produced X-ray radiation sources present a promising alternative for high resolution imaging studies of high-energy-density systems. Betatron X-rays have already proven to hold great potential for imaging of static biological systems, materials for additive manufacturing, and a variety of single-shot experiments with solid targets. Meanwhile, advancements in laser technology during the past decade have enabled scientists to produce high quality electron beams and X-rays at high-repetition-rates (Hz), and LWFA electron beams at kHz repetition rates have already been demonstrated. The advancement in both laser technology and the future outlook of LWFA research at high-repetition-rate begs the development of novel targetry that are equally capable of operate at higher rates. A small source size, higher-repetition-rate accelerator, and replenishing target set the stage for acquiring data at orders of magnitude faster pace.

Within this context, the heart of this work lies in the realization of an original high-vacuum bulk water target – a novel achievement in the realm of high-energy-density experiments - that aligns with the ever-growing demand for high repetition rate studies. Conventional solid targets pose challenges in terms of reproducibility and chamber contamination, particularly in the context of high repetition rates. The innovation of a bulk liquid target, described in Chapter 4 and demonstrated successfully in this thesis, offers a promising avenue for *clean* in situ dynamic experiments, replete with regenerative capabilities. The liquid target concept presents a versatile and repeatable

platform, open to future explorations involving diverse liquids, geometries, configurations, and even higher repetition rates.

Chapter 5 ventured into the realm of propagation-based phase-contrast X-ray imaging employing betatron X-rays generated by LWFA. The chosen platform consists on the generation of a hydrodynamic shock wave in the water jet target by the interaction of a long pulse laser. This endeavor not only validated the potential of this technique for high resolution imaging, but also shed light on crucial dynamics of the shock behavior at unprecedented temporal resoluton. The realization that 3D hydrodynamic effects in high-energy-density experiments often transcend the confines of 2D simulations underscored the critical need for comprehensive studies. In a remarkable revelation, the experiment unraveled the role of a low-density vapor layer enveloping the target due to evaporation from the water due its low volatility in high vacuum (low pressure). This vapor layer enabled a symmetrical heating mechanism due to faster electron heat transport mediated through collisions, thus impacting the target behavior from multiple directions.

Moreover, Chapter 6 marked a significant extension, focusing on the temporal evolution of the shock at later times, and the observation of plasma instabilities that resemble the Richtmyer-Meshkov process through ultra-high-resolution betatron X-ray imaging. The superb spatiotemporal resolution facilitated unprecedented insights into wave growth, unveiling waves at the micron and submicron scales. The growth rates calculated for these waves not only validated their presence but also allowed for comparison with analytical calculations predicting Richtmyer-Meshkov process growth rates.

Chapter 7 brought an additional dimension, probing the interaction of the long-pulse laser with the water target using the relativistic LWFA-produced electron beam as a radiographic probe. This charged-particle based probing tool enabled the exploration of electromagnetic fields arising from the laser-plasma interaction. Through a field-reconstruction analysis, this unique perspective revealed the presence of time-evolving fields with diverse magnitudes. The utilization of a liquid target and a high-repetition-rate accelerator was crucial for allowing the exploration of a variety of regimes regarding the generated fields by varying the laser energy. Multiple studies were indicative of a transition from focusing to strong over-focusing fields dependent on the laser energy that is deposited into the target. Crucially, these strong fields are not observed by the X-ray diagnostics, thus elevating the importance of the electron beam probe as a diagnostic tool in high-energy-density experiments at femtosecond timescales. The measured fields were compared with synthetic electric fields derived from radiation hydrodynamic simulations.

Looking ahead, this thesis lays the foundation for potentially groundbreaking applications and investigations using LWFA systems. The outlook is guided by the vision of utilizing betatron X-rays and LWFA-produced electron beams as diagnostics, offering an exceptional vantage point from two different perspectives that are not typically found together. While NIF currently oper-

ates at low repetition rates, a potential future expansion could benefit immensely from platforms capable of high repetition rate experiments, thereby accelerating progress in our understanding of relevant high-energy-density concepts. The challenges accompanying this outlook are not to be understated. The high X-ray fluxes generated during interactions at NIF pose a significant background that betatron X-ray probes would need to overcome. Addressing this issue would necessitate advancements in laser technology to create exceptionally bright probes. However, as history has shown, scientific and technological progress is marked by surmounting challenges that once seemed insurmountable.

Moreover, the applicability of liquid water targets extends beyond the realm of imaging. These targets hold promise for ion acceleration experiments and potential applications in short-pulse interactions with low-Z liquid targets for electron generation, diversifying their impact. As more studies look into liquid targetry for innovation, their applicability grows into regimes that were previously unthinkable for both research and industry.

In conclusion, this thesis has ventured into uncharted territories, illuminating the intricate world of high-energy-density phenomena in both spatial and temporal resolution scales that have not been explored before. The accomplishments outlined within serve as stepping stones towards a more profound understanding of matter under extreme conditions and the innovative applications that can spring from liquid targets. By embracing the spirit of collaboration, innovation, and determination, the trajectory set by this thesis illuminates a pathway toward a future where the mysteries found in experiments, such as those pursuing inertial confinement fusion, can greatly benefit from plasma-based accelerators and compact radiation sources.

APPENDIX A

Useful Shock Relations

The most useful shock relations relate the Mach number $M_u = u/c_s$ to the downstream and upstream properties of the fluid. Once again, let us assume a polytropic gas with an equation of state relating ϵ to p as,

$$\rho\epsilon = \frac{p}{(\gamma - 1)} \ . \tag{A.1}$$

In this case, γ is the single shock polytropic index, although in real HED experiments the index γ can vary greatly across a shock front. For those situations, once would have the upstream index γ_1 and downstream index γ_2. The shock velocity in the lab frame is $u_s = u_1$ and the upstream Mach number is $M_1 = -u_1/c_s = u_s/c_s$, so for a polytropic gas this is,

$$M_u = u_s \sqrt{\frac{\rho_1}{\gamma_1 p_1}} \ . \tag{A.2}$$

Therefore, substituting this expression into the Euler equations (Eq. 2.67, Eq. 2.68, and Eq. 2.69) and after some algebra, the ratio of pressures can be expressed as

$$\frac{p_2}{p_1} = \frac{\rho_2 (\gamma + 1) - \rho_1 (\gamma - 1)}{\rho_1 (\gamma + 1) - \rho_2 (\gamma - 1)} \ , \tag{A.3}$$

or for different polytropic indices across the shock then,

$$\frac{p_2}{p_1} = \frac{\rho_2 (\gamma_1 + 1) - \rho_1 (\gamma_1 - 1)}{\rho_1 (\gamma_2 + 1) - \rho_2 (\gamma_2 - 1)} \frac{(\gamma_2 - 1)}{(\gamma_1 - 1)} \ . \tag{A.4}$$

Similarly, the density ratios can be obtained,

$$\frac{\rho_2}{\rho_1} = \frac{p_2 (\gamma + 1) + p_1 (\gamma - 1)}{p_1 (\gamma + 1) + p_2 (\gamma - 1)} \ , \tag{A.5}$$

and similarly for different indices,

$$\frac{\rho_2}{\rho_1} = \frac{p_2\left(\gamma_2+1\right)+p_1\left(\gamma_2-1\right)}{p_1\left(\gamma_1+1\right)+p_2\left(\gamma_1-1\right)}\frac{\left(\gamma_1-1\right)}{\left(\gamma_2-1\right)} \ . \tag{A.6}$$

Therefore, by taking the limit as $p_2 \gg 1$ leads to the result,

$$\frac{\rho_2}{\rho_1} \approx \frac{\left(\gamma+1\right)}{\left(\gamma-1\right)} \ . \tag{A.7}$$

This implies that there is a fixed maximum density ratio that can be achieved. In HEDP experiments with a low Z material acting as polytropic gas with index $\gamma = 5/3$ the resulting density jump would be $\rho_2/\rho_1 \approx 4$. Other useful equations include expressing the density jump and pressure difference as a function of the Mach number, using the EE and a similar approach one gets

$$\frac{\rho_2}{\rho_1} = \frac{M_u^2\left(\gamma+1\right)}{M_u^2\left(\gamma-1\right)+2} \ , \tag{A.8}$$

and

$$\frac{p_2}{p_1} = \frac{2\gamma M_u^2-\left(\gamma-1\right)}{\left(\gamma+1\right)} \ . \tag{A.9}$$

The regime in which M_u becomes really large is known as the *strong shock limit*, and it is typically applicable for shocks found in HED experiments. In the strong shock limit, the density ratio still tends towards a fixed value based on γ, while the pressure ratio increases indefinitely. Unfortunately, typically M_u is poorly known during experiments. The uncertainty in M_u arises from the uncertainty in real experimental conditions regarding the temperature or state of a target. Several factors contribute to real experimental conditions such as vacuum cooling, or radiation heating. Nevertheless, the higher M_u the less this matters. An alternative expression for the post-shock pressure can be found in the strong shock limit so that the equation is in terms of shock velocity and initial density,

$$p_2 = \frac{2}{\left(\gamma+1\right)}\rho_1 u_s^2\left[1-\frac{\left(\gamma-1\right)p_1}{2\rho_1 u_s^2}\right] \ . \tag{A.10}$$

Assuming a single value for the shock index γ. Therefore, for strong shocks, a simple approximation for the pressure given a shock velocity is

$$p_2 \approx \rho_1 u_s^2 \ . \tag{A.11}$$

Similarly, it is possible to obtain an estimate of temperature given this pressure by assuming the electrons fully equilibrate with the ions, to be non-degenerate, and ignoring Coulomb interactions

so if $p_2 = (Z_2 + 1)\, k_B T_2 \rho_2 / (A m_p)$ in the strong shock limit one would have

$$k_B T_2 = \frac{A m_p}{(1 + Z_2)} u_s^2 \frac{2\,(\gamma_2 - 1)}{(\gamma_2 + 1)^2} \,. \tag{A.12}$$

From this equation it is also possible to approximate the post-shock temperature of the ions by setting $Z_2 = 0$ and $\gamma_2 = 5/3$ in the previous equation, this is

$$T_{i,2} \approx 10 \times A m_p u_s^2 \,. \tag{A.13}$$

Furthermore, other shock properties worth mentioning include the fact that the velocity ratio across the shock front is the inverse of the density ratio so,

$$\frac{u_2}{u_1} = \frac{\rho_1}{\rho_2} = \frac{(\gamma - 1)}{(\gamma + 1)} \,. \tag{A.14}$$

This is a helpful expression for finding the post-shock particle velocity in the lab frame given by,

$$u_p = u_s + u_2 = \frac{2}{(\gamma + 1)} u_s \,. \tag{A.15}$$

Then $u_p = (3/4) u_s$ for $\gamma = 5/3$ and $u_p = (6/7) u_s$ for $\gamma = 4/3$. Therefore the post-shock pressure in the lab frame would then be given by

$$p_2 = (\gamma - 1)\, \frac{\rho_2 u_p^2}{2} \,. \tag{A.16}$$

Implying that in the strong shock limit and the lab frame of reference one would have an equal amount of kinetic and internal energy densities in a polytropic gas with EOS given by Eq. A.1.

APPENDIX B

Technical Drawing of Water Target

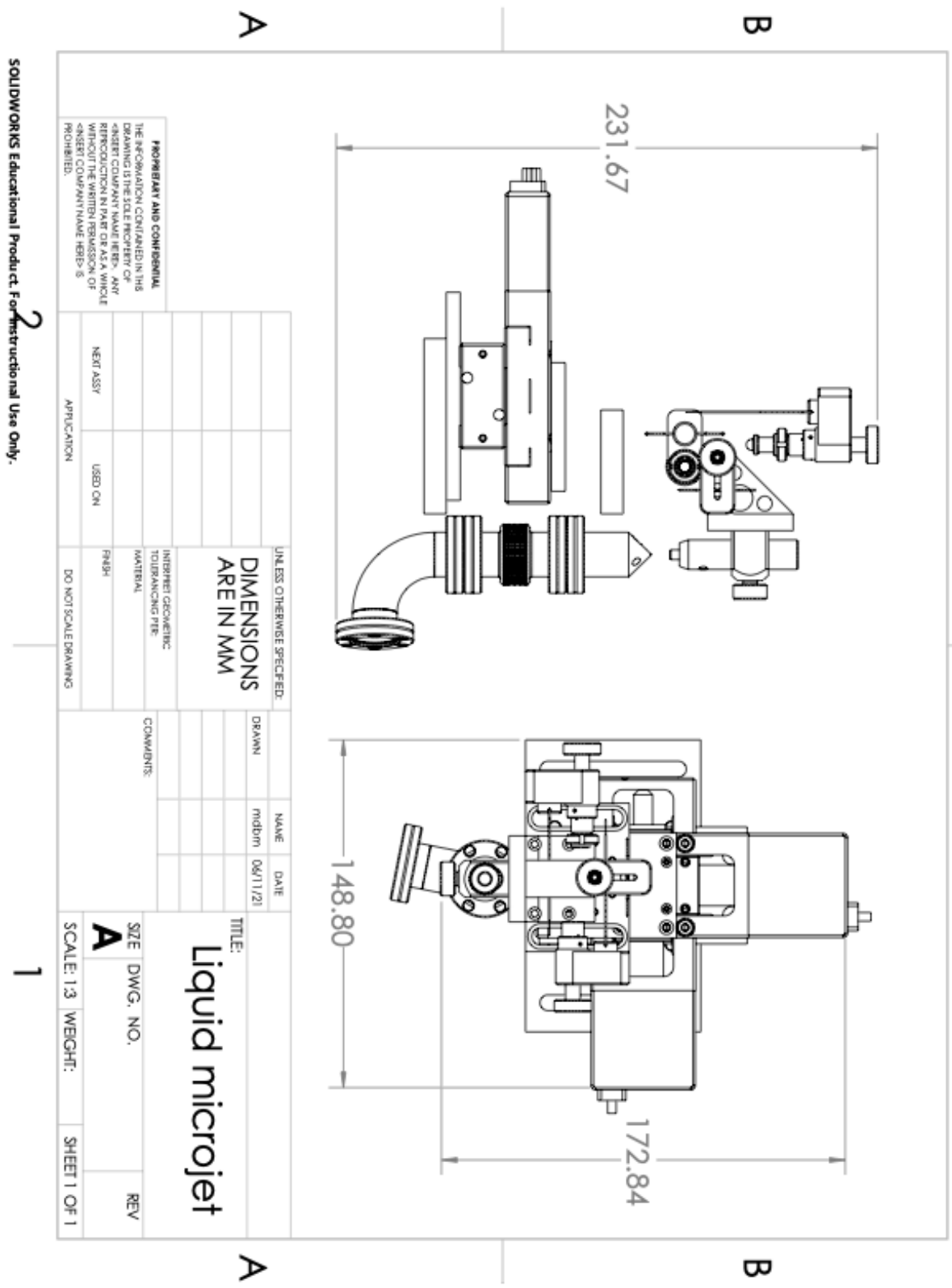

Figure B.1: Technical drawing of target assembly including overall height, width, and depth. All dimensions are in millimeters. The height of the target is typically changed to match focus of experimental probe.

BIBLIOGRAPHY

[1] F. Albert, N. Lemos, J. Shaw, B. B. Pollock, C. Goyon, W. Schumaker, A. M. Saunders, K. A. Marsh, A. Pak, J. E. Ralph, et al. Observation of betatron x-ray radiation in a self-modulated laser wakefield accelerator driven with picosecond laser pulses. *Physical Review letters*, 118(13):134801, 2017.

[2] F. Albert, R. Shah, K. T. Phuoc, R. Fitour, F. Burgy, J.-P. Rousseau, A. Tafzi, D. Douillet, T. Lefrou, and A. Rousse. Betatron oscillations of electrons accelerated in laser wakefields characterized by spectral x-ray analysis. *Physical Review E*, 77(5):056402, 2008.

[3] F. Albert and A. G. R. Thomas. Applications of laser wakefield accelerator-based light sources. *Plasma Physics and Controlled Fusion*, 58(10), 2016.

[4] F. Albert, A. G. R. Thomas, S. P. D. Mangles, S. Banerjee, S. Corde, A. Flacco, M. Litos, D. Neely, J. Vieira, Z. Najmudin, et al. Laser wakefield accelerator based light sources: potential applications and requirements. *Plasma Physics and Controlled Fusion*, 56(8):084015, 2014.

[5] B. E. Allman, P. J. McMahon, K. A. Nugent, D. Paganin, D. L. Jacobson, M. Arif, and S. A. Werner. Phase radiography with neutrons. *Nature*, 408(6809):158–159, 2000.

[6] A. V. Arefiev, B. N. Breizman, M. Schollmeier, and V. N. Khudik. Parametric amplification of laser-driven electron acceleration in underdense plasma. *Physical Review Letters*, 108(14):145004, 2012.

[7] F. Arfelli, M. Assante, V. Bonvicini, A. Bravin, G. Cantatore, E. Castelli, L. Dalla Palma, M. Di Michiel, R. Longo, A. Olivo, et al. Low-dose phase contrast x-ray medical imaging. *Physics in Medicine & Biology*, 43(10):2845, 1998.

[8] S. Atzeni and J. Meyer-ter Vehn. *The physics of inertial fusion: beam plasma interaction, hydrodynamics, hot dense matter*, volume 125, pages 38–101. OUP Oxford, Oxford, 2004.

[9] S. Bajt, A. Barty, K. A. Nugent, M. McCartney, M. Wall, and D. Paganin. Quantitative phase-sensitive imaging in a transmission electron microscope. *Ultramicroscopy*, 83(1-2):67–73, 2000.

[10] J. E. Balmer, T. P. Donaldson, W. Seka, and J. A. Zimmermann. Self-focusing and the initial stages of plasma generation by short laser pulses. *Optics Communications*, 24(1):109–112, 1978.

[11] F. Barbato, S. Atzeni, D. Batani, D. Bleiner, G. Boutoux, C. Brabetz, P. Bradford, D. Mancelli, P. Neumayer, A. Schiavi, et al. Quantitative phase contrast imaging of a shock-wave with a laser-plasma based x-ray source. *Scientific Reports*, 9(1):1–11, 2019.

[12] M. A. Barrios, S. P. Regan, K. B. Fournier, R. Epstein, R. Smith, A. Lazicki, R. Rygg, D. E. Fratanduono, J. Eggert, H.-S. Park, et al. X-ray area backlighter development at the national ignition facility. *Review of Scientific Instruments*, 85(11), 2014.

[13] A. Barty, K. A. Nugent, D. Paganin, and A. Roberts. Quantitative optical phase microscopy. *Optics Letters*, 23(11):817–819, 1998.

[14] V. Berezhiani and I. Murusidze. Relativistic wake-field generation by an intense laser pulse in a plasma. *Physics Letters A*, 148(6-7):338–340, 1990.

[15] L. Bergé, S. Skupin, F. Lederer, G. Méjean, J. Yu, J. Kasparian, E. Salmon, J. Wolf, M. Rodriguez, L. Wöste, et al. Multiple filamentation of terawatt laser pulses in air. *Physical Review Letters*, 92(22):225002, 2004.

[16] R. Boehler. Temperatures in the earth's core from melting-point measurements of iron at high static pressures. *Nature*, 363(6429):534–536, 1993.

[17] M. Born and E. Wolf. *Principles of optics: electromagnetic theory of propagation, interference and diffraction of light*, pages 417–425. Elsevier, Cambridge, 2013.

[18] D. K. Bradley, T. Boehly, D. Brown, J. Delettrez, W. Seka, and D. Smith. Early-time "shine-through" in laser irradiated targets. In *Laser interaction and related plasma phenomena*, pages 323–334. Springer, 1991.

[19] A. Buck, J. Wenz, J. Xu, K. Khrennikov, K. Schmid, M. Heigoldt, J. M. Mikhailova, M. Geissler, B. Shen, F. Krausz, et al. Shock-front injector for high-quality laser-plasma acceleration. *Physical Review Letters*, 110(18):185006, 2013.

[20] S. Bulanov, N. Naumova, F. Pegoraro, and J. Sakai. Particle injection into the wave acceleration phase due to nonlinear wake wave breaking. *Physical Review E*, 58(5), 1998.

[21] A. Casner, L. Masse, B. Delorme, D. Martinez, G. Huser, D. Galmiche, S. Liberatore, I. Igumenshchev, M. Olazabal-Loume, P. H. Nicolai, J. Breil, D. T. Michel, D. Froula, W. Seka, G. Riazuelo, S. Fujioka, A. Sunahara, M. Grech, C. Chicanne, M. Theobald, N. Borisenko, A. Orekhov, V. T. Tikhonchuk, B. Remington, V. N. Goncharov, and V. A. Smalyuk. Progress in indirect and direct-drive planar experiments on hydrodynamic instabilities at the ablation front. *Physics of Plasmas*, 21(12), 2014.

[22] A. F. Center. Flash user's guide. 2005.

[23] A. Charvat, E. Lugovoj, M. Faubel, and B. Abel. New design for a time-of-flight mass spectrometer with a liquid beam laser desorption ion source for the analysis of biomolecules. *Review of Scientific Instruments*, 75(5):1209–1218, 2004.

[24] S. V. Chekalin and V. P. Kandidov. From self-focusing light beams to femtosecond laser pulse filamentation. *Physics-Uspekhi*, 56(2):123, 2013.

[25] M. Chen, E. Esarey, C. B. Schroeder, C. G. R. Geddes, and W. P. Leemans. Theory of ionization-induced trapping in laser-plasma accelerators. *Physics of Plasmas*, 19(3):033101, 2012.

[26] M. Chen, Z.-M. Sheng, Y.-Y. Ma, and J. Zhang. Electron injection and trapping in a laser wakefield by field ionization to high-charge states of gases, 2006.

[27] X. L. Chen and R. N. Sudan. Two-dimensional self-focusing of short intense laser pulse in underdense plasma. *Physics of Fluids B: Plasma Physics*, 5(4):1336–1348, 1993.

[28] S.-w. Chou, J. Xu, K. Khrennikov, D. E. Cardenas, J. Wenz, M. Heigoldt, L. Hofmann, L. Veisz, S. Karsch, et al. Collective deceleration of laser-driven electron bunches. *Physical Review Letters*, 117(14):144801, 2016.

[29] C. E. Clayton, J. E. Ralph, F. Albert, R. A. Fonseca, S. H. Glenzer, C. Joshi, W. Lu, K. A. Marsh, S. F. Martins, W. B. Mori, et al. Self-guided laser wakefield acceleration beyond 1 gev using ionization-induced injection. *Physical Review Letters*, 105(10):105003, 2010.

[30] C. E. Clayton, K.-C. Tzeng, D. Gordon, P. Muggli, W. Mori, C. Joshi, V. Malka, Z. Najmudin, A. Modena, D. Neely, et al. Plasma wave generation in a self-focused channel of a relativistically intense laser pulse. *Physical Review Letters*, 81(1):100, 1998.

[31] J. M. Cole, D. R. Symes, N. C. Lopes, J. C. Wood, K. Poder, S. Alatabi, S. W. Botchway, P. S. Foster, S. Gratton, S. Johnson, et al. High-resolution μct of a mouse embryo using a compact laser-driven x-ray betatron source. *Proceedings of the National Academy of Sciences*, 115(25):6335–6340, 2018.

[32] J. M. Cole, J. C. Wood, N. C. Lopes, K. Poder, R. L. Abel, S. Alatabi, J. S. J. Bryant, A. Jin, S. Kneip, K. Mecseki, D. R. Symes, S. P. D. Mangles, and Z. Najmudin. Laser-wakefield accelerators as hard x-ray sources for 3D medical imaging of human bone. *Scientific Reports*, 5, AUG 18 2015.

[33] S. Corde, K. T. Phuoc, G. Lambert, R. Fitour, V. Malka, A. Rousse, A. Beck, and E. Lefebvre. Femtosecond x rays from laser-plasma accelerators. *Reviews of Modern Physics*, 85(1):1, 2013.

[34] C. A. Coverdale, C. B. Darrow, C. D. Decker, W. B. Mori, K. C. Tzeng, K. A. Marsh, C. E. Clayton, and C. Joshi. Propagation of intense subpicosecond laser pulses through underdense plasmas. *Physical Review Letters*, 74(23):4659, 1995.

[35] T. J. Davis, D. Gao, T. E. Gureyev, A. W. Stevenson, and S. W. Wilkins. Phase-contrast imaging of weakly absorbing materials using hard x-rays. *Nature*, 373(6515):595–598, 1995.

[36] M. De Graef and Y. Zhu. Quantitative noninterferometric lorentz microscopy. *Journal of Applied Physics*, 89(11):7177–7179, 2001.

[37] A. F. De Jong, W. Coene, and D. Van Dyck. On the phase-object function, used in dynamical electron diffraction calculations. *Ultramicroscopy*, 23(1):3–15, 1987.

[38] J. Delettrez. Thermal electron transport in direct-drive laser fusion. *Canadian Journal of Physics*, 64(8):932–943, 1986.

[39] J. Delettrez, D. Bradley, P. Jaanimagi, and C. Verdon. Effect of barrier layers in burnthrough experiments with 351-nm laser illumination. *Physical Review A*, 41(10):5583, 1990.

[40] C. A. Di Stefano, G. Malamud, C. C. Kuranz, S. R. Klein, C. Stoeckl, and R. P. Drake. Richtmyer-meshkov evolution under steady shock conditions in the high-energy-density regime. *Applied Physics Letters*, 106:114103, 2015.

[41] F. W. Doss, J. L. Kline, K. A. Flippo, T. S. Perry, B. G. DeVolder, I. Tregillis, E. N. Loomis, E. C. Merritt, T. J. Murphy, L. Welser-Sherrill, et al. The shock/shear platform for planar radiation-hydrodynamics experiments on the national ignition facility. *Physics of Plasmas*, 22(5), 2015.

[42] R. P. Drake. *High-energy-density physics: Foundation of inertial fusion and experimental astrophysics*, pages 398–424. Springer, New York, NY, 2018.

[43] R. P. Drake, D. R. Leibrandt, E. C. Harding, C. C. Kuranz, M. A. Blackburn, H. F. Robey, B. A. Remington, M. J. Edwards, A. R. Miles, T. S. Perry, R. Wallace, H. Louis, J. Knauer, and D. Arnett. Nonlinear mixing behavior of the three-dimensional rayleigh-taylor instability at a decelerating interface. *Physics of Plasmas*, 11(5):2829–2837, 2004.

[44] D. H. Edgell, W. Seka, R. E. Bahr, T. R. Boehly, and M. J. Bonino. Effectiveness of silicon as a laser shinethrough barrier for 351-nm light. *Physics of Plasmas*, 15(9):092704, 2008.

[45] E. Esarey, R. F. Hubbard, W. P. Leemans, A. Ting, and P. Sprangle. Electron injection into plasma wakefields by colliding laser pulses. *Physical Review Letters*, 79(14):2682, 1997.

[46] E. Esarey, C. B. Schroeder, and W. P. Leemans. Physics of laser-driven plasma-based electron accelerators. *Reviews of Modern Physics*, 81(3):1229, 2009.

[47] E. Esarey, B. A. Shadwick, P. Catravas, and W. P. Leemans. Synchrotron radiation from electron beams in plasma-focusing channels. *Physical Review E*, 65(5):056505, 2002.

[48] M. Faubel, S. Schlemmer, and J. P. Toennies. A molecular beam study of the evaporation of water from a liquid jet. *Zeitschrift für Physik D Atoms, Molecules and Clusters*, 10(2):269–277, 1988.

[49] M. Faubel, B. Steiner, and J. P. Toennies. Photoelectron spectroscopy of liquid water, some alcohols, and pure nonane in free micro jets. *The Journal of Chemical Physics*, 106(22):9013–9031, 1997.

[50] J. Faure, Y. Glinec, A. Pukhov, S. Kiselev, S. Gordienko, E. Lefebvre, J.-P. Rousseau, F. Burgy, and V. Malka. A laser-plasma accelerator producing monoenergetic electron beams. *Nature*, 431(7008):541–544, 2004.

[51] J. Faure, C. Rechatin, A. Norlin, A. Lifschitz, Y. Glinec, and V. Malka. Controlled injection and acceleration of electrons in plasma wakefields by colliding laser pulses. *Nature*, 444(7120):737–739, 2006.

[52] S. Fourmaux, S. Corde, K. T. Phuoc, P. Lassonde, G. Lebrun, S. Payeur, F. Martin, S. Sebban, V. Malka, A. Rousse, and J. C. Kieffer. Single shot phase contrast imaging using laser-produced betatron x-ray beams. *Optics Letters*, 36(13):2426–2428, 2011.

[53] S. Fourmaux, E. Hallin, A. Krol, J.-L. Bourgade, and J.-C. Kieffer. X-ray phase contrast imaging of spherical capsules. *Optics Express*, 28(9):13978–13990, APR 27 2020.

[54] H. Fuchs and H. Legge. Flow of a water jet into vacuum. *Acta Astronautica*, 6(9):1213–1226, 1979.

[55] C. Gahn, G. D. Tsakiris, A. Pukhov, J. Meyer-ter Vehn, G. Pretzler, P. Thirolf, D. Habs, and K. J. Witte. Multi-mev electron beam generation by direct laser acceleration in high-density plasma channels. *Physical Review Letters*, 83(23):4772, 1999.

[56] G. Galinis, J. Strucka, J. C. T. Barnard, A. Braun, R. A. Smith, and J. P. Marangos. Micrometer-thickness liquid sheet jets flowing in vacuum. *Review of Scientific Instruments*, 88(8):083117, 2017.

[57] C. G. R. Geddes, K. Nakamura, G. R. Plateau, C. Toth, E. Cormier-Michel, E. Esarey, C. B. Schroeder, J. R. Cary, and W. P. Leemans. Plasma-density-gradient injection of low absolute-momentum-spread electron bunches. *Physical Review Letters*, 100(21):215004, 2008.

[58] C. G. R. Geddes, C. Toth, J. Van Tilborg, E. Esarey, C. B. Schroeder, D. Bruhwiler, C. Nieter, J. Cary, and W. P. Leemans. High-quality electron beams from a laser wakefield accelerator using plasma-channel guiding. *Nature*, 431(7008):538–541, 2004.

[59] P. Gibbon. *Short pulse laser interactions with matter: an introduction*, pages 31–50. World Scientific, London, 2005.

[60] A. J. Gonsalves, K. Nakamura, C. Lin, D. Panasenko, S. Shiraishi, T. Sokollik, C. Benedetti, C. B. Schroeder, C. G. R. Geddes, J. Van Tilborg, et al. Tunable laser plasma accelerator based on longitudinal density tailoring. *Nature Physics*, 7(11):862–866, 2011.

[61] S. Gordienko and A. Pukhov. Scalings for ultrarelativistic laser plasmas and quasimonoenergetic electrons. *Physics of Plasmas*, 12(4), 2005.

[62] D. Gordon, K. C. Tzeng, C. E. Clayton, A. E. Dangor, V. Malka, K. A. Marsh, A. Modena, W. B. Mori, P. Muggli, Z. Najmudin, et al. Observation of electron energies beyond the linear dephasing limit from a laser-excited relativistic plasma wave. *Physical Review Letters*, 80(10):2133, 1998.

[63] M. C. Gower. Industrial applications of laser micromachining. *Optics Express*, 7(2):56–67, 2000.

[64] N. A. M. Hafz, T. M. Jeong, I. W. Choi, S. K. Lee, K. H. Pae, V. V. Kulagin, J. H. Sung, T. J. Yu, K.-H. Hong, T. Hosokai, et al. Stable generation of gev-class electron beams from self-guided laser–plasma channels. *Nature Photonics*, 2(9):571–577, 2008.

[65] G. N. Hall, C. M. Krauland, M. S. Schollmeier, G. E. Kemp, J. G. Buscho, R. Hibbard, N. Thompson, E. R. Casco, M. J. Ayers, S. L. Ayers, et al. The crystal backlighter imager: A spherically bent crystal imager for radiography on the national ignition facility. *Review of Scientific Instruments*, 90(1), 2019.

[66] J. F. Hansen, H. F. Robey, R. I. Klein, and A. R. Miles. Experiment on the mass stripping of an interstellar cloud following shock passage. *The Astrophysical Journal*, 662(1):379, 2007.

[67] P. W. Hatfield, J. A. Gaffney, G. J. Anderson, S. Ali, L. Antonelli, S. Başeğmez du Pree, J. Citrin, M. Fajardo, P. Knapp, B. Kettle, B. Kustowski, M. J. MacDonald, D. Mariscal, M. E. Martin, T. Nagayama, C. A. J. Palmer, J. L. Peterson, S. Rose, J. J. Ruby, C. Shneider, M. J. V. Streeter, W. Trickey, and B. Williams. The data-driven future of high-energy-density physics. *Nature*, 593(7859):351–361, 2021.

[68] Z. H. He, J. A. Nees, B. Hou, K. Krushelnick, and A. G. R. Thomas. Enhancement of plasma wakefield generation and self-compression of femtosecond laser pulses by ionization gradients. *Plasma Physics and Controlled Fusion*, 56(8):084010, 2014.

[69] B. Hidding, G. Pretzler, J. B. Rosenzweig, T. Königstein, D. Schiller, and D. Bruhwiler. Ultracold electron bunch generation via plasma photocathode emission and acceleration in a beam-driven plasma blowout. *Physical Review Letters*, 108(3):035001, 2012.

[70] N. Holtkamp, I. P. Team, et al. An overview of the iter project. *Fusion Engineering and Design*, 82(5-14):427–434, 2007.

[71] A. E. Hussein, N. Senabulya, Y. Ma, M. J. V. Streeter, B. Kettle, S. J. D. Dann, F. Albert, N. Bourgeois, S. Cipiccia, J. M. Cole, et al. Laser-wakefield accelerators for high-resolution x-ray imaging of complex microstructures. *Scientific Reports*, 9(1):3249, 2019.

[72] J. D. Jackson. *Classical electrodynamics*, pages 407–456. American Association of Physics Teachers, New York, 1999.

[73] D. Kaganovich, A. Ting, D. F. Gordon, R. F. Hubbard, T. G. Jones, A. Zigler, and P. Sprangle. First demonstration of a staged all-optical laser wakefield acceleration. *Physics of Plasmas*, 12(10):100702, 2005.

[74] S. Kalmykov, S. A. Yi, V. Khudik, and G. Shvets. Electron self-injection and trapping into an evolving plasma bubble. *Physical Review Letters*, 103(13):135004, 2009.

[75] S. Karsch, J. Osterhoff, A. Popp, T. Rowlands-Rees, Z. Major, M. Fuchs, B. Marx, R. Hörlein, K. Schmid, L. Veisz, et al. Gev-scale electron acceleration in a gas-filled capillary discharge waveguide. *New Journal of Physics*, 9(11):415, 2007.

[76] H. T. Kim, K. H. Pae, H. J. Cha, I. J. Kim, T. J. Yu, J. H. Sung, S. K. Lee, T. M. Jeong, and J. Lee. Enhancement of electron energy to the multi-gev regime by a dual-stage laser-wakefield accelerator pumped by petawatt laser pulses. *Physical Review Letters*, 111(16):165002, 2013.

[77] J. B. Kim, S. Göde, and S. H. Glenzer. Development of a cryogenic hydrogen micro-jet for high-intensity, high-repetition rate experiments. *Review of Scientific Instruments*, 87(11):11E328, 2016.

[78] P. M. King, N. Lemos, J. L. Shaw, A. L. Milder, K. A. Marsh, A. Pak, B. M. Hegelich, P. Michel, J. Moody, C. Joshi, et al. X-ray analysis methods for sources from self-modulated laser wakefield acceleration driven by picosecond lasers. *Review of Scientific Instruments*, 90(3), 2019.

[79] P. Kirkpatrick. On the theory and use of ross filters. *Review of Scientific Instruments*, 10(6):186–191, 1939.

[80] P. Kirkpatrick. Theory and use of ross filters. ii. *Review of Scientific Instruments*, 15(9):223–229, 1944.

[81] S. Kiselev, A. Pukhov, and I. Kostyukov. X-ray generation in strongly nonlinear plasma waves. *Physical Review Letters*, 93(13):135004, 2004.

[82] P. F. Knapp, M. R. Martin, D. Yager-Elorriaga, A. J. Porwitzky, F. W. Doss, G. A. Shipley, C. A. Jennings, D. E. Ruiz, T. Byvank, C. C. Kuranz, et al. A novel, magnetically driven convergent richtmyer–meshkov platform. *Physics of Plasmas*, 27(9), 2020.

[83] S. Kneip, C. McGuffey, F. Dollar, M. Bloom, V. Chvykov, G. Kalintchenko, K. Krushelnick, A. Maksimchuk, S. P. D. Mangles, T. Matsuoka, et al. X-ray phase contrast imaging of biological specimens with femtosecond pulses of betatron radiation from a compact laser plasma wakefield accelerator. *Applied Physics Letters*, 99(9):093701, 2011.

[84] S. Kneip, C. McGuffey, J. L. Martins, S. Martins, C. Bellei, V. Chvykov, F. Dollar, R. Fonseca, C. Huntington, G. Kalintchenko, et al. Bright spatially coherent synchrotron x-rays from a table-top source. *Nature Physics*, 6(12):980–983, 2010.

[85] S. Kneip, S. R. Nagel, C. Bellei, N. Bourgeois, A. E. Dangor, A. Gopal, R. Heathcote, S. P. D. Mangles, J. R. Marques, A. Maksimchuk, et al. Observation of synchrotron radiation from electrons accelerated in a petawatt-laser-generated plasma cavity. *Physical Review letters*, 100(10):105006, 2008.

[86] J. D. Koralek, J. B. Kim, P. Brža, C. B. Curry, Z. Chen, H. A. Bechtel, A. A. Cordones, P. Sperling, S. Toleikis, J. F. Kern, et al. Generation and characterization of ultrathin free-flowing liquid sheets. *Nature Communications*, 9(1):1–8, 2018.

[87] I. Kostyukov, S. Kiselev, and A. Pukhov. X-ray generation in an ion channel. *Physics of Plasmas*, 10(12):4818–4828, 2003.

[88] I. Kostyukov, A. Pukhov, and S. Kiselev. Phenomenological theory of laser-plasma interaction in "bubble" regime. *Physics of Plasmas*, 11(11):5256–5264, 2004.

[89] H. Kotaki, S. Masuda, M. Kando, J. K. Koga, and K. Nakajima. Head-on injection of a high quality electron beam by the interaction of two laser pulses. *Physics of Plasmas*, 11(6):3296–3302, 2004.

[90] A. L. Kritcher, A. B. Zylstra, D. A. Callahan, O. A. Hurricane, C. R. Weber, D. S. Clark, C. V. Young, J. E. Ralph, D. T. Casey, A. Pak, et al. Design of an inertial fusion experiment exceeding the lawson criterion for ignition. *Physical Review E*, 106(2):025201, 2022.

[91] W. L. Kruer. *The physics of laser-plasma interactions*, pages 60–61. Addison-Wesley, New York, Redwood City, CA, 1988.

[92] N. L. Kugland, D. D. Ryutov, C. Plechaty, J. S. Ross, and H.-S. Park. Invited article: Relation between electric and magnetic field structures and their proton-beam images. *Review of Scientific Instruments*, 83(10), 2012.

[93] C. C. Kuranz, B. E. Blue, R. P. Drake, H. F. Robey, J. F. Hansen, J. P. Knauer, M. J. Grosskopf, C. Krauland, and D. C. Marion. Dual, orthogonal, backlit pinhole radiography in OMEGA experiments. *Review of Scientific Instruments*, 77(10), OCT 2006. 16th Topical Conference on High-Temperature Plasma Diagnostics, Williamsburg, VA, MAY 07-11, 2006.

[94] C. C. Kuranz, R. P. Drake, M. J. Grosskopf, A. Budde, C. Krauland, D. C. Marion, A. J. Visco, J. R. Ditmar, H. F. Robey, B. A. Remington, et al. Three-dimensional blast-wave-driven rayleigh–taylor instability and the effects of long-wavelength modes. *Physics of Plasmas*, 16(5), 2009.

[95] C. C. Kuranz, R. P. Drake, E. C. Harding, M. J. Grosskopf, H. F. Robey, B. A. Remington, M. J. Edwards, A. R. Miles, T. S. Perry, T. Plewa, N. C. Hearn, J. P. Knauer, D. Arnett, and D. R. Leibrandt. Two-dimensional blast-wave-driven rayleigh-taylor instability: experiment and simulation. *Astrophysical Journal*, 696:749–759, 2009.

[96] C. C. Kuranz, H.-S. Park, C. M. Huntington, A. R. Miles, B. A. Remington, T. Plewa, M. Trantham, H. F. Robey, D. Shvarts, A. Shimony, et al. How high energy fluxes may affect rayleigh–taylor instability growth in young supernova remnants. *Nature Communications*, 9(1):1564, 2018.

[97] C. C. Kuranz, H.-S. Park, C. M. Huntington, A. R. Miles, B. A. Remington, T. Plewa, M. A. Trantham, D. Shvarts, A. Shimony, K. Raman, S. MacLaren, W. C. Wan, F. W. Doss, J. Kline, K. A. Flippo, G. Malamud, T. A. Handy, S. Prisbey, C. M. Krauland, S. R. Klein, E. C. Harding, R. Wallace, M. Grosskopf, D. C. Marion, D. Kalantar, E. Giraldez, and R. P. Drake. How high energy fluxes may affect rayleigh-taylor instability growth in young supernova remnants. *Nature Communications*, 9:1564, 2018.

[98] L. D. Landau and E. M. Lifshitz. Fluid mechanics. *Course of Theoretical Physics (Pergamon Press, Oxford, 1987)*, 1987. [Translated from the Russian by JB Sykes and WH Reid].

[99] Lawrence Livermore National Laboratory, 2020. [Online; accessed May 25, 2023]: URL: https://lasers.llnl.gov/news/improving-understanding-of-nif-implosion-instabilities.

[100] Lawrence Livermore National Laboratory, 2022. [Online; accessed May 25, 2023] URL: https://www.llnl.gov/news/lawrence-livermore-national-laboratory-achieves-fusion-ignition.

[101] W. P. Leemans, A. J. Gonsalves, H.-S. Mao, K. Nakamura, C. Benedetti, C. B. Schroeder, C. Tóth, J. Daniels, D. E. Mittelberger, S. S. Bulanov, et al. Multi-gev electron beams from capillary-discharge-guided subpetawatt laser pulses in the self-trapping regime. *Physical Review Letters*, 113(24):245002, 2014.

[102] W. P. Leemans, B. Nagler, A. J. Gonsalves, C. Tóth, K. Nakamura, C. G. R. Geddes, E. Esarey, C. B. Schroeder, and S. Hooker. Gev electron beams from a centimetre-scale accelerator. *Nature Physics*, 2(10):696–699, 2006.

[103] N. Lemos, F. Albert, J. L. Shaw, D. Papp, R. Polanek, P. King, A. Milder, K. A. Marsh, A. Pak, B. B. Pollock, et al. Bremsstrahlung hard x-ray source driven by an electron beam from a self-modulated laser wakefield accelerator. *Plasma Physics and Controlled Fusion*, 60(5):054008, 2018.

[104] J. Lindl. *Inertial confinement fusion: The quest for ignition and energy gain using indirect drive*, pages 101–197. AIP-Press, College Park, MD, 1998.

[105] J. S. Liu, C. Q. Xia, W. T. Wang, H. Y. Lu, C. Wang, A. H. Deng, W. T. Li, H. Zhang, X. Y. Liang, Y. X. Leng, et al. All-optical cascaded laser wakefield accelerator using ionization-induced injection. *Physical Review Letters*, 107(3):035001, 2011.

[106] R. Liu, Z. Wang, T. Sparks, F. Liou, and J. Newkirk. Aerospace applications of laser additive manufacturing. In *Laser Additive Manufacturing*, pages 351–371. Elsevier, 2017.

[107] W. Lu, C. Huang, M. Zhou, M. Tzoufras, F. Tsung, W. B. Mori, and T. Katsouleas. A nonlinear theory for multidimensional relativistic plasma wave wakefields. *Physics of Plasmas*, 13(5):056709, 2006.

[108] W. Lu, M. Tzoufras, C. Joshi, F. S. Tsung, W. B. Mori, J. Vieira, R. A. Fonseca, and L. O. Silva. Generating multi-gev electron bunches using single stage laser wakefield acceleration in a 3d nonlinear regime. *Physical Review Special Topics-Accelerators and Beams*, 10(6):061301, 2007.

[109] W. Lu, M. Tzoufras, C. Joshi, F. S. Tsung, W. B. Mori, J. Vieira, R. A. Fonseca, and L. O. Silva. Generating multi-gev electron bunches using single stage laser wakefield acceleration in a 3d nonlinear regime. *Physical Review Accelerators and Beams*, 10:061301, 2007.

[110] S. P. D. Mangles, G. Genoud, M. S. Bloom, M. Burza, Z. Najmudin, A. Persson, K. Svensson, A. G. R. Thomas, and C.-G. Wahlström. Self-injection threshold in self-guided laser wakefield accelerators. *Physical Review Special Topics-Accelerators and Beams*, 15(1):011302, 2012.

[111] S. P. D. Mangles, C. D. Murphy, Z. Najmudin, A. G. R. Thomas, J. L. Collier, A. E. Dangor, E. J. Divall, P. S. Foster, J. G. Gallacher, C. J. Hooker, et al. Monoenergetic beams of relativistic electrons from intense laser-plasma interactions. *Nature*, 431(7008):535–538, 2004.

[112] S. P. D. Mangles, A. G. R. Thomas, M. C. Kaluza, O. Lundh, F. Lindau, A. Persson, Z. Najmudin, C.-G. Wahlström, C. Murphy, C. Kamperidis, et al. Effect of laser contrast ratio on electron beam stability in laser wakefield acceleration experiments. *Plasma Physics and Controlled Fusion*, 48(12B):B83, 2006.

[113] S. P. D. Mangles, B. R. Walton, M. Tzoufras, Z. Najmudin, R. J. Clarke, A. E. Dangor, R. G. Evans, S. Fritzler, A. Gopal, C. Hernandez-Gomez, et al. Electron acceleration in cavitated channels formed by a petawatt laser in low-density plasma. *Physical Review Letters*, 94(24):245001, 2005.

[114] M. Markevitch and A. Vikhlinin. Shocks and cold fronts in galaxy clusters. *Physics Reports*, 443(1):1–53, 2007.

[115] J. L. Martins, S. F. Martins, R. A. Fonseca, and L. O. Silva. Radiation post-processing in pic codes. In *Harnessing relativistic plasma waves as novel radiation sources from terahertz to X-Rays and beyond*, volume 7359, pages 214–221. SPIE, 2009.

[116] J. L. Martins, S. F. Martins, R. A. Fonseca, and L. O. Silva. Radiation in 1.5 gev and 12 gev laser wakefield acceleration stages from pic simulations. In *AIP Conference Proceedings*, volume 1299, pages 191–196. American Institute of Physics, 2010.

[117] J. L. Martins, S. F. Martins, R. A. Fonseca, and L. O. Silva. X-ray modeling in laser-wakefield accelerators. *IEEE Transactions on Plasma Science*, 39(11):2826–2827, 2011.

[118] C. McGuffey, T. Matsuoka, S. Kneip, W. Schumaker, F. Dollar, C. Zulick, V. Chvykov, G. Kalintchenko, V. Yanovsky, A. Maksimchuk, et al. Experimental laser wakefield acceleration scalings exceeding 100 tw. *Physics of Plasmas*, 19(6):063113, 2012.

[119] C. McGuffey, A. G. R. Thomas, W. Schumaker, T. Matsuoka, V. Chvykov, F. J. Dollar, G. Kalintchenko, V. Yanovsky, A. Maksimchuk, K. Krushelnick, et al. Ionization induced trapping in a laser wakefield accelerator. *Physical Review Letters*, 104(2):025004, 2010.

[120] E. Meijering, M. Jacob, J.-C. Sarria, P. L. Steiner, H. Hirling, and E. M. Unser. Design and validation of a tool for neurite tracing and analysis in fluorescence microscopy images. *Cytometry Part A: the journal of the International Society for Analytical Cytology*, 58(2):167–176, 2004.

[121] A. Modena, Z. Najmudin, A. E. Dangor, C. E. Clayton, K. A. Marsh, C. Joshi, V. Malka, C. B. Darrow, C. Danson, D. Neely, et al. Electron acceleration from the breaking of relativistic plasma waves. *Nature*, 377(6550):606–608, 1995.

[122] W. B. Mori. The physics of the nonlinear optics of plasmas at relativistic intensities for short-pulse lasers. *IEEE Journal of Quantum Electronics*, 33(11):1942–1953, 1997.

[123] S. R. Nagel, K. S. Raman, C. M. Huntington, S. A. MacLaren, P. Wang, M. A. Barrios, T. Baumann, J. D. Bender, L. R. Benedetti, D. M. Doane, et al. A platform for studying the rayleigh–taylor and richtmyer–meshkov instabilities in a planar geometry at high energy density at the national ignition facility. *Physics of Plasmas*, 24(7), 2017.

[124] Z. Najmudin, K. Krushelnick, E. Clark, S. P. D. Mangles, B. Walton, A. Dangor, S. Fritzler, V. Malka, E. Lefebvre, D. Gordon, et al. Self-modulated wakefield and forced laser wakefield acceleration of electrons. *Physics of Plasmas*, 10(5):2071–2077, 2003.

[125] K. Nakamura, W. Wan, N. Ybarrolaza, D. Syversrud, J. Wallig, and W. P. Leemans. Broadband single-shot electron spectrometer for gev-class laser-plasma-based accelerators. *Review of Scientific Instruments*, 79(5), 2008.

[126] K. Nemeth, B. Shen, Y. Li, H. Shang, R. Crowell, K. C. Harkay, and J. R. Cary. Laser-driven coherent betatron oscillation in a laser-wakefield cavity. *Physical Review Letters*, 100(9):095002, 2008.

[127] A. Olivo. Towards the exploitation of phase effects in clinical synchrotron radiation radiology. *Nuclear Instruments and Methods in Physics Research Section A: Accelerators, Spectrometers, Detectors and Associated Equipment*, 548(1-2):194–199, 2005.

[128] A. Olivo and R. Speller. Experimental validation of a simple model capable of predicting the phase contrast imaging capabilities of any x-ray imaging system. *Physics in Medicine & Biology*, 51(12):3015, 2006.

[129] D. Paganin, S. C. Mayo, T. E. Gureyev, P. R. Miller, and S. W. Wilkins. Simultaneous phase and amplitude extraction from a single defocused image of a homogeneous object. *Journal of Microscopy*, 206(1):33–40, 2002.

[130] D. Paganin and K. A. Nugent. Noninterferometric phase determination. In *Advances in Imaging and Electron Physics*, volume 118, pages 85–127. Elsevier, 2001.

[131] A. Pak, K. Marsh, S. Martins, W. Lu, W. Mori, and C. Joshi. Injection and trapping of tunnel-ionized electrons into laser-produced wakes. *Physical Review Letters*, 104(2):025003, 2010.

[132] H.-S. Park, D. M. Chambers, H.-K. Chung, R. J. Clarke, R. Eagleton, E. Giraldez, T. Goldsack, R. Heathcote, N. Izumi, M. H. Key, et al. High-energy kα radiography using high-intensity, short-pulse lasers. *Physics of Plasmas*, 13(5), 2006.

[133] Q. Peng, A. Juzeniene, J. Chen, L. O. Svaasand, T. Warloe, K.-E. Giercksky, and J. Moan. Lasers in medicine. *Reports on Progress in Physics*, 71(5):056701, 2008.

[134] A. Peterzol, A. Olivo, L. Rigon, S. Pani, and D. Dreossi. The effects of the imaging system on the validity limits of the ray-optical approach to phase contrast imaging. *Medical Physics*, 32(12):3617–3627, 2005.

[135] B. B. Pollock, C. E. Clayton, J. E. Ralph, F. Albert, A. Davidson, L. Divol, C. Filip, S. H. Glenzer, K. Herpoldt, W. Lu, et al. Demonstration of a narrow energy spread, 0.5 gev electron beam from a two-stage laser wakefield accelerator. *Physical Review Letters*, 107(4):045001, 2011.

[136] A. Pukhov and J. Meyer-ter Vehn. Laser wakefield acceleration: the highly non-linear broken-wave regime. *Applied Physics B*, 74:355–361, 2002.

[137] A. Pukhov, Z.-M. Sheng, and J. Meyer-ter Vehn. Particle acceleration in relativistic laser channels. *Physics of Plasmas*, 6(7):2847–2854, 1999.

[138] B. A. Remington, H.-S. Park, D. T. Casey, R. M. Cavallo, D. S. Clark, C. M. Huntington, D. H. Kalantar, C. C. Kuranz, A. R. Miles, S. R. Nagel, et al. Rayleigh–taylor instabilities in high-energy density settings on the national ignition facility. *Proceedings of the National Academy of Sciences*, 116(37):18233–18238, 2019.

[139] R. D. Richtmyer. Taylor instability in shock acceleration of compressible fluids. Technical report, Los Alamos Scientific Lab., N. Mex., 1954.

[140] M. D. Rosen. Fundamentals of icf hohlraums. Technical report, Lawrence Livermore National Lab.(LLNL), Livermore, CA (United States), 2005.

[141] P. Ross. Minutes of the oakland meeting. *Physical Review*, 29(425), 1926.

[142] A. Rousse, K. T. Phuoc, R. Shah, A. Pukhov, E. Lefebvre, V. Malka, S. Kiselev, F. Burgy, J.-P. Rousseau, D. Umstadter, et al. Production of a kev x-ray beam from synchrotron radiation in relativistic laser-plasma interaction. *Physical Review Letters*, 93(13):135005, 2004.

[143] H. R. Russell, B. R. McNamara, J. S. Sanders, A. C. Fabian, P. E. J. Nulsen, R. E. A. Canning, S. A. Baum, M. Donahue, A. C. Edge, L. J. King, et al. Shock fronts, electron–ion equilibration and intracluster medium transport processes in the merging cluster abell 2146. *Monthly Notices of the Royal Astronomical Society*, 423(1):236–255, 2012.

[144] S. M. Rytov, A. Kravtsov, and V. Tatarskii. *Principles of statistical radiophysics: wave propagation through random media*, volume 4, pages 141–152. Springer, Berlin; New York, 1989.

[145] M. I. K. Santala, Z. Najmudin, E. L. Clark, M. Tatarakis, K. Krushelnick, A. E. Dangor, V. Malka, J. Faure, R. Allott, and R. J. Clarke. Observation of a hot high-current electron beam from a self-modulated laser wakefield accelerator. *Physical Review Letters*, 86(7):1227, 2001.

[146] K. Schmid, A. Buck, C. M. S. Sears, J. M. Mikhailova, R. Tautz, D. Herrmann, M. Geissler, F. Krausz, and L. Veisz. Density-transition based electron injector for laser driven wakefield accelerators. *Physical Review Special Topics-Accelerators and Beams*, 13(9):091301, 2010.

[147] C. B. Schroeder, E. Esarey, and B. A. Shadwick. Warm wave breaking of nonlinear plasma waves with arbitrary phase velocities. *Physical Review E*, 72(5):055401, 2005.

[148] A. Schropp, R. Hoppe, V. Meier, J. Patommel, F. Seiboth, Y. Ping, D. G. Hicks, M. A. Beckwith, G. W. Collins, A. Higginbotham, J. S. Wark, H. J. Lee, B. Nagler, E. C. Galtier, B. Arnold, U. Zastrau, J. B. Hastings, and C. G. Schroer. Imaging shock waves in diamond with both high temporal and spatial resolution at an XFEL. *Scientific Reports*, 5, 2015.

[149] W. Schumaker, N. Nakanii, C. McGuffey, C. Zulick, V. Chyvkov, F. Dollar, H. Habara, G. Kalintchenko, A. Maksimchuk, K. Tanaka, et al. Ultrafast electron radiography of magnetic fields in high-intensity laser-solid interactions. *Physical Review Letters*, 110(1):015003, 2013.

[150] G. Schurtz, P. D. Nicolaï, and M. Busquet. A nonlocal electron conduction model for multidimensional radiation hydrodynamics codes. *Physics of Plasmas*, 7(10):4238–4249, 2000.

[151] R. C. Shah, F. Albert, K. T. Phuoc, O. Shevchenko, D. Boschetto, A. Pukhov, S. Kiselev, F. Burgy, J.-P. Rousseau, and A. Rousse. Coherence-based transverse measurement of synchrotron x-ray radiation from relativistic laser-plasma interaction and laser-accelerated electrons. *Physical Review E*, 74(4):045401, 2006.

[152] R. J. Shalloo, S. J. D. Dann, J.-N. Gruse, C. I. D. Underwood, A. F. Antoine, C. Arran, M. Backhouse, C. D. Baird, M. D. Balcazar, N. Bourgeois, et al. Automation and control of laser wakefield accelerators using bayesian optimization. *Nature Communications*, 11(1):6355, 2020.

[153] M. Sherlock, J. P. Brodrick, and C. P. Ridgers. A comparison of non-local electron transport models for laser-plasmas relevant to inertial confinement fusion. *Physics of Plasmas*, 24(8):082706, 2017.

[154] W. Shi, Q. Fang, X. Zhu, R. A. Norwood, and N. Peyghambarian. Fiber lasers and their applications. *Applied Optics*, 53(28):6554–6568, 2014.

[155] A. E. Siegman. *Lasers*, pages 2–76. University science books, Mill Valley, CA, 1986.

[156] V. A. Smalyuk, M. Barrios, J. A. Caggiano, D. T. Casey, C. J. Cerjan, D. S. Clark, M. J. Edwards, J. A. Frenje, M. Gatu-Johnson, V. Y. Glebov, et al. Hydrodynamic instability growth and mix experiments at the national ignition facility. *Physics of Plasmas*, 21(5):056301, 2014.

[157] V. A. Smalyuk, J. F. Hansen, O. A. Hurricane, G. Langstaff, D. Martinez, H.-S. Park, K. Raman, B. Remington, H. Robey, O. Schilling, et al. Experimental observations of turbulent mixing due to kelvin–helmholtz instability on the omega laser facility. *Physics of Plasmas*, 19(9), 2012.

[158] V. A. Smalyuk, C. R. Weber, O. L. Landen, S. Ali, B. Bachmann, P. M. Celliers, E. L. Dewald, A. Fernandez, B. A. Hammel, G. Hall, et al. Review of hydrodynamic instability experiments in inertially confined fusion implosions on national ignition facility. *Plasma Physics and Controlled Fusion*, 62(1):014007, 2019.

[159] A. Snigirev, I. Snigireva, V. Kohn, S. Kuznetsov, and I. Schelokov. On the possibilities of x-ray phase contrast microimaging by coherent high-energy synchrotron radiation. *Review of Scientific Instruments*, 66(12):5486–5492, 1995.

[160] L. Spitzer. *Physics of fully ionized gases*. Courier Corporation, 2006.

[161] P. Sprangle, E. Esarey, and A. Ting. Nonlinear theory of intense laser-plasma interactions. *Physical Review Letters*, 64(17):2011, 1990.

[162] C. A. Stan, D. Milathianaki, H. Laksmono, R. G. Sierra, T. A. McQueen, M. Messerschmidt, G. J. Williams, J. E. Koglin, T. J. Lane, M. J. Hayes, et al. Liquid explosions induced by x-ray laser pulses. *Nature Physics*, 12(10):966–971, 2016.

[163] E. A. Startsev and C. J. McKinstrie. Multiple scale derivation of the relativistic ponderomotive force. *Physical Review E*, 55(6):7527, 1997.

[164] S. Steinke, J. Van Tilborg, C. Benedetti, C. G. R. Geddes, C. B. Schroeder, J. Daniels, K. K. Swanson, A. J. Gonsalves, K. Nakamura, N. H. Matlis, et al. Multistage coupling of independent laser-plasma accelerators. *Nature*, 530(7589):190–193, 2016.

[165] C. Stoeckl, G. Fiksel, D. Guy, C. Mileham, P. M. Nilson, T. C. Sangster, M. J. Shoup, III, and W. Theobald. A spherical crystal imager for omega ep. *Review of Scientific Instruments*, 83(3), 2012.

[166] D. Strickland and G. Mourou. Compression of amplified chirped optical pulses. *Optics Communications*, 55(6):447–449, 1985.

[167] K. Ta Phuoc, R. Fitour, A. Tafzi, T. Garl, N. Artemiev, R. Shah, F. Albert, D. Boschetto, A. Rousse, D. Kim, et al. Demonstration of the ultrafast nature of laser-produced betatron radiation. *Physics of Plasmas*, 14(8):080701, 2007.

[168] T. Tajima and J. M. Dawson. Laser electron accelerator. *Physical Review Letters*, 43(4):267, 1979.

[169] M. R. Teague. Deterministic phase retrieval: a green's function solution. *Journal of the Optical Society of America*, 73(11):1434–1441, 1983.

[170] A. G. R. Thomas, C. D. Murphy, S. P. D. Mangles, A. E. Dangor, P. Foster, J. G. Gallacher, D. A. Jaroszynski, C. Kamperidis, K. Lancaster, P. A. Norreys, et al. Monoenergetic electronic beam production using dual collinear laser pulses. *Physical Review Letters*, 100(25):255002, 2008.

[171] R. Tommasini, C. Bailey, D. K. Bradley, M. Bowers, H. Chen, J. M. Di Nicola, P. Di Nicola, G. Gururangan, G. Hall, C. M. Hardy, et al. Short pulse, high resolution, backlighters for point projection high-energy radiography at the national ignition facility. *Physics of Plasmas*, 24(5), 2017.

[172] D. Umstadter, J. K. Kim, and E. Dodd. Laser injection of ultrashort electron pulses into wakefield plasma waves. *Physical Review Letters*, 76(12):2073, 1996.

[173] C. Underwood, G. Gan, Z.-H. He, C. Murphy, A. Thomas, K. Krushelnick, and J. Nees. Characterization of flowing liquid films as a regenerating plasma mirror for high repetition-rate laser contrast enhancement. *Laser and Particle Beams*, 38(2):128–134, 2020.

[174] M. Vargas, W. Schumaker, Z.-H. He, K. Behm, V. Chvykov, B. Hou, K. Krushelnick, A. Maksimchuk, J. A. Nees, V. Yanovsky, Z. Zhao, and A. G. R. Thomas. X-ray phase contrast imaging of additive manufactured structures using a laser wakefield accelerator. *Plasma Physics and Controlled Fusion*, 61(5), 2019.

[175] M. Vargas, W. Schumaker, Z.-H. He, Z. Zhao, K. Behm, V. Chvykov, B. Hou, K. Krushelnick, A. Maksimchuk, V. Yanovsky, et al. Improvements to laser wakefield accelerated electron beam stability, divergence, and energy spread using three-dimensional printed two-stage gas cell targets. *Applied Physics Letters*, 104(17):174103, 2014.

[176] A. Velikovich and L. Phillips. Instability of a plane centered rarefaction wave. *Physics of Fluids*, 8(4):1107–1118, 1996.

[177] A. L. Velikovich. Analytic theory of richtmyer–meshkov instability for the case of reflected rarefaction wave. *Physics of Fluids*, 8(6):1666–1679, 1996.

[178] P. A. Walker, N. Bourgeois, W. Rittershofer, J. Cowley, N. Kajumba, A. R. Maier, J. Wenz, C. M. Werle, S. Karsch, F. Grüner, et al. Investigation of gev-scale electron acceleration in a gas-filled capillary discharge waveguide. *New Journal of Physics*, 15(4):045024, 2013.

[179] W. C. Wan, G. Malamud, A. Shimony, C. A. Di Stefano, M. R. Trantham, S. R. Klein, D. Shvarts, C. C. Kuranz, and R. P. Drake. Observation of single-mode, kelvin-helmholtz instability in a supersonic flow. *Physical Review Letters*, 115(4):5001, 2015.

[180] Y. Wan, O. Seemann, S. Tata, I. A. Andriyash, S. Smartsev, E. Kroupp, and V. Malka. Direct observation of relativistic broken plasma waves. *Nature Physics*, 18(10):1186–1190, 2022.

[181] S. Wang, C. E. Clayton, B. E. Blue, E. S. Dodd, K. A. Marsh, W. B. Mori, C. Joshi, S. Lee, P. Muggli, T. Katsouleas, et al. X-ray emission from betatron motion in a plasma wiggler. *Physical Review Letters*, 88(13):135004, 2002.

[182] X. Wang, R. Zgadzaj, N. Fazel, Z. Li, S. A. Yi, X. Zhang, W. Henderson, Y.-Y. Chang, R. Korzekwa, H.-E. Tsai, et al. Quasi-monoenergetic laser-plasma acceleration of electrons to 2 gev. *Nature Communications*, 4(1):1–9, 2013.

[183] R. W. Waynant. *Lasers in medicine*, pages 211–325. CRC press, New York, 2011.

[184] J. Wenz and S. Karsch. Physics of laser-wakefield accelerators (lwfa). *arXiv preprint arXiv:2007.04622*, 2020.

[185] S. W. Wilkins, T. E. Gureyev, D. Gao, A. Pogany, and A. W. Stevenson. Phase-contrast imaging using polychromatic hard x-rays. *Nature*, 384(6607):335–338, NOV 28 1996.

[186] J. C. Wood, D. J. Chapman, K. Poder, N. C. Lopes, M. E. Rutherford, T. G. Whites, F. Albert, K. T. Behm, N. Booth, J. S. J. Bryant, P. S. Foster, S. Glanzer, E. Hill, K. Krushelnick, Z. Najmudin, B. B. Pollock, S. Rose, W. Schumaker, R. H. H. Scott, M. Sherlock, A. G. R. Thomas, Z. Zhao, D. E. Eakins, and S. P. D. Mangles. Ultrafast imaging of laser-driven shock waves using betatron X-rays from a laser wakefield accelerator. *Scientific Reports*, 8, 2018.

[187] J. Workman, J. Cobble, K. Flippo, D. C. Gautier, D. S. Montgomery, and D. T. Offermann. Phase-contrast imaging using ultrafast x-rays in laser-shocked materials. *Review of Scientific Instruments*, 81(10), OCT 2010. 18th Topical Conference on High-Temperature Plasma Diagnostics, Wildwood, NJ, MAY 16-20, 2010.

[188] J. G. Wouchuk and F. Cobos-Campos. Linear theory of richtmyer–meshkov like flows. *Plasma Physics and Controlled Fusion*, 59(1):014033, 2016.

[189] C. Yamanaka. Inertial confinement fusion: The quest for ignition and energy gain using indirect drive, 1999.

[190] C. J. Zhang, J. F. Hua, Y. Wan, C.-H. Pai, B. Guo, J. Zhang, Y. Ma, F. Li, Y. P. Wu, H.-H. Chu, et al. Femtosecond probing of plasma wakefields and observation of the plasma wake reversal using a relativistic electron bunch. *Physical Review Letters*, 119(6):064801, 2017.

[191] C. J. Zhang, J. F. Hua, X. L. Xu, F. Li, C.-H. Pai, Y. Wan, Y. Wu, Y. Q. Gu, W. B. Mori, C. Joshi, et al. Capturing relativistic wakefield structures in plasmas using ultrashort high-energy electrons as a probe. *Scientific Reports*, 6(1):29485, 2016.

[192] O. Zhou, H.-E. Tsai, T. M. Ostermayr, L. Fan-Chiang, J. Van Tilborg, C. B. Schroeder, E. Esarey, and C. G. R. Geddes. Effect of nozzle curvature on supersonic gas jets used in laser–plasma acceleration. *Physics of Plasmas*, 28(9), 2021.

[193] A. B. Zylstra, O. A. Hurricane, D. A. Callahan, A. L. Kritcher, J. E. Ralph, H. F. Robey, J. S. Ross, C. V. Young, K. L. Baker, D. T. Casey, et al. Burning plasma achieved in inertial fusion. *Nature*, 601(7894):542–548, 2022.

[194] A. B. Zylstra, A. L. Kritcher, O. A. Hurricane, D. A. Callahan, J. E. Ralph, D. T. Casey, A. Pak, O. L. Landen, B. Bachmann, K. L. Baker, et al. Experimental achievement and signatures of ignition at the national ignition facility. *Physical Review E*, 106(2):025202, 2022.